Improvement of the Performance of Broad Energy Germanium Detectors for Gamma-ray Spectroscopy

Thesis submitted in accordance with the requirements of
the University of Liverpool for the degree of Doctor in Philosophy
by

Najat Ali

September 2017

Acknowledgements

I would like to take this opportunity to thank people who have helped me over the last four years and made this work possible. I would not be able to mention them all as I am sure to forget some, but I will try and list a few of them. Apologies if I miss you out.

I start by thanking my supervisor Dr. Andy Boston for firstly granting me the chance to pursue my PhD within the nuclear physics group at the University of Liverpool and for his constant help and support throughout the entire course of my work. I would like to thank him for his patience, advice and encouragement over the last four years.

Many thanks go out to Prof. Paul Nolan for the useful discussion and feedback on the work presented in Chapter 5. Special thanks to Dr. Dan Judson who never fails to help me out in my lab work, I can never describe his support that gave me when I needed it the most. Thanks must go to Dr. Carl Unsworth and my colleague Craig for their help about the MTSort stuff.

I would also like to take this opportunity to thank the whole nuclear physics group who have made my PhD journey so great. Words cannot express thanks enough to my colleagues, past and present, for every moment we have shared in the last four years. Special thanks to the PhD students who have been there for me on the viva day, and thanks so much for the cakes and drinks! That is highly appreciated, you made me feel home.

Finally, I would like to thank my family for their great support and encouragement, not only through this course but always in everyday life. My mum and dad; Turkia and Ali, my husband; Abdulati, my brothers; Abdul-hakiem, Norie, Abdul-kariem, Omar, Tohami, and of course, my (little helpers!) sons; Yazed and Ahmed, I would never have been able to finish my study without you. Thanks very much!

Abstract

The project presented in this thesis aims at improving the performance of High Purity Germanium (HPGe) detectors through the optimisation of their peak-to-Compton (P/C) response, which in turn will improve the sensitivity of these detectors. This can benefit different applications of HPGe detectors such as dosimetry, radioactive waste characterisation and environmental sample counting. In order to achieve this goal, the application of Pulse Shape Analysis (PSA) to gamma-ray spectroscopy measurements was carried out with a Canberra unique Broad Energy Germanium (BEGe) detector using a calibration source and an environmental sample in a Marinelli counting geometry.

The first stage of the PSA technique applied in this work was the storage of a data set containing 1024 samples of the charge signal induced for each event, the Moving Window Deconvolution (MWD) derived energy and the time stamp information. This has been accomplished using a full digital acquisition system, which makes use of the Caen DT5780 digitiser with 100MHz sampling rate and 14bit dynamic range. Once the data have been stored, they were investigated offline using the MTSort software in order to extract the required information.

The offline analysis, which is the second stage of PSA in this work, involved the calculation of the pulse height of the stored signals, which reflects the energy deposited inside the detector, using the baseline average window determination method. In addition to this, the considered risetime parameters t30 and t90 (the times taken for the pulse to rise from 10% to 30% and 10% to 90% of its maximum height) were measured for all recorded pulse shapes. As the interactions occur in different positions within the detector and hence different charge trajectories, there was a variation in the calculated risetime, producing a distribution in time.

To account for these effects, risetime filtering was employed. In this, matrices of t90 versus t30 distributions were obtained for the different gamma radiations emitted by the calibration source. This allowed the P/C ratio to be optimised by preferentially selecting risetime regions of interest on the t90 vs. t30 maps, where full-energy photopeaks events are more likely to be located on these risetime distributions. Setting risetime regions of interest on these maps is referred in this work as risetime filters (or gates). Energy spectra have been successfully reconstructed from the selected events using each risetime map. A detailed spectroscopic analysis has been carried out for the created energy spectra to assess the efficacy of the risetime filters applied. This has been performed through quantitatively measuring the P/C ratios for full-energy photopeaks in the post-filtered energy spectra. In addition, the ratio efficiency of photopeaks has been measured using the post-filtered energy spectra. The methodology and results of the successful application of PSA to the recorded charge signals have been presented. The results

have shown that the optimised P/C ratio obtained after the successful application of PSA has increased, for example, 33% for ^{241}Am, 37% for ^{137}Cs, and 38% for ^{40}K. The main parametric PSA algorithms that have successfully improved the P/C response can now be implemented in the Caen firmware to be used for detector applications such as environmental sample counting or nuclear waste essays.

Contents

List of Figures

List of Tables

Chapter 1

Introduction

BEGe detectors [Can14] are a particular class of HPGe detectors, which can be used to detect gamma rays in a broad energy interval, typically from 3 keV to 3 MeV. The configuration of the BEGe detector crystal is characterised by the short and flat cylindrical shape, which greatly improves the efficiency below 1 MeV for samples counted close to the detector.

The BEGe detectors are of point contact design having a unique electrode structure that serves to minimise series noise through a reduction of capacitance, resulting in excellent energy resolution, in both low and high energy regions, in addition to a low energy performance. They are fabricated from a highly purified material with a low impurity profile that improves charge collection at high energies. This ensures good peak shape over the entire mid-range, where most tightly grouped gamma-ray photopeaks of interest (e.g. environmental spectra) are located. BEGe detectors are commercially available detectors, provided by Canberra, with active areas from 20 cm^2 to 65 cm^2 and with thicknesses ranging from 20 to 30 mm. They are normally provided with thin composite carbon windows, so that transmission as low as 10 keV is facilitated. Section 4.1 gives a full description of the configuration of the BEGe detector used in this work.

There are many applications in which BEGe Detectors can be utilised:

- Routine sample counting.
- Internal dosimetry applications such as actinide lung burden analysis.
- Nuclear waste assay systems particularly those involving special nuclear materials.
- Environmental sample counting.
- Academic research for studying the neutrinoless double beta decay such as the GERmanium Detector Array (GERDA) [M+11a].

1.1 Operational Characteristics of γ-ray Spectrometers

Germanium detectors are major of importance in gamma-ray spectroscopy applications and their performance can be measured quantitatively using the energy resolution, counting efficiency and P/C ratio. A full understanding of these indices is needed to allow the efficiency of a detector for a particular application to be determined.

1.1.1 Energy Resolution

The ability of a spectrometer to provide a precise measure of the energy deposited by incident radiation is fundamentally essential in radiation spectroscopy. This not only provides an accurate detailed description of the gamma rays emitted by the nucleus but also permits the analysis of complex gamma spectra involving many different energies such as environmental spectra. Such spectra most gamma ray lines of interest are located near each other above a high level of background particularly at low energy regions of gamma spectra. Energy resolution [Kno10] is the index of the detector performance, which is used to express the precision of the energy measured by the detector system. It is [G+95a], [Kno10] measured by the Full Width at Half Maximum (FWHM) of a typical full energy peak (or response function) in an energy spectrum due to the detection of a monoenergetic gamma ray. The smaller the figure for the width of the response function, the better the detector will be capable to resolve fine detail in the incident energy of radiation, the better defined an energy spectrum becomes. HPGe detectors have superior *intrinsic* energy resolution, (W_I), and therefore they are preferred over any detector type for radiation spectroscopy. There are a number of factors, which contribute to the intrinsic energy resolution of the detector system. These include the sources of random noise within the detector itself and the electronic components following the detector to process the electrical signal, any drift of the operational characteristics of the detector during the course of the measurements, and statistical fluctuation resulting from the discrete nature of the charge carriers forming the detector signal. Which of these factors is the dominant over the other factors will depend on the energy of radiation and the physical properties of the detector. These factors are explained in detail in Chapter 3 and quantitatively determined for the detector system used in this work in Chapter 4. In the context of nuclear structure experiments, there is another contribution added to the energy resolution measured by the detector due to Doppler shifting of the gamma-ray energy being measured. This contribution, (W_D), is only relevant when the radiation source is not at rest in the lab frame (e.g. when measuring gamma rays emitted following nuclear reactions). The Doppler effect can then introduce an energy spread that might be significant in germanium detectors. As this is not the case in this work, this factor therefore will not be considered here. For further reading relevant to this factor, the reader is referred to [B+96].

1.1.2 Detection Efficiency

The counting efficiency of a gamma-ray detector can be described in a number of different ways: absolute efficiency, intrinsic efficiency and relative efficiency. The *absolute efficiency*, ϵ_{abs}, is the index used to relate the number of detected events to the number of gamma rays emitted from a source of radiation,

$$\epsilon_{abs} = \frac{N_{detected}}{N_{emitted}} \ . \tag{1.1}$$

The absolute efficiency is dependent on the detector properties and source-to-detector distance. The *intrinsic efficiency*, ϵ_{int}, is used to relate the number of detected events to the number of gamma rays incident on the detector,

$$\epsilon_{int} = \frac{N_{detected}}{N_{incident}} \ . \tag{1.2}$$

The intrinsic efficiency is a strong function of the physical properties of the detector, such as size and material, and the energy of the incident gamma rays. For an isotropic source[1], the two efficiencies can be related geometrically by

$$\epsilon_{int} = \epsilon_{abs}\left(\frac{4\pi}{\Omega}\right) \ , \tag{1.3}$$

where Ω is the solid angle subtended by the detector from the source. In order to remove the dependence of intrinsic efficiency on the physical properties of a detector, it is convenient to tabulate the counting efficiency of the detector relative to an industrial standard. Consequently, the *relative efficiency* can be calculated by measuring first the absolute efficiency of the detector using a ^{60}Co gamma-ray source placed 25 cm from the detector face, then dividing this value by the absolute efficiency of a 3 in. $\times$ 3 in. Sodium Iodide detector obtained in the same measuring conditions.

From the point of view of the nature of the event detected, the detection efficiency of a detector can be divided into two classes; *peak efficiency*, ϵ_{peak} and *total efficiency*, ϵ_{total}. The peak efficiency is the number of detected events that deposit their full energy in a detector. Those events fall into a photopeak of interest in a pulse height spectrum. The peak efficiency is not sensitive to experimental conditions such as scattering from objects surrounding the detector. Therefore, it is the most common type of efficiency used in gamma spectroscopic measurements. The total efficiency, however, is a measure of all events detected regardless if they deposit part or full energy in the detector and can be affected by structural objects near the detector or the radiation source.

1.1.3 Peak-to-Compton (P/C) Ratio

This factor is a measure of the combined effects of detector energy resolution and detector full-energy peak efficiency. The ratio is used to [Kno10] describe the number of events in the highest photopeak channel relative to the number of events in a typical channel of the Compton continuum linked to that peak. This part of the continuum is to be taken in the relatively flat region of the distribution lying just to the left of the rise towards the Compton edges (see Fig. 4.7, p. 48). In this figure, for the 1332.5 keV gamma ray peak,

[1] No attenuation takes place between the source and detector.

the ratio is traditionally measured as the number of counts in the maximum channel of the peak to the mean count per channel in the interval from 1040 to 1096 keV.

This ratio can be influenced by two key factors: the detector size and the detector environment. First of all, it can be seen in Fig. 2.3, p. 11, that (for Z = 32) Compton scattering is the dominant interaction mechanism of γ-rays over a large energy range of 150 keV - 8 MeV and consequently a significant number of counts is expected below the full energy peak caused by Compton scattering events in which the scattered radiation escapes from the detector. For a large detector, the probability of capturing all the gamma energy before escaping from the detector will be therefore enhanced. This will result in an increase in the number of events contributing to the full energy peak and a reduction in the number of events in the Compton distribution at the same time, hence, an improvement in the P/C ratio.

The second factor is related to the detector environment. Materials surrounding the active volume of the detector, such as dead layers, detector cryostat and shielding, will cause Compton-scattered gammas entering the detector, which can add to the Compton continuum and not to the photopeak, thus reducing P/C ratio. The ratio is therefore heavily affected by the variable laboratory conditions, and in order to enhance this index of detector performance from the detector shielding point of view, the design or configuration of cryostat-shield detector system must be taking into consideration, this is treated in more detail in Section 2.3.7.

When P/C ratio is high, the detector counting ability to measure low energy peaks in the presence of Compton continuum from higher-energy gammas is improved, and subsequently increasing the detector sensitivity. This thesis contributes towards improving this index of detector performance through the use of Pulse Shape Analysis technique as will be conducted in Chapter 6.

1.2 Thesis Overview

This project is aimed at optimising the spectroscopic performance of BEGe detectors using PSA of charge signals produced from gamma-ray interactions within the detector crystal. The methodology and results of the successful application of PSA to the recorded charge signals have been presented. A brief Summary of the thesis structure is highlighted as follows:

- **Chapter 1** offers an introduction on the HPGe detector utilised in this study as well as the operational characteristics of γ-ray spectrometers used to assess the performance of HPGe detector systems. In addition, thesis review and structure are presented.

- **Chapter 2** describes the principles of gamma-ray spectroscopy, which provides an essential understanding for the work undertaken in this thesis. This chapter contains some topics including a brief description of the High Purity Germanium (HPGe) detectors and their common configurations. A summary on detector shielding design and the background in γ-ray detection systems is also given.

- **Chapter 3** outlines the noise and energy resolution in germanium detector systems. This chapter aids to understand about the various sources of noise, which are because of the uncertainties in processes occurring in both the detector and the electronic system.

- **Chapter 4** provides an experimental and theoretical characterisation of the HPGe detector under study, which is a Canberra BE2825. In this Chapter, a detailed description of the high resolution γ-ray spectroscopy including the detector configuration is presented. The experimental measurements included the energy, absolute efficiency and peak-to-Compton ratio. The theoretical study of the detector response involved MCNP, MCNP PTRAC and GAMOS simulations. The performance factors used to assess the performance of the detector model optimised by MCNP are Peak to Compton ratio and absolute efficiency. The MCNP detector model was utilised in GAMOS to simulate pulse-height and position distributions of γ-ray interactions inside the detector. This complete study was performed using gamma-ray point sources in a standard detector top geometry.

- **Chapter 5** presents the procedures of the soil samples collection and preparation as a part of the work presented in this thesis. In addition, their radioactivity measurements by gamma-spectroscopic analysis techniques are also presented in details.

- **Chapter 6** describes the main methodology developed in this work and the results of the successful application of PSA for the improvement of the performance of Broad Energy Germanium detectors for gamma-ray spectroscopy.

- **Chapter 7** gives a brief summary of the prominent findings in this thesis and a future step has also been stressed.

Chapter 2

Principles of γ-ray Spectroscopy

Introduction

The performance of radiation detectors designed to detect gamma radiation such as germanium detectors relies on ionisation produced by the energy transferred to electrons of the detector medium [Kno10]. A full understanding of their response to radiation therefore requires a familiarity with the fundamental mechanisms by which gamma radiation interacts and loses its energy in the detector. Gamma-ray photons are released from the de-excitation of a nuclear state and correspond to transitions between well-defined nuclear levels [Bos99]. They are uncharged and have no mass and indirectly ionise or excite the medium through which they pass. Their detection thus depends on their probability of undergoing an interaction with an atomic electron that transfers all or part of the photon energy in the detector volume. When gamma photons interact with the detector material, they create ionisation. The resulting energetic electrons lose their energy by further ionisation and excitation of atoms and through bremsstrahlung production, until they have lost all of their energy [Kno10]. The subsequent distance travelled by an electron in the detector depends on its energy and the density of the detector material. For a typical γ-ray energy interacting in germanium, the range of the secondary electrons produced is less than a mm [Muk76]. These electrons are charged and then detected as a signature that the gamma photons were present.

2.1 Gamma-ray Interactions with Matter

Although a variety of interaction mechanisms are possible for gamma rays in a detector material, only three fundamental types are significant in the detection of gamma radiation:

- Photoelectric absorption
- Compton scattering
- Pair production

From a gamma spectrometry point of view, these mechanisms will be treated here briefly to permit the features seen in a typical gamma-ray spectrum to be explained. Each mechanism results in either the partial or total transfer of the gamma-ray photon energy to the energy of electrons of the detector material. Other types of interactions

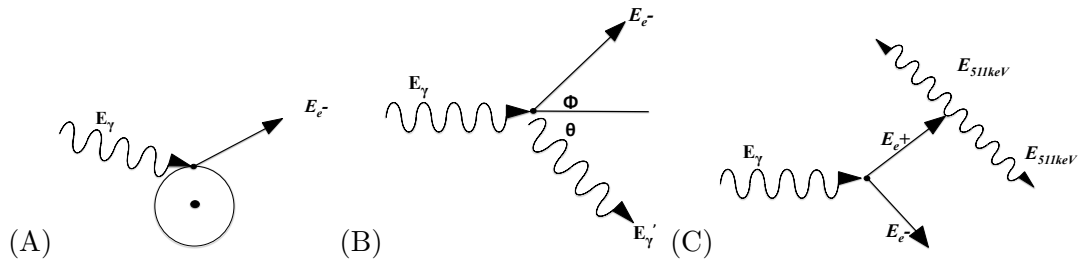

Figure 2.1: Schematic diagram of photon interactions at γ-ray energies, (A) photoelectric effect, (B) Compton scattering, (C) pair production.

such as Rayleigh scattering which does not result in energy deposition within the detector material will not be discussed here as it is not important for radiation detection.

2.1.1 Photoelectric Absorption

In this process, Fig. 2.1(A), the gamma-ray photon undergoes an interaction with an atomic electron, usually from the most tightly bound shell (K-shell) [Bos99], in which the electron absorbs the complete energy of the photon and is consequently ejected by the atom with a kinetic energy given by [Kno10]:

$$E_{e^-} = E_\gamma - E_b \ , \tag{2.1}$$

where E_γ is the incident photon energy and E_b is the photoelectron binding energy in its original orbital. In germanium, the energy binding the K electron in its shell amounts to 11 keV. The ejection of the electron results in the formation of an ionised atom with a vacant orbital left behind in one of its bound shells, which is subsequently filled through the capture of a free electron from the absorber material and/or the internal rearrangements of electron shells of the atom, leading to the liberation of the electron binding energy in the form of a characteristic X-ray photon. In most cases, this X-ray is rapidly reabsorbed giving rise to an output pulse that is proportional to the total photon energy. For small detectors, there is, however, a significant chance for a sufficient number of K X-rays to escape from the detector causing an escape peak in the observed spectrum. This peak emerges below the full-energy peak by an amount equal to the energy difference corresponding to the characteristic K X-ray energy for germanium. This X-ray escape peak is more probable for low-energy gamma rays because there is a strong tendency for interactions to occur near the detector surface. The probability of a photoelectric process depends on gamma-ray energy and the atomic number, Z, of the detector material. A rough approximation of the probability can be expressed as [Kno10]:

$$\mu_{PE} = \frac{Z^n}{{E_\gamma}^{3.5}} \ , \tag{2.2}$$

where the exponent n varies in the range 4 and 5.

For high-Z materials such as Germanium (Z = 32) photoelectric absorption is the predominant mode of interaction for relatively low-energy gamma rays up to 150 keV.

2.1.2 Compton Scattering

In this process the incident gamma-ray photon interacts with an electron in the absorbing material. This interaction differs from the photoelectric process in that the photon transfers only a fraction of its energy to the electron, which becomes a recoil electron, and the less tightly bound electrons in the outer shells, where $E_\gamma \gg E_b$, are only involved in the process. The incoming γ-ray photon is reflected (or scattered) through an angle θ with respect to its incident direction, this is shown schematically in Fig 2.1(B). The relationship between the energy of the scattered photon, $E_\gamma{}'$, the incident photon energy, E_γ, and scattering angle for any given interaction is given by [Kno10]:

$$E_\gamma{}' = \frac{E_\gamma}{1 + \frac{E_\gamma}{m_0c^2}(1 - \cos\theta)} \ , \tag{2.3}$$

where m_0c^2 is the electron rest mass (511 keV).

Owing to the conservation of energy and momentum, the incident energy is shared between the recoil electron and the scattered photon. Because the scattering angles θ can be any value between 0^o and 180^o, the maximum energy transferred to the recoiled electron can vary from zero to a large portion of the incident γ-ray energy which is still less than the total energy that can be transferred by the same photon in a photoelectric interaction. The interaction probability of Compton scattering is dependent on the number of electrons available as scattering targets and hence rises linearly with the atomic number, Z, of the absorbing material. The distribution of scattering angles is given by the *Klein-Nishina formula* for the different scattering cross sections $d\sigma/d\Omega$:

$$\frac{d\sigma}{d\Omega} = Z{r_0}^2 \left(\frac{1}{1 + \alpha(1 - \cos\theta)} \right)^2 \left(\frac{1 + \cos^2\theta}{2} \right) \left(1 + \frac{\alpha^2(1 - \cos\theta)^2}{(1 + \cos^2\theta)[1 + \alpha(1 - \cos\theta)]} \right) , \tag{2.4}$$

where $\alpha = h\nu/m_0c^2$ and r_0 is the classical electron radius [Kno10].

This distribution is shown in Fig. 2.2 for different incident gamma-ray energies and illustrates that there is a strong tendency for forward scattering at high values of the γ-ray energy, but as energy decreases, scattering is close to isotropic, with a small reduction in scattering probability at $\theta = 90^o$.

2.1.3 Pair Production

Pair production [Kno10] takes place in the Coulomb field of a nucleus where an incident gamma ray, with energy exceeding 1022 keV, disappears and its energy is transformed

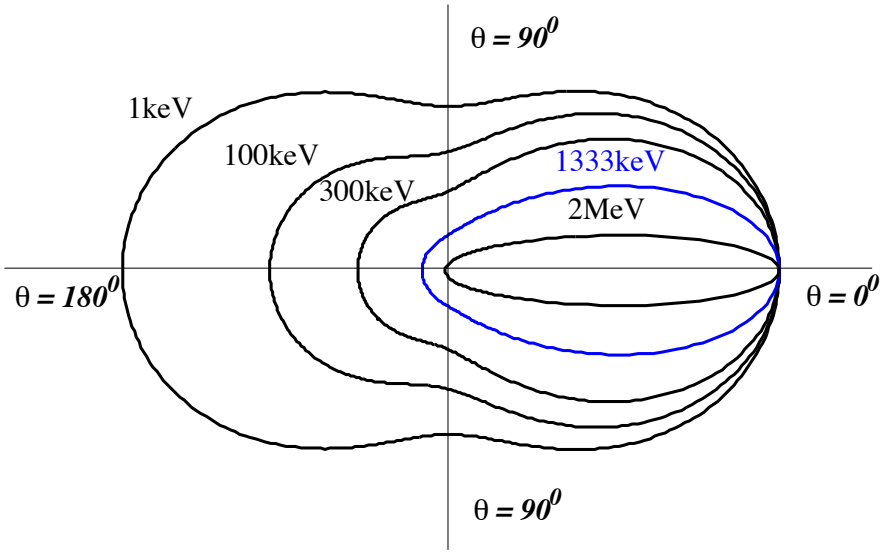

Figure 2.2: A polar plot of the angular distribution of Compton scattered photons (incident from the left) for a selected γ-ray energies, as predicted by Klein-Nishina formula (Equation 2.4). The values are calculated for photons scattered in germanium (Z = 32) and are normalised to $\theta = 0^o$.

into the rest mass of the electron-positron pair. The excess energy above this threshold is shared as a kinetic energy by the electron and positron. These two charged particles will then lose all their energy within a few millimeters to the absorbing material. The positron eventually annihilates with a nearby electron after slowing down, creating two annihilation quanta (511 keV each) emitted back to back as demonstrated in Fig. 2.1(C). Although the pair production process is energetically possible at 1022 keV, practically the probability for the process remains small until the gamma-ray energy is roughly twice this value. The probability varies approximately as the square of the absorber atomic number and increases sharply with energy.

The relative probability of the three mechanisms explained above for different absorber materials and γ-ray energies are shown in Fig. 2.3.

2.2 Attenuation Coefficients

The combined effect of all the interaction mechanisms discussed above on the intensity of a γ-ray beam after passing through some material can lead to the removal of photons from the beam either by absorption or scattering away from the beam direction. This amount of attenuation is a strong function of energy and the probability per unit length that the gamma-ray photon is removed from the beam can be defined as:

$$\mu(E) = \mu(E)_{Photoelectric} + \mu(E)_{Compton} + \mu(E)_{Pair} \ , \tag{2.5}$$

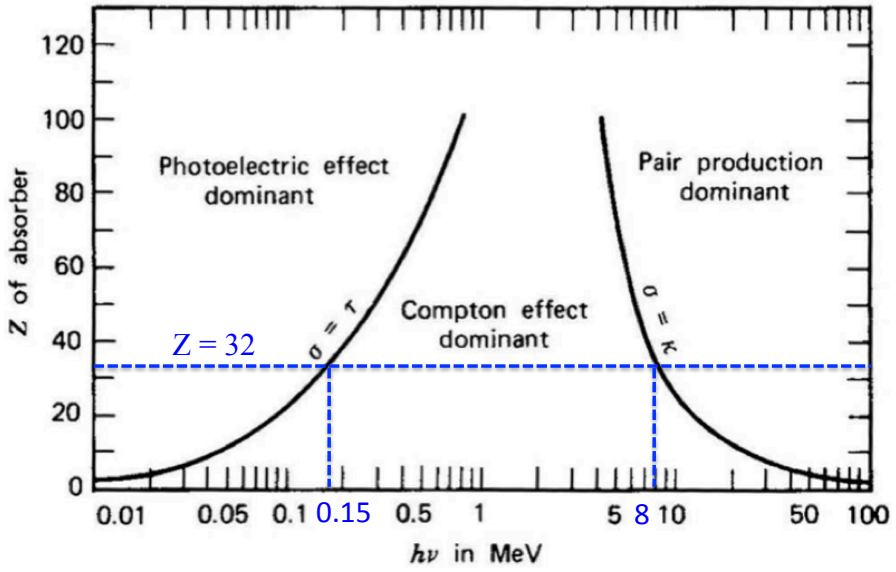

Figure 2.3: The relative importance of the three major types of γ-ray interaction as a function of absorber atomic number Z and γ-ray energy $E_\gamma = h\nu$. For germanium (Z = 32), Compton scattering is the dominant process of interaction for the energy range ($> 150\,\text{keV} - 8\,\text{MeV}$) ([Kno10]; used with permission from *The Atomic Nucleus* by R. D. Evans. Copyright 1955 by the McGraw-Hill Book Company).

where $\mu(E)$ is called as the *linear attenuation coefficient* (cm^{-1}) and is simply the sum of the attenuation due to each of these interactions. The number of transmitted photons I after the beam has travelled a distance t can be characterized in terms of the initial incident number of photons I_0 as:

$$I = I_0 e^{-\mu t} \,. \tag{2.6}$$

Equation 2.6 can also be written using the mass attenuation coefficient, the ratio of the linear attenuation coefficient to the density of the detector material,

$$I = I_0 e^{-(\mu/\rho)\rho t} \,, \tag{2.7}$$

where μ/ρ (cm^2/g) is the *mass attenuation coefficient*, ρ represents the density of the travelled material and ρt (g/cm^2) is termed as the mass thickness and is used as a measure of the thickness of the absorber material used in radiation measurements rather than physical thickness [Kno10].

The total mass attenuation coefficient for germanium, and the contributions from the photoelectric absorption, Compton scattering and pair production are indicated in Fig. 2.4, p. 12. For photoelectric absorption, the probability increases rapidly as energy decreases but then drops at gamma-ray energies just below the binding energies of electrons in the various shells of the germanium atom. These discontinuities in the low-energy region are called *absorption edges*. The highest energy edge at 11 keV is

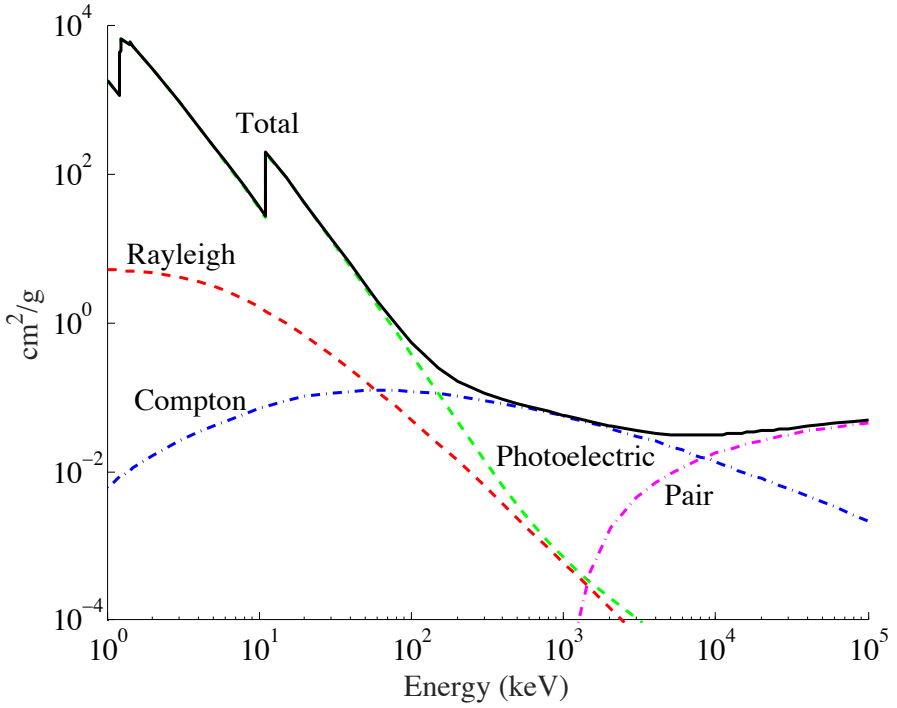

Figure 2.4: Photon mass attenuation coefficient, μ/ρ (cm^2/g), for γ-rays incident on germanium. Data reproduced from [NIS16].

consequently related to the binding energy of the K-shell electron. Similar edges corresponding to L-shell electron can be seen in the curve. The interaction probability of Compton scattering is a slowly varying function of gamma-ray energy, it decreases gradually at higher gamma-ray energies. For the photon energy range ($>$ 150 keV $-$ 8 MeV), Compton scattering is the dominant interaction mechanism. At gamma-ray energy above 8 MeV, pair production is the predominant interaction and the probability for this process rises sharply with energy.

2.3 Semiconductor Detectors for γ-ray Spectrometry

Semiconductor detectors essentially act as solid-state ionisation counters and their use as radiation sensors can result in a large number of charge carriers for a given incident radiation event. Accordingly, semiconductor detectors have the advantage over any other common detectors, such as gas counters, that they give a precise measure of the energy of the incident radiation. Additionally, the detection material is denser and thus the detector provides a higher stopping power and can be smaller than the equivalent gas-filled detector [Kno10].

2.3.1 Band Structure

The periodic structure [Kno10] of crystalline solids creates broad bands of permitted energy for electrons that are present within the solid. In that, the electron energy will be restricted to one of the energy bands within the lattice. The structure of these bands

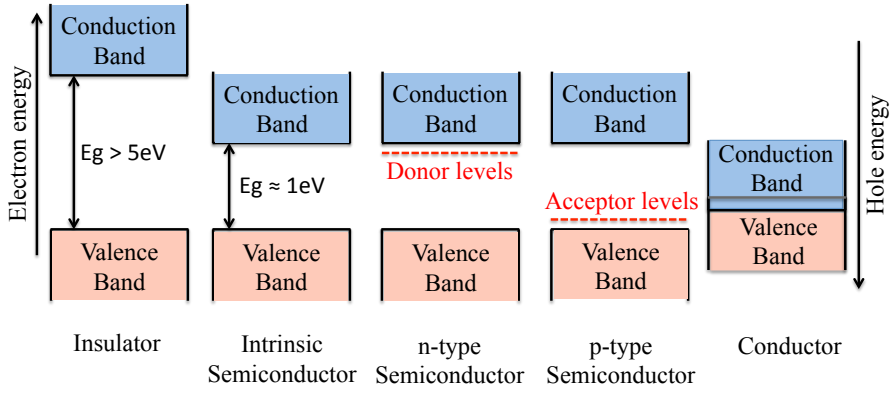

Figure 2.5: Distribution of electrons in energy bands for insulators, intrinsic semiconductors, n-type semiconductors, p-type semiconductors and conductors.

control the electrical properties of the solid. A schematic illustration of the energy bands in insulators, semiconductors and conductors is shown in Fig. 2.5. Electrons in the lower, *valence band* are corresponding to those electrons that are bound to specific lattice sites within the crystal; these are involved in the covalent bonding that constitute the inter-atomic forces between neighbouring atoms within the crystal. On the contrary, the higher, *conduction band* represents electrons, which are free to move throughout the crystal and hence contribute to the electrical conductivity of the material. For conductors, both bands are either overlapped or the valence band is not fully occupied which means there are always electrons free to move through the material. In insulators and semiconductors, there is an energy gap or band gap, E_g, between these bands, in such that an electron must gain enough energy to cross the band gap before it can move through the crystal. The classification of the material as a semiconductor or an insulator is determined by the size of this gap; a large bandgap $E_g > 5\,eV$ will classify a material as an insulator and a small band gap (0.665 eV in Ge, 1.115 eV in Si) represents a semiconductor.

In semiconductors, under thermal excitation, a valence electron is liberated across the bandgap into the conduction band, creating an electron in the empty conduction band and consequently it leaves behind a vacancy, called a *hole*, in the full valence band. Both the electron and hole are collectively known as an *electron-hole pair* and are the information carriers for a semiconductor detector. Conductivity in insulator materials is minimal even in the presence of excitation energy.

When gamma-radiation interacts with semiconductors, it is possible for electron-hole pairs to be produced in the same manner, the number of which is proportional to the energy deposited; it is this that serves as the basis for γ-ray detection with semiconductor diode detectors, which will be discussed in more details in Section 2.3.3.

2.3.2 Doping

In an entirely pure semiconductor, under thermal excitation, all the electrons in the conduction band and all the holes in the valence band must always be exactly the same; such material is referred to as *intrinsic* semiconductor. Practically, this material cannot however be made to such high levels of purity and it always contains a low amount of remaining chemical impurities even after the best purification processes such as *zone refining* technique, that used to produce ultrapure germanium, described in Section 2.3.4.

Semiconductor materials can be categorized into three different groups according to their electrical properties dominated by electrically active impurites remaining in the material [Kno10]: *n-type*, *p-type*, and *compensated* semiconductors. These active impurities donate to the material either from a trace amount intentionally added during the fabrication process to give the material certain electrical characteristics, called *dopants* or as a remaining amount after using purification methods. A brief summary of the three different types of semiconductors is given as following:

- **N-Type Semiconductors**: this semiconductor material has excess negative electrons available for conduction. An example of an n-type semiconductor is phosphorous doped germanium. The element of germanium is Group IV having a tetrahedral crystal structure, in which each atom creates a bound with four nearest neighbours. The impurity atom phosphorous (valence 5) replacing a germanium atom (valence 4) will, therefore, have a weakly bound electron, which have a *donor* energy level just below the conduction band, depicted in Fig. 2.5. and can be easily excited by thermal energy into the conduction band. The sites of the ionised donor impurities in the lattice will represent net positive charges which are not, however, considered as those holes left behind when a valence electron is promoted to the conduction band from a normal covalent bond throughout the crystal and the reason for this is that, these ionised donors are not part of the lattice and cannot contribute to the electrical conductivity of the material. The electric conductivity is determined by the flow of electrons, and holes play just a small role. In this case, the electrons are the majority carriers, and holes the minority carriers.

- **P-Type Semiconductors**: in contrary to n-type semiconductor, this material provides positive holes for conduction. An example of a p-type material is boron doped germanium. In this case, germanium atoms are now replaced with boron atoms (valence 3) in the lattice sites. Each impurity has one unsaturated covalent bond at *acceptor* level, situated just above the valence band, shown in Fig. 2.5, which is filled by an electron excited from the valence band leaving a hole behind for conduction. Under the influence of an electric field, a neighbouring valence electron can move to fill this vacancy leaving another hole behind, which represents the new position of the hole, in this way, holes contribute to the conductivity of the

semiconductor material. In p-type material, holes are the majority charge carriers and electrons are the minority charge carriers.

- **Compensated Semiconductors**: if a semiconductor, e.g. germanium, is compensated then the number of donor imurities is equal to the number of acceptor impurities. Practically this can only be achieved by lithium ion drifting process, in which lithium atoms are drifted through a p-type germanium material, the electrons contributed by the lithium atoms will be captured at the acceptor sites and remain there if the material is continuously maintained at a sufficiently low temperature. Detectors produced from pure germanium have been an alternative choice to those produced from lithium drifting (known as Ge (Li) detectors) because they can be allowed to warm to room temperature between uses, whereas, Ge(Li) detectors must be stored, as well as operated, at liquid nitrogen temperature to avoid the diffusion of the lithium ions from the crystal.

2.3.3 The p-n Junction

The operation of a semiconductor detector is dependent on the electrical properties of the junction created when n- and p-type semiconductors are brought together within a good thermodynamic contact [Kno10]. There will be a strong tendency for electrons and holes to move towards each other at the boundary, Fig. 2.6[A], resulting in a region empty of charge carriers in the vicinity of the interface of the two materials. The region, over which the free charge carriers are no longer available, is referred to as the *depletion region*. The effect of carrier diffusion across the junction results in building up a net positive space charge on the n side and a net negative space charge on the p side of the junction. The build up of net charge causes an electric potential difference to be developed across the junction in the reverse direction, which ultimately becomes great enough to stop further charge migration. This potential difference, at equilibrium, is known as the *contact potential*, Vc. It causes an electric field to be extended over the width of the depletion region, where a sharp change in the charge density is significant and the potential has some ingredient, the profiles of the variation in space charge density, electric potential and electric field are shown in Fig. 2.6[B],[C],[D] respectively. It can be seen from the profiles that, the sharp gradient of charge density and potential is existing at the boundary where the subsequent electric field is at maximum.

When an external voltage is applied in the direction opposite to the normal potential difference (*forward* bias), in which a positive voltage is applied to the p side of the junction with respect to the n side, the contact potential, seen by an electron from one side to the other, will be reduced. Under these conditions, the majority carriers (holes on p side and electrons on the n side) will migrate back towards the junction, closing the depletion region and conducting large current to flow through the junction. Instead, if the junction is *reverse* biased, where the p side of the junction is made negative with respect to the n side, the natural potential is now enhanced and charge will travel a greater distance across the junction, resulting in creation of a larger sensitive volume

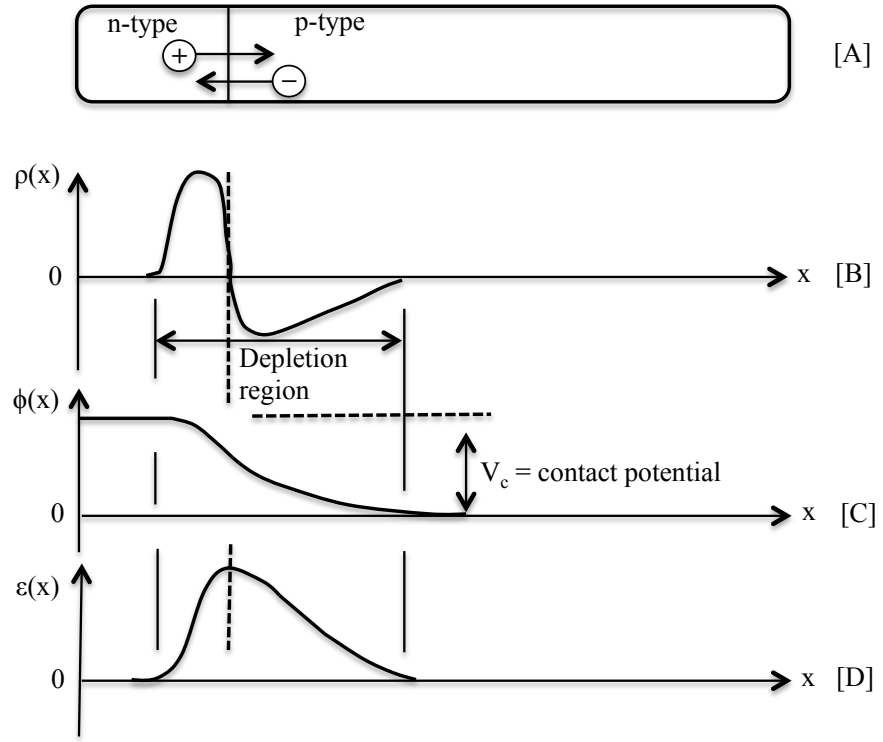

Figure 2.6: A schematic view of [A] an ideal p-n junction formed at the interface between n-type and p-type showing the effect of carrier diffusion across the junction. [B-D] The space charge density $\rho(x)$, electric potential $\varphi(x)$ and electric field $\varepsilon(x)$ as a finction of position across the junction when it is in equilibrium. Reproduced from [Kno10].

conducting a low current, or *leakage current*, across the junction, created by the residual minority carriers (holes on n side and electrons on the p side) which are free to diffuse across the junction. In most cases, this current is small (in the order of a fraction of a nanoampere) and is rarely a significant current source. The other source of leakage current is due to surface effects explained in Section 3.3.1. Reverse bias the junction acts as the basis of the operation of a p-n junction diode detectors.

Operating a p-n semiconductor junction diode under a substantial reverse bias (in the order of thousands of volts) is essential for the detection of rediation, especially for applications involving gamma-ray spectroscopy, in order to create an electric field across the crystal necessary to efficiently collect the charge carriers released by radiation interactions within the sensitive volume of the detector.

2.3.4 High Purity Germanium (HPGe) Detectors

Germanium detectors designed for the measurements of gamma-ray energy requires a depletion region or active volume of the order of a centimetre or more because γ-radiation can travel large distances between interactions [Kno10]. The thickness of the depletion

region is given by:

$$d = \left(\frac{2\epsilon V}{eN}\right)^{1/2}, \tag{2.8}$$

where V is the reverse bias voltage, N is the net impurity concentration, ϵ is the dielectric constant and e is the electronic charge.

The thickness of germanium that can be depleted by applying a certain bias voltage is inversely proportional to the impurity concentration in the bulk material. In order to maximise the depth of active volume, the net impurity concentration must be reduced. Refining the germanium material to very high level of purity is one of the approaches that can be taken to reach this goal. The introduction of *zone refining* technique resulted in the production of ultrapure germanium with impurity levels as low as 10^9 atoms/cm^3, which compares to 10^{12} atoms/cm^3 for germanium of normal semiconductor purity. In this technique, the starting material is bulk germanium of already high purity, which is further refined by locally heating the material and slowly passing a melted zone repeatedly from one end of the sample to the other. Under the zone melts, impurities tend to be more soluble and they, therefore, are preferentially transferred to the molten zone and are swept from the sample. This will result in a highly purified material, having low impurity profile, that is used to grow a large single crystal. Germanium detectors that are developed from this ultrapure germanium are usually described as High Purity Germanium (HPGe) detectors. If the remaining low-level impurities are acceptors, the electrical properties of the crystal is mildly p-type. Similarly, if donor impurities remain, high purity n-type is made.

Table 2.1 compares the key properties of germanium with silicon, which are the two dominant semiconductor materials for detector applications.

It is impossible to operate HPGe detectors at room temperature. At nonzero temperature, there is a high probability of thermal excitation of valence electrons into the conduction. This is as a result of the small size of the bandgap between the valence band and the conduction band of germanium material (0.7 eV). The number of electrons that can jump across the bandgap is proportional to,

$$e^{-(\frac{E}{2KT})}, \tag{2.9}$$

where E is the bandgap [Kno10]. When Ge is operated at liquid nitrogen (LN_2) temperature (KT = 77 K^o), there is a factor of 10^{18} less excitations than at room temperature (KT = 300 K^o). For this reason, germanium detectors of any type must be cooled during the course of the measurement to significantly reduce the thermal noise, and accordingly the excellent energy resolution is not affected by the associated noise. The HPGe detector used in this work is a p-type detector, whose signals are dominated by hole collection. The dewar configuration of the detector system used in this work can be seen in Fig. 4.2(A), p. 37.

Properties of Intrinsic Silicon and Germanium	**Si**	**Ge**
Atomic number	14	32
Atomic weight	28.09	72.60
Stable isotopes	28-29-30	70-72-73-74-76
Density (300 K); g/cm^3	2.33	5.32
Atoms/cm^3	4.96 $\times 10^{22}$	4.41 $\times 10^{22}$
Dielectric constant (relative to vacuum)	12	16
Forbidden energy gap (300 K); eV	1.115	0.665
Forbidden energy gap (0 K); eV	1.165	0.746
Intrinsic carrier density (300 K); cm^{-3}	1.5 $\times 10^{10}$	2.4 $\times 10^{13}$
Intrinsic resistivity (300 K); $\Omega.cm$	2.3 $\times 10^{5}$	47
Electron Mobility (300 K); $cm^2V.s$	1350	3900
Hole Mobility (300 K); $cm^2V.s$	480	1900
Electron Mobility (77 K); $cm^2V.s$	2.1 $\times 10^{4}$	3.6 $\times 10^{4}$
Hole Mobility (77 K); $cm^2V.s$	1.1 $\times 10^{4}$	4.2 $\times 10^{4}$
Energy per electron-hole pair (300 K); eV	3.62	
Energy per electron-hole pair (77 K); eV	3.76	2.96
Fano factor (77 K)	0.084 - 0.16	0.057 - 0.129

Table 2.1: Table presenting properties of Intrinsic Silicon and Germanium relevant to their use in radiation detection [Kno10], [B$^+$68].

2.3.5 Properties of other Materials for γ-ray Detection

There are more semiconductor materials other than silicon or germanium that can be utilized for constructing detectors used in gamma-ray spectrometry. These materials (see Table 2.2) are consisting of more than a single chemical element and have a high density and higher atomic number compared with Si or Ge, and therefore excellent stopping power. Their much higher atomic number interprets into significantly higher photoelectric absorption for X-ray and gamma ray, which is the preferred gamma-ray interaction within a spectrometer. CdTe and HgI_2 are the most widely explored compound semiconductors for radiation spectroscopy and have found their way into commercial production, but in practice, their use is restricted to limited applications by a number of factors as follows:

First of all, these materials have large bandgap values, compared with germanium, and hence have the advantages that they can be operated at room temperature, so from Equation 2.9, and for CdTe, for example, there is a factor of 10^7 less excitation than in germanium. However, a large bandgap means that the average ionisation energy, that is required to excite an electron across the bangap and producing electron-hole pair, increases. The large ionisation energy reduces the number of charge carriers excited per unit of deposited energy, increasing statistical fluctuations and hence resulting in a worse energy resolution. In addition to this, they are difficult to be created as pure as germanium in large active volume with a satisfactory crystalline perfection due to [Kno10], [G$^+$95a] the complex crystal structure of these materials. This leads to excessive charge

Material	Atomic Number	Bandgap⋆ eV	Electron-hole⋆ eV	Density g/cm^3	Mobility⋆ (cm^{2}V^{-1}S^{-1})	
					Electrons	Holes
CdTe	48,52	1.47	4.43	6.06	1000	80
CdZnTe*	48,30,52	1.64	5.00	6.00	–	–
HgI_2	80,53	2.13	4.22	6.30	100	4
GaAs	31,33	1.45	4.51	5.35	–	–
PbI_2	82,53	2.60	7.68	6.16	–	–
GaSe	31,34	2.03	6.30	4.55	–	–
Bi_2S_3	31,33	1.30	–	6.73	–	–
AlSb	13,51	1.62	5.05	4.26	–	–
CdSe	48,34	1.75	–	5.74	–	–

Table 2.2: Properties of some semiconductor materials other than Ge and Si [G$^+$95a]. ⋆Bandgap, electron-hole creation energies and mobilities are given at 300 K. $^{(*)}$ This material is taken from [Pri11c].

carrier losses from trapping and recombination and hence poor charge collection efficiency. A more fundamental disadvantage of these materials also arises from the lower values of the charge carrier mobilities compared to Ge and Si as illustrated in Table. The charge carriers can then be vulnerable to trapping, affecting the charge collection efficiency, and complete charge collection can only be achieved over distances of less than 1 mm [G$^+$95a]. This translates into that only small detectors can be made using these materials. Because compact size of these materials can only be obtained, their use is mostly limited to X-ray and low-energy gamma-ray measurements [Kno10], [G$^+$95a], in which the deposited energy and resulting induced charge signal is relatively small. In such cases they require cooling to reduce the leakage current that can affect the small signal and thereby improve the energy resolution of these detectors. By taking all that into consideration with the remarkable reduction in the number of excitations in Ge when the operating temperature is reduced to 77 K (see Section 2.3.4) results in that Ge is an effective material for constructing detector crystals [Kno10] whose volume is large enough to be of interest for application to gamma-ray or X-ray spectroscopy. For more information on compound semiconductors and their use as radiation detectors, the reader is referred to [O$^+$04], [M$^+$97].

Despite the drawbacks of the compound semiconductors and their poorer energy resolution compared to germanium semiconductor detectors, they have a better energy resolution than that of scintillation detectors. To explain that, the number of charge carriers in Ge is N = 350 (electron-hole pair per keV), whereas Sodium Iodide (NaI) has an equivalent parameter (photoelectrons per keV of 5). Another high Z scintillator detectors is Bismuth germinate (BGO), which produce photoelectrons per keV of 0.5. Hence, the best resolution arises from the increased number of information carrying particles produced per unit of deposited energy, which is the fundamental reason why semiconductors, in general and germanium in particular, gives superior resolution than scintillators.

To summarise, germanium is the most common material for gamma-radiation detection. This is attributed to three main factors.

- The unrivalled energy resolution achievable with germanium at 77 K over other detector materials as a result of the low values of both ionisation energy, ϵ, and the Fano factor compared with other materials such as Si or NaI[1].
- The availability of germanium material in high purity as near perfect single crystals, this allow to create a large depletion region which is required in gamma-ray spectroscopy; this is highlighted in more detail in Section 2.3.4.
- Germanium, compared to Si, has high enough absorption coefficient due to the high atomic number, which increases the stopping power for gamma rays because of the increased density of electrons with which gamma rays may interact.

2.3.6 Configurations of HPGe Detectors

All HPGe detectors are manufactured from the resultant high purity germanium crystals, which are fabricated into the required shape. A process for the creation of ultrapure germanium with impurity profiles as low as 10^9 atoms/cm^3 is highlighted in Section 2.3.4. There are a number of different configurations in order to suit a particular application. This section will outline briefly the different configurations of germanium detectors as follows:

Planar Configuration

Planar detectors can be produced starting with germanium material with the highest available purity, either n or p type. They are manufactured from grown crystals with a cylindrical shape, which forms the basis of most HPGe configurations. They are thin detectors (as wafer) with typical volume limited to tens of cm^3 by the diameter[2] of the grown crystal and the depth of the slice cut from it [Kno10]. In this configuration, electrical contacts must be provided on the two flat surfaces of the wafer in order to form the junction of the detector. If the bulk of the detector is of particular type, p (or n), a heavily doped surface layer of the opposite type, n^+ (or p^+), in comparison to the bulk of the detector, is embedded on the surface of the wafer. This contact is referred to as the *rectifying contact*, and it forms the junction of the detector. The other contact is provided at the rear surface and it is generally of the same impurity type as the main body of the detector. Therefore, no semiconductor junction exists at this back surface. This rear contact serves as a *blocking*, or *noninjecting contact* in which the population of electrons (or holes) is very low. The role of the blocking contact is to allow the relatively free flow of charge, holes (or electrons), caused by ionising radiation in one direction and

[1] In sodium iodide detectors, the value for the Fano factor is one. The equivalent to ϵ is the energy required to produce a photoelectron at the photocathode of the photomultiplier, which is about 170 eV (see Knoll (1989), p. 312). Thus, FWHM of Ge is 3% of that of NaI

[2] Typical diameter up to 50 mm and typical depth up to 20 mm [G$^+$95a]

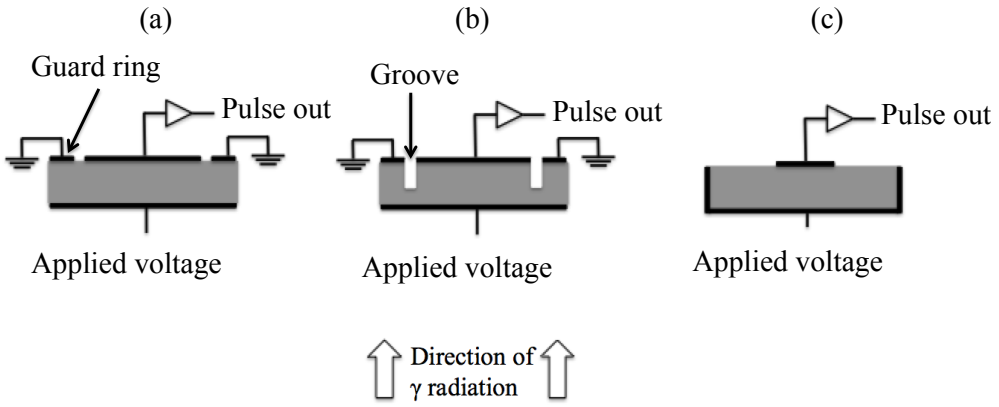

Figure 2.7: A schematic illustration of three different configurations of planar detectors. The solid black lines are nominal and represent the electrode surfaces. (a) The readout contact is protected from the leakage current, flowing across the disk surface, by a narrow guard ring. (b) The guard ring and the readout contact are further separated by a groove provided into the detector active volume. (c) A wraparound contact surrounds the disk excluding the full rear surface, where a small-diameter readout contact is placed. Reproduced from [Kno10].

at the same time presenting a large resistance to its leakage current, flowing through the bulk of the crystal and also across its surface, in the opposite direction. The detector is then depleted by reverse biasing the n^+-p (or p^+-n) junction, in which a positive voltage is applied to the n^+ contact with respect to the p^+ contact. In both cases, the effective depletion region begins from the central region of the rectifying contact and extends deeper into the bulk of the wafer as the voltage is increased until the detector becomes fully depleted, or alternatively expressed, the electric field is always a maximum at the rectifying contact and decreases linearly to a minimum at the blocking contact at the detector rear. This principle serves as the basis of the detector of interest used in this work, which will be explained in more details later in this chapter.

The n^+ contact can be formed by direct implantation of donor atoms, such as phosphorous, using an accelerator, which results in a very thin contact layer to serve as an entrance window for weakly penetrating radiations such as low-energy X-rays. However, the implantation technique has a severe drawback that the radiation damage caused by this technique produces acceptors sites in germanium. Instead, the lithium evaporation and diffusion onto one surface of the disk is still used, but resulting in a somewhat thicker surface dead layer. The p^+ contact is formed by boron implantation.

Planar detectors may also be fabricated begining with compensated or intrinsic germanium material rather than n- or p-type as described above. This kind of planar detectors is known as lithium-drifted planar detectors, in which lithium drifting is used to compensate the natural p-type impurities in germanium in order to convert the bulk of the detector to intrinsic material. The number of the donors and the number of acceptors in the intrinsic material are exactly the same. Electric contacts are still to be

provided to form the diode, however, there is no difference between the rectifying contact and the blocking contact. Detectors produced using lithium drifting process (see Ref. [Kno10], p. 468) known as Ge(Li), have the disadvantage of having to be stored, as well as operated, at 77 K in order to prevent the migration of the lithium ions within the germanium crystal, which [G+95a] destroys the electrical properties of the created intrinsic material. Therefore these devices are no longer produced since 1980s because of the introduction of the ultra-pure material used in HPGe detectors.

Planar detectors require high operating voltage in order to be able to collect charge carriers. This voltage appears across the side surfaces of the wafer and can result in a significant leakage current, which can deteriorate the detector energy resolution. As the structure of planar detectors is generally aimed to produce a detector with the best energy resolution, therefore, different configurations can be utilized for planar detectors in order to suppress the effects of this leakage current as shown in Fig. 2.7. In *guard ring* configuration, the collecting electrode is not covering the entire surface of the detector, but a narrow guard ring is employed on the readout surface around the boundary of the readout electrode, and the two are separated by a small gap. In this case, the surface leakage current is conducted to ground and it no longer affects the measured signal. This geometry has a disadvantage of poor charge collection properties due to trapping and recombination in regions where the active volume is excluded near the edges of the wafer, leading to pulses with smaller than proper amplitude. The second geometry is *grooved* configuration, in which a groove is provided into the active volume to increase the effective gap surface area that separates the guard ring and the collecting electrode. Another variant for planar detectors is *wraparound* configuration, in which a wraparound electrode is extended from one planar surface to also cover the side surface of the disk, and the collecting electrode is a point like contact fabricated on the opposite planar surface.

Coaxial Configuration

The production of large active volume detectors is needed for gamma ray spectroscopy in order to provide high efficiency for the detection of gamma rays [Kno10]. To achieve this goal, detectors are constructed using a different geometry that can include more of the crystal volume into a single finished detector. Such geometry is the *true coaxial* configuration. A coaxial detector has two electrical contacts; one is deposited on the outer cylindrical surface of the crystal. A second cylindrical contact is formed by removing the core of the HPGe crystal and another contact is deposited over the inner cylindrical surface. Using coaxial geometry, it is possible to construct the crystal long in the axial direction and producing active volumes as large as 800 cm^3.
The coaxial configuration has the advantage of having lower capacitance (lower electronic noise) than it would be possible using the planar configuration. There are three common shapes of coaxial detectors as shown at the top of Fig. 2.8. The most common shape of coaxial detector is the *closed-ended coaxial* configuration, in which only part

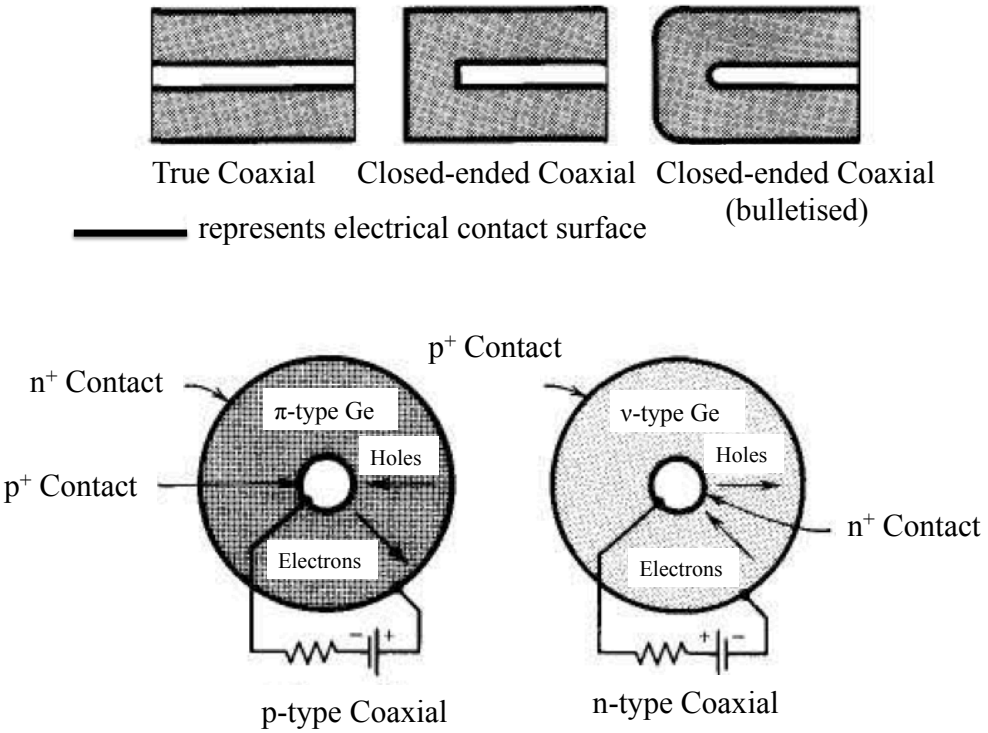

Figure 2.8: A cross-sectional view of three common shapes of large volume coaxial detectors is shown at the top. The outer electrode covers the side surface of a cylindrical crystal and the flat front (left) surface in both closed-ended cases. The electrode configurations corresponding to n- and p-type coaxial are presented at the bottom. Reproduced from [Kno10].

of the central core is removed and the outer contact is extended over the flat front end of the crystal. Detectors constructed using this configuration, with thin outer contact, have the advantage of providing a planar front surface that can acts as an entrance window for weakly penetrating radiations. To strength the electric field inside the detector crystal, the central hole is extended to reach close to the front surface and the front corners of the crystal and hole are rounded. This configuration is known as *bulletised closed end coaxial*.

Arrangements of electrical contacts on coaxial Ge detectors produced from p- and n-type material are shown at the bottom of Fig. 2.8. A p^+ contact, about 0.3 μm thick, is made by ion implantation of boron, while an n^+ contact, about 600 μm thick, is made by diffusion of lithium. In the operation, the thick contact (n^+) is positively biased and the thin contact (p^+) is negatively biased. In both cases, the outer surface has the rectifying contact, which forms the semiconductor junction and the depletion region grows inwards as the voltage is increased until reaching the inner hole. This choice requires lower voltage to deplete the detector than it would be if the inner surface has the rectifying contact. Additionally, a higher electric field value in the outer regions of the crystal is more maintained in this configuration. For photon energies greater than about 100 keV, n-type and p-type detectors of the same dimensions are equally efficient.

At lower energies, the thin window of an n-type coaxial detector makes it much more efficient than the p-type.

Well Configuration

HPGe detectors are also manufactured using [Kno10] *well* configurations in which the casing material housing the detector crystal is shaped to provide an easy sample positioning. Small radioisotope sources can then be placed within this well for measurements. This configuration has the advantage of maximising the detection efficiency of the detector as the active volume of the detector nearly surrounding the source. However, this outweighs the drawback of summing effects especially when isotopes with many coincident gammas are measured. Moreover, due to the higher capacitance of the detector and the subsequently higher electronic noise, the resolution performance of well type detectors is worse than coaxial detectors, particularly at low energies. In addition to this, the well configuration only houses a small sample volume. The following two sections present two common geometries of well detectors manufactured by Canberra [Can14].

- **Traditional Well Detectors**: the traditional germanium Well detectors, manufactured by Canberra, are fabricated from High-Purity p- or n-type germanium with a blind hole, leaving at least 15 mm of active detector thickness at the bottom of the well. The casing material housing the detector crystal is made of aluminum with a sidewall thickness of 0.5 mm and a 1 mm thick bottom. These detectors have intrinsically good low energy response due to the thin ion-implanted contact inside the well on the detector element (compared to the 0.5 mm of aluminum). This allows spectroscopy from 20 keV up to 10 MeV. The well configuration provides approximately 4 counting geometry leading to high absolute efficiency. For applications where small, low-activity samples may be encountered, this high counting efficiency results into lower detection limits or shorter counting times to achieve a given detection limit.

- **Small Anode Germanium Well Detectors (SAGe Well)**: the Canberra SAGe well detectors are fabricated with a blind hole, like the traditional well detectors, leaving at least 20 mm of active detector thickness at the bottom of the well, allowing approximately 4π counting geometry. In comparison with the Traditional Well and Coaxial Detectors, the SAGe detectors offer superior low and medium-energy resolution performance. This is as a result of the low detector capacitance associated with the small anode technology. In such that, the thin diffused contact inside the well is approximately 50 μm thick and the thin-walled aluminum insert in the detector end cap is 0.5 mm on the sides and a 1 mm thick bottom, allowing spectroscopy down to 20 keV. Furthermore, these detectors have excellent resolution for higher energy gamma rays as well as maximum efficiency for small samples.

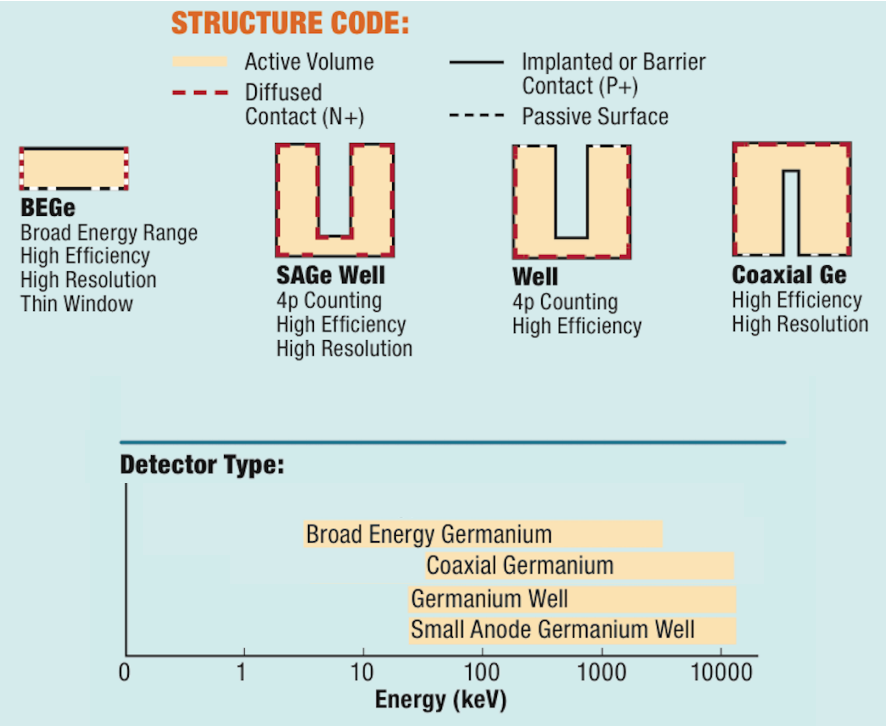

Figure 2.9: A schematic representation to depict some of the various detector geometries that are available from Canberra, the energy range they cover, and their prominent performance characteristics. Reproduced from [Can14].

Point Contact Detectors

- **MAJORANA**: apart from BEGe detectors, another example of point contact detectors is those incorporated into the MAJORANA DEMONSTRATOR [Ell06], [B+07]. These detectors are large volume, p-type HPGe cylindrical crystals. Each detector has a unique electrode structure, where an n+ contact surrounds the detector crystal, excluding a small area at the centre of the detector rear, where a p+ contact (signal readout contact) is located. This unique electrode structure results in a low electrode capacitance that improves low energy resolution. In addition to this, these detectors offer charge collection and signal induction characteristics ideally suited for the task of identifying events from multiple energy depositions [C+11].

Fig. 2.9 represents the various detector configurations described above, the energy range they cover as well as their prominent performance characteristics. For full description of these detectors and other types, the reader is referred to [Can14].

2.3.7 Background and γ-ray Detector Shielding

The construction and the configuration of a shielding system for gamma-ray detectors is an important contributing factor to the detector performance. In order to assure that

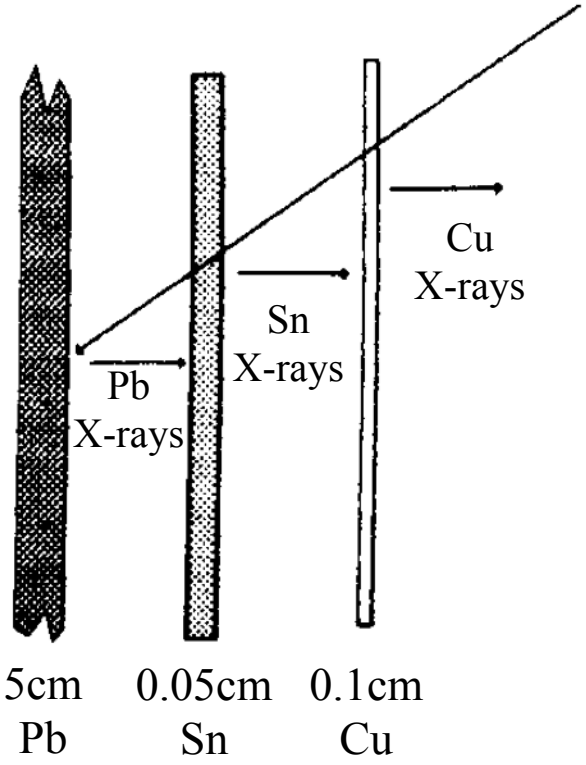

Figure 2.10: Schematic diagram, reproduced from[Pri11c], to depict the composition of the graded shielding designed for the detector utilised in this work (Fig. 4.2A). The shielding consists of lead (Pb), tin (Sn) and cooper (Cu) elements. The lead characteristic X-rays of energy 70-85 keV are absorbed by tin, which its characteristic X-rays are in turn absorbed by a layer of copper. The thicknesses of the elements are also shown.

the detector system has low background and is suitable for routine usage and applications such as environmental counting, the detector must be provided with some degree of external shielding. This will reduce the background counting rate caused by cosmic radiation and natural radioactivities in nearby materials and surrounding surfaces. Detector shielding can also provide a degree of isolation from other radioactive sources that might be measured or transferred during the measuring time [Kno10]. Having reduced the background a reduction in the level of the *minimum detectable activity*, (MDA), measured by the system can be accomplished. The background radiation is mainly due to a combination of:

- The natural radioactivity present in the detector constituent materials
- The natural radioactivity in the shielding materials
- Radiations released from the activity of earth's surface (or terrestrial radiation) and laboratory structures
- Radioactivity in air surrounding the detector (e.g. radon gas)

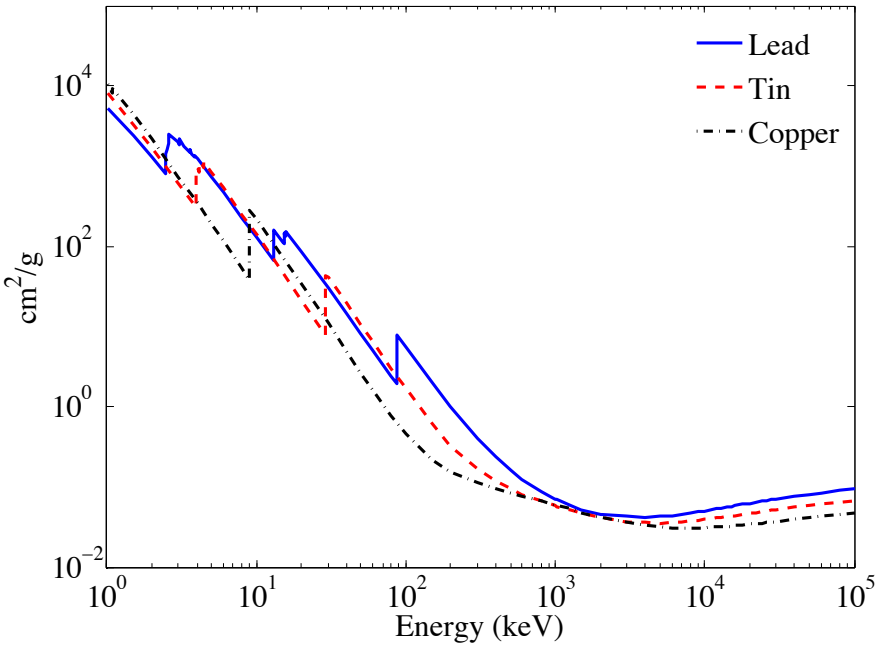

Figure 2.11: The total mass attenuation coefficients, μ/ρ (cm^2/g), of the graded shielding composition showing the migration of X-rays toward low energy range. Data reproduced from [NIS16].

- The primary and secondary components of the cosmic radiation

For environmental measurements, the most significant component of background radiation is the terrestrial and facility gamma radiation such as the radioactive potassium, ^{40}K; which is a common component in building construction materials. which can be reduced by providing an adequate shielding for the detector, this is explained in the following section.

- **Detector Shielding Design**
  The shielding design is important from several aspects [Kno10]. From gamma-ray spectrometry point of view, the shielding construction is a key factor regardless of the activity level of the sample being counted. An inappropriate choice of material types and/or thicknesses could lead to an elevated background continuum with a resultant compromise in system performance and/or long-term reliability. The detector aimed for gamma ray counting must be housed inside shielding to [K+14] shield from photons of cosmic and terrestrial origin, hence to [Kno10] improve its signal-to-background ratio. The most widely utilized material for the construction of detector shields is *lead* because of its effectiveness at eliminating many of the cosmic-ray components. This is as a result of its high density and large atomic number, however, its drawback is the emission of fluorescent X-rays after the photoelectric absorption of gamma rays takes place. This will produce a number of X-ray peaks in the region of 70-85keV of the measured energy spectra.

For low-level counting experiments and environmental applications where low-energy gamma-ray measurements are anticipated, these X-rays are a severe limitation. Providing *graded shields*, as shown in Fig. 2.10 can solve this problem by significantly reducing the effects of photo-fluorescence from the higher energy K X-rays of lead. The graded shielding designed for the detector used in this work is constructed from a cylindrical aged lead shield of about 5cm thickness molded in one piece. Using thickness beyond 5cm, in addition to the considerable cost that would entail, may also result in a substantial reduction in the resultant counting rate because of the build up of Compton scattering events, which are due to cosmic interactions within the lead shield [Kno10]. Lead shielding is incorporated by an internal liner of 0.05cm tin to absorb the lead X-rays produced by photoelectric interaction of gamma rays with lead. This will result instead in the production of tin fluorescent X-rays, which can in turn be absorbed by a layer of 0.1cm copper. The total attenuation coefficients of surrounding materials of the graded shielding is shown in Fig. 2.11. It can be seen that the migration of KX-rays towards lower energies due to the attenuation effect of the graded shielding. The dimensions of the free surface within the shielding enclosure are 24.7 cm diameter $\times$ 34 cm deep.

Chapter 3

Detector Noise and Energy Resolution

Introduction

The energy resolution is one of the key properties of semiconductor detectors in gamma-ray spectroscopy. The intrinsic energy resolution [Kno10] attained in a germanium detector system is normally determined by a combination of three major elements, which are [G+95a] due to the uncertainties in processes taking place in both the detector and the electronic system:

- W_S - the FWHM corresponding spread owing to the inherent statistical fluctuations in the number of charge carriers.
- W_C - the FWHM equivalent component due to the variations in the charge collection efficiency.
- W_E - the FWHM equivalent noise that can be attributed to the electronic components of the signal-processing chain.

Because these various sources of noises are independent of each other, their contributions to the overall energy resolution must be added together in quadrature. The full width at half maximum, W_I, can then be synthesized as follows [G+95a]:

$$(W_I)^2 = (W_E)^2 + (W_S)^2 + (W_C)^2 \ . \tag{3.1}$$

Each element will be explained individually in a brief summary in the following sections.

3.1 Charge Production

This noise [Kno10] scales with the counting statistics of electron-hole (e-h) pairs produced for a given amount of deposited energy in a germanium detector and it is [HB+14] a fundamental inherent limitation on the measured energy resolution. Because the process of the creation of an electron-hole pair obeys Poission statistics, such that, if the number of electron-hole pairs N are created by the absorption of gamma-ray energy E,

the standard deviation on N, σ_N is equal to the square root of N,

$$\sigma_N = \sqrt{N} \ . \tag{3.2}$$

The number of electron-hole pairs produced will be proportional to the total energy absorbed E, this means that if ϵ is the average energy necessitated to create one electron-hole pair ($\epsilon = 2.96 \times 10^{-3}$ keV at 77 K [Kno10]), then,

$$\sigma_N = \sqrt{E/\epsilon} \ . \tag{3.3}$$

It can be seen from Equation 3.2 and Equation 3.3 that, as N increases, there will be a reduction in the statistical fluctuation in the number of charge carriers per pulse. This means that, a larger number of information carriers results in a lower uncertainty on the energy resolution, which can be achieved by choosing the detector material with low ionisation energy, ϵ. Germanium detectors have relatively low ϵ compared to any other type of common detectors, consequently, they have superior energy resolution.

In terms of the full energy at half maximum of the peak and for an assumed Gaussian shape of the peak, the (W_S) is given by [Kno10]:

$$W_S = 2.35\sqrt{\epsilon E} \ . \tag{3.4}$$

It can be observed that, (W_S) is proportional to the square root of the gamma-ray energy, which means that, at high energies (e.g. 1332.5 keV) the predicted uncertainty is significantly larger than the total found in practice from all the uncertainties of Equation 3.1. The reason for the difference is that Poisson statistics does not strictly apply to the production of charge carriers in a semiconductor. The energy to create an e-h pair is constrained to a narrow region of a few eV, which restricts the spread in N. This is interpreted by introducing a correction factor F, the *Fano factor*, that takes this discrepancy into account, and is used to quantify the departure of the observed variation in the number of charge carriers produced by ionisation from that predicted by Poisson theory [Kno10], [G$^+$95a]. By incorporating this factor into Equation 3.4, (W_S) can be rewritten as:

$$(W_S)^2 = (2.35)^2 F \epsilon E \ . \tag{3.5}$$

The Fano factor [Fan47] is an experimentally determined factor and it has been calculated and presented in Section 4.3.1. It's value spans within a large range of published values between 0.057 and 0.129 [G$^+$95a], [Kno10], [Z$^+$70], [Bil67], [P$^+$69] and [S$^+$70], which is owing to the difficulty in taking into consideration all other sources of uncertainty in the number of charge carriers.

3.2 Charge Collection

The charge collection process depends on the electric field strength across the detector active volume and can be enhanced using a high bias voltage. The effect of incomplete charge collection appears as a low-energy tail on the full-energy peak in the spectrum [G+95a]. This effect does not follow a Gaussian distribution contrary to the statistical fluctuations in the number of produced charge carriers, and the noise introduced in signal processing electronics as will be discussed in the following section, that broaden the energy peak into a Gaussian shape. For the configuration of the electrode structure of the detector used in this work, the electric field lines are non-uniform as they are if the readout contact covers the entire bottom surface. This may limit the charge collection efficiency because of trapping or recombination of charges in the low electric field regions [Kno10]. Charge collection effects are more prevalent in the coaxial geometry detectors as well as in large-volume detectors with relatively large charge collection distances [Kno10]. This can lead to ballistic-deficit effects due to the long charge collection times as will be highlighted in the following section.

3.2.1 Ballistic Deficit

The variation in the charge collection time (or time profile) of the current signal of HPGe detector, which is fed into the processed electronics, can vary with the number and site of gamma-ray interactions. This means, there will be a range of charge collection times in the pulse shapes recorded by the detector. If the detector system has ballistic deficit effects, the amount of energy deposited in the detector for pulses with long charge collection times will be underestimated by the system, thus producing poorer energy resolution and poorer peak shape. This effect can be partially compensated by simply increasing the electronic shaping time (charge integration time) to account for the longest charge collection times. However, because of the electronic noise, there is a practical limit to the shaping time constant (see Section 3.3 and Section 3.4), so many pulses will not achieve their full height before the pulse is shaped, which means, there will be a reduction in the recorded pulse-height due to the variation in the charge collection times. In the digital domain, there is another practical approach to correct for this effect, which is by processing the detector signals with a trapezoid digital filter. This will be explained in detail in Chapter 6.

3.3 Electronic Noise

Electronic noise is considered as a contributing element to energy resolution in semiconductor radiation detectors [M+11b]. It is related to the influence on an electronic signal of random statistical processes such as the thermal vibration of charges in electronic components following the detector and the discrete nature of electric charge. From the

point of view of minimising the detector capacitance, the readout contact (p+) of the detector used in this work is made considerably smaller compared to the full surface of the detector rear. This geometry has the advantage of decreasing the detector capacitance, which results in minimising the electronic noise and hence improving the signal-to-noise ratio. This is particularly important when measuring low-energy gamma rays. The electronic noise effects can be classified into three main categories, in which, they are distinguished by the different ways they respond to input operating parameters such as the electronic shaping time constant. These categories are [G+95a]: *parallel noise, series noise* and *flicker noise*.

3.3.1 Parallel (or Current) Noise

Parallel noise generally scales with currents flowing in components at the input to the preamplifier. Most parallel noise is attributed to two main sources:

- **Shot Noise:** This source represents the leakage current flowing through the detector element and its circuitry. The origins [Kno10] of this leakage current are associated with both the bulk volume and surface of the detector. *Bulk leakage currents* can be generated when reverse biasing the detector junction. For this biasing, the minority carriers will be conducted and are free to diffuse from the normal p and n regions of the detector resulting in a *steady-state current* that will be roughly proportional to the area of the junction. The second mechanism by which the bulk leakage can be caused is the *thermal generation* of electron-hole pairs within the depletion region, which clearly increases with the volume of the depletion region and can be minimized by cooling the detector material. The second origin of the leakage current of the detector comes from the edges of the junction, where relatively large voltage gradients must be maintained over small distances. The rate of this *surface leakage current* can change greatly, depending on such factors as humidity and any contamination of the detector surface by fingerprints, etc. These factors must be taken into consideration to keep the surface leakage rate within tolerable levels.
  Detector leakage currents must flow through the detector bias resistor, which provides both the signal to the preamplifier and high voltage to the detector. When such leakage currents become large enough, the actual bias voltage applied to the junction is reduced from that of the voltage source by the product of the leakage current and the bias resistance. Therefore, the supply voltage must be raised to compensate for the voltage drop across the resistor.

- **Thermal (or Johnson) Noise:** This noise is due to the thermal motion of charge carriers in critical resistors such as the preamplifier feedback resistor and detector bias resistor. Parallel noise can be reduced by:

  1. Cooling the detector material and feedback and bias resistors.

2. Keeping the feedback resistor large.
3. Using a short electric shaping time constant (discussed in Section 3.4).
4. Using an auto-reset preamplifier as there is no feedback resistor.

3.3.2 Series (or Voltage) Noise

This source of noise arises from the leakage current in the preamplifier field-effect transistor (FET) due to the total input capacitance (of the detector, FET, feedback capacitor and interconnecting cables). Series noise can be minimized by:

- Reducing the input capacitive loading on the detector caused by interconnecting cabling, ground loops, microphonics or radio-frequency pickup. This can be achieved by mounting the preamplifier as close to the detector as practically applicable.
- Lowering the temperature (cooling the FET and feedback resistor).
- Using low noise FET.
- Increasing the shaping time constant (discussed in Section 3.4).

3.3.3 Flicker Noise (1/f Noise)

This noise is attributed to currents flowing in all active components and increases with count rate. An example of noise source under this category is the effects of capture and release of charges in the input FET [Kno10]. It is generally much smaller than either parallel or series noise.

Since the various sources of electronic noise are independent of each other, their contributions must be combined in a similar fashion to Equation (3.1) to obtain the total effect of the electronic noise.

3.4 Dependence of Electronic Noise on Shaping Time and Capacitance

As an illustration of the relative importance of various sources of electronic noise in the measured signal-to-noise ratio, Fig. 3.1 presents a schematic diagram showing the variation with the shaping time made in the filtering or shaping operation. The figure demonstrates that, the contribution of series noise tends to become less significant as the shaping time is raised, which is a completely different dependence to that of parallel noise. There will be an optimum value of the shaping time constant in which the overall electronic noise contribution will lead to a *minimum* called the noise corner. The 1/f noise contributes to the electronic noise in a way that does not change with varying the shaping time [Kno10]. At this optimum time constant, the series and parallel noise contributions are equal. In this work, an experimental optimisation of the shaping

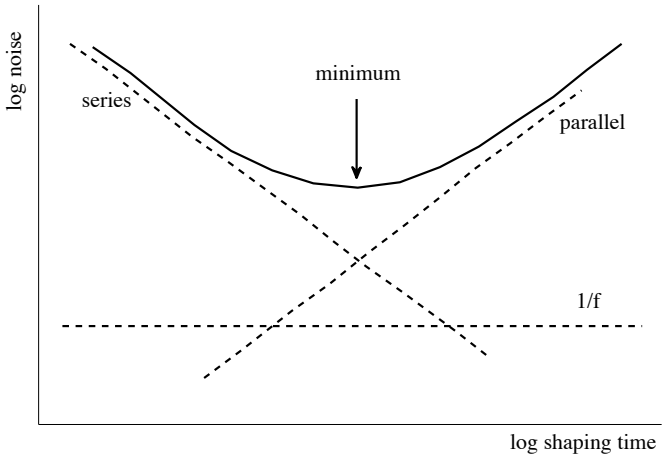

Figure 3.1: Variation of the various electronic noise contributions as a function of the shaping time in the pulse processing electronics (arbitrary data in log scale), showing a minimum total at a particular time constant that results in equal contributions from series and parallel noise. The 1/f noise contribution is unaffected by the shaping time. Reproduced from [Kno10].

time has been carried out as part of the initial setup of the detector system, in an attempt to keep the electronic noise as a whole to a minimum. The contribution of series noise is a strong function of the detector capacitance and will decrease dramatically with low electrode capacitance. However, the relative contribution of parallel noise remains independent of this capacitance. Accordingly, a key point can be drawn here that, considering reducing the contribution of series noise using a detector with low capacitance value will shift the minimum to a shorter time constant. Whereas, decreasing the parallel noise will move the minimum to a longer time constant which is not desirable if the counting rate is very high. Therefore the detector with low capacitance can be operated at high event rates before pulse pile-up reaches a given level of severity [Kno10]. The unique electrode structure of the germanium detector in use, as will be discussed in Section 4.1, has the advantage of minimising the detector capacitance ($\sim$1 pF). The overall noise contribution is therefore considerably reduced and thus the detector offers excellent energy resolution.

Chapter 4

Characterisation of the HPGe detector under study

Introduction

The characterisation of high purity germanium detectors used for environmental or industrial applications, such as dosimetry and nuclear waste characterisation, is an active area of research in the field of nuclear physics [B+10]. This goal requires a detailed understanding of the detector response to different gamma radiations. In order to achieve this task, a detailed experimental study along with comprehensive simulation studies have been carried out. This chapter will report on complete characterisation of the spectroscopic performance of the HPGe detector utilised in this work using three quantitative metrics; energy resolution, absolute efficiency and peak-to-total ratio. These metrics are standard measurements which are routinely used when describing the detector performance. The type of HPGe detector used for this research is a broad energy germanium detector, which is manufactured by Canberra [Can14] and can be utilised to detect gamma rays in a wide energy range of 3 keV to 3 MeV. A detailed description of the detector configuration is presented in the following section.

4.1 Detector Configuration

The BEGe detector (model BE2825) used consists of a p-type HPGe crystal with a cross-sectional area of 28 cm^2 and a thickness of 26 mm, The detector is mounted inside an aluminium end-cap and copper support. A cross sectional side view of the detector is shown in Fig. 4.1(A). A 0.6 mm thick carbon epoxy window is placed 5 mm above the front face of the crystal so that transmission as low as 10 keV is facilitated. The detector has a unique electrode structure, wherein a lithium-drifted n+ contact surrounds the crystal excluding a small area at the centre of the detector rear where a boron-implanted p+ contact is embedded. Due to the low electrode capacitance of $\sim$1 pF [HB+14], which is a result of this unique electrode structure, the detector offers excellent energy resolution and peak shape as well as low noise performance over the energy range of 3 keV $-$ 3 MeV.

A schematic diagram of the detector configuration is shown in Fig. 4.1(B). According to the manufacturer's recommendation, the detector is operated under a high voltage bias of +4000 V (DC). When γ-ray interaction takes place in the detector, electron-hole pairs are liberated and swept through the detector by [HB+14] the electric field

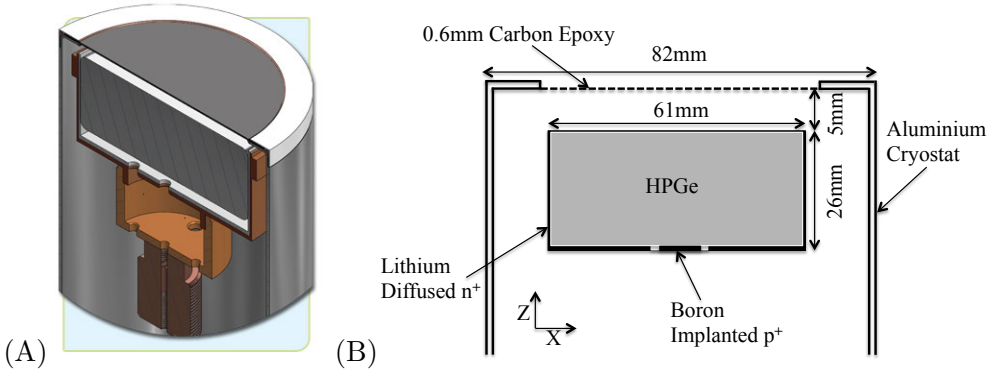

Figure 4.1: (A) Cross sectional side view of the BEGe detector [Can14]. (B) Schematic diagram of the detector and cryostat (or endcap) with the data provided by the manufacturer.

trajectory. While electrons move towards the n+ contact, holes travel towards the p+ contact and can be read out by subsequent processing electronics. The detector is also operated at liquid nitrogen temperature to [K+14] reduce the leakage current (this term is explained in Section 2.3.3.) and to increase the mobility of the charge carriers.

4.2 Experimental Methods

4.2.1 Digital Electronic Setup

The high-resolution gamma-ray spectrometry system, shown in Fig. 4.2A, consists of the BE2825 (s/n b12116) detector, and is located in the Central Teaching Laboratory, University of Liverpool. A diagrammatic representation of the corresponding modules used to acquire data is shown in Fig. 4.2B. In this experimental setup, the detector is coupled with a Canberra 2002CSL charge sensitive preamplifier, which processes the initial signal data generated on the p+ contact readout with a gain of 80 mV/MeV. The preamplifier output signal (exponential pulse) is fed into the input of the Canberra Lynx Digital Signal Analyzer [Lyn16]; where the amplification of the preamplifier pulse, pole zero correction and the signal digitisation take place. The digital system digitises the preamplifier signal at a speed of 100 MHz and quantised at 14-bit resolution to be acquired in a multi channel analyser to produce a pulse height spectrum. The accumulated pulse height spectrum is taken directly to a PC and analysed using the Canberra Prospect software [Pro16]. The software is used to perform a number of tasks, such as [K+14]: peak searching, peak evaluation, energy calibration, nuclide identification, data acquisition, storage, display and on-line analysis of the collected energy spectra.

4.2.2 Data Acquisition

The detector spectroscopic performance has been measured in the standard (detector top) source geometry with the detector biased at the recommended operating voltage,

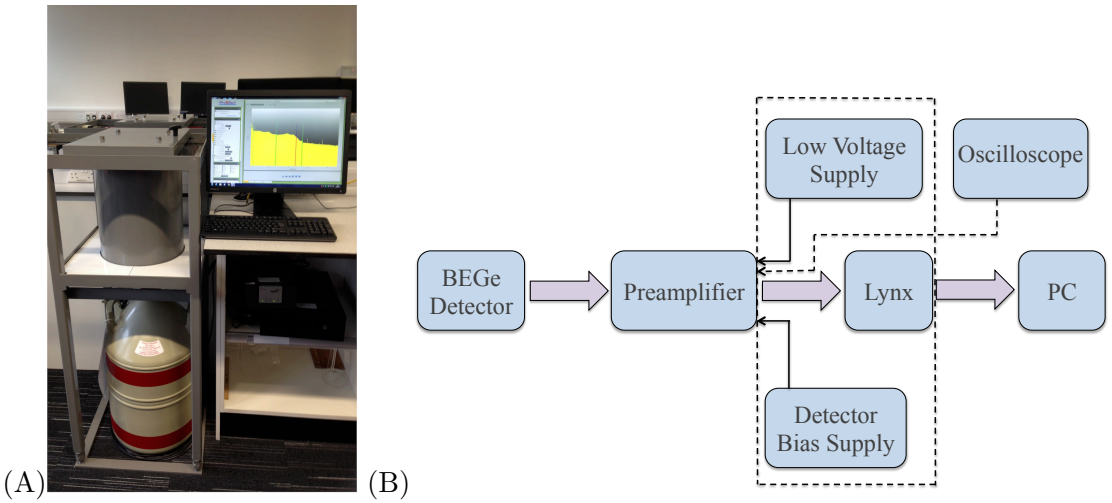

Figure 4.2: (A) The high resolution gamma-ray spectrometry system. (B) Schematic diagram of the detector and signal processing electronics.

using the three standard measurements; absolute efficiency, energy resolution and peak-to-total ratio. The data acquisition settings, required for producing the energy spectra, were input into the Prospect software to the values shown in Table 4.1, p. 38, and used for all subsequent measurements using the Lynx digital system, including the environmental measurements presented in Chapter 5. The energy filter parameters presented in the table are optimised for high-energy resolution for this detector. The optimisation procedure is not shown here as it is irrelevant to the scope of this chapter.

Before proceeding to the spectroscopic measurements, the detector system was calibrated to 0.27 keV/channel using a multi-point energy calibration and a quadratic fit function in Prospect. Such that, precise calibration over the energy range of 2.24 MeV for a 8 K Multi Channel Analyser (MCA) (i.e. 8192 channels) was achieved. The number of channels in the MCA was chosen to be 8192 in order to maintain good peak resolution[1].

During the experimental data acquisition, uncollimated point-like γ-ray sources, each containing a different nuclide (given in the following section), were independently placed at a distance of 25.10±0.05 cm above the centre of the detector face. At such a distance, dead time[2] and count rate losses due to pulse pile-up were negligible. In addition to this, the live time of the acquisition system was chosen to be 2700 s, unless stated otherwise, with a dead time of 1.9%. This ensured good precision on the net peak area[3] of the full-energy photopeaks with the statistical uncertainty, as determined by the Prospect software, below 2.3% for all peaks considered. Pulse height spectra were

[1]The concept of choosing the spectrum size is highlighted in the context of peak area and resolution measurements in the subsection "Peak Area Determination" in Section 5.4.2.

[2]Dead time is a measure of the fraction of events lost from the counting system as events occur quickly because of the random nature of radioactive decay. The dead time loss can become relatively severe when high count rates are encountered.

[3]The terms of the net peak area and its variance is described in detail in section titled "Peak Area Determination" in Chapter 5.

Parameter	Function	Parameter Value
GAIN SETTINGS		
Conversion Gain	To set the desired number of the MCA.	8192
Coarse Gain	To adjust peaks to the desired energy-channel relationship, producing the energy calibration data.	2.0
Fine Gain	It is combined with the coarse gain to set the total system gain.	0.8
LLD (%)	To define the lower level discriminator (LLD) as a percentage of the MCA's full scale.	0.1
ULD (%)	To define the Upper level discriminator (ULD) as a percentage of the MCA's full scale.	100
FILTER SETTINGS		
Trapezoid Rise Time (μs)	Equally sets the rise time and fall time of the digital energy filter.	8.8
Trapezoid Flat Top (μs)	It matches the energy filter to the detector charge collection time to compensate for ballistic deficit effects.	1.2
PUR Guard	It defines the Pile-Up Rejection Guard parameter to set the minimum time between events to cause "no rejection" of the events.	1.1

Table 4.1: Information on the gain and energy filter parameters set in the Lynx pulse processing card during data acquisition. For more comprehensive definition of these parameters, the reader is referred to the user manual [Lyn16]. Similar definitions on filtering parameters in the context of digital filtering techniques can be found in Section 6.3.1.

acquired separately and analysed using the Prospect software, allowing the performance metrics of the detector to be quantitatively measured.

4.3 Experimental Results

4.3.1 Energy Resolution

The experimental energy resolution was determined by irradiating the detector with a variety of certified point-like γ-ray sources ^{241}Am, ^{137}Cs, ^{60}Co and ^{152}Eu with radioactivity[4] of 179.43 kBq, 23.88 kBq, 370.25 kBq and 369.48 kBq respectively at the time of measurement, having energies ranging between 59.54 keV (from ^{241}Am) to 1408.1 keV (from ^{152}Eu).

The energy spectra with sufficient statistics in the evaluated full-energy photopeaks were collected over the acquisition system live time stated above (2700 s). In such that, for the ^{137}Cs photopeak, the net peak area was greater than 2.5×10^4 counts. Whereas, for the ^{60}C and ^{241}Am photopeaks, a minimum of 2×10^5 and 5×10^5 counts was

[4] Amount of gamma radiation emitted from a source (in Becquerel).

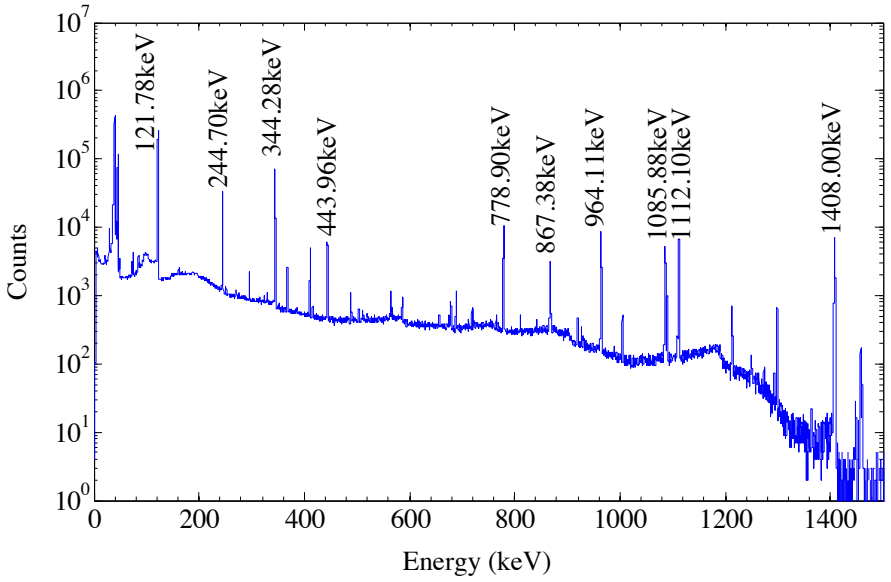

Figure 4.3: Experimental energy spectrum of a ^{152}Eu point source positioned centrally 25.1 cm above the detector front face, measured over a full acquisition system live time of 2700s using the high-resolution gamma-ray spectrometry system shown in Fig. 4.2. The γ-ray photopeaks considered for analysis (with emission probability greater than 2%) are indicated on the plot.

collected in their net peak areas respectively. For the energy spectrum of ^{152}E, the net areas of photopeaks considered for analysis (for all energies with emission probability greater than 2%) were in the range between 1.5×10^4 and 5.3×10^4 counts except those for the 121.78 keV, 244.10 keV and 344.28 keV photopeaks, where a minimum of 7×10^5, 1×10^5 and 2×10^5 counts respectively was acquired. The pulse-height distribution acquired for the ^{152}Eu source is given as an example in Fig. 4.3. Experimental energy spectra obtained using the ^{241}Am and ^{60}C point sources are shown as an example of low and high gamma ray energies in Fig. 4.8, p. 52 and 4.9, p. 53 respectively for comparison purposes as will be conducted in advance.

Using the Prospect software, the FWHM value was extracted from a Gaussian fit for each energy photopeak and was presented in Table 4.2 and plotted as a function of energy in Fig. 4.4. It can be noted from the table that, the FWHM increases from 0.76 keV at 59.54 keV to 1.68 keV at 1408 keV. The uncertainty on these values does not exceed 0.01 keV except the value at 867.44 keV, the uncertainty is 0.02 keV. The value of FWHM at 1332.50 keV (^{60}Co) is 1.65 keV and it shows a slight improvement over the one quoted by the manufacturer, which is 1.72 keV. A quadratic fit of the $(FWHM)^2$ as a function of energy, E, has been created using MatLab software:

$$(FWHM)^2 = 0.465 + 1.83\times10^{-3}E + 9.59\times10^{-8}E^2 \ . \tag{4.1}$$

The coefficients of this fit can be used to calculate the major components of noise discussed in Chapter 2, which contribute to the total energy resolution $(W_T)^2$ of the germanium detector.

Source ref.	Nuclide	Energy (keV)	FWHM (keV)
NPRL 406	^{241}Am	59.54	0.76
NPRL 404	^{137}Cs	661.66	1.25
NPRL 607	^{60}Co	1173.24	1.59
		1332.50	1.65
NPRL 617	^{152}Eu	121.78	0.83
		244.10	0.96
		344.28	1.03
		443.96	1.11
		778.90	1.36
		867.38	1.43
		964.08	1.47
		1085.87	1.51
		1112.07	1.54
		1408.00	1.68

Table 4.2: Measured values of FWHM of BEGe detector using ^{241}Am, ^{137}Cs,^{60}Co and ^{152}Eu sources. Due to the large statistics, the uncertainty on these values does not exceed 0.01 keV except the value at 867.44 keV, its uncertainty is 0.02 keV. The energy (or energies) corresponding to each γ-ray source are according to Ref. [Nuc13].

From 3.1 and 4.1, we have:
$(W_E)^2 = 0.465$ corresponds to the contribution from electronic noise.
$(W_S)^2 = 1.83{\times}10^{-3}E$ is the noise resulting from statistical fluctuations in the number of generated charge carriers.
$(W_C)^2 = 9.59{\times}10^{-8}E^2$ is due to the incomplete charge collection.

The fitted values of $(W_T)^2$, $(W_E)^2$, $(W_S)^2$ and $(W_C)^2$ have been calculated and plotted in Fig. 4.4. It can be noted that the fitted value of FWHM complies with the experimental data well. The electronic noise, $(W_E)^2$, for the BE2825 b12116 detector is 0.682 keV ($=\sqrt{0.465}$). It is superior to a typical germanium detector because of the low capacitance ($\sim$1 pF) of the p + readout contact which is [Kno10] often a dominant factor in the total noise characteristics of the preamplifier.

It can be also seen that the contribution from the statistical variance, W_S, becomes significant above 240 keV, which contributes to the limitation on energy resolution performance of the BE2825 detector. In this work, fano factor, F, has been calculated from the $(W_S)^2$ element of the fit and rearrangement of Equation 3.5 as:

$$F = \frac{(W_S)^2}{(2.35)^2 \epsilon E} = \frac{1.83 \times 10^{-3}}{(2.35)^2 \times 2.96 \times 10^{-3}} \approx 0.112 \ . \tag{4.2}$$

This value is within the range of published values mentioned in Section 2.3.4. The figure also shows that the incomplete charge collection, W_C, is linearly proportional to the gamma radiation energy and its relative importance to the overall energy resolution

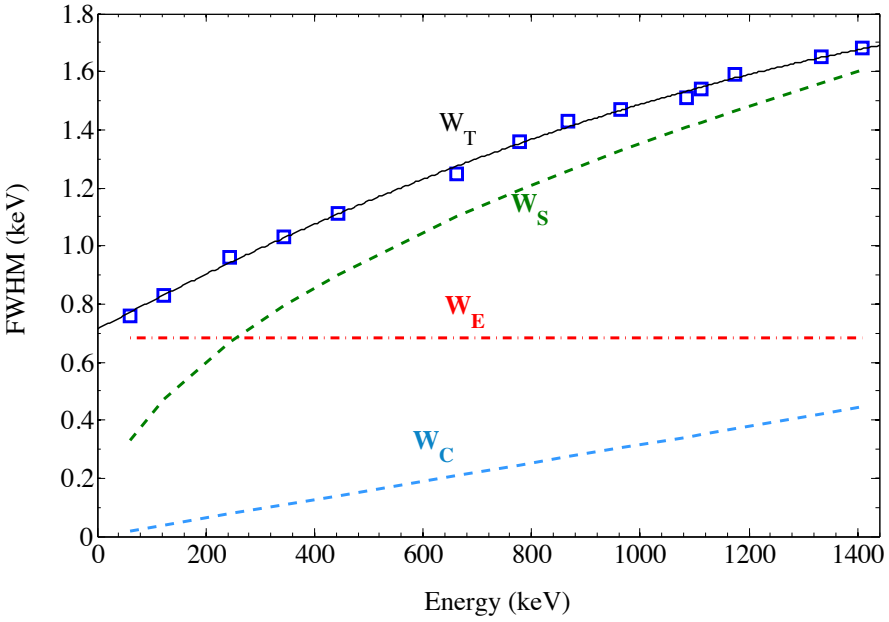

Figure 4.4: Measured energy resolution (or FWHM) as a function of incident γ-ray energy of certified point-like γ-ray sources ^{241}Am, ^{137}Cs, ^{60}Co and ^{152}Eu independently placed at a distance of 25.10±0.05 cm above the centre of the detector face. The uncertainties are not drawn (i.e. not visible), their values do not exceed 0.01 keV except that at 867.44 keV, its uncertainty is 0.02 keV. The curves illustrate the estimated contributions to the total FWHM, W_T, where W_E, W_S and W_C show the contributions due to electronic noise, statistical variations in the number of the electron/hole pairs produced and incomplete charge collection, respectively.

is negligible for the whole energy range, as the detector energy resolution has been measured whilst biased at the recommended operating voltage. The contribution to the total energy resolution stems primarily from the inherent statistical fluctuations. The results of this investigation emphasize the excellent energy resolution, which is due to the low contribution from electronic noise.

4.3.2 Absolute Efficiency

The absolute efficiency, ε_{abs}, as a function of energy was experimentally measured using the same energy spectra collected for the energy resolution determination. The following expression was used to calculate the experimental values,

$$\varepsilon_{abs} = \frac{N_P}{L_T \times A \times P_\gamma} \ , \tag{4.3}$$

where N_P is the net photopeak count as determined by the Prospect software, L_T is the live time of the acquisition system, A is the radioactivity of the source (in Becquerel) at the time of measurement and P_γ is γ-ray emission probability.

The only considered source of uncertainty on the calculated absolute efficiency arises from the uncertainty on the estimate of the net photopeak area as given by the Prospect

Source Reference	Nuclide	Energy (keV)	Measured Efficiency ($\times 10^{-4}$)	Uncertainty (1σ)% <
NPRL 406	^{241}Am	59.54	29.00	1
NPRL 404	^{137}Cs	661.66	4.60	1
NPRL 607	^{60}Co	1173.24	2.57	1
		1332.50	2.18	1
NPRL 617	^{152}Eu	121.78	27.30	1
		244.70	14.90	1
		344.28	9.71	1
		443.96	7.97	2
		778.90	4.16	1
		867.38	3.69	3
		964.08	3.33	1
		1085.87	2.93	1
		1112.07	2.76	1
		1408.00	2.28	1

Table 4.3: Energy versus experimental efficiency data (in arbitrary units). The 1σ relative uncertainty quoted is due to the variance on the estimate of the net peak area determined by the Prospect software.

program. The absolute efficiency values of full-energy photopeaks considered for analysis with their calculated relative uncertainties are shown in Table 4.3.

The experimental efficiency response curve is shown in Fig. 4.5. It can be noted that the decrease in the calculated absolute efficiency values as the energy increases is caused by the higher probability of gamma rays to escape the detector at higher energies. For example, the absolute efficiency at 1408 keV is approximately 8% of that at 59.54 keV.

At low energies (e.g X-rays), the efficiency curve typically has a turning point because low energy γ-ray photons are more probable to be absorbed in the front dead layer of the detector crystal before reaching the depletion region. Because the dead layer is very thin (5 μm according to the MCNP simulation results in Section C.7), subsequently the turning point would occur at lower energy than used in these measurements.

However, the electronic noise of the detector system has been found in Section 4.3.1 to be 0.682 keV. This means that, measuring the absolute efficiency at lower γ-ray energy with low uncertainty to be comparable with those quantified above, may not be possible in the presence of that level of electronic noise.

4.3.3 Peak-to-Total (P/T) Ratio

The ideal gamma-ray sources for measuring the peak-to-total ratio would be monoenergetic sources that emit a single gamma ray at an energy of interest, with no other observed γ- or X-rays. An example of such sources is ^{54}Mn, which has a single 834.8 keV gamma ray. In this case, the complications arising from the contributions of additional gamma rays and/or X-rays will be avoided. For such single gamma source, the total number of counts recorded minus the room background would be used when evaluating

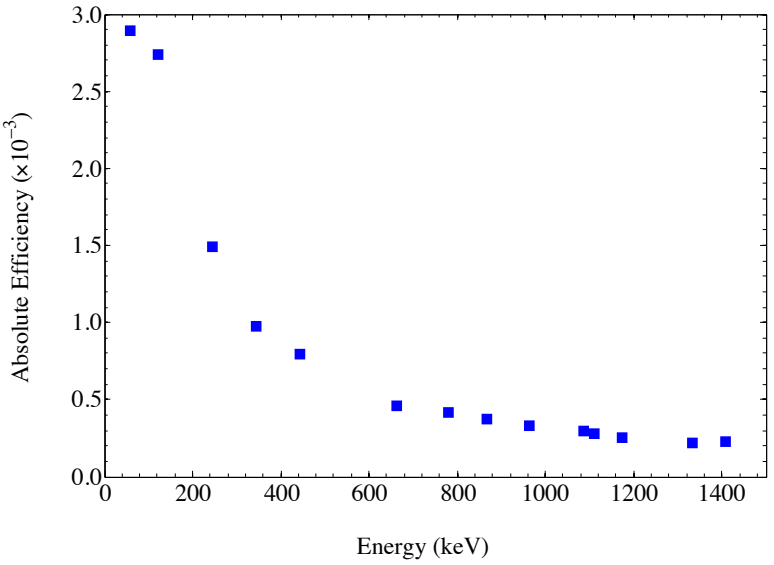

Figure 4.5: Measured absolute efficiency as a function of energy. The uncertainties are drawn, but not visible because their values (shown in Table 4.3) are small due to the large statistics.

the peak to total response. However, in the laboratory, sources with a single gamma ray and no X-rays are limited. Therefore, sources with more than one gamma emitted had to be used. For our measurements, the peak to total (P/T) has been determined using the certified point-like gamma-ray emitters, ^{241}Am (59.54 keV), ^{137}Cs (661.66 keV) and ^{60}Co (1173.24 keV, 1332.50 keV), with radioactivity of 384.96kBq, 216.17 kBq and 48.73 kBq respectively at the time of measurement. These gamma-ray emitters are relatively uncomplicated sources and considered to be the most suitable ones for the measurements of peak-to-total ratios.

P/T values were calculated from each experimentally acquired energy spectrum using Equation 4.4,

$$P/T = \frac{N_P}{N_T} \ , \tag{4.4}$$

where N_P is the net photopeak count as determined by the Prospect software and N_T is the total number of counts under the spectrum. A small correction was applied to N_T, in that the number of counts below 12 keV, 30 keV and 100 keV for the ^{241}Am, ^{137}Cs and ^{60}Co energy spectra respectively were omitted[5]. Then N_T calculated for ^{241}Am, ^{137}Cs and ^{60}Co will be the total number of counts under the spectrum from the last channel in the full-energy photopeak down to 12 keV, 30 keV and 100 keV respectively. In addition, the background subtraction was also applied to N_T, in that a room background spectrum was acquired and the background counts in channels corresponding to those ranges for each source spectrum were also subtracted.

[5]This correction is to set the energy spectra acquired with an energy threshold to compensate for the noise of the data acquisition system. This can also be applied in the Prospect software, by setting the LLD parameter before acquiring each energy spectrum.

Source Reference	Nuclide	Energy (keV)	Measured P/T (%)
NPRL (190)	^{241}Am	59.54	50.26
NPRL (470)	^{137}Cs	661.66	16.61
NPRL (484)	^{60}Co	1173.24	6.75
		1332.50	5.93

Table 4.4: Measured P/T values as a function of energy. The 1σ relative uncertainty is because of the counting statistics as determined by Prospcet. The statistics are large enough that relative uncertainties become negligible (<0.01%).

The P/T ratio as a function of gamma-ray energy is presented in Table 4.4. It can be seen from the table that, the ratio significantly decreases as the energy increases. This is because it becomes more probable for the higher energy gamma rays to escape the detector.

4.4 Detector Modelling

In order to accurately characterise the detector performance under study through a Monte-Carlo based technique, as accurate as possible representation of the geometrical setup of the detector is needed. To achieve this target, the description of the detector setup geometry has been as detailed as possible in the simulation. In this study, the HPGe BE2825 (s/n b12116) has been simulated using two unique pieces of software,

- **MCNP[MCN]:** is a general-purpose Monte Carlo N-Particle transport code system that can be utilised for neutron, photon or electron transport.
  - **MCNP Particle Track (PTRAC)[MCN]:** is Particle Track Output Card included in the MCNP software and used for γ-ray tracking algorithms.
- **GAMOS[GAM14]:** which is Geant4-based Architecture for Medicine-Oriented Simulation and it is based on Geant4 toolkit[A$^+$03], [A$^+$06].

The simulated data from both programs have been processed and analysed using a set of MatLab codes.

The motivation behind using the MCNP and GAMOS softwares is that, first of all, MCNP − the main program used for simulating the HPGe BE2825 detector in use − is an internationally recognised and accredited Monte Carlo transport code, used to simulate the transport of neutrons, photons and electrons. The transport kernel is validated and is therefore widely used by the Nuclear Industry. The MCNP transport code is also the standard code used by Canberra, the detector manufacturer, to generate the detector characterisation files (in combination with measurements) used for the ISOCS [V$^+$05b] detector calibration procedure. MCNP uses continuous-energy nuclear and atomic data libraries. For photon transport − the subject of the discussion − the MCNP code takes account of incoherent and coherent scattering, the possibility of

fluorescence emission after photoelectric absorption, absorption in pair production with local emission of annihilation radiation and bremsstrahlung. The MCNP simulation presented in the following sections was performed using MCNP4C[MCN] version, which was released on February 29, 2000 and is the first major release of MCNP since version 4B (February 4, 1997).

GAMOS − the second program utilised in this work − is a software system allowing to perform GEANT4-based simulations using a scripting language that facilitates the use of GEANT4 by avoiding the need of C++ programming. Its aims are to provide an easy-to-use interface to GEANT4 as well as the flexibility, thus the user can take advantage of the extension of the existing functionality that the GEANT4 toolkit offers. A detailed description of the main characteristics of GAMOS and its available functionalities can also be found in [P+14], [P+11].

Owing to the proprietary nature of the detector's manufacturer, in which descriptive details for some of the detector components (e.g, dead layers) have been withheld, an extensive suite of detector model optimisations using MCNP4C, therefore, had to be carried out in order to reach the best accurate validated model of the detector in use. The final validated model was then used for characterising the detector response for a standard (detector top) source geometry through the performance matrices; the peak-to-total ratio and the absolute efficiency from pulse height distributions generated by the simulation.

The PTRAC and GAMOS simulations were aimed to gain more confidence on the final detector model validated in the MCNP simulation. They were utilised to reconstruct energy and position distributions for gamma ray depositions taking place inside the detector. Therefore, these simulations would provide a step towards gamma-ray tracking. The PTRAC and GAMOS energy distributions were then compared with those acquired from the experiment and the MCNP simulation as will be presented in advance.

4.4.1 MCNP Modelling

The main geometrical features of the experimental configuration that have been constructed in the MCNP simulation, involving the elemental composition of the detector components accompanied with their detailed dimensions and densities, are presented in Table 4.5. The majority of the detector components were mainly taken from the manufacturer provided documents. However, for the unknown components, the front and side/back dead layers were optimised by the MCNP simulation, and their values shown in the table are the optimal values that gave the best simulation to the experiment. The material configuration within the detector cryostat (Crystal holder) was estimated and its dimensions were chosen according to the best of our knowledge gained from an extensive research in the literature such as [Can14], [F+14], [L+10], [B+13].

The certified point-like γ-ray sources used in the experimental measurements (^{241}Am, ^{137}Cs and ^{60}Co) were implemented in detail in the Monte Carlo codes using the SDEF

Component	Composition	Density (g/cm^3)	Dimension
Detector Parameters			
Ge Crystal	Ge	5.32	61 mm diameter & 26 mm thick
Front dead layer	Ge	5.32	5 μm thick
Side/bottom dead layer	Ge	5.32	800 μm thick
Groove inside the crystal	Vacuum	0	22 mm OD$^{(\star)}$ 14 mm ID$^{(\circ)}$ 3 mm Depth
Carbon composite window	Carbon epoxy	1.42, C(83.4%), O(9.3%), H(7.3%)	0.6 mm
Detector endcap	Al	2.7	1.5 mm thick, 82 mm OD & 169.4 mm length
Crystal holder	Cu	8.92	1.5 mm thick 64.02 mm OD
Graded Shielding Parameters			
Lead	Aged Pb	11.34	35 cm OD, 5 cm thick & 34 cm length$^{(\diamond)}$
Tin	Aged Sn	7.31	24.9 cm ID & 0.05 cm thick
Copper	Aged Cu	8.92	24.7 cm ID 0.1 cm thick

Table 4.5: Parameters of the BEGe detector used in the simulation.
$^{(\star)}$The outside diameter of the groove.
$^{(\circ)}$The inside diameter of the groove.
$^{(\diamond)}$Length of the graded shielding for Lead, Tin and Copper.

card[6], which describes the position of the source, the energy of photons emitted by the source in MeV and the γ-ray emission probability. These sources were used to calculate the peak-to-total ratios and the absolute efficiencies of full energy photopeaks. The same source-to-crystal distance utilised in the experiment (25.1 cm) was used in the simulation. Moreover, the elemental composition, dimension and density of the graded shielding[7] surrounding the detector were also included in the simulation to the values shown in Table 4.5.

MCNP Run

For the final detector model (Fig. C.5, p. 149) to be reached and validated, a set of MCNP photon transport codes had to be written and then run independently for photon energies of 59.54 keV (^{241}Am), 661.66 keV (^{137}Cs) and 1173.24 keV, 1332.50 keV

[6]This card is described in Section C.3.3 with some example codes generated in this thesis to show how it was implemented in the input codes.
[7]This term is explained in the subsection titled "Detector Shielding Design" in Section 2.3.7.

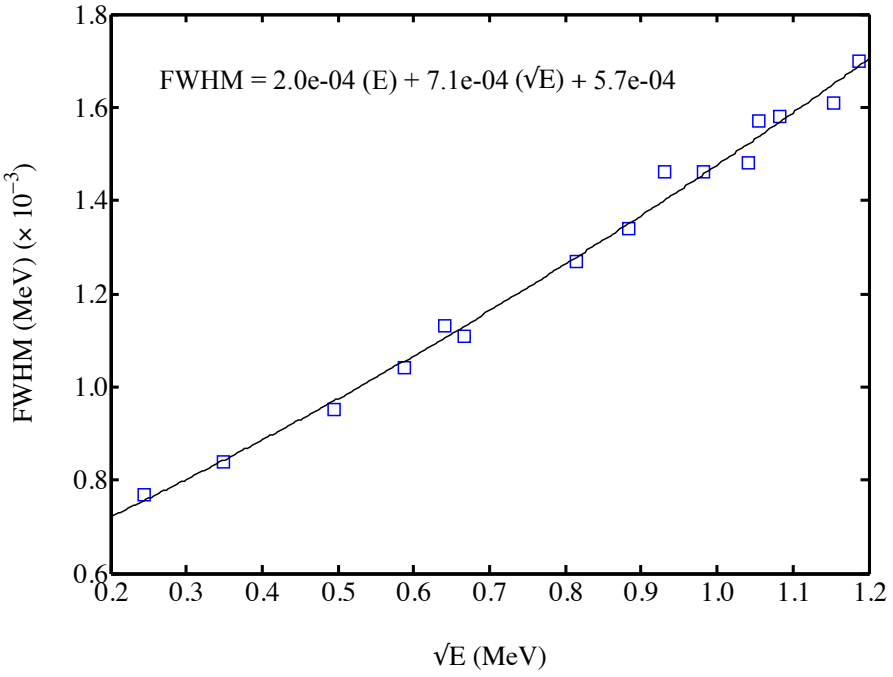

Figure 4.6: Gaussian energy broadening fit. The parameters of this fit, which were implemented in the simulation, specify the FWHM of the observed energy broadening in the BEGe detector. The experimental method for measuring the FWHM is presented in Section 4.2.2 and the results are shown in Section 4.3.1.

(^{60}Co). The type of results accumulated from the Monte Carlo calculations in this work is the energy distribution of pulses generated in the germanium detector by the incident gamma radiation in addition to the total energy deposition in the detector crystal. In MCNP terminology, this accumulation of results is called the pulse-height tally and it is given the designation F8[8]. Therefore, the quantities scored by this tally represent the histogram of the energy depositions. In this work, the energy histogram was binned into equidistant energy windows of 0.273 keV in accordance with the width of MCA channels used for the experimental energy distributions, so the bins covered the range up to 2.237 MeV.

In the MCNP runs, the execution of the Monte Carlo calculations was chosen to be terminated, using the problem cutoff card, NPS[9], after a number of simulated particles up to 1×10^9 has been transported in the run by MCNP. In such that, the estimated statistical relative error assigned to any of the values scored in the F8 tally was $< 0.1\%$ at the 1σ level.

It must be mentioned that, the charge collection process is not modeled by the MCNP code. Hence, in order to better simulate the pulse-height response of the BEGe detector to these photon energies, the FWHM of the photopeaks, as observed in the experiment, must be included in the simulation. This will be explained as follows:

[8]Section C.3.4.1 provides a brief description of the energy deposition tally (F8) with some example codes generated in this thesis to show how it was implemented in the input codes.

[9]This card is explained in Section C.3.6 with some example codes generated in this thesis to show how it was implemented in the input codes.

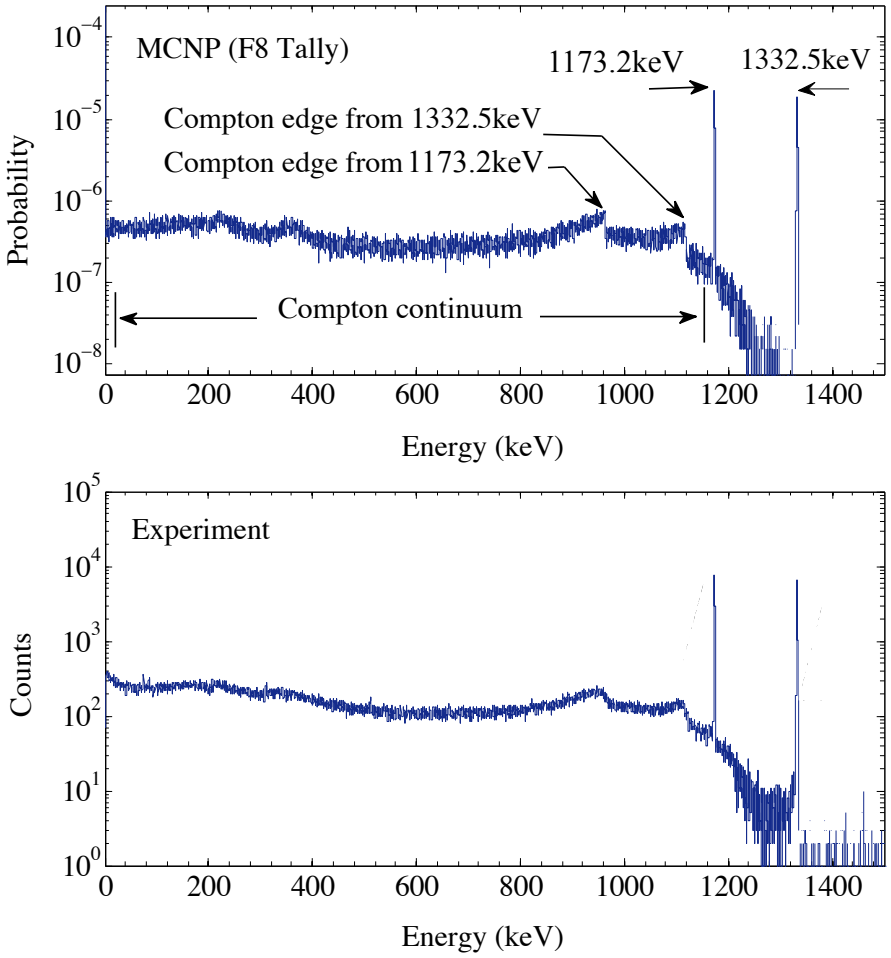

Figure 4.7: An example of pulse height spectrum simulated by MCNP (top panel) for incident gamma ray energy of 1173.24 keV and 1332.50 keV from a ^{60}Co point source positioned centrally 25.1 cm above the detector front face. It exhibits how the energy depositions tallied in F8 are broadened by the Gaussian energy broadening (GEB) card. The corresponding energy spectrum measured in the experiment (see Section 4.2.2) is also shown (bottom panel) for comparison.

The desired FWHM is well described by the parameterisation:

$$FWHM = a + b\sqrt{E + CE^2} \ . \tag{4.5}$$

The experimental energy resolution (FWHM) presented in Section 4.3.1 is plotted as a function of the squared root of the energy of photopeaks for ^{241}Am, ^{137}Cs, ^{60}Co and ^{152}Eu in Fig. 4.6. The FWHM values are fitted in MatLab with a quadratic function as presented in the figure.

Subsequently, the parameters a, b and c extracted from the fit are:

$$a = 5.7 \times 10^{-4}$$
$$b = 7.1 \times 10^{-4}$$
$$c = 2.0 \times 10^{-4}$$

The parameter a, is attributed to the electronic fluctuation (offset or intercept), whereas, b corresponds to the uncertainty in the charge production and c is attributed to the incomplete charge collection inside the detector. Values of these parameters, which describes the FWHM of the observed energy broadening, were then implemented in the MCNP input codes using the Gaussian energy broadening (GEB) card[10].

After the MCNP runs were completed, the peak-to-total ratios were calculated by dividing the total area under the peak by the total area under the entire spectrum. The total peak area was obtained by direct summation of the sampled energies under the photopeak area. The total area under the spectrum was corrected in accordance with the experimental energy threshold to compensate for the noise of the data acquisition system, in which all the tallied energies below 12 keV (for ^{241}Am spectrum), 30 keV (for ^{137}Cs spectrum) and 100 keV (for ^{60}Co spectrum) down to zero energy were omitted. Then each acquired peak area was corrected for its γ-ray emission probability in order to obtain the absolute efficiency for that full-energy peak.

Fig. 4.7 shows an example of pulse height spectrum simulated for the incident gamma ray energy of 1173.24 keV and 1332.50 keV from ^{60}Co to exhibit how the energy deposition values tallied in F8 are broadened by the Gaussian energy broadening (GEB) card. The significant similarity in the importance of the various spectral features of the detector response including the Compton continuum and the Gaussian width (FWHM) of the full-energy photopeaks are evident in the experimental and simulated spectra.

4.4.2 PTRAC and GAMOS Modelling

As already mentioned, the aim of the PTRAC and GAMOS simulations is to generate energy and position distributions for gamma ray depositions occurring inside the detector utilising the final model validated in the MCNP simulation shown in Fig C.5, p. 149. The geometry of the detector setup has been defined in a simple text file, which gives a full description of the detector system arrangement including the geometry of the graded shielding, aluminum cap, copper support, carbon epoxy window.

[10]This card is explained in Section C.3.4.1 with some example codes generated in this thesis to show how it was implemented in the input codes.

Nuclide	Energy (keV)	Measured P/T ($\times 10^{-2}$)	MCNP P/T ($\times 10^{-2}$)
^{241}Am	59.54	50.78	50.57
^{137}Cs	661.66	16.70	17.78
^{60}Co	1173.24	6.92	7.40
^{60}Co	1332.50	6.10	6.96

Table 4.6: Measured and MCNP P/T values for the BEGe BE2825 detector. The 1σ relative uncertainty for measured and simulated values (<<1%) compromises contributions from the statistical uncertainty in each bin in the pulse height distribution based on the Poisson distribution where the uncertainty is $\sqrt{c}$ for c counts.

PTRAC Simulation

In order to track[11] gamma ray interactions taking place in the detector crystal, particle track (PTRAC) output card[12] was inserted in the MCNP photon transport input codes (discussed in Section 4.4) created for photon energies of 59.54 keV (^{241}Am), 661.66 keV (^{137}Cs) and 1173.24 keV, 1332.50 keV (^{60}Co). These codes were produced describing the detector geometry, source and material definitions, and particle photon tallying. Running an MCNP input code with a PTRAC card generates blocks of "event lines" which gives a full description of the entire history of a photon of a given energy moving in a defined direction that begins at a given position. Each block forms a two-dimensional data structure of a particle and all the daughters, which in turn generate other daughters since the PTRAC algorithm separates progeny particles from the parent particle. Because of this, two branches within the tree data structure of a particle cannot follow the parent particle in a linear one-dimensional format. An example with a full explanation of a PTRAC block produced by the specified PTRAC card keywords implemented in this work (stated below), using ^{241}Am γ-ray point source, is presented in Section D.2.1.3.

The PTRAC card was implemented in the input code (see E.1) as following:

```
PTRAC  FILE = ASC  WRITE = all  TYPE = P  CELL = 1  MAX = -1×10^8
```

`FILE = ASC` is to generate an ASC output file.
`WRITE = ALL` specifies x, y, z location of gamma rays interactions in the detector with related cell and material numbers. In addition, u, v, w direction cosines, energy weight, and time.
`TYPE = P` for writing photon events only "Single Particle Transport".
`CELL = 1` if any track of the photon history enters the detector crystal, which is described as cell 1 in the input code, all filtered events for the history are written to the PTRAC output file.
`MAX = -1E+08` sets the maximum number of events to write to the PTRAC output file.

[11] Particle history in MCNP terminology.
[12] For an exhaustive description of this card, the reader is referred to Appendix D

Nuclide	Energy (keV)	Measured ε_{abs} ($\times 10^{-4}$)	MCNP ε_{abs} ($\times 10^{-4}$)
^{241}Am	59.54	30.10	34.70
^{137}Cs	661.66	5.12	5.41
^{60}Co	1173.24	2.87	1.30
^{60}Co	1332.50	2.52	1.22

Table 4.7: Measured and MCNP efficiency values for the BEGe BE2825 detector. The 1σ relative uncertainty for measured and simulated values (<<1%) compromises contributions from the statistical uncertainty in each bin in the pulse height distribution based on the Poisson distribution where the uncertainty is $\sqrt{c}$ for c counts.

The negative value means that the MCNP run will be terminated when this value is reached.

The output produced by the PTRAC card (Appendix D) contains the full simulated history of the gamma ray inside the detector.

GAMOS Simulation

GAMOS simulations were performed using GAMOS version 5.0.0 [GAM14]. Two input codes are required for each run; one is an input (execute) file containing Geant4 and GAMOS commands, the second describes the detector geometry (see Appendix E, Section E.2). To simulate gamma ray interactions, we need to create hits (or deposits of energy) inside the detector. This can be accomplished in GAMOS by treating the detector crystal described in the geometry file as a sensitive volume in order to record hits within it. A sensitive volume class was therefore used in the input code. The sensitive class used in this work is *GmSDSimpleExactPos*[GAM14]. To simulate energy-broadening effects, a reconstructed hit builder *GmRecHitBuilder1to1*[GAM14] had to be used. The reconstructed hit builder serves to merge hit energies that are close to each other, so the energy output is the sum of hits energies in a track and the resulted position is the weighted sum of the hit positions weighted by the energy of each hit.

4.5 Simulation Results

4.5.1 MCNP Results

In order to quantitatively evaluate the values of the peak-to-total ratio and the absolute efficiency obtained from the simulation against the experimentally determined values for the γ-ray sources; ^{241}Am, ^{137}Cs and ^{60}Co, the latter values must be recalculated in the same manner utilised for determining the simulated values. To achieve this, the data of the experimental energy spectra acquired for these gamma ray sources and the room background were exported from Prospect into a CSV file where the area of the evaluated photopeaks can be deduced by direct summation of the contents of the peak

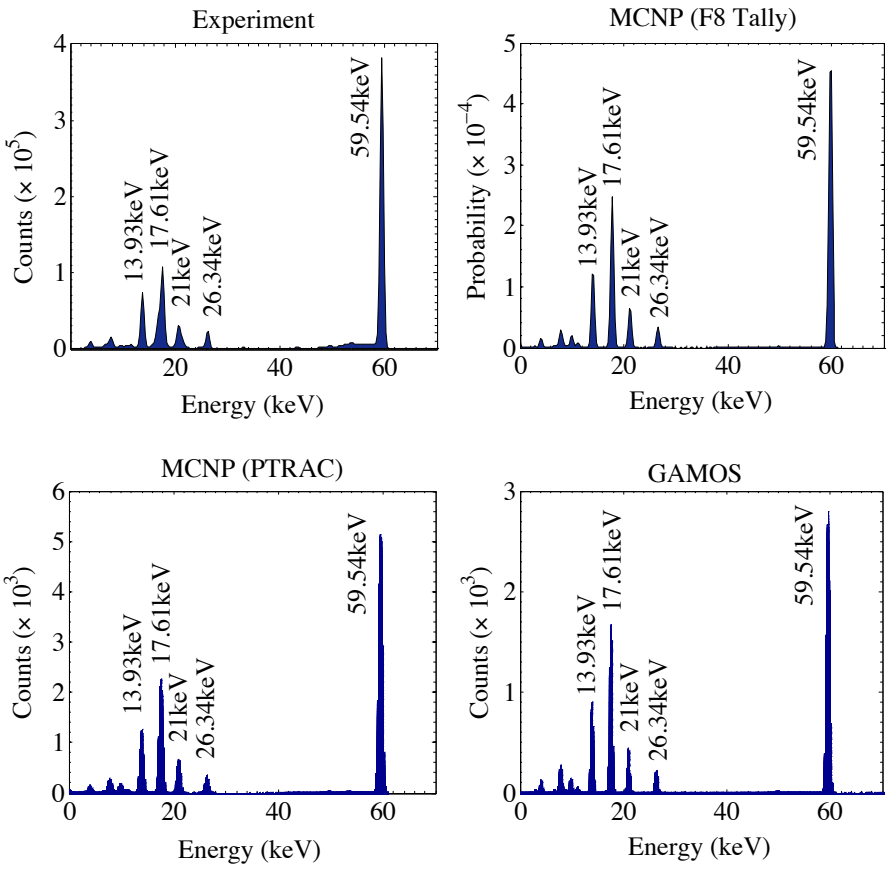

Figure 4.8: Comparison of the measured (left top panel) and simulated distributions of the energy deposited in the detector crystal for incident gamma-ray energy of 59.54 keV from ^{241}Am point source positioned centrally 25.1 cm above the detector front face. The simulated spectra were plotted using data generated by F8 tally (right top panel), PTRAC card (left bottom panel) and GAMOS (right bottom panel).

minus the background counts for the photopeak region. The energy threshold correction and the background subtraction were also applied to the total area of the spectrum. The absolute efficiency for photopeaks and the peak-to-total ratio were determined utilising Equation 4.3 and Equation 4.4 respectively. Subsequently, a straightforward comparison between the measured and simulated values was performed as shown in the following sections: The uncertainty in the measured absolute efficiencies and the peak-to-total ratios are due to the statistical uncertainty on the content of each channel in the energy spectrum based on the Poisson distribution where the uncertainty is $\sqrt{c}$ for c counts. Whereas, the relative uncertainty on the MCNP determined values is calculated from the statistical relative error assigned by MCNP to any of the binned energy values scored in the F8 tally.

Peak to Total

A summary of the MCNP and measured P/T ratios is presented in Table 4.6. It can be noted from the table that, the MCNP calculation slightly overestimates the ratios over the whole energy range 59.54 − 1332.50 keV with differences from 0.21% to 1.08%. The

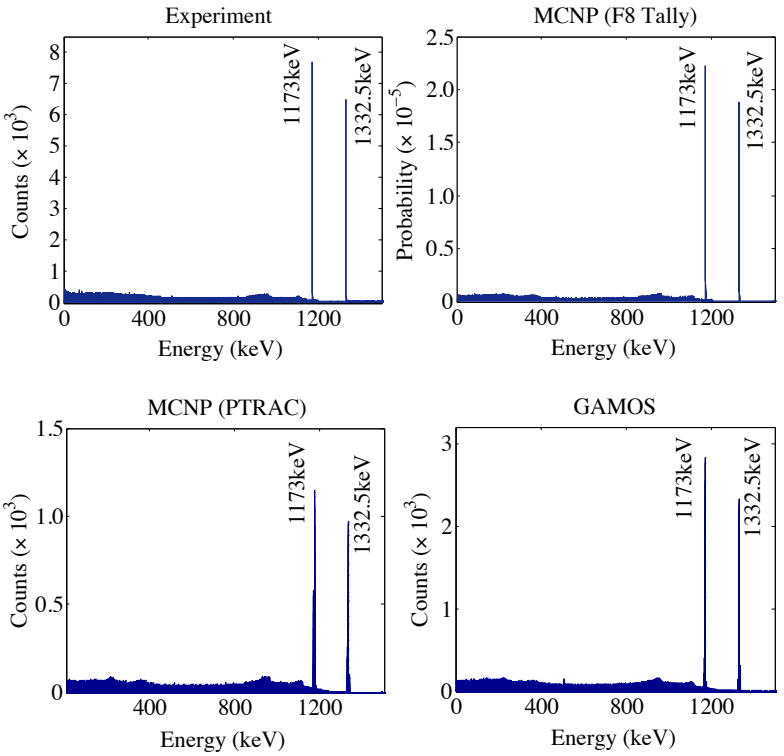

Figure 4.9: Comparison of the measured (left top panel) and simulated distributions of the energy deposited in the detector crystal for incident gamma-ray energy of 1173.24 keV and 1332.50 keV from ^{60}Co point source positioned centrally 25.1 cm above the detector front face. The simulated spectra were plotted using data generated by F8 tally (right top panel), PTRAC card (left bottom panel) and GAMOS (right bottom panel).

discrepancy between the simulation and the experiment can be attributed to a number of possible explanations. First of all, the materials that surround the source and the detector were not all included in the simulation. These materials include the source holder, liquid nitrogen dewar, cover of the shielding castle as well as the source plastic button itself, etc. The Compton-scattered gammas from these surrounding materials can influence the total number of detected gamma rays in the overall detector response. In such that, the scattered photons will add only to the Compton continuum of the γ-ray pulse height spectrum and not to the photopeak, resulting in a reduction in the peak-to-total ratio [Kno10]. Second, MCNP calculations [V$^+$05a], [H$^+$03] do not consider regions of low charge collecting electric field and regions of partially sensitivity in the dead layers where the charges are not completely collected.

Absolute Efficiency

A comparison of the theoretical values of the absolute efficiency calculated by MCNP with the experimentally acquired values is made in Table 4.7. It can be seen from the table that, there is a good agreement between the experiment and the simulation for the 59.54 keV and 661.66 keV gamma-ray energies, however, for those from ^{60}Co, the MCNP calculation underestimates their absolute efficiency values. A possible explanation has

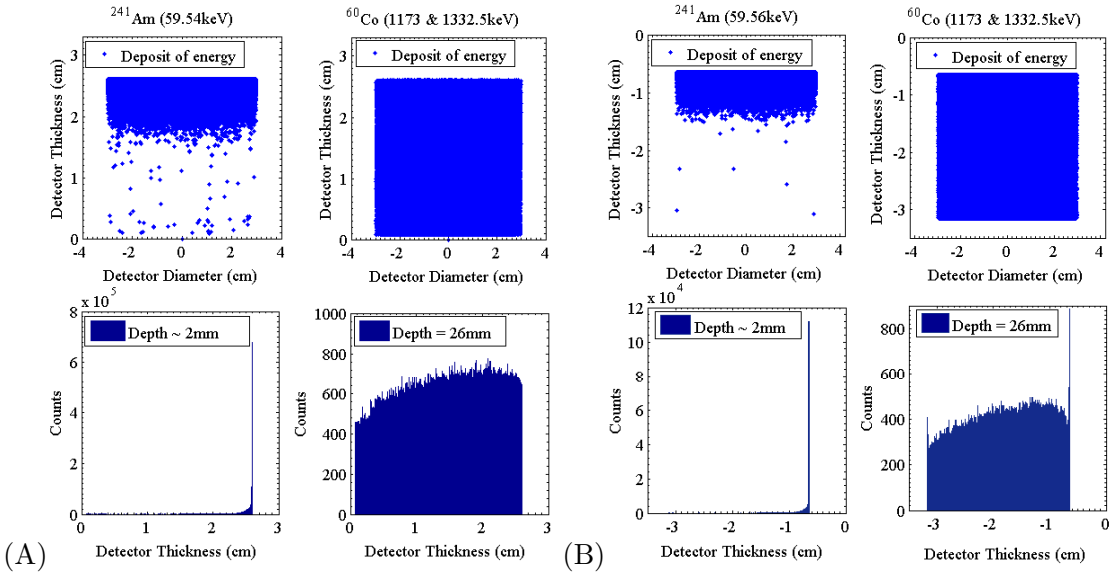

Figure 4.10: Position distributions of gamma-ray interactions for ^{241}Am and ^{60}Co point sources created by (A) PTRAC simulation and (B) GAMOS simulation. An estimate of the depth of the vast majority of gamma-ray interactions is indicated on the plots.

been presented in the previous section in regard with the characteristic charge collection process of the detector, which is not accounted for by MCNP.

4.5.2 PTRAC and GAMOS Results

MatLab analysis codes have been created for processing the PTRAC and GAMOS output files. The MatLab program offers high functional capability for deriving information from extremely large files and can access the output file for reading line by line. The program extracts the energy deposited in the detector and plots the energy distributions. Each PTRAC output file ($\sim$ a total of 2 Gbytes of data) or GAMOS output file ($\sim$ a total of 34 Mbytes of data) was created for a particular radioactive point source specified in the input code. Three different radioactive sources (^{241}Am, ^{137}Cs, ^{60}Co) were used individually in the PTRAC and GAMOS input codes. The PTRAC energy spectra were derived only from photons that undergo scattering and/or photoelectric absorption. In MCNP terminology, this is known as collision and termination events. Collision and termination ones describing the secondary particles generated in the PTRAC output code are excluded from the calculation, as they are not originating from the gamma sources in use (see Appendix D, Section D.2.1.3).

GAMOS energy spectra were reconstructed by straightforward histograming of the energy values calculated by GAMOS. Pulse height distributions for the point γ-ray sources ^{241}Am and ^{60}Co generated from the deposits of energy calculated by MCNP PTRAC and GAMOS are shown side by side with that created from the energy values tallied in the energy deposition tally F8 as well as the experimentally determined spectrum in Fig. 4.8 and Fig. 4.9 respectively. It can be seen from Fig. 4.8 that, there

is a noticeable discrepancy in the width between the simulated and the experimentally acquired spectra concerning the emission intensities of the L X-rays emitted by [Nuc13] the ^{237}Np resulting from the alpha decay of the ^{241}Am source (13.93 keV, 17.61 keV and 21 keV). It is evident that the L X-rays emission intensities derived from the theoretical calculations are relatively higher (i.e. narrower) in comparison with those measured in the experiment. This discrepancy can be attributed to the spectral resolution difficulties using the current germanium detector and much higher-resolution gamma spectroscopy technique is required in order to distinguish between all the L X-ray peaks. Therefore, the fine structure within the L X-rays was not accounted for in the simulation.

In order to examine gamma rays typically interact with the detector crystal, the MCNP positions (x, y, z) of scattering and photoelectric events are stored in arrays and then histogrammed as a function of the detector thickness. These are presented in Fig. 4.10(A). Additionally, positions (x, y, z) of hits created by GAMOS are also plotted and histogrammed as a function of the detector thickness as shown in Fig. 4.10(B).

Chapter 5

Environmental Radioactivity and Soil Sample Measurements

Introduction

The main aim of this chapter is to characterise the content of radioactive elements found in environmental samples in question by measuring their gamma activities using gamma-spectroscopic analysis techniques. This is required in order to evaluate the amount of radioactivity concentrations of the samples (discussed in Sections 5.3 and 5.4). This chapter will give an introduction on radioactivity in the environment. This introduction is illuminating on two main topics: the first topic is about the various decays forms by which the radioactive elements are transformed (or decay out) into more stable forms. The second topic explains the different sources of radioactivity and their origins found in the environment; from cosmos to man-made. These topics will be briefly described in the next two sections as follows:

5.1 Radioactive Decay

There are various forms of radioactive decay that many nuclides[1] can undergo to form more stable nuclides. The radioactive-decay process involves [Pri11a] the emission of alpha (α), beta (β) and gamma (γ) radiations. Alpha radiation consists of helium nuclei, while beta radiation represents high-energy electrons or anti-electrons and gamma rays are very short wavelength electromagnetic radiation. Another form of radioactive decay by which some very heavy nuclei are transformed into stable nuclei is spontaneous fission or induced fission. The next sections highlight these forms of radioactive decay as follows:

5.1.1 Alpha Decay

A heavy nucleus (mass number A $>$ 209) will often decay by emitting an α-particle, losing mass as it does so, and symbolically illustrated as:

$$(A, Z) \rightarrow (A - 4, Z - 2) + \alpha \ .$$

An α particle is a helium-4 nucleus ($^4He^{2+}$). It has a mass of 4.0026 units and charge $2e$, where e is the charge of a proton. It is an ionising particle and does not travel far

[1] All elements with atomic number Z $>$ 83 are unstable (or radioactive) nuclei

in material, but does ionise and excite a large number of atoms along its travelled path. A sheet of paper, skin or a few cm of air would stop an α particle of energy 4 MeV to 6 MeV. Examples of α-active nuclei are: ^{238}U (4.5 MeV α) and ^{239}Pu (5.16 MeV α).

5.1.2 Beta Decay

Radioactive nuclei of all masses can decay by emitting either an electron (in β^--decay) or a positron (in β^+-decay) and this can be symbolically illustrated as:

$$\beta^- - decay : (A, Z) \rightarrow (A, Z+1) + \beta^- + \overline{\nu}$$

$$\beta^+ - decay : (A, Z) \rightarrow (A, Z-1) + \beta^+ + \nu$$

An electron (charge $-e$) and a positron (charge $+e$) are light particles ($\sim$1/1823 unit). They are ionising particles (like α particles) and, at a typical decay energy of about an MeV, a β particle will be stopped by a few mm of solid material. Examples of β^--active nuclei are: ^{14}C (0.16 MeV β), ^{35}S (0.17 MeV β), ^{90}Sr (2.28 MeV β). Electron capture has the same effect as β^+-decay, but no charged particle is emitted. Examples include: ^{40}K, ^{123}Te and ^{138}La.

5.1.3 Gamma Decay

Most β-active and α-active nuclei emit γ rays, which occurs following a decay that leaves the daughter nucleus in an excited state. Gamma radiations are photons with zero mass and no charge. They are not easily stopped and γ rays of an MeV will penetrate many cm of solid matter. Examples of γ-active nuclei are: ^{22}Na (E_γ = 1274 keV), ^{40}K (E_γ = 1460 keV), ^{60}Co (E_γ = 1173 keV, 1332 keV) and ^{137}Cs (E_γ = 662 keV).

5.1.4 Fission

Some very heavy nuclides may decay by spontaneous fission or by fission following the capture of a neutron or other particle. The fission-decay process involves the emission of several neutrons and the production of two fission fragments in the mass range of about 80 to 160. The resultant fragments are radioactive and decay by β^-, γ (and seldom, neutron) emission. Examples of fissionable nuclei include: ^{235}U and ^{239}Pu.

5.2 Environmental Radioactivity: from Cosmos to Man-Made

In the environment, there is a variety of radioactivity sources ranging from naturally occurring radioactive nuclides to those that are synthesised from anthropogenic activities[2]. These sources of radiation are explained in the following sections:

[2]Human activities such as weapons testing conducted from 1945 to 1963, construction of nuclear power plants and reprocessing facilities - nuclear reactors and accelerator laboratories.

5.2.1 Natural Sources of Radioactivity

The environmental natural radioactivity [Pri11a] stems from both extraterrestrial sources initiated from outside the earth called *cosmic radiation*, as well as from radioactive elements contained in the earth's crust. The radioactivity of the earth involves the *primordial radionuclides* whose half-lives are effectively long, so that they have survived since their formation, in addition to the secondary radionuclides (or progenies) that are formed in their decay chains (or series). These sources of natural radioactivity are briefly outlined as follows:

Cosmic-Ray Produced Radionuclides

Cosmic radiation [Pri11a] consists of charged particles having a wide range of energies deriving primarily from outside the solar system. It is made up of 87% protons, 11% α particles, 1% of nuclei with Z between 4 and 26 and 1% of high-energy electrons. These particles have energy ranging from 10^4 MeV to 10^{13} MeV. The high-energy particles of cosmic rays can interact with atoms and molecules in the atmosphere and create radioactive isotopes, called *cosmogenic radionuclides*, such as ^{7}Be /^{10}Be, ^{3}H, ^{14}C, etc. Some other reaction products are also produced such as electrons and mesons. Cosmic rays can also induce fission in, for instance, ^{235}U producing fission fragments and more neutrons, which may also be captured by uranium creating heavier radioactive nuclei. Although cosmic radiation provides a continuous bombardment of the earth's atmosphere, only a fraction of cosmic rays can actually reaches the surface of the earth and be detected by radiation detectors.

Primordial Radionuclides

Primordial radionuclides (or terrestrial) found in the environment can be divided into two classes [Pri11a]; radionuclides that occur singly because they decay into a stable nuclei, and radionuclides arising as components of decay chains of radioactive elements.

- **Nuclides Occurring Singly**: The most important component of terrestrial origin that occurs singly is the radioactive potassium-40 (^{40}K). It decays, with a 1.26 $\times$ 10^9 year half-life, either into ^{40}Ca by β^- emission with 1.314 MeV (89% yield), or into an excited state of ^{40}Ar by electron capture. The ^{40}Ar excited state decays very quickly to the ground state and a 1460 keV gamma ray (11%) as well as characteristic Ar X-rays are emitted. The major source of ^{40}K in soils is due to the application of fertilisers. The average 70 kg person also contains about 140 g of potassium of which the activity concentration of ^{40}K is about 5.7 kBq. From the point of view of gamma-ray spectroscopy, the 1460 keV gamma ray often results in an identifiable peak in the background spectra from γ-ray detectors.

- **Nuclides Occurring in Chains**: Uranium and Thorium are examples of natural radioactive nuclides that occur in chains and are found in the earth's crust. Alternatively expressed, they are members of long decay chains involving a number

of daughter products, which are also radioactive, and emitting α or β particles, which are often followed by gamma de-excitation.

The decay chain of Uranium starts with the parent nucleus ^{238}U and includes daughter products such as: ^{226}Ra, ^{214}Pb and ^{214}Bi, whereas, the decay chain of Thorium begins with the parent nucleus ^{232}Th and contains daughter products such as: ^{228}Ac, ^{224}Ra, ^{212}Pb and ^{208}Tl. Those daughter products are α and β emitters, and after their decay, they are left in an excited state and de-excite by emitting γ rays.

5.2.2 Man-Made Radionuclides

Anthropogenic activities can also result in radioactivity in the environment. The principal artificial sources of environmental radiation are medical exposure for diagnoses and therapy. Another contributor to radioactivity in the environment is nuclear fission, which is used as a source of power for both military and commercial purposes. Fission products also originated with atmospheric fallout from past weapons testing and from nuclear power plants accidents and reprocessing program. The major contributors to the global fallout (or artificial) radionuclides in the environment from nuclear accidents are Chernobyl [B$^+$16] in 1986 and Fukushima [D$^+$16] in 2011, which are classified as the most severe accidents occurred in nuclear power industry. For example, in the Chernobyl accident, about [CA17] 8.5 x 10^{16} Bq of ^{137}Cs (one of the most significant radionuclides from the perspective of exposures to people and the environment) was liberated to the atmosphere and carried across the international boundaries [UNS88], [M$^+$15].

5.3 Soil Sample Measurements

As this project is dedicated for industrial and environmental applications, this entails collection of environmental samples for gamma-spectroscopic analysis. Gamma emitters can be widely distributed in the environment and they present in various geological formations such as soil, plants, water and rocks etc. [K$^+$16] [S$^+$05]. Samples of soil were chosen for γ-activity measurements in the current work as soil is considered to be the most important source of gamma radiation in the environment. The main reason for that is; that soil covers the major sources of natural radionuclides such as ^{238}U, ^{232}Th, ^{226}Ra, ^{222}Rn, ^{210}Pb, ^{40}K etc., and fallout radionuclides such as ^{137}Cs [K$^+$16], which is the most prominent isotope among different fallout radionuclides and can be detected by its gamma energy 661.8 keV.

In the UK, it has been demonstrated in literature [C$^+$16], [R$^+$96] that, the British Nuclear Fuel (BNFL) waste-reprocessing plant on Sellafield Limited nuclear site in North-West England is the major contributor to the fallout radionuclides, such as ^{137}Cs and ^{241}Am, in the coastal areas of NW England. This reprocessing facility has been, under authorization, releasing low-level radioactive wastes as liquid effluents into the Irish Sea

since 1952, with highest discharged activities in the early 1970s [G+95b]. The radionuclides discharged are being diluted and spread out from the discharge point, hence they have washed on the English, Scottish, Welsh and Irish coasts during tidal flow.

Subsequently, much research related to estimation of the radionuclide activity concentrations, in coastal areas of NW England, were published such as; [C+16], [R+96]. However, there are no previous studies related to measurements of radioactivity levels in environmental samples collected from West Kirby in literature (up to the time of writing this thesis). Therefore, soil samples were chosen to be taken from this site.

West Kirby, a tide-washed coastal area in NW England bordering the Irish sea, is located on the eastern side of the mouth of the Dee Estuary and is situated between $53^o22'22.87''$ N and $3^o11'3.01''$ W (Fig. 5.1).

The objective of this chapter is mainly focused on obtaining the baseline data on radioactivity concentrations in 11 representative soil samples collected from West Kirby. This chapter is also intended to provide a comprehensive analysis procedure to determine the radioactivity concentrations in soil samples using the experimental methods discussed in section 5.4. This section also includes the statistical analysis procedure used in the calculations of sample activities.

Although low levels of radioactivity have been found in this site, these results are still of importance as they can serve as reference data records on artificial radionuclides, detected in this study area at the time of this work, for researchers who [C+16] focus on understanding the distribution, accumulation of radionuclides in contaminated coastal areas of NW England, and the results are also useful for investigating any possible changes in environmental radionuclide activity concentration with time because of the anthropogenic activities.

5.4 Experimental Methods

5.4.1 Soil Sampling and Sample Preparation for γ Spectrometry

The procedures of soil sample collection and preparation prior to their radioactivity measurement by gamma-spectroscopic analysis, are described in two separate stages:

- **First Stage**: involves the *field work*, in which soil samples up to ∼30 cm depth were randomly collected from five undistributed sampling points in West Kirby, Spring 2014 (Fig. 5.1). Soil samples were taken by inserting plastic drainpipes into different sampling points. Five cores were appropriately coded according to the Global and Positioning System (GPS) of their locations. Sampling points were selected on the basis of different soil consistency. Two cores were classified as wet samples (saturated with water) and two as damp samples (moderately wet), whereas the other one was classified as a moist sample (slightly wet, or not quite dry). The selected cores analysed for this work were one wet core and one moist core. The wet core was collected from a tide-washed area in the site, at a

sampling point located between $53^o22'30''$ N and $3^o11'27''$ W, to obtain a water-saturated soil sample, whereas the moist one was taken from a drier sampling point, positioned between $53^o22'23''$ N and $3^o11'24''$ W, which is less frequently inundated compared to the other sampling point, for a slightly wet soil sample. Cores were then transported to the low-background radiation detection laboratory at the University of Liverpool for sample preparation.

- **Second Stage**: represents the *lab work*, in which the final sample arrangement and the gamma-ray spectroscopic measurements were taken place. Following sample collection, each core was sliced every ∼5 cm, transferred to a baking tray and placed in an electric oven at 110 C^o for 24 hours to ensure that any moisture was removed from the samples. Each unit sample was passed through a 2 mm mesh sieve to [S+05] homogenise it and eliminate impurity such as stones and roots. Each post-sieved unit was then transferred into a 250 ml labeled Marinelli beaker. The containers were firmly sealed and weighted. The approximate net weight of each sample was about 0.5 kg. The total number of the final prepared samples obtained from cores corresponded to 11 individual soil samples.

Having completed the sample preparation, this allowed their γ-ray spectroscopic measurements to be performed. Measuring samples was carried out by the high-resolution HPGe gamma-ray spectrometry shown in Fig. 4.2, p. 37, which makes use of 61 mm diameter × 26 mm thickness HPGe BE2825 detector. A detailed description of the detector system setup as well as the data acquisition settings used to collect the energy spectra, are given in Section 4.2. The energy spectra were acquired and analysed using the Canberra Prospect program. In addition to this, the acquired spectra were stored for offline analysis using the Fitzpeaks program.

5.4.2 Gamma Spectroscopic Measurements

This section gives a representative overview on the experimental procedures utilised to measure the natural and fallout radioactivities from soil samples. The procedures followed here serve as a basis in estimating the radioactivity levels of different environmental samples in a Marinelli counting geometry using gamma spectrometers. To enable the calculation of the activity concentration values, the performance of the BEGe detector system must be first characterised by the energy calibration and its full peak detection efficiency. This will be discussed in detail in the following section.

Energy Calibration

The energy calibration of the system was carried out using a certified, mixed radionuclide standard of known energies and activities. The source is in a resin matrix within a 250 ml Marinelli flask in order to have the same counting geometry as the evaluated samples. In this geometry, the calibration source surrounds the germanium detector in order to maximise the detection efficiency of the detector.

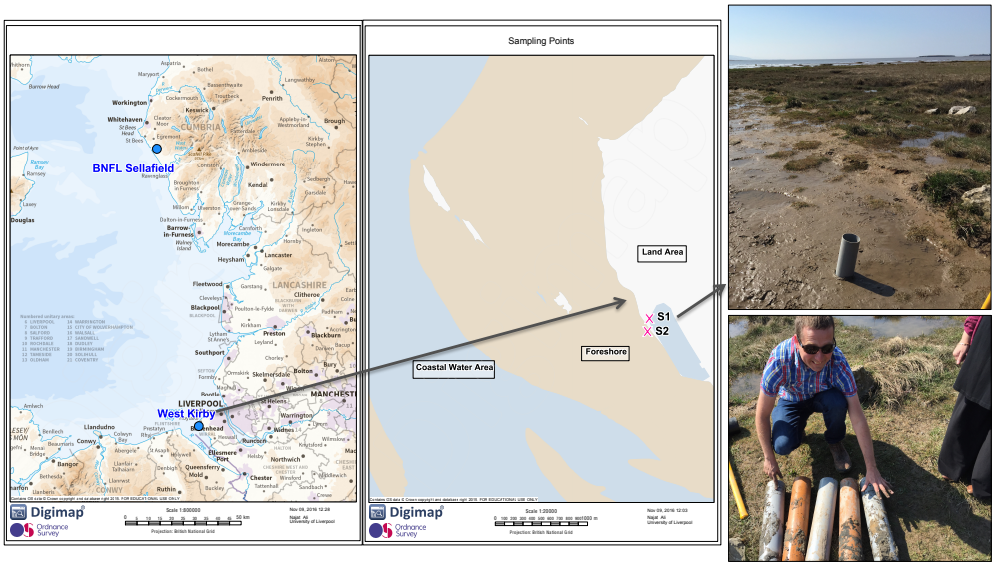

Figure 5.1: A map showing the West Kirby site from Which soil samples were collected and the location of the Sellafield Limited nuclear site (BNFL). A view of the sampling location indicating cores sites (S1: the moist sampling point, S2: the wet sampling point) is given as well as the final collected samples.

The Marinelli calibration source NPRL 604[3] covers a wide energy range between 59.5 keV (from the decay of ^{241}Am) and 1836.1 keV (from the decay of ^{88}Y) and was analysed in the same conditions as for the soil samples. The source was directly placed on the detector endcap for counting and the energy calibration spectrum was collected over the acquisition system live time of 86,512 s (a day) with a negligible dead time of 1.16%. The net peak area (this term is described in section "Peak Area Determination", p. 64) of low activities was $>$ 15000 counts for ^{139}Ce and ^{113}Sn, and $>$ 3000 counts for ^{88}Y. The counting statistical uncertainty[4] was found in the order of 0 - 1% for high activities (^{241}Am, ^{109}Cd, ^{57}Co, ^{137}Cs and ^{60}Co) and between 6% $-$ 24% for the low activities (^{139}Ce, ^{113}Sn and ^{88}Y). The energy spectrum collected was calibrated to 0.34 keV/channel using a multi-point energy calibration and a quadratic fit function in Prospect to allow precise calibration over an energy range of 2.79 MeV for a 8K MCA system (or 8192 channels),

$$E_\gamma(keV) = c(C_\gamma)^2 + b(C_\gamma) + a \ , \tag{5.1}$$

where C_γ is the channel number for the center of the photopeak (centroid) corresponding to each gamma-ray energy E_γ. The energy calibration coefficients are: a is the offset (or intercept), b is the energy calibration factor, has units of $energy(keV)/channel$, and c is a quadratic term, which is typically added to account for small nonlinearities. The peak centroid for each energy peak was recorded and a plot of E_γ vs. C_γ has been reproduced

[3]The certificate information of the Marinelli calibration source used can be found in Appendix A.

[4]Relative standard deviation, expressed as a percentage, is always used to express uncertainties of counting throughout this document.

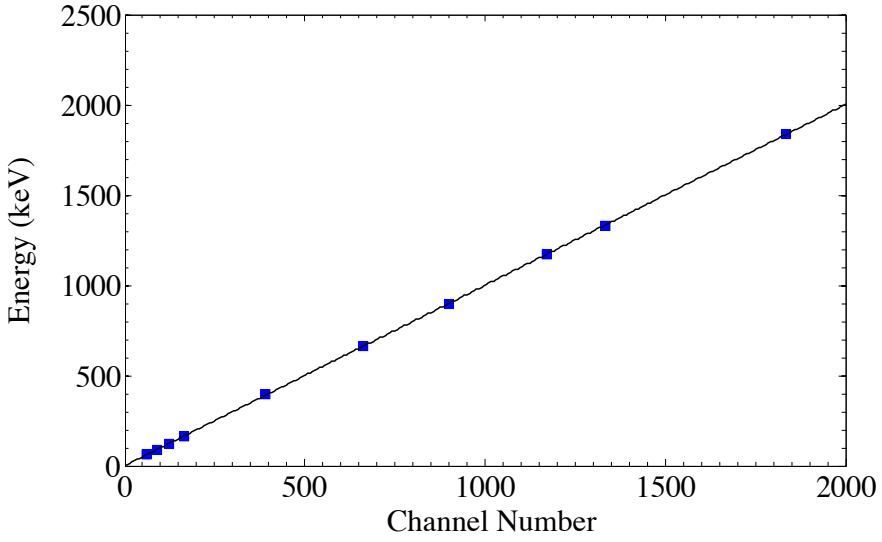

Figure 5.2: Calibrated energy (keV) as a function of channel number for the HPGe BE2825 (b12116) detector using the Marinelli calibration source, NPRL 604. The curve illustrates the quadratic fitting of the calibration data.

in MatLab to determine the calibration coefficients, Fig. 5.2. The quadratic fit (black line) of the data has also been shown in the figure and given in the following form,

$$E_\gamma(keV) = 6 \times 10^{-11}(C_\gamma)^2 + 0.34(C_\gamma) - 0.31 \ . \tag{5.2}$$

Because the detector data acquisition electronics are not absolutely stable, the values of a, b and c may drift slightly with time. Therefore, the energy calibration was repeated on a weekly basis during the sample measurements in order to avoid any drift in the later soil samples measurements. An example spectrum of the calibrated energy spectrum acquired for the Marinelli calibration source NPRL 604 is presented in Fig. 5.3.

Peak Area Determination

In order to allow the amount of radiation emitted from a radioactive nuclide to be quantified, the peak area (number of counts under a peak) must be determined. In principle, the peak area is simply calculated by adding the contents of all channels under the peak. This gives the *gross area* of the peak. However, in all measured γ spectra, peaks are superimposed on an underlying continuum, which might be the Compton continuum from ^{40}K or/and from gamma rays at higher energy from the radioactive source being measured. This continuum must be corrected for the gross area in order to obtain the *net peak area* for that nuclide. If the background beneath the peak also contains an actual peak from other natural radioactivity in the environment surrounding the detector, this must be subtracted from the gross area (this is treated separately in section "Peaked Background Corrections", p. 68).

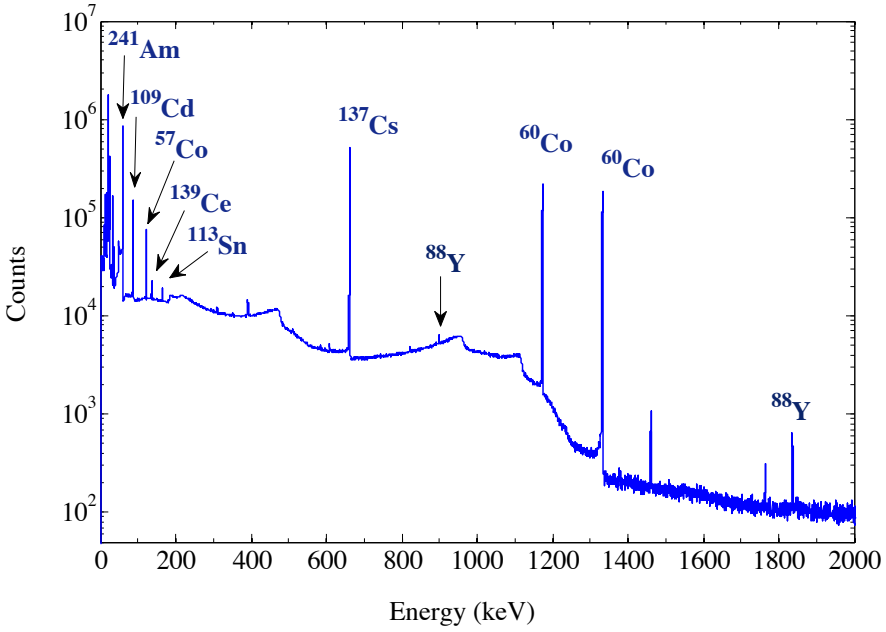

Figure 5.3: Calibrated energy spectrum for the Marinelli calibration source NPRL 604, measured over a full acquisition system live time of 86,512 s with a negligible dead time of 1.16% using the high-resolution γ-ray spectrometry system shown in Fig. 4.2. The γ-ray photopeaks considered for analysis are indicated on the plot.

The Prospect software will calculate the net peak area by subtracting a *step* background (if well-defined peak) drawn between the lower and upper background regions (highlighted in red) set about the peak, Fig. 5.4. This step results mainly from Compton scattering of photons into the detector and from the escape of photoelectrons from the detector crystal, which lead to a slightly higher background on the low-energy side of the photopeak. The lower and upper background regions, which are averaging over a number of channels, are used to estimate the peak background that will be subtracted from the peak gross area to give the net count (highlighted in blue). This method is called the *Total Peak Area with Extended Background*.

The larger the number of channels the more the step background shape is smoothed the more precise (less uncertain) the background estimation will be, however there are reducing returns in terms of improvement in precision and the user should find the proper compromise. Additionally, in the case of the presence of the neighboring peaks, the width of the background regions will be limited. It must be noted that the net area obtained, is not affected by the number of channels used for the background estimate, but only on the precision with which it is measured. The estimation of the peak area is given by [Pri11b]:

$$Area(A) = \sum_{i=L}^{U} C_i - n\left(\sum_{L-m}^{L-1} C_i + \sum_{U+1}^{U+m} C_i\right)/2m \ , \tag{5.3}$$

where C_i is the counts in the ith channel under the peak, n is the number of channels

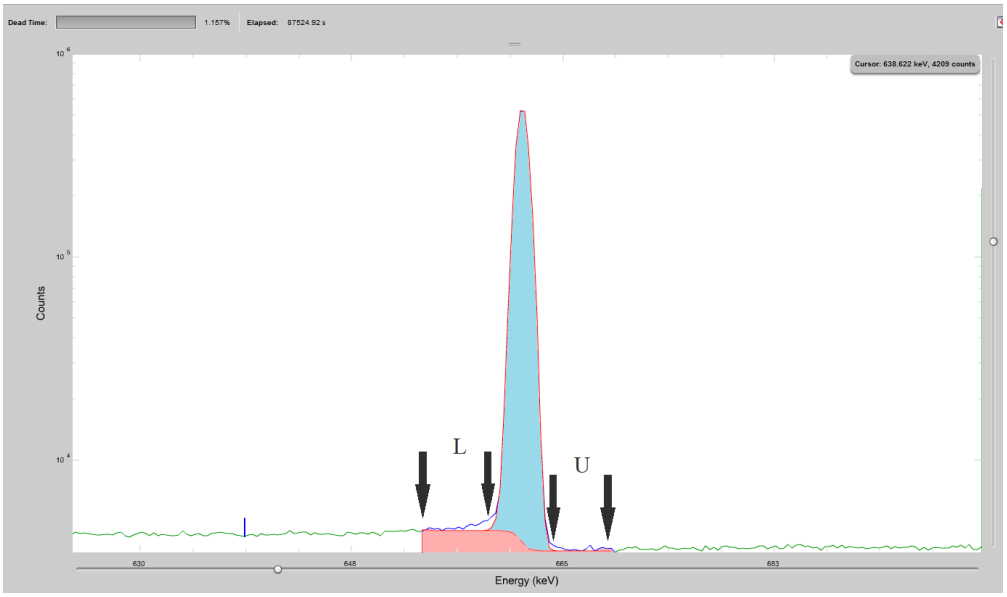

Figure 5.4: An example of a typical Gaussian peak fit obtained with the Prospect software using the extended background method, indicating the quality of the fit and showing the spectral step background (in red) used by the software in determining the net peak area (in blue). The example displays the gamma-ray spectrum in the region of the 661.7 keV photopeak from decay of ^{137}Cs acquired using the Marinelli calibration source NPRL 604. L and U are the lower and upper edges of the peak, and the number of channels used for each background region is m = 15 channels.

covered by the peak region, m is the number of channels used for each background region, and C_{L-1} and C_{U+1} are the counts immediately beyond the lower and upper edges of the peak respectively. The second term in the area expression gives the n times the mean background count per channel beneath the peak. The software also determines the position of the peak centroid (channel number), which is converted to the corresponding energy value (661.7 keV) using the pre-defined energy calibration parameters in Equation 5.2.

The variance on the net area will include the variance on the estimate of the area of the background beneath the peak. This is given by [Pri11b]:

$$Var(A) = \sum_{i=L}^{U} C_i - n^2 \left(\sum_{L-m}^{L-1} C_i + \sum_{U+1}^{U+m} C_i \right) / 4m \tag{5.4}$$

For poorly-defined peaks, the uncertainty on the background estimate can dominate the total variance of the peak area. However, in case of well-defined peaks, as shown in the figure, this variance will be much less affected by the background uncertainty. The uncertainty of the peak area over an acquisition system live time of 86,512 s was 0.1% of 1σ.

The uncertainty on the peak area estimation can also be affected by the size of the energy spectrum. As the spectrum size increases the number of counts in each background channel decreases and thus, unless m increases, the background uncertainty and

subsequently the net area uncertainty rises. On the other hand, the large spectrum size is preferred for maintaining good peak resolution (or FWHM). Therefore, the spectrum size is a tradeoff between area measurement precision and peak resolution. As a reasonable compromise, 8192 channels was chosen for the current measurements.

Efficiency Calibration

To carry out the absolute efficiency calibration, following the energy calibration, the net peak area was extracted from a Gaussian fit using the region of Interest (ROI) feature in Prospect for each energy peak[5] using the calibration source NPRL 604 (as shown in Fig. 5.4). The absolute efficiency calibration was then deduced using Equation 5.5.

$$\varepsilon_{abs} = \frac{N_{peak}}{L_T \times A_\gamma} \ , \tag{5.5}$$

where N_{peak} is the net peak area, L_T is the live time of the acquisition system and A_γ is the gamma emission rate, γ/s, (= activity of the radionuclide in the source (becquerel) $\times$ gamma branching ratio[6], P_γ).

It should be stressed that, Equation 5.5 only gives an estimation of the full-energy photopeak efficiency and not the nuclide detection efficiency or the intrinsic efficiency that would include consideration of the detector size and shape, or total efficiency, which considers incomplete detection events such as those in the Compton continuum.

First of all, the activity of each radionuclide, A_γ, was corrected for the time of the measurement using the following formula,

$$A_\gamma = A_0 e^{-\left(\frac{LN(2)}{T_{1/2}}\right)T} \ , \tag{5.6}$$

where A_0 is the initial activity of the radionuclide at the date of the source production, T is the time difference since the production date until the time of the measurements, and $T_{1/2}$ is the half-life of the radionuclide. The uncertainty on the calculated absolute efficiency is due to the uncertainty of the net counts under the photopeak defined by the Prospect fittings.

The efficiency calibration was also carried out in the Fitzpeaks program using the experimental energy spectrum, and values obtained were compared to those acquired from Prospect. A step by step guide to setting up the program, inputting the energy spectrum of the NPRL 604 calibration source and performing the energy, peak width (or FWHM), and efficiency calibrations, are all explained in Appendix B.
The calculated values of the absolute efficiency as a function of gamma-ray energy are presented in Table 5.1 and plotted in Fig. 5.5. It should be noted that the absolute efficiency decreases as the energy increases. The absolute efficiency at 1835.96 keV and

[5]The radionuclides ^{51}Cr (320.1 keV) and ^{85}Sr (514.0 keV) shown in the certificate were no longer detected at the time of the measurement as they were decayed out from the source.

[6]The fraction of the total decays leading to a given branch, or alternatively expressed, the probability of gamma emission at the energy used. It is referred to as gamma ray abundance.

Nuclide	Energy (keV)	Prospect		Fitzpeaks	
		ε_{abs}	1σ (%)	ε_{abs}	1σ (%)
^{241}Am	59.5	4.52×10^{-2}	0.08	4.49×10^{-2}	1.20
^{109}Cd	88.0	5.07×10^{-2}	0.27	5.17×10^{-2}	0.70
^{57}Co	122.1	5.44×10^{-2}	0.53	5.46×10^{-2}	0.70
^{139}Ce	165.9	4.71×10^{-2}	4.51	4.74×10^{-2}	5.20
^{113}Sn	391.7	2.41×10^{-2}	3.90	2.39×10^{-2}	4.70
^{137}Cs	661.7	1.30×10^{-2}	0.07	1.30×10^{-2}	0.30
^{88}Y	898.0	8.43×10^{-3}	7.90	9.51×10^{-3}	9.80
^{60}Co	1173.2	7.20×10^{-3}	0.10	7.20×10^{-3}	0.20
^{60}Co	1332.5	6.41×10^{-3}	0.10	6.41×10^{-3}	0.20
^{88}Y	1836.1	4.83×10^{-3}	3.36	5.25×10^{-3}	4.70

Table 5.1: Energy versus experimental absolute full-energy photopeak efficiency (in arbitrary units). The Prospect values were deduced using Equation 5.5 and compared to those generated from the Fitzpeaks program. The 1σ is due to the uncertainty on the net counts under the photopeak defined by the Prospect or Fitzpeaks fittings.

661.64 keV is about 11% and 29% respectively of that at 59.54 keV. This is because the high energy gamma rays are more likely to escape the detector.

Peaked Background Corrections

In any measured gamma-ray spectrum, the background beneath a photopeak may (or may not) consist of an actual peak from the natural sources of radioactivity found in the environment surrounding the detector and from other sources (see Section 5.2). For example, the 1460 keV gamma ray from ^{40}K, which is of terrestrial origin, often results in an identifiable peak in the background spectra from the gamma-ray detector in use. This actual peak is referred to as the "*peaked background*" and must be corrected separately after the measurements. Therefore, following the performance of the energy calibration, background measurement was then taken under the same conditions as the samples.

For the reliability of the background corrections, measurements of background distributions were taken regularly on a weekly basis during the course of the sample measurements to make sure an accurate background subtraction is made for each sample. The counting time of the background spectra were 86,378 s ($\sim$ a day). The Fitzpeaks output of an analysed energy spectrum of the room background is shown in Fig. B.4, p. 134. This is needed in determination of the sample activity where the net peak are of the peaked background (if found) must be subtracted from that of the measured radionuclide from samples in order to give a corrected net peak area of gamma ray of that radionuclide. Additionally, the background energy spectra are needed when determining the Minimum Detectable Activity (MDA) of the system. This can be explained briefly as following:

The minimum detectable activity is a key measure of gamma spectrometer performance, indicating to the detection sensitivity of the detector system. It represents the

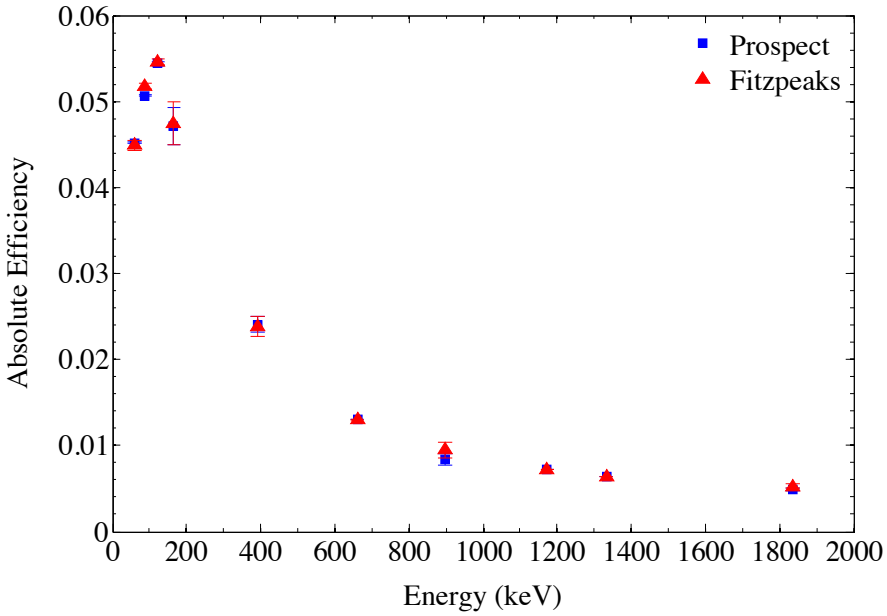

Figure 5.5: The measured absolute full-energy photopeak detection efficiency of the HPGe BE2825 (b12116) detector as a function of energy, using the NPRL 604 Marinelli calibration source. The Prospect values, deduced using Equation 5.5, are in excellent agreement with those produced from the Fitzpeaks program.

minimum amount of radionuclide that can be determined reliably in a specific confidence degree.

The calculation of the MDA of the BEGe detector system for a given nuclide, at the 95% confidence level, was based on Currie's derivation [Cur68], with one simplified formulation being,

$$MDA(Bqkg^{-1}) = \frac{L_D}{L_T \times \varepsilon_\gamma \times P_\gamma \times m} \ , \tag{5.7}$$

where L_T is the counting live time of the acquisition system (in sec), P_γ is the emission probability for a specific energy photopeak, ε_γ is the absolute efficiency of the BEGe detector, m is the mass of the sample, and L_D is the detection limit (in counts), which is defined as the expected net count from the sample at which a significant count can be recorded.

L_D, with a confidence limit of 95%, for a certain ROI can be given as:

$$L_D = 2.71 + 4.65\sigma_B \ , \tag{5.8}$$

where σ_B is the standard deviation in background counts. This background arises from several sources: general background, which may or may not exhibit a peak at the energy of interest, and is extracted from the measured background spectrum, and is corrected separately apart from the other source of background, which appears from Compton continuum resulting from other high γ energies in the measured sample. The background

from the Compton continuum is extracted by subtracting the net peak area of the full energy photopeak from the gross count in the ROI.

The MDA of the BEGe detector system was calculated for the counting time of 86,378 s for monoenergetic gamma-ray radionuclides; ^{241}Am, ^{137}Cs and ^{40}K and it is found that, they can be reliably (at a confidence level of 95%) detectable by the system at 4.19, 4.52 and 58.77 Bq kg^{-1} respectively.

Sample Statistical Analysis

Samples were placed directly on the front face of the detector. The acquisition live time for each sample was approximately one day. The counting geometry of all samples and the calibration source used for energy and efficiency calibration was kept unchanged. The Fitzpeaks output of the analysed energy spectrum for the (25-30 cm) sample from the wet core is presented in Fig. B.5, p. 135.

A range of discrete-line gamma-ray energy transitions from spectral peaks ranging from 60 keV to 2.6 MeV were initially analysed independently in order to quantitatively determine the activity concentration of each gamma-ray peak. The activity determination, however, requires the identification of the radionuclides detected in samples. The natural occurring radionuclides found have been related to characteristic decays of various decay elements within the uranium (^{238}U) and thorium (^{232}Th) radioactive decay chains, as shown in Table 5.2, in order to obtain the overall activity concentration associated to each decay chain. This will be explained in details later in this section.

The activity concentration of a gamma-ray peak (A_γ) is calculated by taking into consideration any possible peak in the background under the peak, the absolute full-energy photopeak detection efficiency of the germanium detector at this energy, ε_{peak}, and the decay branching ratio, P_γ, for the energy photopeak. The *specific activity* concentration of each gamma-ray photopeak is expressed in Bq/kg as:

$$A_\gamma(Bq/kg) = \frac{CR_P - CR_{PB}}{P_\gamma \times \varepsilon_{abs} \times m} \ , \tag{5.9}$$

where CR_P is the net photopeak count rate ($= N_{peak}/L_T$), CR_{PB} is the count rate for a possible peaked background beneath the photopeak (if found), and m is the mass of the evaluated sample in kg.

The uncertainty on the measured activity concentration, ΔA_γ, was considered only for the uncertainty on the estimate of the net peak area defined by the Prospect fitting to the photopeak. Hence, the combined standard uncertainty of the activity concentration of a gamma-ray peak of a radionuclide was estimated as:

$$\Delta A_\gamma = K * \Delta CR_{sub} \ , \tag{5.10}$$

where K is a constant ($= 1/P_\gamma \times \varepsilon_{abs} \times m$). The absolute efficiency calibration error is not included. ΔCR_{sub} is the combined uncertainty of the subsequent count rate resulting

Isotope	Daughter	Energy (keV)	Gamma Emission Probability (%)
^{238}U	^{214}Pb	242.0	7.4
		295.2	19.3
		351.9	37.6
	^{214}Bi	609.3	46.1
		768.4	4.9
		1120.3	15.1
		1238.1	5.8
		1377.7	4.0
		1764.5	15.4
^{232}Th	^{228}Ac	209.2	3.9
		270.2	3.5
		338.3	11.3
		463.0	4.4
		794.9	4.2
		911.2	25.8
		964.8	5.0
		969.0	15.8
	^{212}Pb	238.6	43.3
	^{208}Tl	510.7	22.6
		583.2	84.5
		860.6	12.4
		2614.5	99.0

Table 5.2: The detected gamma-ray energy transitions associated with the decay progenies within the uranium (^{238}U) and thorium (^{232}Th) radioactive decay chains. The radioactivities of ^{238}U and ^{232}Th were evaluated from which they have been inferred from these transitions.

from the background count rate subtraction. It is calculated by the next formula,

$$\Delta CR_{sub} = \sqrt{(\Delta CR_P)^2 + (\Delta CR_{PB})^2} \ , \tag{5.11}$$

where ΔCR_P is the uncertainty associated to the peak count rate, which is obtained by dividing the uncertainty of the net counts under the photopeak, determined by the Prospect peak fitting, by the live time of the acquisition system over the measuring time as given in the next equation,

$$\Delta CR_P = \frac{\Delta N_P}{L_T} \ . \tag{5.12}$$

where ΔCR_{PB} is the uncertainty associated to the background count rate, which is calculated in a similar way as Equation 5.12.

If there is more than one gamma-ray peak observed for a particular radionuclide, the total (or *mean*) activity of that radionuclide is then extracted by averaging the activities of the various gamma-ray peaks weighted by the error associated to their activities. This is performed using the next formula,

$$A_{(nuclide)} = \frac{\sum\limits_{x} \frac{A_{\gamma_x}}{(\Delta A_{\gamma_x})^2}}{\sum\limits_{x} \frac{1}{(\Delta A_{\gamma_x})^2}} \ , \tag{5.13}$$

where A_{γ_x} (Bq/kg) is the specific activity of a gamma-ray peak associated to a radionuclide calculated from Equation 5.9.

For example, ^{214}Pb (see Table 5.2), one of the nuclides detected in the collected soil samples, its mean activity was deduced from 242.0 keV, 295.2 keV and 351.9 keV peaks. ΔA_{γ_x} is the associated error calculated from Equation 5.10.

The combined uncertainty on $A_{nuclide}$ is then calculated using the errors ΔA_{γ_x} as follows:

$$\Delta A_{(nuclide)} = \frac{1}{\sqrt{\sum\limits_{x} \frac{1}{(\Delta A_{\gamma_x})^2}}} \ . \tag{5.14}$$

In order to obtain the total activity (A_T) coming from a certain decay chain, the activity concentrations of all radionuclides occurring as components of the decay chain of radioactive elements were combined in a similar fashion to Equation 5.13, but in this case, the terms of the activity and the uncertainty in the equation will now be corresponding to the total activity of the radionuclide obtained from Equation 5.13 and its combined uncertainty from Equation 5.14. The manner of determining that being: the weighted mean value of the activity concentration of ^{238}U in all samples (from uranium (^{238}U) radioactive series) was evaluated from which has been inferred from gamma-ray transitions associated with its decay progenies detected (^{214}Bi and ^{214}Pb). Whereas the activities of ^{228}Ac, ^{212}Pb and ^{208}Tl were used to determine the activity of ^{232}Th (presenting thorium (^{232}Th) radioactive series).

The activity concentration of ^{40}K, ^{241}Am and ^{137}Cs were deduced using their direct gamma-ray peaks of 1461, 59.5 and 661.6 keV respectively using Equation 5.9.

The mean measured activity of the sample can be obtained by a straightforward summation of the mean activities of ^{238}U, ^{232}Th, ^{40}K, ^{241}Am and ^{137}Cs using the formula,

$$A_{sample} = \sum_{i} A_{(nuclide)} \ . \tag{5.15}$$

The combined uncertainty on the total sample activity can be obtained from,

$$\Delta A_{sample} = \sqrt{\sum_i (\Delta A_{(nuclide)})^2} \ , \tag{5.16}$$

where $\Delta A_{(nuclide)}$ is the uncertainty on the mean activity of ^{238}U, ^{232}Th, ^{40}K, ^{241}Am or ^{137}Cs.

5.5 Results and Discussions

This section is aimed at presenting a vertical representation of the activity profiles of naturally occurring radionuclides, ^{40}K, ^{238}U and ^{232}Th, and artificial radionuclides, ^{241}Am and ^{137}Cs, in soil samples collected from West Kirby. The presence of the activities of ^{241}Am and ^{137}Cs reflects the continuing action of the sedimentary process caused by tidal flow from the Irish sea, which is contaminated by historical released-level radioactive waste discharged from the nuclear plant at Sellafield. Such that, the radioactivity is still being deposited and washed at this coastal area.

As already mentioned, the activity concentrations have been calculated in two steps. The first step is to evaluate the mean activity concentration for each radionuclide from its gamma-ray energy transitions observed in the collected energy spectra. The second step is to combine the mean activity concentrations of radionuclides, which are occurring as components of uranium (^{238}U) or thorium (^{232}Th) radioactive decay chains, as shown in Table 5.2, in order to obtain the total activity, A_T, coming from each decay chain at a certain depth.

Fig. 5.6 and Fig. 5.7 show the vertical distributions of the specific activity concentrations (Bq kg^{-1}) for ^{241}Am, ^{137}Cs, ^{40}K, ^{238}U and ^{232}Th, plotted as a function of depth for the wet and moist sampling points respectively.

A summary statistics for the activity concentration of ^{241}Am, ^{137}Cs, ^{40}K, ^{238}U and ^{232}Th in soil samples as a function of depth for the two locations, are given in Table 5.3 and Table 5.4. The uncertainty ($\pm$ values) presented are due to the uncertainty on the estimate of the net peak area defined by the Prospect peak fittings.

First of all, it can be observed from Fig. 5.6 (wet core) that, the trend of the activity profiles of ^{241}Am and ^{137}Cs is quite consistent by varying depth. However, the trend only exhibits a variation at depth 25 cm where the specific activity has dropped to 1.66 Bq kg^{-1}and 7.78 Bq kg^{-1} for ^{241}Am and ^{137}Cs respectively. The general shape of the Prospect trend of both profiles showed excellent agreement with the Fitzpeaks trend. The reason for this sudden decline of the activity concentration of these radionuclides is unknown. However, this may be attributed to the change in the soil content at that depth during the sample preparation resulting in a change in the radioactivity concentration of these radionuclides.

The activity concentrations for ^{241}Am and ^{137}Cs at different depths are higher for this core in comparison with the corresponding results obtained for the moist core by a

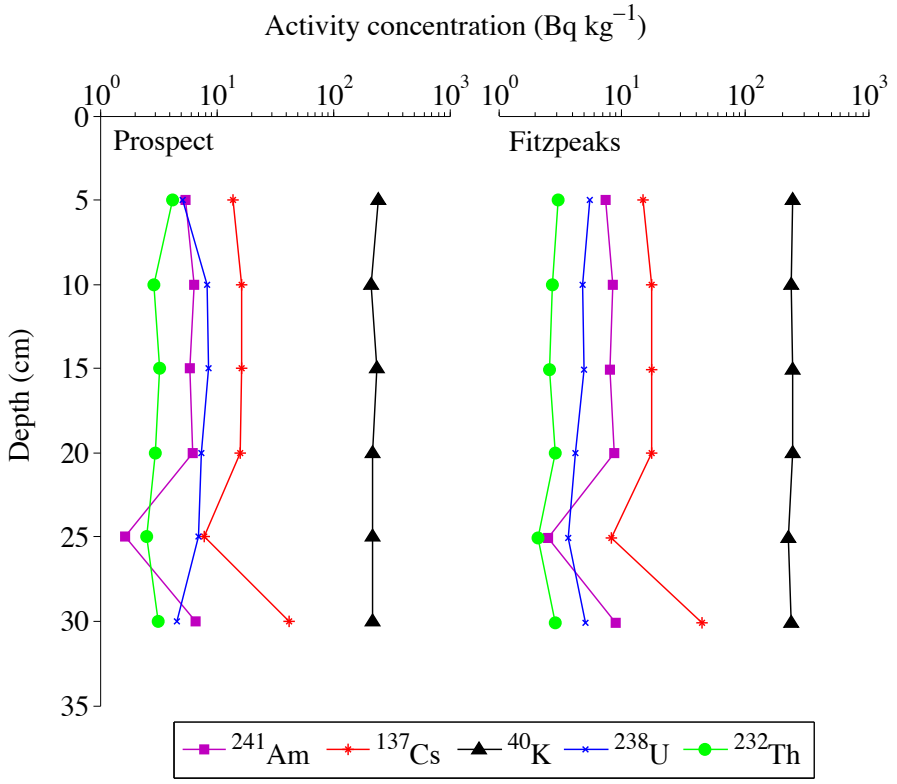

Figure 5.6: Depth distribution of activity concentrations for ^{241}Am, ^{137}Cs, ^{40}K, ^{232}Th and ^{238}U From the wet core. Activity profiles were calculated using Prospect fittings (left), and Fitzpeaks fittings (right).

Depth (cm)	Activity concentration (Bq kg^{-1})				
	^{241}Am	^{137}Cs	^{40}K	^{238}U	^{232}Th
5	5.48±0.39	13.83±0.36	247.7±8.9	5.09±0.51	4.21±0.41
10	6.37±0.40	16.47±0.36	213.1±8.0	8.24±0.35	2.93±0.30
15	5.99±0.39	16.22±0.39	240.0±7.9	8.99±0.31	3.25±0.28
20	6.32±0.35	16.18±0.35	216.7±8.5	7.48±0.36	2.99±0.29
25	1.66±0.31	7.78±0.30	218.7±8.2	7.10±0.33	2.50±0.28
30	6.62±0.42	41.62±0.42	218.0±7.4	4.55±0.44	3.18±0.27
Range	(1.66−6.62)	(7.78−41.62)	(213.1−247.7)	(4.55−8.99)	(2.50−4.21)

Table 5.3: Summary statistics for the activity concentration for ^{241}Am, ^{137}Cs, ^{40}K, ^{232}Th and ^{238}U for the wet core. The full range and average activity for each radionuclide at this location are shown.

factor of 3, as shown respectively in Table 5.3 and Table 5.4. This excludes the activity concentrations found at depth 25 cm, where their values are slightly lower than those obtained for the moist sampling points. The difference in the activity level of these radionuclides between the two sampling points can be explained by the spatial variation in radioactivity deposition at these two sampling points, since the sampling point of the wet core is frequently more inundated by tidal current compared to the other one, which can result in higher level of radioactivity contents of these radionuclides at this sampling

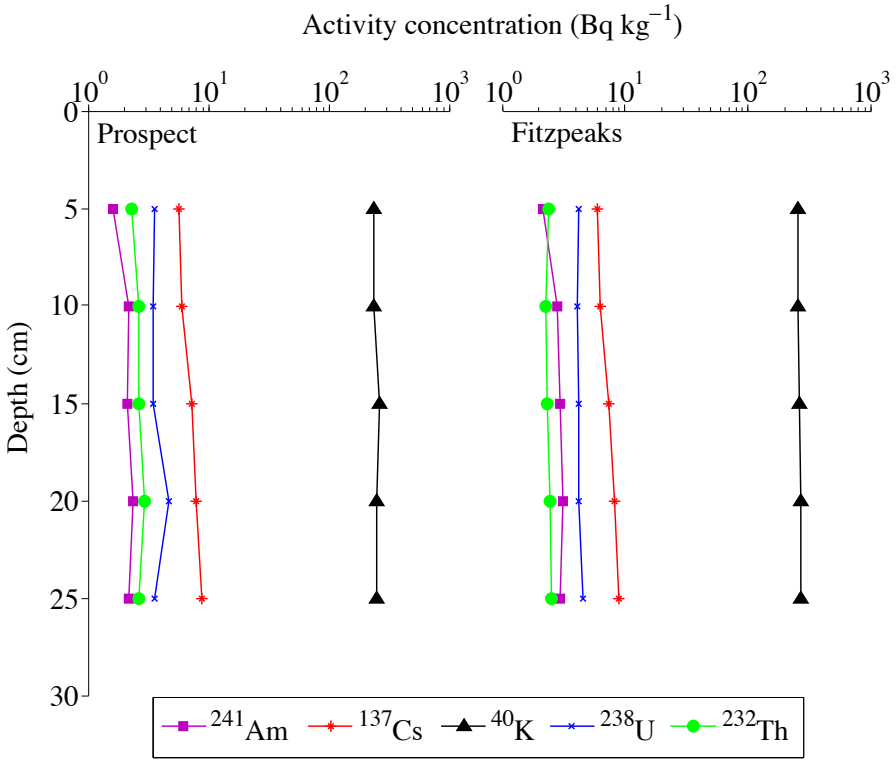

Figure 5.7: Depth distribution of activity concentrations for ^{241}Am, ^{137}Cs, ^{40}K, ^{232}Th and ^{238}U From the moist core. Activity profiles were calculated using Prospect fittings (left), and Fitzpeaks fittings (right).

Depth (cm)	Activity concentration (Bq kg^{-1})				
	^{241}Am	^{137}Cs	^{40}K	^{238}U	^{232}Th
5	1.63±0.29	5.70±0.34	237.0±7.7	3.54±0.48	2.29±0.31
10	2.17±0.38	5.96±0.34	239.7±8.0	3.45±0.50	2.66±0.31
15	2.15±0.29	7.29±0.20	266.9±7.4	3.50±0.45	2.64±0.27
20	2.35±0.35	8.03±0.42	250.2±7.9	4.69±0.48	2.98±0.33
25	2.18±0.28	8.96±0.31	249.2±8.3	3.54±0.50	2.63±0.31
Range	(1.63−2.35)	(5.70−8.96)	(237.0−266.9)	(3.45−4.69)	(2.29−2.98)

Table 5.4: Summary statistics for the activity concentration for ^{241}Am, ^{137}Cs, ^{40}K, ^{232}Th and ^{238}U for the moist core. The full range and average activity for each radionuclide at this location are shown.

point.

Secondly, the trend of the activity profiles of the naturally occurring radionuclides, ^{40}K, ^{238}U and ^{232}Th, is shown to be steady with varying depth. The general trend of the activity profiles of ^{40}K and ^{232}Th are in good agreement with that acquired using the fitzpeaks program. However, the activity profile trend of ^{238}U acquired by prospect and that obtained by Fitzpeaks are statistically consistent. The activity concentrations of ^{40}K at different depths are lower for the wet core compared to the corresponding activities for the moist core except the surface activity. This could be interpreted by

that, as the main source of ^{40}K is the application of fertilisers, so it is expected for the drier sampling point to have a higher level of ^{40}K compared to the wet sampling point. The reason for the higher level of the surface radioactivity of ^{40}K at the wet sampling point is that, ^{40}K is being deposited and washed out at the surface of this sampling point during the tidal currents. The activity concentrations of ^{232}Th and ^{238}U are also shown to be higher for this core in comparison with the corresponding results obtained for the moist core.

Finally, for the general trends of the activity profiles of all radionuclides acquired from the moist core, Fig. 5.7, are almost consistent and there is no any reasonable fluctuations at all different depths. This is also evidently supported by the Fitzpeaks results.

Generally speaking, despite the low levels of radioactivity that have been found in these sampling points, these results serve as a reference point in time on the artificial and naturally occurring radionuclides detected in this study area. The record of these radionuclides can aid researches who focus on understanding the distribution, accumulation of radionuclides over time in coastal areas of NW England, for example as reviewed in [C$^+$16]. Moreover, this helps identify any potential variations in environmental radioactivity concentration with time because of the anthropogenic activities.

Chapter 6

Pulse Shape Analysis

Introduction

The optimisation of high purity germanium detector performance for different gamma-ray interactions is an active area of research in the field of nuclear physics. For some commercial applications such as environmental sample counting or analysis of highly radioactive waste, accurate characterisation of radionuclides within samples is required. HPGe detectors are the most often utilised detectors in such applications because of their excellent energy resolution. However, the shortcoming of these detectors is their poor peak-to-Compton background response that limits the ability of these detectors to detect radionuclides with low radioactivities. This drawback is mainly due to the Compton scattering effect which leads to a significant continuum in the energy spectrum, causing a considerable increase in the peak background. For example (shown in Fig. F.3, p. 173), the Compton background from high-energy gamma emissions such as ^{137}Cs could make it difficult to detect low radioactivities from low-energy gamma emissions such as ^{241}Am. Therefore, this project is aimed at developing a direct method to improve the P/C background response of germanium detectors, thus increasing their sensitivity, which will benefit different applications of these detectors. To achieve this, digital pulse processing techniques were applied to gamma spectroscopy measurements with a BEGe detector using environmental samples in a Marinelli counting geometry. Digitised detector traces (or waveforms) from a Digital Acquisition (DAQ) system have been recorded for offline analysis, which involved the application of pulse shape analysis technique that allowed the P/C response of the detector to be improved.

6.1 Traditional Analog Pulse Processing

Data acquisition systems for nuclear spectroscopy traditionally make use of almost all-analog chains, where electronics consist of the Charge Sensitive Preamplifier (CSP) and the analog shaping amplifier followed by peak sensing Analog-to-Digital Convertor (ADC) as shown in Fig. 6.1. The signal coming from the detector is integrated by the charge sensitive preamplifier on a capacitor C, which is put in parallel with a discharging resistor R, in order to convert the collected charge into a voltage step. The characteristic preamplifier output will have pulses with short rise time followed by a long exponential tail with decay time ($\tau = RC$). The charge pulse amplitude is proportional to the energy deposited by the radiation in the detector, and set by the capacitor value $V_{out} = Q/C$.

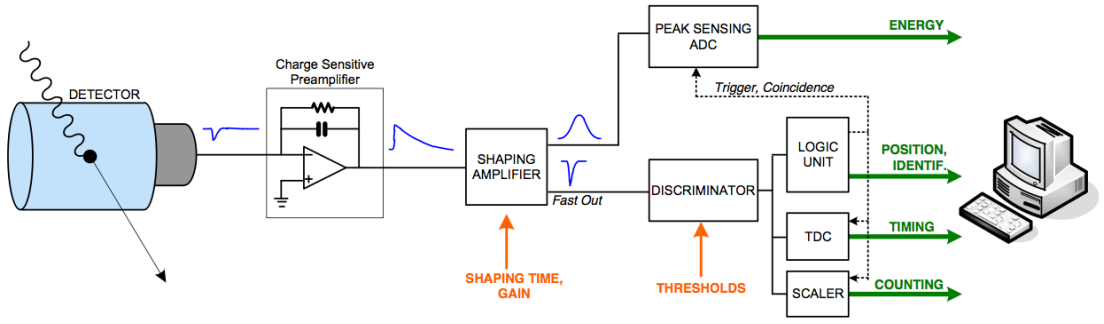

Figure 6.1: Block diagram for analog pulse processing for obtaining timing and energy information from a detector [Cae16b].

In order to allow full charge collection from the detector, the CSP is normally adjusted to provide a long decay time for the pulse (typical decay times are on the order of 50 μs). Since the pulses occur at random times, as radioactive decay is a random process, they will sometimes overlap especially if the count rate[1] is large. A second unwelcome feature when using a CSP is the sharp peak top, which means the maximum is only held for a short time, making any subsequent pulse height analysis with the required precision difficult. The third drawback is, all high frequency noise components are passed through by the CSP circuit leading to poor signal-to-noise ratio. In order to overcome (or significantly improve) these features, the pre-amplified signal is fed into a shaping spectroscopy amplifier that produces a quasi-Gaussian output without affecting the input pulse amplitude. In the final stage, the output from the shaping amplifier is fed into a peak sensing ADC, where digitisation and the evaluation of the pulse height take place. The digitised values will be filled into a histogram that represents the energy (or pulse height) spectrum.

In order to obtain information on the precise arrival time of a pulse in the detector, the pulses coming from the detector are handled differently than they would be when extracting the pulse height spectrum (discussed above). The components of a basic measurement scheme tailored for obtaining timing information from a detector are shown in Fig. 6.1. To maintain the timing information carried out by the fast linear rising of the detector signal, this fast component is usually fed into a fast amplifier (or timing amplifier, which might be included into the shaping amplifier) that reproduces the signal. The output of the fast amplifier is fed into a chain made out of a Time-to-Digital Converter (TDC), Discriminator (Constant-Fraction Discriminator, CFD), and/or a scaler for pulse-rate counting or pulse timing acquisition. Logic units are used to provide information about the pulse shape for the particle identification or to generate triggers. Coincidence units, can also be used in timing systems to make coincidences. Such devices are usually based on the overlap coincidence principles. For further information on

[1] It is a measurement of the rate of recorded pulses meeting certain acceptance conditions in a pulse processing system.

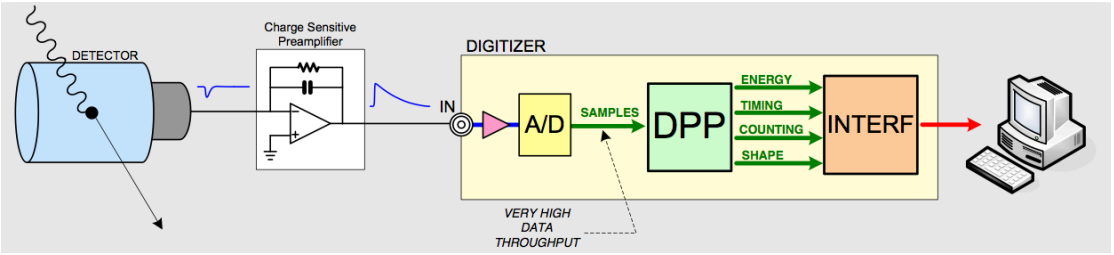

Figure 6.2: Block Diagram of a Digitiser-based Spectroscopy System [Cae16b].

some common modular instruments used in timing measurements, the reader is referred to [Kno10].

6.2 Digital Pulse Processing (DPP)

In fully digital systems for pulse processing, the preamplifier output will be digitised first and then filtered for the events of interest by the application of algorithms. Because the digitisation of the detector signal occurs at a very early stage compared with analog signal processing, drifts and instabilities are much reduced, providing extremely good stability and reliability.

A block diagram of a digitiser-based spectroscopy system is shown in Fig. 6.2. All blocks from the shaping amplifier to the PC, in Fig. 6.1, are here replaced with a single device, the digitiser.

The application of digital pulse processing techniques to γ-spectroscopy measurements with HPGe detectors allows the signal-to-noise ratio of the system to be optimised. In an analog chain, the adjustments of the digital pulse shapes cannot be practically realised, whereas, in a digital system this can be easily accomplished via software configuration without the need to modify the hardware as in the case of analogue systems.

Digital pulse processing is a fully numerical analysis of the detector pulse signals, providing the functionality of analog shaping units. Sophisticated algorithms implemented in digital systems can be used to provide the energy value and timing information for each individual pulse. The numerical analysis of the pulse shape can be performed in real time as soon as the input pulse from the detector is digitised. However, because of the limited time available between signal pulses, it is increasingly more difficult to process the data in the real time especially at higher count rates. Therefore, the digital data can be sent directly to memory and the pulse shape analysis completed offline.

6.3 Digital Filtering Techniques

There are a variety of systems based on digital pulse filtering concepts that have been used in the field of HPGe detector γ-ray spectrometry. Recently, new systems have been developed. For example, two specific designs, the Canberra Lynx Digital Signal

Analyzer (used for the work presented in Chapter 4 and 5) and the Caen DT5780 Dual Digital Multi Channel Analyser [Cae16a], have been extensively used in a variety of high-resolution gamma-spectroscopy applications.

For the work presented in this chapter, the digitiser DT5780 has been used, which is a compact desktop system integrating 2 independent 16k channel Digital MCA and HV/LV power supply capabilities for gamma and X-ray spectrometry. The digitiser is utilised to acquire spectroscopic data and is fully compatible with high-energy resolution detectors that are coupled using charge sensitive preamplifiers. The DT5780 is equivalent to a traditional spectroscopy acquisition chain made of shaping amplifier and peak sensing ADC, as shown in Fig. 6.1, providing a digital replacement of those modules. The DT5780 also offers additional functionalities such as calculating the trigger time tag or making coincidences and anti-coincidences. The DT5780 houses:

- 2× 100 MHz 14-bit flash ADC (10 ns sample size) on single ended inputs with BNC connectors, featuring 4-step configurable input range (0.6/1.4/3.7/9.5 V_{pp}) and adjustable DC offset via a 16-bit DAC on each input in the full range.
- 2× ±5 kV 300 μA HV bias outputs On SHV connectors. Channel polarity negative, positive mixed selectable by ordering options.
- 2× ±12 V (100 mA) and ±24 V (50 mA) voltage outputs through DB9 connectors for preamplifiers power supply.

The digitiser DT5780 is also equipped with a powerful Field Programmable Gate Array (FPGA), which is a Large-Scale Integrated (LSI) circuit, where the DPP calculation for the digitised pulse shape, received from the flash ADC, takes place. Alternatively expressed, after digitisation, the stream of samples is managed by the FPGA programmed to execute on-line digital pulse processing on the digitised signals in order to apply the MCA based on the pulse height algorithms. According to the manufacturer [Cae16a], the recursive algorithms implemented in its FPGA rely on the Jordanov [J+94b], [J+94a] trapezoidal filter and they are called Digital Pulse Processing for Pulse Height Analysis (DPP-PHA) algorithms. The digital pulse processing algorithms applied on each digitised signal are:

- Trigger and Timing Filter (TTF)
- Pole-Zero Correction
- Trapezoidal Filter (Energy Filter)
- Baseline Restorer

The aim of the trigger and timing filter is to identify the input pulses, generate a trigger on them and provide trigger time stamps (this filter will not be considered here for discussion). The pole-zero correction accounts for the preamplifier decay (see Section 6.3.1). The trapezoidal filter converts the digitised pulse into a symmetric trapezoidal

shape that is generally preferred for optimum signal-to-noise ratio in the measurement of pulse height [Gou72] (see Section 6.3.2). The baseline restorer operates on the output of the trapezoidal filter and calculates the trapezoid baseline used in pulse height calculations (see Section 6.3.3).

The digitiser, therefore, acts as a spectroscopy data acquisition system that can provide energy from the pulse height measurements and timing information in addition to a portion of the waveform[2] for debugging, monitoring and sophisticated pulse shape analysis that cannot be implemented online by the FPGA. The digitiser samples the signal continuously and writes the spectroscopic data (i.e. energy value and the time stamp information together with a portion of the waveform) into an on-board 32 bit wide FIFOs (First In First Out) memory or buffers. The sampling process is disabled while the data is calculated (DPP calculations) and saved into a local for each trigger signal. As soon as the buffer content reaches a certain size, it is made available for readout and the acquisition continues in another buffer.

The digital trapezoidal filter is based on the Moving Window Deconvolution (MWD) technique for signal processing in pulse height measurements. This technique permits the conversion to be represented as a sequence of measurements of the integrated charge for each event and subsequently by applying a simple oversampling scheme to achieve a high accuracy for the calculation of the pulse height [G+94]. The conversion process takes four stages in which the convolution of these stages will result finally in an MWD filter transfer function. These stages, shown in Fig. 6.3, are as follows:

- **Stage (1)**: The preamplifier output - with short rise time followed by a long exponential decay time - is digitised by the flash ADC as illustrated in the upper panel.

- **Stage (2)**: Transforms the digitised preamp signal from a continuous discharge signal into a transistor reset (step-like) signal, second panel, by cancelling the exponential decay time introduced by the RC-feedback circuit of the preamp, using a pole-zero digital cancellation circuit. This will provide a flat maximum pulse height with smaller variance.

  Equation (2) removes the exponential decay of the preamp signal and calculates how much each channel would have decayed for the given decay constant and adds that amount back to the initial value. The value calculated from the equation is the uncorrected value of the current channel, minus the corrected value from the previous channel, plus the uncorrected value from the previous channel. This just helps to smooth out some of the noise.

- **Stage (3)**: Differentiates the output of stage 2 to give a square pulse, in which the analysis range is reduced to a finite window around the pulse that is wide enough to not substantially affect the function of the shaping filter, as shown in the third panel.

[2] A sequence of samples within the data acquisition window

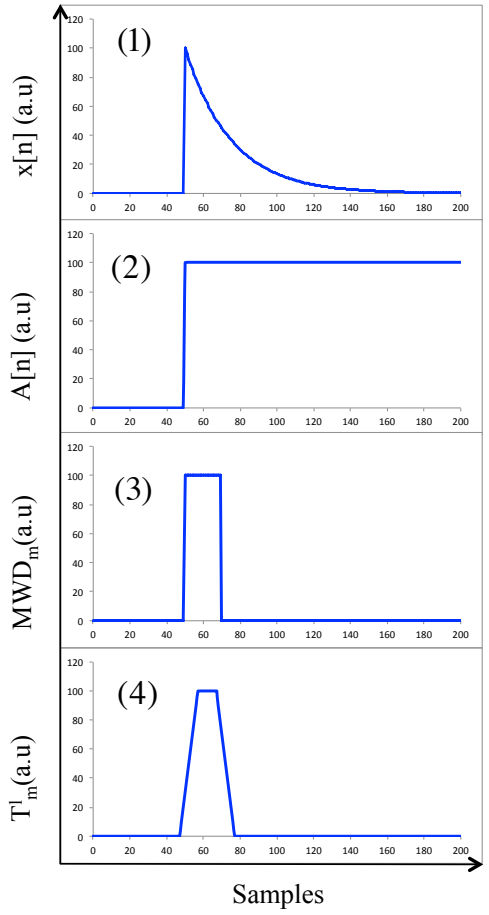

$$x[n] \tag{1}$$

$$A[n] = x[n] - (1 - (1/\tau))x[n-1] + A[n-1] \tag{2}$$

$$MWD_m[n] = x[n] - x[n-m] + \frac{1}{\tau}\sum_{k=n-m}^{n-1} x[k]$$
$$= A[n] - A[n-m] \tag{3}$$

$$T'_m[n] = MA(MWD_m[n])$$
$$= \frac{\left(\sum_{k=n-l}^{n-1} MWD_m[n]\right)}{l} \tag{4}$$

Figure 6.3: The different steps of the pulse height reconstruction, based on the MWD technique, applied to a typical digitised preamp signal (1). The second pulse (2) is obtained after the pole-zero cancellation. This step is followed by the differentiation stage to obtain a square pulse (3). The resulting trapezoid (4) illustrates the output response of the digital system. The equations at the right hand side of the figure shows the digital recursive algorithms (DPP-PHA) [J+94b], [J+94a] implemented in the digitiser's FPGA, to give the corresponding output responses and resulting finally in a trapezoidal shape.

Equation (3) plots the difference between the amplitude of the two channels that are separated by a set number of channels, which is defined as "m" in the equation (so the difference between channels x and $x + m$). If the values of channel x and $x + m$ are the same, 0 is plotted so it is only sensitive to the changing regions of the plot. This transforms the step function from equation (2) into a square pulse. The width of the square pulse (i.e. the flat top of the trapezoid) is given by the value of m.

- **Stage (4)**: Operates moving average filters (noise filtering) over the output of stage 3 to smooth out noise and gives a trapezoidal shape as illustrated in the lower panel. Alternatively expressed, the differentiation (return to baseline) and noise smoothing changed the time profile and shaped the pulse into a trapezoid.

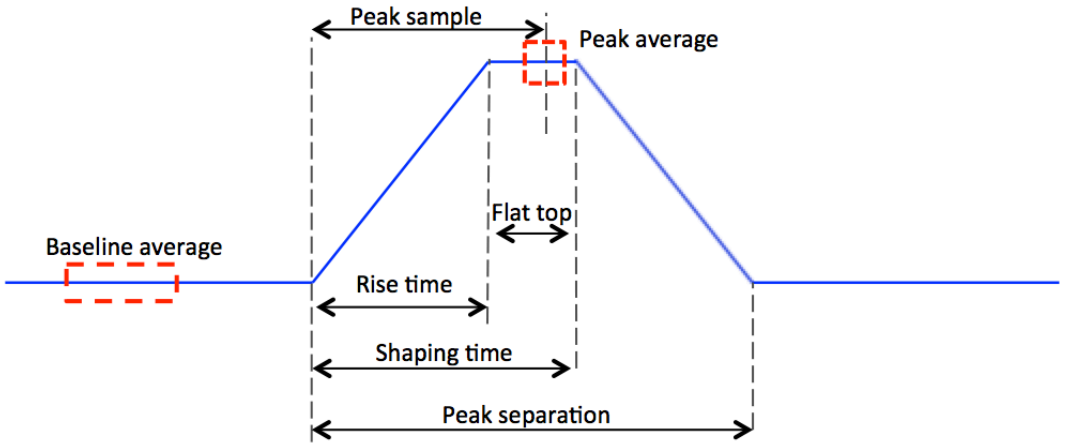

Figure 6.4: The trapezoidal filter parameterisation.

> Equation (4) runs a moving average over the step function. The number of channels included in the average is given by the parameter "I" in the equation. Basically, if, for example, the value of I was 5, it would add the values in channels 1, 2, 3, 4 and 5 together from the input spectrum and then divides this number by 5 to get the average of these channels and put this average in channel 1 of the output spectrum, it will then add together the values from channels 2, 3, 4, 5 and 6, take the average of these 5 channels and put this into channel 2 of the output spectrum etc all the way across the spectrum. This size of the averaging window I determines the risetime of the trapezoid.

The resulting trapezoid can be narrow (fast) or wide (slow) depending on the length of the smoothing averages (baseline average and peak average shown in red in Fig. 6.4). The fast filter is used for timing while the slow one is used for energy determination. The pulse amplitude is evaluated towards the end of the flat top of the slow trapezoid.

From the digital γ-ray spectroscopy point of view, these main digital filters implemented in the digitiser will be discussed in more details in the following sections.

6.3.1 Pole-Zero Correction

As in the analog Gaussian shaper, the trapezoidal digital shaper also requires an accurate pole-zero cancellation to prevent the preamplifier pulses, which are characterised by short rise time and a long decay time, from overlapping with a resulting distortion of the pulse height measurement [Cae16a]. Therefore, the preamplifier output must return to true zero between pulses so that the peak is restored to its initial value. To accurately set the pole-zero cancellation, the trapezoid decay time must be set correctly by the user, according to the preamplifier decay time, $\tau = RC$. Once the decay time of the preamplifier is known, it is possible to correct for the distortion in the pulse height reconstruction caused by the decaying tail through the pole-zero correction. This will give the trapezoid a constant flat top as illustrated in Fig. 6.5. The right hand side

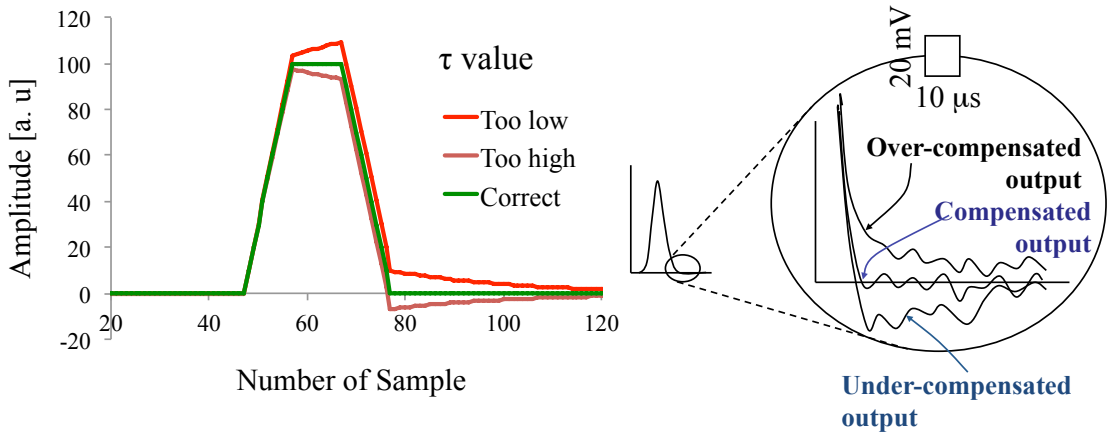

Figure 6.5: Pole-zero effects of undershoot (brown curve) and overshoot (red curve) of the trapezoid, reproduced from [Pri11c].

of the figure shows the subsequent effect of the undershoot and overshoot appeared in the pulse height distribution. Pole-zero cancellation is therefore an essential adjustment for a correct evaluation of the trapezoid baseline and consequently for proper energy determination.

6.3.2 The Energy (or MWD) Filter

As already stated, the digital pulse-processing unit DT5780 has a trapezoidal filter, also known as a MWD filter, with the shape adjustable in several ways, using a number of shaping characteristic parameters, Fig. 6.4. These free parameters include: the length of the flat top, the rise/fall time of the trapezoid, the length of the moving averaging filters for the calculation of the trapezoid baseline (i.e. baseline average filter) and for averaging the flat top (i.e. peak average filter), and the delay between start of the flat top and start of averaging the flat top amplitude. Therefore, the digital filter exhibits digital control on these shaping parameters in order to be modified for optimum performance for a given detector system, suitable for particular experimental conditions.

First of all, the rise time (the charge integration time) is defined as the time it takes for the shaped signal to go from the baseline to the start of the trapezoid flat top. It is a function of the detector and is equal to the fall time. In connection with the traditional analog systems, the trapezoid rise time equals $2 - 2.5$ the shaping time used in these systems.

The flat top time is the "wait" time after reaching the flat region. Adding flat top window (charge collection time) is a practical approach in the digital domain to compensate for ballistic deficits. If the width of the flat top window is modified to a value longer than the longest detector charge collection time, the effect will be essentially eliminated. As will be explained in the following section, the energy is evaluated towards the end of the flat top region of the trapezoid, therefore, the flat top duration should be increased to at least fully accommodate both the peak average plus the delay time

between the start of the flat top and start of the peak average. Consequently maximum improvement in the energy resolution and the symmetry of the peak can be achieved.

Finally, the total trapezoid duration, which is equal to twice the trapezoid rise time and the trapezoid flat top, represents the pulse processing time.

6.3.3 Baseline Restoration

The trapezoidal filter includes a baseline restorer [Cae16a], which runs on the output of the trapezoidal filter and calculates the baseline of the trapezoid. The baseline is calculated by averaging a programmable number of samples before the start of the trapezoid. During the ramp up, the averaging of the baseline is frozen and used in the height calculations. Once the trapezoid is returned to the baseline during the ramp down, the baseline averaging restarts.

The average of the flat top amplitude is also needed in order to accurately evaluate the trapezoid peak height. It is calculated by averaging a certain number of samples (it is also called the peaking area) towards the end of the flat top duration. The reason for this delay is, to avoid including the unstable flat top start in the calculation of the peaking area as well as to wait for the full charge collection. The difference between the flat top height and the average baseline gives the trapezoid amplitude that reflects the original input pulse height or energy released by gamma radiation in the detector. Averaging over a number of samples in the flat top region before subtracting the baseline helps reduce the fluctuations on the energy evaluation due to frequency noise.

Therefore, operating moving averages on the trapezoidal filter output permits for the removal of high frequency noise, which results in an improvement in the energy resolution. For high counting and throughput rates, moving average values should be reduced. When two consecutive pulses are separated by less than the duration of the baseline average window, this means that the baseline interval will not fit entirely between the pulses. Subsequently, data from a previous baseline extrapolation will be used for more than a single peak. This means that, the baseline is not properly calculated for every pulse but those that are well separated, which can significantly worsen the energy resolution. Therefore a compromise is sought between resolution and stability at high counting rates when setting up the length of these averaging filters.
More generally speaking; the main aim of the shaping filter is to shape the preamplifier signal using shaping time parameters in a way where the unwanted frequency components (noise contributions) that are added to the signal by electronics are removed. Chapter 2 treats in full details the behaviour of the various noise contributions as a function of shaping time. For low counting rate applications where resolution is desired over signal throughput, larger shaping time is favoured, while lower shaping times are desirable for high counting rate situations. Therefore, a key reference point can be drawn here that, the optimum operating values of shaping time parameters depend on the tradeoff between the energy resolution and the signal throughput for each application and this tradeoff is well handled by the trapezoidal digital filter.

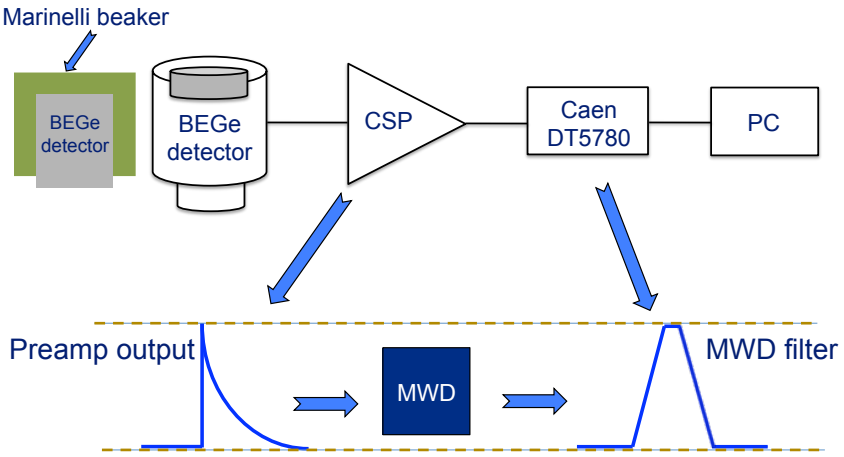

Figure 6.6: Schematic diagram of the DAQ system. The Marinelli counting geometry used for the calibration source and the environmental sample is shown in green.

6.4 Experimental Methods

6.4.1 Digital Electronic Setup

The DAQ system utilised for the main work of this thesis is schematically shown in Fig. 6.6. It consists of a HPGe BE2825 detector (model b12116) (the detector configuration is explained in detail in Chapter 4), which is coupled with a Canberra 2002CSL Charge Sensitive Preamplifier with a gain of 100 mV/MeV. The preamplifier output from the detector was fed into the digitiser Caen DT5780 through one of two independent 16k channels Digital MCA integrated by the digitiser. The preamplifier pulse is digitised over an input vertical range of ± 1.125 V using a flash ADC at a speed of 100 MHz (sampling in 10 ns steps) and quantised at 14-bit resolution. The MWD algorithms implemented in the digitiser FPGA, Fig. 6.3, p. 82, are then used to transform the digitised preamplifier output signal into a trapezoid in real time to extract the energy value. The digital information provided by the digitiser were the derived MWD energy, time stamp information, a value for the signal baseline as well as a sequence of samples of the digitised preamplifier pulse. This digital data was readout to a Linux DAQ PC.

The digital system was controlled using MIDAS (Multi Instance Data Acquisition System) [MID16] and energy spectra were recorded online by the MIDAS software to check for statistics. The data acquisitions, using this system, were performed according to the following order:

- An initial spectroscopic measurement for extracting energy calibration coefficients using the standard calibration point source ^{152}Eu (NPRL S1).
- A series of spectroscopic measurements to carry out the trapezoidal filter optimisation for best energy resolution, using an uncollimated point like γ-ray source containing radioactive ^{137}Cs (NPRL 126).

- An energy calibration measurement using the Marinelli standard calibration source (NPRL 604). The acquired calibration data serves as a reference with a known, well defined energy-pulse height relationship for the Marinelli counting geometry (shown in green, Fig. 6.6) utilised in this work.
- An environmental soil sample measurement in the same Marinelli counting geometry using a prepared soil sample (at depth 25 − 30 cm) discussed in Chapter 5.
- A background measurement for the detector system, taken under the same counting geometry as the calibration source.

The experimental methods used for the energy calibration and system optimisation are explained in Section 6.4.3 and Section 6.4.4 respectively. For the subsequent measurements, the Marinelli calibration source and the environmental sample were individually placed on the detector endcap for counting. In such that, the calibration source (or the environmental sample) is surrounding the germanium detector cryostat in order to maximise the detection efficiency of the detector.

The rate[3] of events recorded by the MIDAS software for the calibration source, the sample and detector background was shown to be 155, 14 and 9 counts/s respectively. Data was acquired over a very long counting period of a day (for the calibration source), 4 days (for the environmental sample) and 2.8 days (for the detector background), to ensure that a minimum of 13×10^6, 5×10^6 and 2×10^6 signals were recorded for the calibration source, the environmental sample and detector background respectively.

The signals recorded for the NPRL 604 source, the environmental sample and the detector background, were performed for offline pulse shape analysis. Detector waveforms were, therefore, written to disk along with the extracted MWD energy values and time stamps for all signal pulses. Each waveform for each event was stored in a sample window of 10.24 μs across 1024 samples with 10 ns per sample. The pre-trigger value[4] used is at half the sample window time, 5.12 μs, (shown in blue) to ensure the rising edge of the charge pulse was centered in the 1024 sample range. An example of a digitised preamplifier pulse recorded by the detector system is presented in Fig. 6.7. The storage of the digital information approaches approximately 20.18 GB for NPRL 604 source, 7.03 GB for the environmental sample and 3.4 GB for the background measurements. Statistical details on the energy spectra acquired over the acquisition system live time are given in Section 6.4.4.

6.4.2 System Dead Time

The dead time of the current counting system (system 1) was measured directly by recording the NPRL 604 data from the detector simultaneously along with the DAQ

[3]It is representative of the recorded counting rate of the digital system not the actual interaction rate as dead time losses are not accounted for here.

[4]This tells the FPGA card how far back to look in its FIFO to account for the finite pulse processing time of the measuring system.

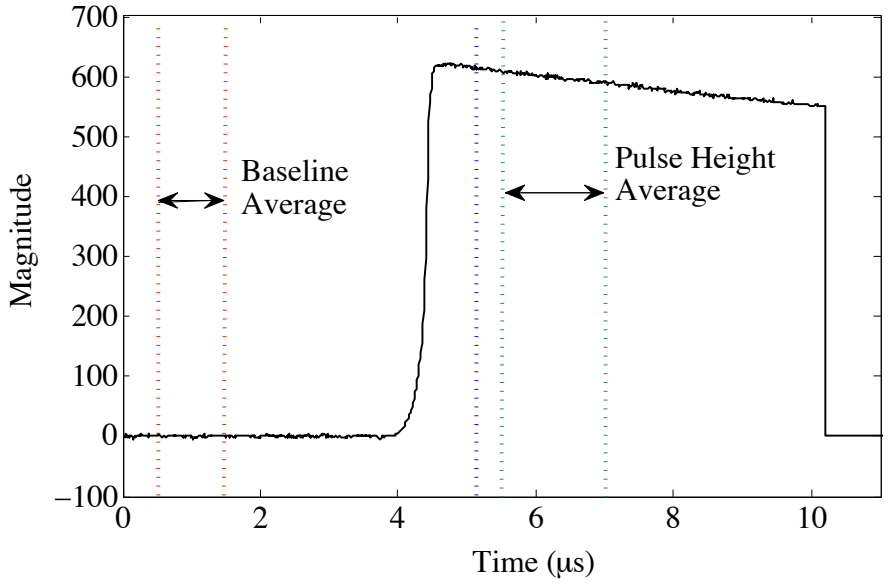

Figure 6.7: An experimental example of a digitised charge sensitive preamplifier pulse recorded utilising the experimental scheme presented in Fig. 6.6.

system presented in Fig 4.2 (system 2), which had a small dead time of 1%. By [Kno10] directly observing the rate of counts in both counting systems, the dead time could be determined by measuring the ratio of the recorded count rate of system 2, corrected for its dead time, to the observed count rate of system 1. This ratio was given to be 3.2 and could be used to correct for the events that were lost from the counting system. The dead time was then calculated to be 69.1% for the current system, subsequently, the count rate of the NPRL 604 source corrected for this dead time was approximately 500 cps.

In an attempt to investigate the influence of the length of the stored sample window on the dead time of the counting system, data was also acquired for different input count rates with a pulser input to the preamplifier. The pulser data was set to be equivalent to a 1460 keV gamma-ray emission and was used to provide information on the count rate losses while varying the length of the sample acquisition window. The count rate response as a function of the sample window width is presented in Fig. 6.8 for different input count rates.

It can be seen in the figure that at the lowest input count rate (300 cps), the response of the recorded count rate is not affected by the variation in the length of the sample window. Whereas, at the higher input count rates[5], the observed count rate starts to decrease at a sample window above $\sim 7.2\,\mu$s. Below this value, the response of the output count rate is clearly shown to be stable. At $10.24\,\mu$s, which is the length of the sample acquisition window chosen for the current experiment, the output count rate has dramatically decreased from 500 cps to 388 cps and from 450 cps to 318 cps.

[5]They are set to be comparable to and relatively lower than the count rate of the NPRL 604 calibration source.

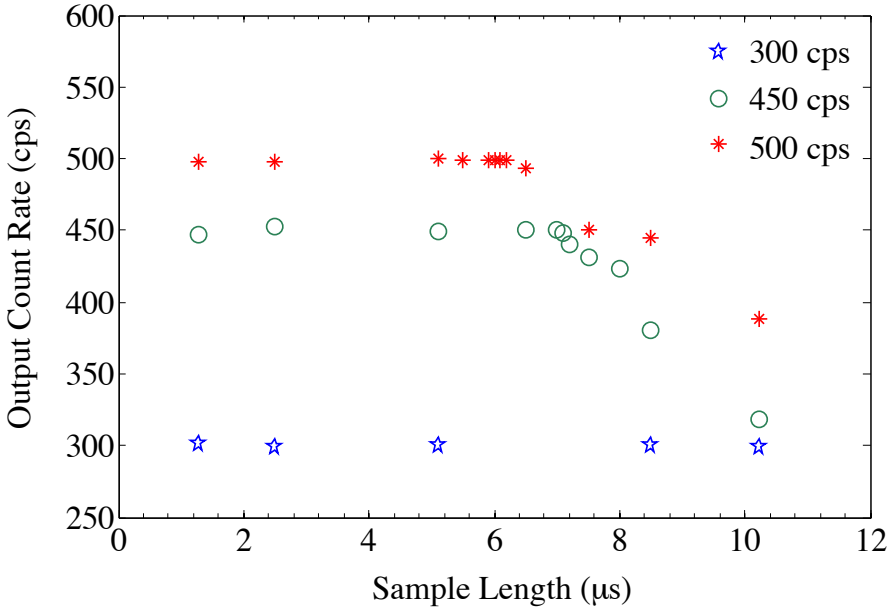

Figure 6.8: The count rate response as a function of the sample window width. The input count rates are the parameter for the three curves.

Pulser measurements have confirmed the impact of the increase in the sample window on the count rate losses of the counting system. As already mentioned that, each waveform was saved to memory along with an energy value and time stamp information. Therefore, the 1024 samples plus the digital pulse processing time taken to issue the energy and time stamp for each waveform together are causing the dead time.

6.4.3 System Calibration

Prior to the filter optimisation, the coefficients of the energy calibration are required. To do this, a calibration point source ^{152}Eu was placed 10.00 ± 0.05 cm above the centre of the detector face for counting. The energy spectrum was acquired using the MIDAS data acquisition software. The channel number (or position) of each energy peak centroid determined by the software was recorded. Subsequently a linear calibration function was produced in MatLab using these experimental data, so an energy calibration factor of 0.2486 keV/channel and an offset of $-$ 0.15 were obtained. These same coefficients were used to calculate the energy resolution values when investigating the digital filter optimisation.

6.4.4 Energy Filter Optimisation

In this work, the trapezoidal filter adjustments were performed for the rise time, flattop of the trapezoid, and the length of the baseline average window. These parameters were varied to study their influence on the energy resolution. The resulting profile represents the behaviour of the trapezoid filter as illustrated in Fig. 6.9 and Fig. 6.10. The

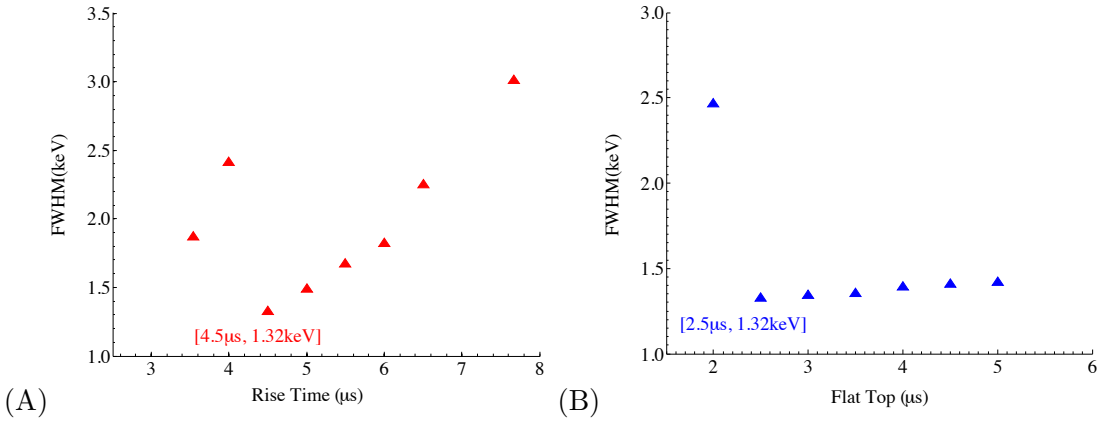

Figure 6.9: The energy resolution (or FWHM) of the 662 keV γ-ray line of ^{137}Cs acquired with the trapezoid filter for (A) different rise times, (B) different flat top times. The statistics are large enough that errors become negligible ($<<$ 0.01%). The best shaping time found is 4.5 μs and 2.5 μs for the rise time and flat top time respectively.

optimisation of these parameters was carried out using an uncollimated ^{137}Cs radioactive point source (NPRL 126).

During the experimental data acquisition, the source was placed at a distance of 10.00 $\pm$ 0.05 cm above the centre of the detector face. At such a distance, count rate losses due to pulse pile-up were negligible. Additionally, the variation of the digital filter parameters was performed in defined steps, as discussed below, and the measuring time was chosen to be 1,200 s for each step, unless stated otherwise, so that good precision on the net area of the ^{137}Cs full-energy photopeak was achieved. Such that the statistical uncertainty, as determined by the MIDAS software fitting, on the net peak area did not exceed 1.5%.

Trapezoid Rise Time

The length of the trapezoid rise time was changed from 3.54 to 7.67 μs in steps of 0.5 μs. As it can be seen from Fig. 6.9A that, the lower impact of the length of the rise time on the ^{137}Cs peak width is at 4.5 μs, where the corresponding FWHM is 1.32 keV, which is the optimum energy resolution obtained across the entire range. Beyond 4.5 μs, it is obvious that, the ability of the trapezoid filter to provide narrower peak width tends to degrade dramatically. Below this rise time value, the FWHM of this peak starts to rise. In this region, the trapezoid exhibits an anomalous behaviour and the reason for the sudden increase of the peak width at 4 μs is unclear, which can be however thought that, the trapezoid in this region is unstable.

Trapezoid Flat Top

The effect of the length of the trapezoid flat top on the ^{137}Cs peak width was also studied independently, by changing the width of the flat top across the time range of 2 - 5 μs in steps of 0.5 μs with the same measuring time (1,200 s) for each step. It can be seen

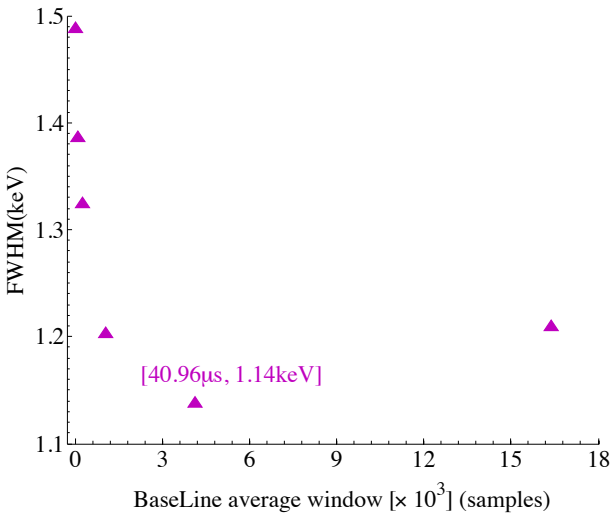

Figure 6.10: Energy resolution measurement as a function of the baseline average window using the 662 keV γ-ray line of ^{137}Cs.

from Fig. 6.9B that, the optimal flat top time that provides the best energy resolution is 2.5 μs, indicating that the variation in the charge collection times of the detector is effectively accommodated by the trapezoid flat top at that value. The FWHM at this flat top value is given as 1.32 keV, which is the same FWHM value driven by the rise time filter. The trend of the trapezoid flat top above the optimal flat top time is slightly degrading until 5 μs. Below 2.5 μs, the energy resolution has reduced dramatically, which means that the trapezoid is not successfully handling the ballistic deficit effects below this flat top value.

Baseline Average Window

For the baseline average window, the behaviour of the trapezoid filter is shown in terms of number of samples, Fig. 6.10. The average baseline has been modified at different programmable values (pre-defined by the program) starting from 16, 64, 256, 1024, 4096 to 16384 samples, using the same measuring time (1,200 s). The optimum width of the baseline average window is given at 4096 (= 40.96 μs[6]) corresponding to FWHM of 1.14 keV. As the number of samples rises, the trapezoid filter rapidly reduces the peak width and hence improves the energy resolution. It can be noted that, the final energy resolution derived by the filter has been improved from 1.32 to 1.14 keV through optimising independently the three parameters.

An example spectrum of the ^{137}Cs photopeak, as fitted by the MIDAS software is presented in Fig. 6.11. The spectrum is collected using the obtained optimum rise/flat top times and baseline average window shown in Fig. 6.9 and Fig. 6.10 respectively, using the measuring time of 57,600 s. As such, the statistical uncertainty determined by

[6]It is already mentioned that the signal issued from the flash ADC is sampled at equal intervals of 10 ns steps.

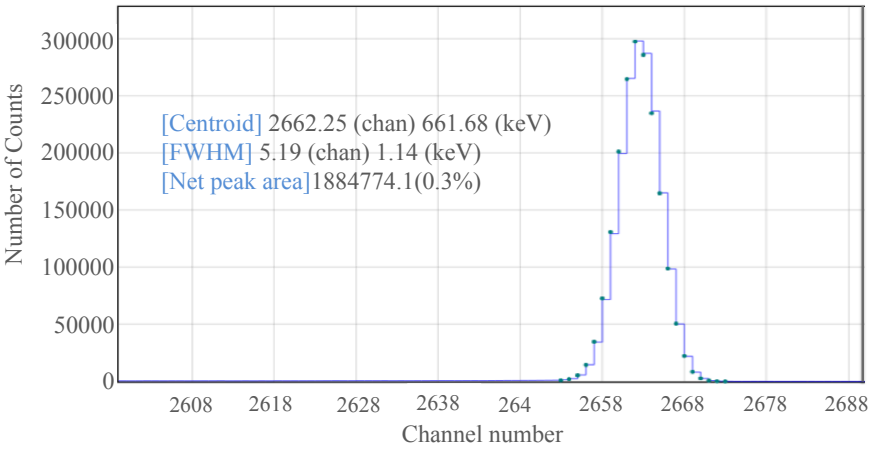

Figure 6.11: A sample spectrum of the ^{137}Cs full-energy photopeak, fitted by the MIDAS software, collected over the acquisition system live time of 57,600 s using the optimised MWD filter parameters shown in Fig. 6.9 and Fig. 6.10. Information on the peak fit is also shown. Values shown in keV were calculated from the linear calibration function "$keV = 0.2486\ channel - 0.15$" given in Section 6.4.3.

the software on the net peak area did not exceed 0.3%.

It can be noted that, the above optimisation of the trapezoid parameters is just performed for the 662 keV γ-ray energy. The optimal rise time, flat top time and the baseline average window obtained were, however, used to acquire a data set of detector traces for the subsequent measurement using the mixed Marinelli NPRL 604 calibration source, which has a wide range of energy from 59.5 keV up to 1332.5 keV. It is not practical to find the optimal shaping time that gives the best energy resolution for every single γ-ray energy emitted by the Marinelli source. This would involve acquiring the data set once for each optimal shaping time, which is impractical for the subsequent offline data analysis.

6.4.5 Data Acquisition

After optimising the MWD filter parameters for best detector energy resolution, their optimal values were set in the MIDAS software to be applied to the subsequent spectroscopic measurements for the calibration source and environmental sample counting as well as background corrections. A summary of the main parameters describing the trapezoid filter (MWD) is given in Table 6.1.

First of all, using the mixed Marinelli calibration source NPRL 604, an experimental digital data of pulse shapes generated following gamma-ray interactions in the detector was recorded utilising the experimental scheme presented schematically in Fig. 6.6, p. 86, with an energy threshold set at 12.5 keV above noise. The experimental energy spectrum was collected over an acquisition system live time of 26701.8s with a dead time of 69.1% of the full acquisition time, 86,400 s. In such that, the net peak area of small photopeak intensities was $>$ 40,000 counts for ^{109}Cd and ^{57}Co, and that of high photopeak intensities was $>$ 200,000 counts for ^{241}Am, ^{137}Cs and ^{60}Co. This means good

Parameter	Input Value (μs)
Pre-trigger	5.12
Trapezoid Rise Time	4.5
Trapezoid Flat Top	2.5
Peak Sample	6.5
Baseline Average Window	40.96
Decay Time Constant	50
Sample Window Length	10.24

Table 6.1: Settings of Moving Window Deconvolution parameters for data acquisition using the digital trapezoidal filter.

precision on the net area of these photopeaks was achieved; since the counting statistical uncertainty over this acquisition system live time on their net peak areas, as determined by the MIDAS fitting, was found to be 2% for the small photopeak intensites. For the high photopeak intensites, it was shown to be 1% except that for ^{241}Am, which was 3%.

Fig. 6.12 shows the energy spectrum reconstructed offline from the stored waveforms, as will be described in Section 6.5.1.

Following the calibration source measurement, an environmental counting measurement using the prepared soil sample was carried out. In order to quantitatively evaluate photopeaks of radionuclides detected in the sample, it was necessary to correct for any peaked background found beneath the evaluated photopeaks.

Therefore, once the sample measurement was made, a data set of detector background was also acquired. Both sets of measurements have been taken under the same counting geometry as the calibration source. Energy spectra for the sample and background, with sufficient statistics in photopeaks considered for analysis (these are mentioned in Section 6.8.1 and Section 6.9.2), were collected over a long counting time of 345,660 s (4 days) and 246,180 s (2.8 days) respectively. In that, for the sample energy spectrum, the net peak areas of small activities, as determined by the MIDAS fittings, were in the range of 3,000 − 9,000 counts and those of higher activities were in the range of 10,000 and 45,000 counts. The counting statistical uncertainties over the full acquisition time on all net peak areas were in the range of 1% − 7%. For the background spectrum, the net peak areas of detected activities were in the range of 1,200 − 7,000 counts, except that of ^{40}K which was >13,000, with counting statistical uncertainties in the range of 1% − 25%. Fig. 6.13 represents the energy spectra of the environmental sample and detector background produced offline from the stored waveforms, as will be described in Section 6.5.1.

The unintended difference in the full acquisition time of both measurements was scaled out in the offline calculations, in such that the count rate of the net peak area of a radionuclide photopeak is corrected for that of its associated peaked background (if found) instead of the direct subtraction of their net peak areas.

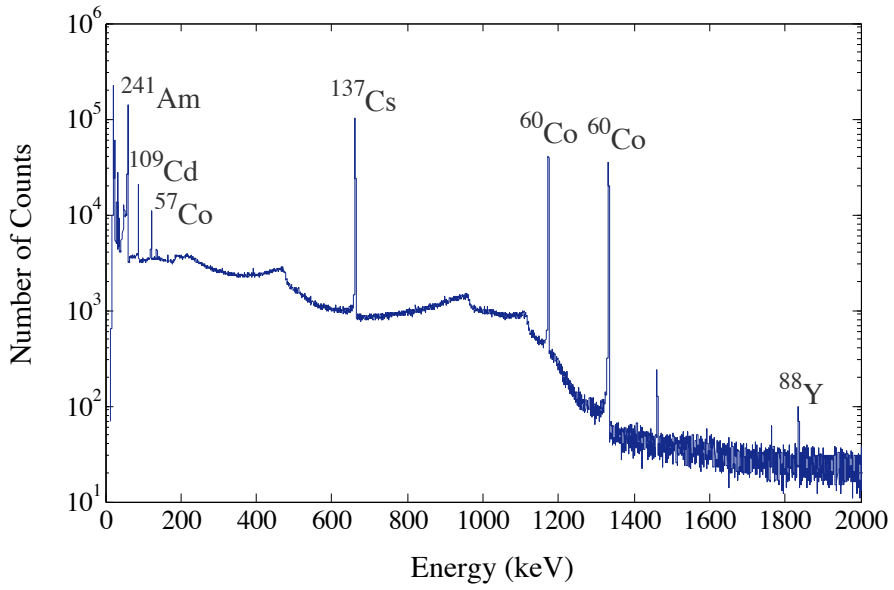

Figure 6.12: The calibrated energy spectrum of the Marinelli calibration source NPRL 604, reconstructed offline using the MWD energy determination method (discussed in Section 6.5.1) and reproduced in MatLab, measured over a full acquisition time of 86,400 s with a dead time of 69.1% utilising the experimental scheme setup presented in Fig. 6.6, p. 86. The radioactive nuclides are indicated on the plot.

6.5 Data Processing and Outputs

In the analysis stage, stored waveforms using the calibration source were processed with MTSort [MID16], which is a Liverpool Nuclear Physics group data-sorting package used to sort spectroscopic data acquired from various DAQ systems. The MTSort package reads in the digitised data that stored from the experimental stage and can output analysed spectra that have been gain matched and gated on energy or time regions of interests.

In order to run MTSort, a file of sorting instructions must be supplied, which is written in the MTSort Language. This data file includes; a description of the experimental setup, declared spectra (histograms) required, analysis commands to be applied to each event being sorted, and a location of the data files to be processed and analysed. Additionally, a C-code is required, which is written in C++. The C-code is utilised to read in data and calculate energy based on the digitised detector traces acquired from the DAQ system. The sort file utilises this C-code to create one- and two-dimensional (1D and 2D) distributions based on the original instructions in the input sort file.

The output generated in this work included the energy spectra, which were gain matched and analysed, 1D and 2D pulse shape risetime distributions as well as Folds, which contain the counts that are registered as interactions within the detector according to the requirements entered in the sort file. The MTSort outputs were saved and further analysis was accomplished with MatLab. The procedures of pulse shape analysis for

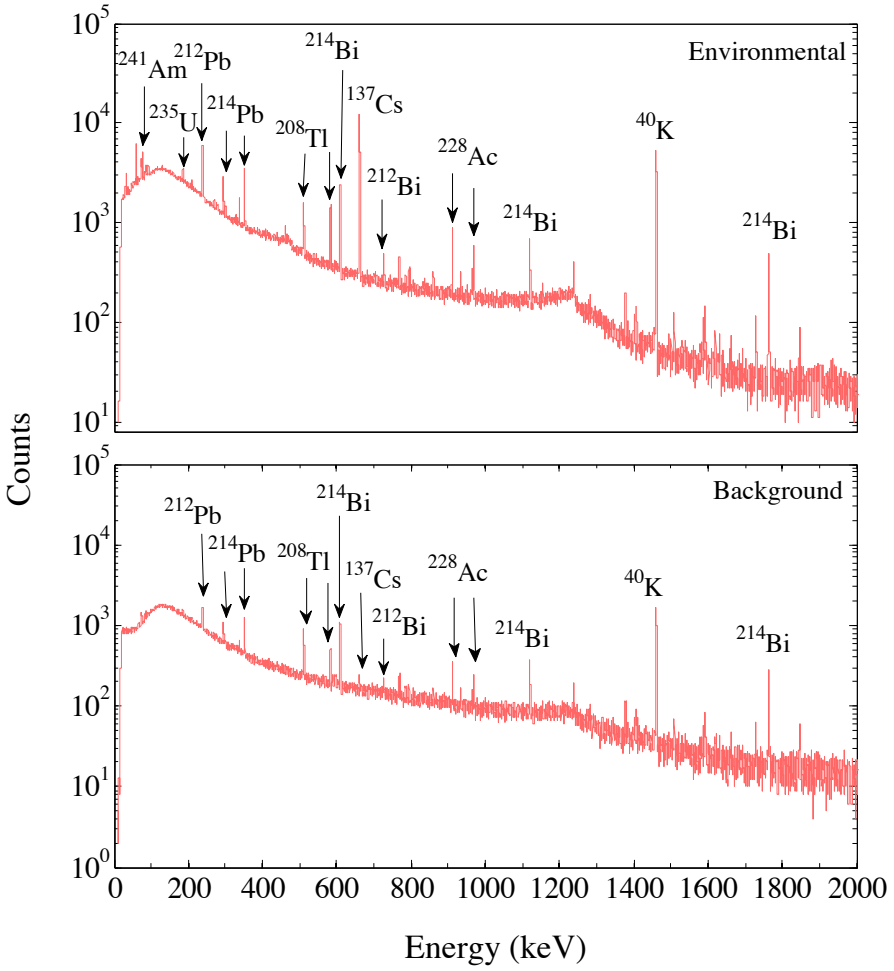

Figure 6.13: The calibrated energy spectra, reconstructed offline using the MWD energy determination method (discussed in Section 6.5.1) and reproduced in MatLab, for the environmental sample (upper panel) and the detector background (lower panel) measured over a full acquisition time of 345,660 s (4 days) and 246,180 s (2.8 days) respectively, using the experimental scheme setup shown in Fig. 6.6, p. 86. The detected radionuclides found in the environmental sample as well as their corresponding peaked background considered for corrections are also shown.

the acquired waveforms performed through MTSort will be detailed in the following sections.

6.5.1 Pulse Height (or Energy) Distribution

The energy deposited inside the detector from all signals recorded in the experiment for each data set was reconstructed in MTSort using two energy determination methods:

- **Baseline difference (BLD)**: it is a measure of the difference between the charge pulse height and the average baseline. In this work, the baseline was calculated by averaging 100 samples from 50 to 150, corresponding to the range of 0.5 μs − 1.5 μs of the sample window as illustrated in Fig. 6.7, p. 88. The average of the full pulse height was calculated across a wider range of samples from 550 to 700,

starting at 5.5 μs after the beginning of the sample window. The energy is then a simple subtraction of the two averages.

- **Moving Window Deconvolution (MWD)**: the pulse height distribution is produced from the recorded energy values derived by the MWD algorithms implemented in the FPGA card. As already discussed in Section 6.3, the algorithms account for the preamplifier decay, providing a flat maximum pulse height with smaller variance. Therefore, the pulse height distribution created from the recorded MWD energies has energy resolution superior to that obtained from the baseline difference.

Pulse height distributions reconstructed using the BLD (or MWD) energy determination method are referred to in this work as BLD (or MWD) energy spectra. For the calibration data set, the BLD and MWD energy spectra obtained were calibrated to 0.3 keV/channel in the MTSort software using a quadratic calibration function to allow precise calibration over an energy range of 2.49 MeV for 8192 channels. In such that, the peak centroid (C_γ) for each energy photopeak (E_γ), as defined by the histogram of the BLD (or MWD) spectrum viewed by the MTSort program, was recorded. A plot of E_γ versus C_γ for the BLD (or MWD) spectrum has been produced in MatLab in order to determine the quadratic fit function to extract the calibration coefficients. The two sets of calibration coefficients obtained from the two methods were roughly the same, which then entered in the sort file to apply the calibration. The energy spectra reconstructed in advance for the other data sets (sample and natural background) were also calibrated in the MTSort program using the same calibration coefficients.

A comparison between the calibrated BLD and MWD energy spectra is presented in Fig. 6.14. It can be noted from the figure that, the BLD and MWD photopeaks for 60 keV, 88 keV and 122 keV emitted from ^{241}Am, ^{109}Cd and ^{57}Co respectively are very similar in Gaussian shape. For the high-energy photopeaks, the low energy tail of BLD photopeaks is evident. Subsequently, the typically energy resolution obtained using the baseline difference method is relatively deteriorated. The width of the BLD photopeaks for the 662 keV, 1173 keV and 1333 keV is typical of the 1.8 keV, 2.2 keV and 2.3 keV FWHM respectively while that for the corresponding MWD photopeaks is typical of the 1.6 keV, 1.9 keV and 2.0 keV FWHM respectively.

The cause of the distortion in the pulse height reconstruction using the BLD method is that the preamplifier decaying tail is not removed (pole-zero cancellation). However, it can be noted that, the energy resolution obtained from the BLD method was not very significantly worsened by the uncorrected decaying tail. This could be explained by the long detector waveform recorded (10.24 μs) and hence the long averages used when determining the pulse height and baseline values.

For the advanced spectroscopic analysis in Section 6.5.3, these spectra are referred to as "*original spectra*" and will be quantitatively compared with all processed energy spectra resulting after the application of PSA on the NPRL 604 data set.

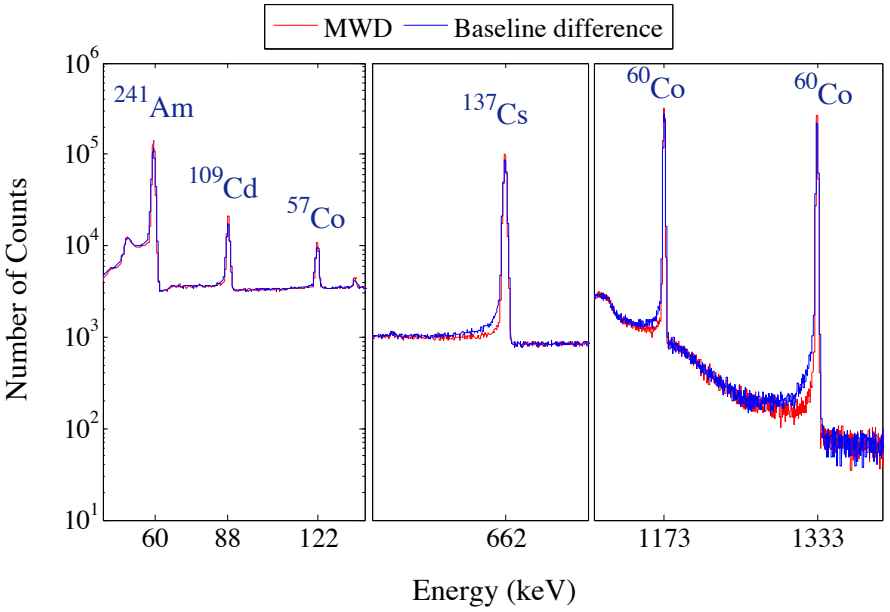

Figure 6.14: The calibrated energy spectrum for the calibration NPRL 604 source, reconstructed offline in the MTSort software using the baseline difference (BLD) (in blue) and moving window deconvolution (MWD) (in red) energy determination methods. These spectra were reproduced in MatLab. The radioactive nuclides are indicated on the plot.

6.5.2 Parametric Rise Time Analysis

Following the γ-ray interactions inside the detector, charge carriers (electron-hole pairs), which are created within the depletion region, are swept out of the region by the application of high voltage towards the appropriate electrodes in opposite directions. Subsequently, the motion of the charge carriers induces the charge (or current) pulse from the detector. The time required to collect charge carriers (pulse time profile) in HPGe detectors depends on their physical characteristics such as size and geometry, and mainly on the γ-ray interaction position. Moreover, the charge collection time is dependent on the number of the energy depositions within the detector as many γ-ray pulses arise from various interactions, such as multiple Compton scattering followed by photoelectric absorption, occuring at widely separated points inside the detector [Kno10]. This dependency reflects the undesired variation in the rise time of the measured charge signals across the detector.

Therefore, in order to investigate the time profile of the charge pulse, it is appropriate to consider the time until the signal reaches a certain fixed fraction of its maximum height. As the electronic noise is inevitably added to the signal, this makes it difficult to determine precisely the point at which the signal started. Consequently, the rise time calculations will be difficult to perform. This problem can be solved by considering the time for a signal to go from some small fraction of its height to some larger fraction. In this work, the rise time of the charge pulse, Fig. 6.15, is characterised by two parameters defined as:

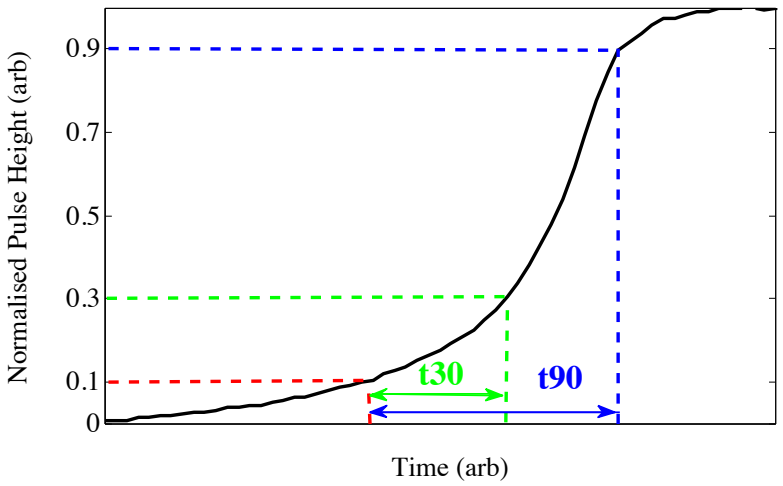

Figure 6.15: An experimental example of a pulse shape to illustrate risetime parameters. The time taken from 10% to 30% of the pulse height is t30 and the time taken from 10% to 90% of the pulse height is indicated t90.

- **t30**, which is the time spent for the pulse to rise from 10% to 30% of its maximum height.
- **t90**, which is the time spent for the pulse to rise from 10% to 90% of its maximum height.

For the following calculations, the rise time of pulse shapes for the NPRL 604 calibration source was measured in MTSort on an event-by-event basis. The rise time measurement was performed for all partially and fully deposited photons of the different γ-ray energies emitted by the source, from all different interaction positions within the detector.

T90 Versus T30 Distribution

After the rise time calculations have been performed, each t90 value was referenced to its t30 value in the MTSort program, such that, a distribution of the calculated values of t90 as a function of the calculated values of t30 was produced and presented in Fig. 6.16. The plot represents a risetime map of t90 versus t30 distribution for different gamma-ray interactions inside the detector.

For visualisation purposes, the 2D distribution was zoomed in for illustration so the vast majority of t30 and t90 times can be simply compared. It can be observed from the 2D risetime map that, the risetime profile is extended across a wide range of rise times. Moreover, t90 times vary significantly compared to t30 times, causing the profile to be shifted towards t90 axi.

This can be explained by the increased probability of the occurrence of multiple interactions by gamma rays within the detector, where the γ-ray pulses generated for these interactions become elongated, as will be discussed in the following section. Subsequently the t90 times are longer and have a larger range than the t30 times.

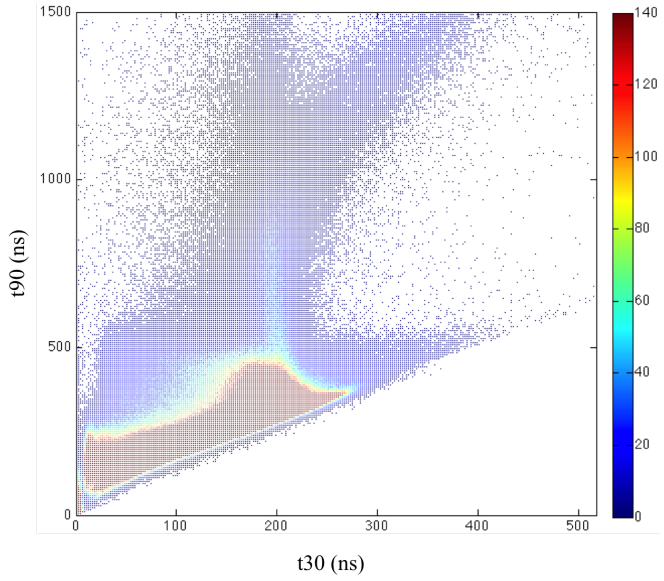

Figure 6.16: Matrix of (ungated) t90 versus t30 risetime distribution for all partially and fully deposited γ-ray photons, from different γ-ray interaction positions across the detector, emitted from the Marinelli NPRL 604 calibration source, including the natural background. The map was generated with limits of 0 to 4096 in the MTSort software but in this figure the scale of t90 and t30 was set to a smaller value for visualisation purposes only.

This risetime distribution, however, provides a general representation of the overal response of the pulse shapes as the response is determined for all recorded signals arisen from all different interaction positions across the detector.

Therefore, in order to better understand the observed response, it was essential to distinguish between events corresponding to each gamma ray emitted by the source as the high-energy gamma rays are more probable to undergo bulk interactions within the detector as opposed to mostly shallow interactions for the low-energy gamma rays. Thus, differentiating between events corresponding to different gamma radiations will provide a better representation of the variation in rise time. This will be the subject of discussion in the following section.

Gated T90 Versus T30 Distributions

As already stated, it is required to differentiate the events corresponding to only full-energy photopeaks of the different gamma radiations. This will aid better understanding of the differences between risetime responses for different γ-ray energies, as it would be expected in advance.

Therefore, using the BLD full energy photopeaks for the NPRL 604 source shown in Fig. 6.14, matrices of t90 vs. t30 were individually produced for events corresponding to each full-energy photopeaks. To perform this, the threshold level values corresponding to the lower level discrimination (LLD) and the upper limit discrimination (ULD) of each full-energy photopeak were defined from the histogram of the spectrum viewed by

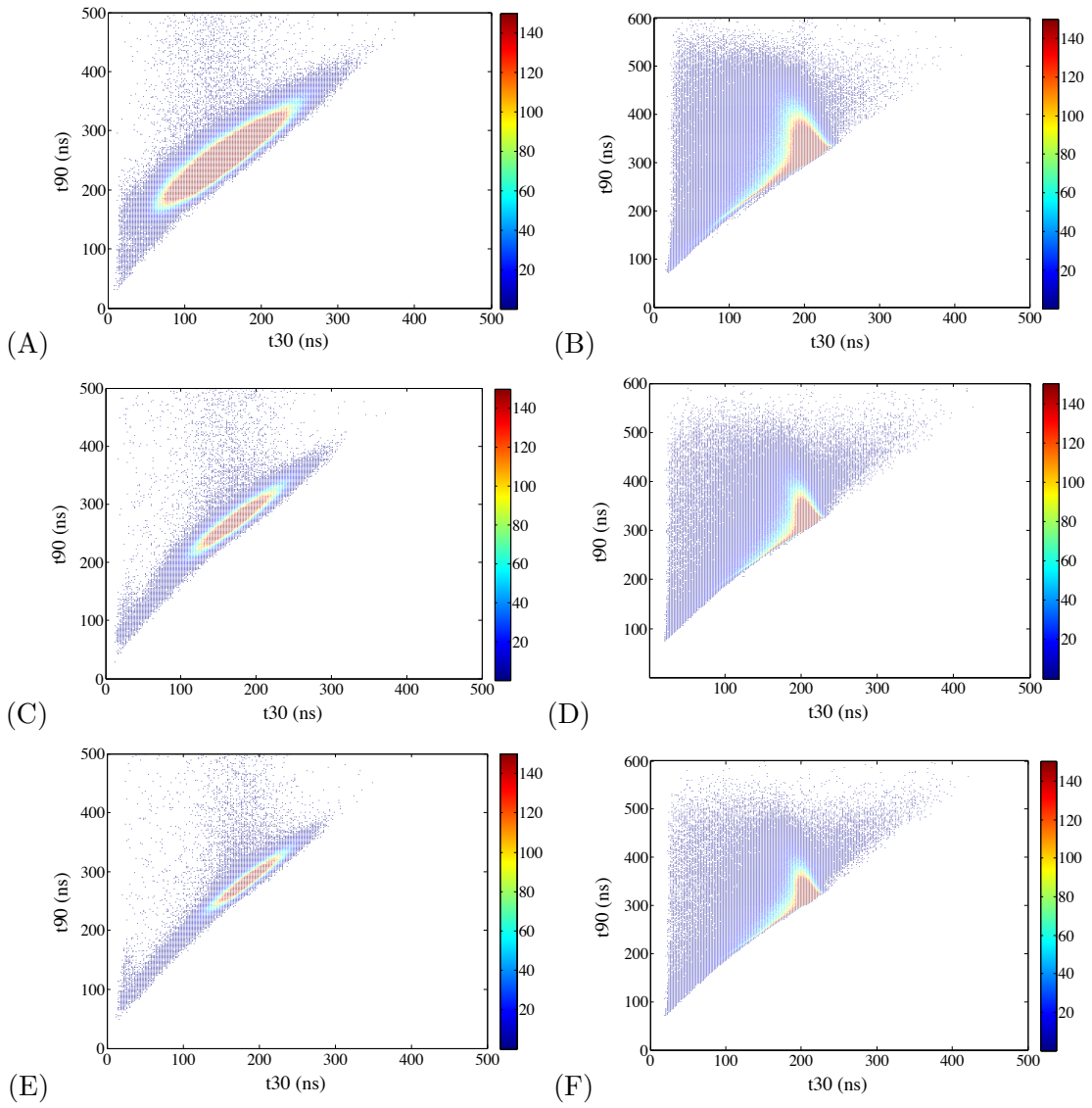

Figure 6.17: Matrices of gated t90 versus t30 risetime distributions produced by gating on energy region of interests. Left panels (A, C and E) represent the risetime maps produced for the full-energy photopeaks of 60 keV, 88 keV and 122 keV respectively, whilst right panels (B, D and F) for full-energy photopeaks of 662 keV, 1173 keV and 1333 keV respectively. The maps were generated with limits of 0 to 4096 in the MTSort software but in this figure the scale of t90 and t30 was set to a smaller value for visualisation purposes only.

the MTSort program and then entered in the sort code to gate the risetime response, shown in Fig. 6.16, on the defined energy region of interest of each peak. In such that, BLD energy gates of 4.0 keV, 4.8 keV, 4.2 keV, 7.8 keV, 8.5 keV and 8.8 keV set around the 59.5 keV, 88 keV, 122 keV, 661.7 keV, 1173.2 keV and 1332.5 keV BLD photopeaks respectively were applied to the NPRL 604 data, as the BLD width of these photopeaks is typical of the 1.5 keV, 1.5 keV, 1.5 keV, 1.8 keV, 2.2 keV and 2.3 keV FWHM respectively. By running the MTSort, only those gamma rays that have deposited energy within the LLD − ULD range of each peak will be used to produce a risetime map representing

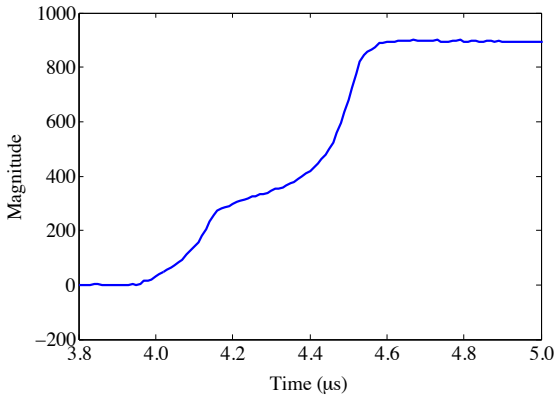

Figure 6.18: An experimental example of a pulse shape response shows the occurrence of multiple interactions by a 1333 keV gamma ray within the detector, where a discontinuity and elongation features can be seen. A 8.75 keV BLD energy gate at 1333 keV was applied to the NPRL 604 pulse shapes data set.

that peak.

The generated risetime maps are referenced in this work as "*gated t90 versus t30 distributions*". These maps are presented in Fig. 6.17 and considered as the pre-filtered risetime maps preceding the subsequent filtering. In the meanwhile, the t90 versus t30 distribution produced from the raw data set (Fig. 6.16) is referred to as "*ungated t90 versus t30 risetime distribution*". These maps demonstrate the relationship between the shape of the risetime response of the detector and the energy of the corresponding gamma rays interacting inside the detector crystal.

It should be remembered that, all photopeaks are superimposed on an underlying continuum, which is the Compton continuum from natural background such as ^{40}K (1460 keV) and from high energy gamma rays emitted from the radioactive nuclides being measured. Therefore, events in the energy regions of interest also contain those corresponding to Compton background that are included into the created risetime maps.

It can be noted from the plots that, the risetime distributions for the full-energy photopeaks of 662 keV, 1173 keV and 1333 keV (Fig. 6.17B,D,F) show similar structures and in comparison with those for the low energy photopeaks (as will be discussed below), they are slower and more broadened across a wider range of rise times, as a range of t90 $\approx$ (80 to 600) ns across a range of t30 $\approx$ (10 to 400) ns is observed in these profiles. This can be attributed to the increased probability of Compton scattering, which is the dominant interaction that a photon can undergo with those energies. This means that, events contributing to these full-energy photopeaks are highly likely to contain multiple interactions, such as multiple Compton scattering followed by photoelectric absorption of the scattered photon, which cause a discontinuity and elongation of the pulse leading edge as illustrated in Fig. 6.18. As a result of that, the charge pulse of such an event will take a more varied and longer time to reach t90 according to the number and the position of the gamma-ray interactions for each event.

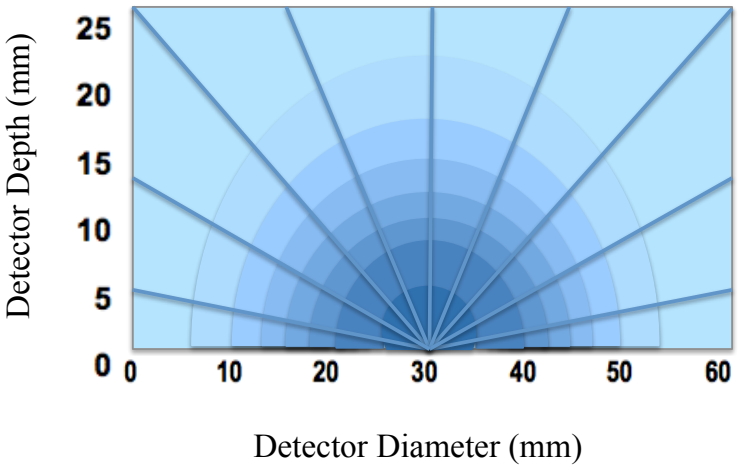

Figure 6.19: Schematic illustration showing the electric field lines and equipotential surfaces (colours) for the BEGe detector. Holes will drift towards the point like contact due to the application of high voltage on the outer contact.

From the point of view of γ-ray interaction position, multiple interactions which occur in the bulk of the detector are expected to contribute considerably to the variation in risetimes due to the high probability of capturing all the gamma energy through various interactions before leaving the detector. However, multiple Compton scatterings that occur in the edges of the detector are expected to escape from the detector without depositing full energy and not to contribute to the spread in pulse shapes. Additionally, the events that contribute to these risetime maps are expected to occur, on average, throughout the bulk of the detector volume closer to the p+ contact, where [HB+14] there is an increased radial variation in the weighting potential (an explanation of this term can be found in [Kno10], [He01]) as a function of depth as depicted in Fig. 6.19, which results in a significant variation in the recorded pulse shapes. It has been demonstrated in this study [HB+14] that, the change in weighting potential through the detector depth is most significant at the detector centre, resulting in significant spread in drift times for interactions occurring in this region. The signals generated for interactions close to the p+ contact are more likely to initially have a fast leading edge, followed by a period of slower charge collection.

On the other hand, the risetime distributions for the full-energy photopeaks of 60 keV, 88 keV and 122 keV (Fig. 6.17A,C,E) show similar profiles, which are very different in shape and range from the previous ones. These profiles are shown to be faster, much lower varied and spread in risetime values, as a range of t90 $\approx$ (50 to 400) ns across a range of t30 $\approx$ (10 to 300) ns is observed. The reason for this is that, photoelectric absorption is the main interaction process for these energies, which means that, the single photoelectric events are the dominant contributor to these photopeaks.

The low-energy gamma rays are expected to be absorbed close to the detector top

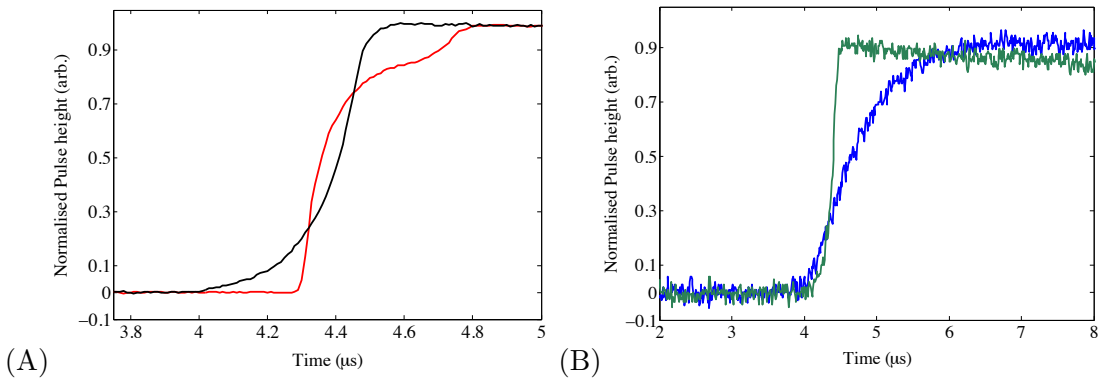

Figure 6.20: Charge pulse response of the BEGe detector to single and multiple γ-ray interactions. The pulse shapes in (A) show the charge signals resulting from a typical single interaction (in black) and multiple interactions (in red). The pulse shapes in (B) show the charge signals resulting from typical single interactions, viewing the effect of the noise that is superimposed on the whole charge signal. The signals are resulted from the full absorption peak of (A) 1173 keV and (B) 122 keV gamma rays. BLD energy gates of 8.5 keV and 4.2 keV set around the BLD full absorption peaks of 1173 keV and 122 keV respectively were applied to the pulse shape data set of the NPRL 604 source.

and side surfaces[7], as opposed to mostly throughout the bulk of the detector volume for high-energy γ-ray interactions, where [HB+14] the weighting potential is weak and less varied (see Fig. 6.19). Therefore, the variation in risetime for these energies is controlled by the radial distance of the interaction position, instead of the detector depth. In such that, the charge collection time increases as the radial distance rises. Holes produced following γ-ray interactions in the detector top and side surfaces (i.e. far from the p+ contact) are moved relatively slowly towards the contact because of the weak weighting potential at the outer surfaces. This will result in an initially shallow gradient in the leading edge of the generated signal, which will then rise sharply as the charge traverses the region of the increased weighting potential closer to the p+ contact and any further variation in charge collection times as a function of radial distance becomes negligible. It is also suggested that [HB+14], the weighting potential is slightly stronger at small radial distances (i.e. centre of the detector top surface), therefore, holes move faster towards the p+ contact, leading to shorter t30 times than at the edges.

This means that, the charge pulse spent more varied and longer time to reach 30% of its maximum. Thus, the variation in pulse shapes mainly resulted in the early stages of the charge collection time (t30).

Fig. 6.20 shows experimental examples of normalised pulse shapes illustrating the response of the BEGe detector to single and multiple gamma-ray interactions, using high (1173 keV) and low (122 keV) γ-ray energies. The pulse shapes have been acquired when BLD energy gates of 8.5 keV and 4.2 keV, set around the BLD 1173 keV and 122 keV photopeaks respectively, were applied to the pulse shape data set of the NPRL

[7]Marinelli counting geometry is used, where the calibration source is surrounding the germanium detector cryostat.

604 source. The figure shows how the pulse shape response to multiple interactions (red pulse in (A)) is clearly different from the other pulse shapes resulted from single interactions. It can also be noted in pulses generated from single interactions the effect of the noise on these signals, that is superimposed on the whole charge signal.

In addition, pulses with charge trapping can also contribute to the broadening of the distributions, because some of the charge carriers do not drift to the collecting electrode in the expected time, hence, they have longer charge collection time. Charge trapping is, however, expected to have a negligible effect on the spread in these risetime responses. This can be supported by the argument that as the long charge collection of these pulses delays the peaking time (time between the beginning of the pulse and the maximum), it also reduces the recorded pulse amplitude (i.e. incomplete charge collection), which in turn reduces the photopeak resolution. The incomplete charge collection has already been quantitatively measured to have a negligible affect on the energy resolution performance of the detector in use as discussed in Section 4.3.1.

The creation of the 2D risetime response for different γ-ray energies will, therefore, aid allocate the risetime ranges of t30 and t90 of interest for each γ-ray energy, this will be the subject of discussion in the following section.

2D Risetime Filters (or Gates)

In order to define a 2D risetime region of interest for each full-energy photopeak (shown in Fig. 6.14), a polygonal-shaped gate in two dimensions was set on each gated t90 versus t30 risetime map shown in Fig. 6.17. Each polygonal-shaped gate consists of a set of preferentially selected (x, y) coordinate pairs, which represents t30 (x) and t90 (y). A coordinate pair $(t30, t90)$ being processed will pass the polygonal gate if the point it defines falls within the polygonal shape defined by the gate. Alternatively expressed, if a $(t30, t90)$ pair matches the polygonal gate condition it will then pass the defined gate. The application of these coordinate pairs on the risetime maps is a function that is enabled by the MTSort software and the selection of these pairs can be performed manually.

As already mentioned in the previous section, each gated t90 versus t30 risetime distribution is produced from events of a full-energy photopeak included into a pre-defined range (LLD − ULD), which also contain events from Compton background. The polygonal gates, which are shaped using these 2D risetime distributions, will allow to preferentially exclude events, which are expected to add to the Compton continuum (this term is explained in Section 2.3.7) on which the photopeaks are superimposed. Therefore, these risetime filters and those created in advance (Section 6.5.3 and Section 6.7.1), which are essentially the main parametric PSA algorithm in this work, can be effective digital filters, hence they are implemented in the MTSort program for filtering pulse shapes in order to further enhance the signal-to-noise ratio.

On applying the selection on a risetime map, care was taken to avoid any potential removal of events that are most likely to correspond to full-energy absorption of the

gamma rays for the related risetime map, which can otherwise significantly degrade the counting efficiency (or intensity) of the full-energy photopeak. Events that are mostly excluded out of a polygonal-shaped gate are those that are expected to be Compton scattering events, from other higher energy γ-rays emitted from the radioactive nuclides being measured and from natural background such as ^{40}K, in which the scattered photon escaped from the detector before full energy deposition.

For the risetime map produced for the full-energy photopeak of 60 keV (Fig. 6.17A), a polygonal array was created consisting of 13 coordinate pairs of $(t30, t90)$, which were set manually on this risetime map. In such that, the selected $(t30, t90)$ pairs are surrounding an intensified region of t30 (50 to 283) ns across a range of t90 (149 to 380) ns. This region contains a large fraction of the events, which are expected to be corresponding to the full energy absorption of the 60 keV gamma rays. Similarly, for the polygonal arrays created for the risetime maps of the 88 keV and 122 keV gamma-ray energies (Fig. 6.17C, E), each array contains 8 coordinate pairs of $(t30, t90)$ surrounding a concentrated region of t30 (100 to 258) ns across a range of t90 (197 to 358) ns and t30 (121 to 255) ns across a range of t90 (218 to 353) ns respectively.

For the risetime map of the 662 keV full-energy photopeak (Fig. 6.17B), a polygonal array made of 10 coordinate pairs of $(t30, t90)$ covering the risetime ranges of interest of t30 (76 to 252) ns and t90 (166 to 474) ns, was created. Whereas, the risetime map of the 1173 keV full-energy photopeak (Fig. 6.17D), was gated within the risetime ranges of t30 (60 to 234) ns and t90 (162 to 444) ns, using 9 coordinate pairs of $(t30, t90)$, and that for the 1332 keV photopeak (Fig. 6.17F) was gated within the risetime ranges of interest of t30 (80 to 238) ns and t90 (178 to 438) ns, using 11 coordinate pairs of $(t30, t90)$.

It can be noted that, the polygonal gates created for the risetime maps of the 60 keV, 88 keV and 122 keV full-energy photopeaks are shaped over a narrower risetime ranges of t30 and t90 compared to those created for the risetime maps of the 662 keV, 1173 keV and 1333 keV gamma-ray energies. Therefore, it is suggested that more Compton scattering events are expected to be suppressed by these gates. On the other hand, full energy events are expected to be considerably affected resulting in a reduction in photopeak intensities.

A 2D risetime filter for the ungated t90 versus t30 map, shown in Fig. 6.16, was also created by gating the map within the risetime ranges of t30 (5 to 288) ns and t90 (41 to 1105) ns, using 23 coordinate pairs of $(t30, t90)$. This was needed to allow a quantitative comparison to be made with the other risetime filters discussed above.

For viewing the setting of the polygonal-shaped gates on the ungated (and gated) t90 versus t30 distribution(s) for the full-energy photopeaks of the different γ-ray energies emitted by the NPRL 604 source, the reader is referred to Appendix F (Fig. F.3 and Fig. F.2 respectively).

To help refer to these filters throughout the text, the six risetime filters produced are given the following designations:

g(t30, t90)$_{60\,\mathrm{keV}}$:
Shaped using the 2D rise time map for the full-energy γ-ray peak of 60 keV, shown in Fig. 6.17A.
g(t30, t90)$_{88\,\mathrm{keV}}$:
Shaped using the 2D rise time map for the full-energy γ-ray peak of 88 keV, shown in Fig. 6.17B.
g(t30, t90)$_{122\,\mathrm{keV}}$:
Shaped using the 2D rise time map for the full-energy γ-ray peak of 122 keV, shown in Fig. 6.17C.
g(t30, t90)$_{662\,\mathrm{keV}}$:
Shaped using the 2D rise time map for the full-energy γ-ray peak of 662 keV, shown in Fig. 6.17D.
g(t30, t90)$_{1173\,\mathrm{keV}}$:
Shaped using the 2D rise time map for the full-energy γ-ray peak of 1173 keV, shown in Fig. 6.17E.
g(t30, t90)$_{1333\,\mathrm{keV}}$:
Shaped using the 2D rise time map for the full-energy γ-ray peak of 1333 keV, shown in Fig. 6.17F.
g(t30, t90)$_{\mathrm{All\ Energies}}$:
Shaped using the 2D rise time map for all partially and fully deposited γ-ray photons, from different γ-ray interaction positions across the detector, shown in Fig. 6.16.

There is an analogy between setting threshold values LLD and ULD on a full-energy peak, and setting (x, y) coordinate pairs on a gated t90 versus t30 risetime distribution related to that peak. Both are preferentially selected (manually) by the user in order to define an energy (first case) and risetime (second case) region of interest.

In contrast, for the first case, a risetime map is created from events included into the LLD − ULD range of the full-energy peak, which is conventionally known as gating on energy region of interest to acquire a risetime distribution. However, in the second case, the polygonal-shaped gate is used to filter out the raw pulse shapes from which an energy spectrum will be generated. In this work, this technique can be referred to as gating on risetime region of interest to obtain an energy spectrum. The output energy spectra created by these shaped 2D risetime gates following their application to the calibration data set of pulse shapes will be discussed in the following section.

Application of Risetime Filters

After the 2D risetime filters have been shaped, they were defined in the sortfile through which to filter the event-by-event data. The risetime filters were individually applied to the data set in order to reconstruct, using the baseline difference energy calculation

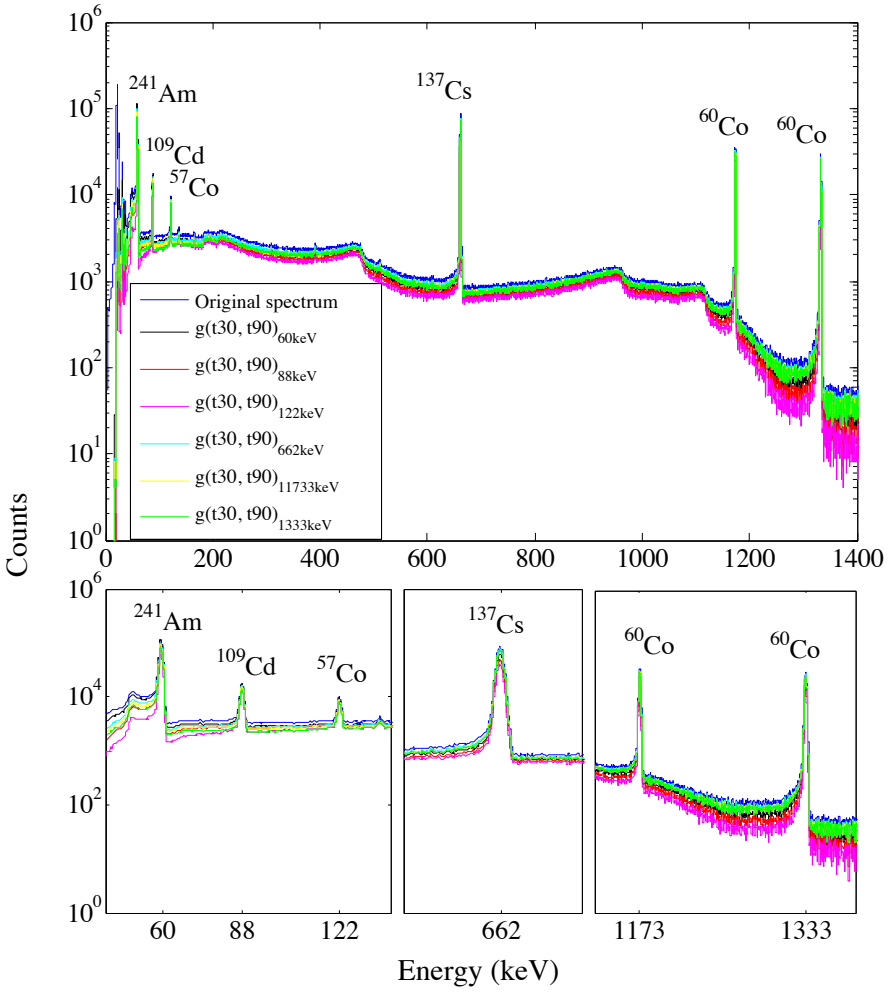

Figure 6.21: The BLD energy distributions generated before (Original spectrum) and after the application of the single risetime filters, g(t30, t90)$_{60\,\mathrm{keV}}$, g(t30, t90)$_{88\,\mathrm{keV}}$, g(t30, t90)$_{122\,\mathrm{keV}}$, g(t30, t90)$_{662\,\mathrm{keV}}$, g(t30, t90)$_{1173\,\mathrm{keV}}$ and g(t30, t90)$_{1333\,\mathrm{keV}}$ to the NPRL 604 data set of pulse shapes. The upper panel shows a view of the whole energy range and the lower panels represent the low (left panel) and high (middle and right panels) energy regions . It can be clearly identified that, the fraction of counts remaining after the application of each risetime filter is shown to be lower compared to the original spectrum.

method[8], an energy spectrum from each risetime filter, Fig. 6.21. Through the event processing, an energy spectrum is being accumulated if only a $(t30, t90)$ value being processed matches the risetime filter definition. Each subsequent energy spectrum generated will be related to its associated risetime filter by which the total events of the energy spectrum were passed. In order to measure the efficacy of these risetime filters, the BLD post-filtered (or t30t90-gated) energy spectra were quantitatively analysed, this will be presented in the following section.

[8]The baseline difference energy determination method is used mostly in the analysis as it does not mask the detector performance.

6.5.3 Data Analysis

The photopeaks in the produced BLD t30t90-gated energy spectra that were considered for spectroscopic analysis are: 59.5 keV (^{241}Am), 88 keV (^{109}Cd), 122 keV (^{57}Co), 661.7 keV (^{137}Cs), 1173.2 keV and 1332.5 keV (^{60}Co). The low activities, 165.9 keV (^{139}Ce), 391.7 keV (^{113}Sn) and 898 keV (^{88}Y), were not evaluated here due to the relatively large uncertainty because of the low statistics of their net photopeak areas. The photopeaks considered were then fitted using the GF3 peak-fitting program [GF316], allowing the photopeak to be evaluated through measuring a number of performance-testing indices such as the peak-to-Compton ratio, the energy resolution and the absolute efficiency. Additionally, the uncertainty associated to each calculated index can be quantified. As already mentioned in Section 1.1.3 that, the P/C factor is a measure of the combined effect of detector energy resolution and full-energy photopeak efficiency at the same time, therefore the ratio calculation is considered to be the best measure of the spectrum quality. Results of the quantitative performance metrics for these t30t90-gated energy spectra are discussed in Section 6.6.

Combined 2D Risetime Filters

It has been found, as it will be shown in "Results" section, that the energy spectrum that exhibited the highest P/C ratios is that reconstructed using the risetime filter g(t30,t90)$_{122\,\mathrm{keV}}$. On the other hand, the efficiency values for this energy spectrum are shown to be the lowest amongst the other post-filtered energy spectra, which means that the full-energy absorption events have been affected. As a result of that, a trade-off between the maximisation of P/C ratio and increasing efficiency values could not be made using these single risetime filters. Consequently, it was essential to find out other optimal case scenarios where a better compromise can be attained. In order to accomplish this task, the performance of two and more risetime filters was combined in MTSort (as it will be explained below) in an attempt to improve the efficiency values with maintaining high P/C ratios. The combined risetime filters created are:

g(t30, t90)$_{122\,\mathrm{keV},\ 1333\,\mathrm{keV}}$: A combination of g(t30, t90)$_{122\,\mathrm{keV}}$ and g(t30, t90)$_{1333\,\mathrm{keV}}$.
g(t30, t90)$_{662\,\mathrm{keV},\ 1333\,\mathrm{keV}}$: A combination of g(t30, t90)$_{662\,\mathrm{keV}}$ and g(t30, t90)$_{1333\,\mathrm{keV}}$.
g(t30, t90)$_{122\,\mathrm{keV},\ 1173\,\mathrm{keV}}$: A combination of g(t30, t90)$_{122\,\mathrm{keV}}$ and g(t30, t90)$_{1173\,\mathrm{keV}}$.
g(t30, t90)$_{122\,\mathrm{keV},\ 662\,\mathrm{keV},\ 1173\,\mathrm{keV}}$: A combination of g(t30, t90)$_{122\,\mathrm{keV}}$, g(t30, t90)$_{622\,\mathrm{keV}}$ and g(t30, t90)$_{1173\,\mathrm{keV}}$.

In MTSort, the risetime gates for each combination were re-applied on the data set at the same time in order to filter out two sets of pulses from which an energy spectrum could be reconstructed. It must be emphasised here that; because gates are partially overlapped so care was taken when combining these gates in the sortfile. In such that, if the combined gates were matched by a (t30, t90) value being processed, the latest

defined gate in the sortfile would be the one this value has passed and subsequently one event would be counted and accumulated in the total reconstructed energy spectrum.

It can be noted that as the number of the combined risetime gates increases the total counts of the accepted pulses passed these filters rises, hence, the counting efficiency for each peak rises. However, pulses from Compton background (noise) are more likely to pass, which in turn, decreasing the P/C ratio. Therefore, a tradeoff similar to that made when shaping the trapezoid digital filter in real time (in the experimental stage), exists here too in order to maximise the photopeak efficiency without affecting the P/C ratio. This tradeoff was well handled by combining the output of two risetime filters as it would be expected later.

Examples of the BLD energy distributions generated before and after the application of the single risetime filters, g(t30, t90)$_{122\,\mathrm{keV}}$ and g(t30, t90)$_{1333\,\mathrm{keV}}$, and the combined risetime filter g(t30, t90)$_{122\,\mathrm{keV},\,1333\,\mathrm{keV}}$ to the NPRL 604 data set of pulse shapes are presented in Fig. 6.22.

6.6 Results Stage I

6.6.1 Peak-to-Compton (P/C) Ratio

The peak-to-Compton ratio has been measured from the t30t90-gated energy spectra produced following the application of risetime filters and from the original energy spectrum generated from the NPRL 604 raw data set. The ratio was calculated using Equation 6.1,

$$P/C = \frac{N_{\text{max. ch.}}}{\overline{N}_{\text{Compton}}} \ , \tag{6.1}$$

where $N_{\text{max. ch.}}$ is counts in the maximum channel of the evaluated photopeak, $\overline{N}_{\text{Compton}}$ is mean counts/channel in the Compton region linked to that peak.

According to the Klein-Nishina formula, Equation 2.4, the main source of Compton background arises from high gamma-ray energies (e.g. 1332 keV from ^{60}Co) from the calibration source, (e.g. 1460 keV from ^{40}K) from the natural background because they are highly likely to interact through a single energy deposition, where the scattering angle is $< 90^0$ (forward scattering). This effect can be seen in Fig. 2.2, p. 10. Therefore, Compton region that used to be linked to all measured photopeaks is in a 6.8 keV-wide region between 38.8 keV and 45.5 keV, which is just below the Ge-escape peak of 60 keV gamma-ray energy.

The uncertainty on the calculated P/C ratio arises from the statistical uncertainty on the estimate of the counts of full energy deposits in the photopeak max channel and that of the Compton events in the specified Compton region. In the GF3 program, the standard deviation on each estimate is taken as the square root of the number of counts.

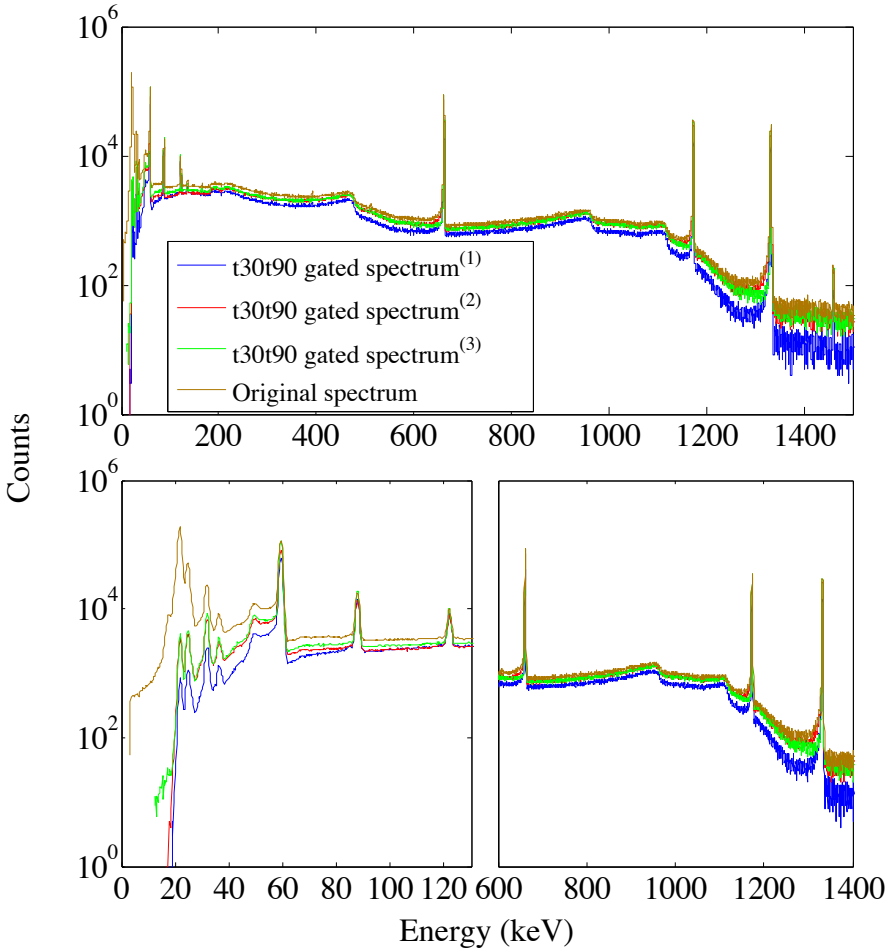

Figure 6.22: Examples of the BLD energy distributions generated before (Original spectrum) and after the application of the single risetime filters, g(t30, t90)$_{122\,\mathrm{keV}}$ (t30t90 gated spectrum$^{(1)}$) and g(t30, t90)$_{1333\,\mathrm{keV}}$ (t30t90 gated spectrum$^{(2)}$), and the combined risetime filter, g(t30, t90)$_{122\,\mathrm{keV},\ 1333\,\mathrm{keV}}$ (t30t90 gated spectrum$^{(3)}$), to the NPRL 604 data set of pulse shapes. The upper panel shows a view of the whole energy range and the lower panels represent the low (left panel) and high (right panel) energy regions . It can be clearly identified that, the fraction of counts remaining after the application of the combined risetime filter is shown to be higher compared to those acquired using the the single risetime filters.

The combined uncertainty on the ratio was then evaluated using the following formula,

$$\Delta P/C = P/C\sqrt{\left(\frac{\Delta N_{\text{max. ch.}}}{N_{\text{max. ch.}}}\right)^2 + \left(\frac{\Delta \overline{N}_{\text{Compton}}}{\overline{N}_{\text{Compton}}}\right)^2}\,, \tag{6.2}$$

where $\Delta N_{\text{max. ch.}}$ is the standard deviation on the estimate of the counts of full energy deposits in the photopeak max channel as defined by the GF3 program. $\Delta \overline{N}_{\text{Compton}}$ is the combined uncertainty on the mean counts per channel in the specified Compton region, which is in turn evaluated as:

$$\Delta\overline{N}_{\text{Compton}} = \frac{\Delta N_{\text{Compton}}}{\text{Channel number of Compton region}} \,, \tag{6.3}$$

where $\Delta N_{\text{Compton}}$ is the standard deviation on the estimate of the Compton events within the Compton region as defined by the GF3 program.

The P/C ratio is conventionally quoted for the 1332 keV gamma ray from ^{60}Co, which is a standard γ-ray photopeak in gamma spectroscopy analysis and it has been used to decide which is the post-filtered energy spectrum of the best quality. However, all photopeaks at lower energies were analysed and considered for the comparisons to examine the P/C ratio response across the entire energy range, hence to quantify the efficacy of the risetime filters, by which the filtered energy spectra were produced, in a wide energy range.

For comparison, the percentage of the P/C ratios for the original energy spectrum were normalised to those for each post-filtered energy spectrum constructed from events that passed each polygonal-shaped gate, according to Equation 6.4, and plotted as a function of energy in Fig. 6.23.

$$(P/C)_{Norm.}(\%) = \frac{(P/C)_{\text{original}} \times 100}{(P/C)_{\text{t30t90-gated}}} \tag{6.4}$$

The combined uncertainty on the normalised ratio was then evaluated in a similar way as Equation 6.2 by the next formula,

$$\Delta(P/C)_{Norm.} = (P/C)_{Norm.} \sqrt{\left(\frac{\Delta(P/C)_{\text{original}}}{(P/C)_{\text{original}}}\right)^2 + \left(\frac{\Delta(P/C)_{\text{t30t90-gated}}}{(P/C)_{\text{t30t90-gated}}}\right)^2} \,, \tag{6.5}$$

where $\Delta(P/C)_{\text{original}}$ and $\Delta(P/C)_{\text{t30t90-gated}}$ are the uncertainties on the P/C ratio, calculated by Equation 6.2, for the original and post-filtered energy spectrum respectively.

The relative uncertainty of $(P/C)_{Norm.}$ is then determined as following,

$$\text{Relative Uncertainty } (1\sigma\ \%) = \frac{\Delta(P/C)_{Norm.} \times 100}{(P/C)_{Norm.}} \tag{6.6}$$

It can be seen from Fig. 6.23 that, the normalised ratios calculated are shown to improve for most of the post-filtered energy spectra using the different gates. In the figure, the improved P/C ratios exhibit values less than 100% which is the normalised value of the P/C ratios for the unfiltered energy spectrum. The P/C response has shown no improvement after the application of g(t30, t90)$_{122\,\text{keV},\ 662\,\text{keV},\ 1173\,\text{keV}}$ for the whole energy range, since the P/C values are almost equal ($\sim$ 100%) to those obtained from the original energy spectrum before the gate application. Whereas, the P/C ratios for the post-filtered energy spectra produced using g(t30, t90)$_{60\,\text{keV}}$ have degraded at the 662 keV, 1173 keV and 1333 keV γ-ray energies compared to the original spectrum. The P/C ratios obtained at these energies have values in the range 101% to 105%. This means

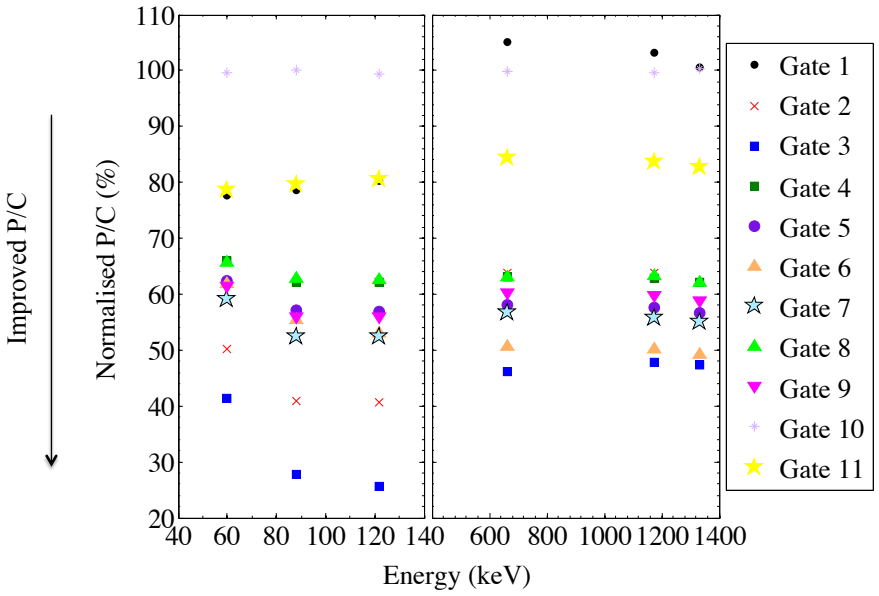

Figure 6.23: The percentage of the peak-to-Compton (P/C) ratios for the unfiltered (or original) energy spectrum normalised to those for each post-filtered energy spectrum constructed from events passed each shaped risetime filter (or polygonal-shaped gate), as a function of energy. The uncertainties are not drawn because their values are << 0.01%, so they are considered to be negligible. The different shaped risetime filters by which the post-filtered energy spectra were reconstructed are: Gate 1 = g(t30, t90)$_{60\,\mathrm{keV}}$, Gate 2 = g(t30, t90)$_{88\,\mathrm{keV}}$, Gate 3 = g(t30, t90)$_{122\,\mathrm{keV}}$, Gate 4 = g(t30, t90)$_{662\,\mathrm{keV}}$, Gate 5 = g(t30, t90)$_{1173\,\mathrm{keV}}$, Gate 6 = g(t30, t90)$_{1333\,\mathrm{keV}}$, Gate 7 = g(t30, t90)$_{122\,\mathrm{keV},\ 1333\,\mathrm{keV}}$, Gate 8 = g(t30, t90)$_{662\,\mathrm{keV},\ 1333\,\mathrm{keV}}$, Gate 9 = g(t30, t90)$_{122\,\mathrm{keV},\ 1173\,\mathrm{keV}}$, Gate 10 = g(t30, t90)$_{122\,\mathrm{keV},\ 662\,\mathrm{keV},\ 1173\,\mathrm{keV}}$, Gate 11 = g(t30, t90)$_{\mathrm{All\ Energies}}$. For more interpretation of the reference to each gate in this figure, the reader is referred to the last subsection in Section 6.5.2 and Section 6.5.3.

that, these risetime filters have not successfully excluded out the signals generated for Compton scattering interactions occurred close to the detector outer surfaces, in which the scattered photon escaped from the detector before full energy deposition. Therefore, these two gates have exhibited the worst P/C performance.

The best energy spectrum that gave the highest P/C ratios is that reconstructed using the risetime filter g(t30, t90)$_{122\,\mathrm{keV}}$ especially at low energy region. The raw values of P/C, obtained using this gate, at 60 keV, 88 keV and 122 keV were calculated to be 51, 12 and 7 respectively which are 59%, 72% and 74% higher than the corresponding ratios for the original energy spectrum. At high-energy region, the raw P/C ratios at 662 keV, 1173 keV and 1333 keV were shown to be 34, 13 and 12, which are 54%, 52% and 53% higher than the corresponding ratios for the original energy spectrum. This can be interpreted that, the risetime filter has rejected a large fraction of events corresponding to Compton background events.

Similar improvement has been achieved using the gate g(t30, t90)$_{1333\,\mathrm{keV}}$ at high energy region. The raw values of P/C were calculated to be 31 for ^{137}Cs and 13, 11 for the first and second peak of ^{60}Co respectively. They are 49%, 50% and 51% higher

than the corresponding ratios for the original energy spectrum. At low energy region, the P/C response has improved, however not as much as that obtained using g(t30, t90)$_{122\,\mathrm{keV}}$. The ratio values at 60 keV, 88 keV and 122 keV were shown to be 34, 6 and 3 respectively which are 38%, 44% and 47% higher than the corresponding ratios for the original energy spectrum. It is suggested that, as the polygonal gate of this filter was shaped over a wider risetime ranges of t30 and t90 compared to the risetime filter g(t30, t90)$_{122\,\mathrm{keV}}$ (see the subsection titled "2D Risetime Filters (or Gates)"), this means that more Compton scattering events are highly likely to pass the filter leading to a reduction in the P/C ratios especially for the low energy photopeaks.

It can be concluded that, as the gate g(t30, t90)$_{122\,\mathrm{keV}}$ has provided the highest improvement in the P/C response at the low energy region, this gate, therefore, can be an effective risetime filter for supressing Compton background events especially when analysing complex gamma spectra such as environmental spectra. Such spectra, most gamma ray lines of interest are located near each other above a high level of background especially at low energy regions of gamma spectra.

6.6.2 Detector Efficiency Response

The impact of performing risetime filtering on the photopeak efficiency has also been assessed. This will provide a better appreciation of the efficacy of the shaped risetime filters. By doing this, the number of counts in the maximum channel of photopeaks determined by GF3 was recorded before and after processing the data set of pulse shapes with risetime filters. Subsequently, the ratio of the photopeak intensity for the post-processed energy spectrum to that of the corresponding photopeak for the energy spectrum associated with the raw data could be calculated and quantitatively compared for the various risetime filters. The percentage ratio is expressed as:

$$\varepsilon\ (\%) = \frac{(N_{\text{max. ch.}})_{\text{t30t90-gated}} \times 100}{(N_{\text{max. ch.}})_{\text{original}}}\ , \tag{6.7}$$

where $(N_{\text{max. ch.}})_{\text{t30t90-gated}}$ count in maximum channel of photopeak in the filtered spectrum, $(N_{\text{max. ch.}})_{\text{original}}$ count in maximum channel of related photopeak in the original spectrum.

The uncertainty on the percentage ratio was then combined in a similar fashion to Equation 6.5 by the next formula,

$$\Delta\varepsilon = \varepsilon\sqrt{\left(\frac{\Delta(N_{\text{max. ch.}})_{\text{t30t90-gated}}}{(N_{\text{max. ch.}})_{\text{t30t90-gated}}}\right)^2 + \left(\frac{\Delta(N_{\text{max. ch.}})_{\text{original}}}{(N_{\text{max. ch.}})_{\text{original}}}\right)^2}\ , \tag{6.8}$$

where $\Delta(N_{\text{max. ch.}})_{\text{t30t90-gated}}$ and $\Delta(N_{\text{max. ch.}})_{\text{original}}$ are the standard deviation on the estimate of the counts of full energy deposits in the photopeak max channel, as determined by the GF3 program, for the post-filtered and original energy spectrum respectively.

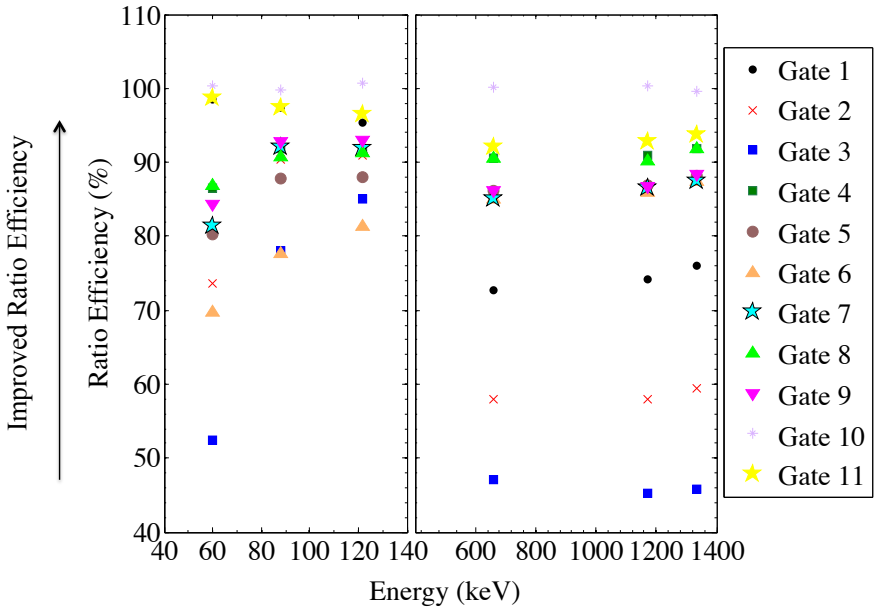

Figure 6.24: The percentage of the ratio efficiency (counts in the highest channel in the full-energy photopeak in each post-filtered energy spectrum divided by those in the corresponding photopeak in the unfiltered (or original) energy spectrum) as a function of energy. The uncertainties are not drawn because their values are $<<$ 0.01%, so they are considered to be negligible. The different shaped risetime filters by which the post-filtered energy spectra were reconstructed are: Gate 1 = g(t30, t90)$_{60\,\mathrm{keV}}$, Gate 2 = g(t30, t90)$_{88\,\mathrm{keV}}$, Gate 3 = g(t30, t90)$_{122\,\mathrm{keV}}$, Gate 4 = g(t30, t90)$_{662\,\mathrm{keV}}$, Gate 5 = g(t30, t90)$_{1173\,\mathrm{keV}}$, Gate 6 = g(t30, t90)$_{1333\,\mathrm{keV}}$, Gate 7 = g(t30, t90)$_{122\,\mathrm{keV},\ 1333\,\mathrm{keV}}$, Gate 8 = g(t30, t90)$_{662\,\mathrm{keV},\ 1333\,\mathrm{keV}}$, Gate 9 = g(t30, t90)$_{122\,\mathrm{keV},\ 1173\,\mathrm{keV}}$, Gate 10 = g(t30, t90)$_{122\,\mathrm{keV},\ 662\,\mathrm{keV},\ 1173\,\mathrm{keV}}$, Gate 11 = g(t30, t90)$_{\mathrm{All\ Energies}}$. For more interpretation of the reference to each gate in this figure, the reader is referred to the last subsection in Section 6.5.2 and Section 6.5.3.

The relative uncertainty of ε is then calculated as following,

$$\text{Relative Uncertainty } (1\sigma\ \%) = \frac{\Delta\varepsilon \times 100}{\varepsilon} \tag{6.9}$$

The graph presented in Fig. 6.24 displays, for comparison, the percentage of the ratio of the photopeak intensity for the post-processed energy spectrum to that of the corresponding photopeak in the original energy spectrum, as a function of energy.

The ratio represents the fraction of events remaining in each photopeak following the application of risetime gates. It can be seen from the figure that, there is a reduction in the photopeaks intensity for all t30t90-gated energy spectra using the different gates, except for that filtered using g(t30, t90)$_{122\,\mathrm{keV},\ 662\,\mathrm{keV},\ 1173\,\mathrm{keV}}$. The γ-ray spectrum generated by this gate has photopeak efficiency values equal to those for the unfiltered energy spectrum. This means that, events that are corresponding to full-energy deposition have survived following filtering with that gate. However, this spectrum has not shown any improvement in the P/C response, since the normalised P/C ratios of

photopeaks have values of $\sim$ 100% as shown in Fig. 6.23. This has been discussed in Section 6.6.1.

Crucially, the photopeak intensity is dramatically reduced after the application of g(t30, t90)$_{122\,\mathrm{keV}}$. This can be seen evidently in the high-energy region, where the fractions of events remaining in the highest channel of 662 keV, 1173 keV and 1333 keV photopeaks following processing with the gate are 47%, 45% and 46% respectively. This means that a large fraction of events corresponding to full-energy depositions has been rejected by the filter, leading to a dramatic reduction in the intensity of the full-energy photopeaks. This argument can be supported by the fact that, the polygonal gate of this filter is shaped over the narrowest ranges of t30 and t90 compared to all other risetime filters (see the subsection titled "2D Risetime Filters (or Gates)"). On the other hand, as explained in the previous section that, the gate has generated an energy spectrum of the best P/C performance.

Therefore, these two gates have not provided a good tradeoff between the maximisation of the P/C ratio and maintaining high photopeak efficiency. When processing the data set with the risetime filter g(t30, t90)$_{122\,\mathrm{keV},\,1333\,\mathrm{keV}}$, which is a combination of the single risetime filters of the best P/C performance (g(t30, t90)$_{122\,\mathrm{keV}}$ and g(t30, t90)$_{1333\,\mathrm{keV}}$), an optimal tradeoff was achieved. In such that, the degraded photopeaks intensities resulted using these single risetime gates have improved due to the larger number of pulses accepted by the combined risetime filter. However, This improvement has been achieved at the expense of the P/C ratio performance as more pulses generated from Compton scattering escaping the detector, were expected to pass the filter. Hence, obtaining a better compromise between the maximisation of the P/C ratio and the reasonable photopeak intensity.

This combined risetime filter has significantly increased the events corresponding to the full-energy depositions left in the maximum channel of all photopeaks following filtering with g(t30, t90)$_{122\,\mathrm{keV}}$ from, for example, 52% to 81% at 60 keV and from 46% to 87% at 1333 keV. Furthermore, the gate has improved the peak intensity using g(t30, t90)$_{1333\,\mathrm{keV}}$ from 70% to 81% at 60 keV, from 78% to 92% at 88 keV and from 81% to 92% at 122 keV, while at the high energy region, the photopeak efficiency values have been maintained the same (85%, 86% and 87% at the γ-ray energies 662 keV, 1173 keV and 1333 keV respectively). At the full-energy peaks of 60 keV, 88 keV and 122 keV, the P/C ratios using g(t30, t90)$_{122\,\mathrm{keV},\,1333\,\mathrm{keV}}$ have been found to be 41%, 48% and 48% respectively higher than the corresponding peaks in the original energy spectrum. This improved response in the P/C ratio at low energies is slightly higher than that provided by g(t30, t90)$_{1333\,\mathrm{keV}}$ but lower than that delivered by g(t30, t90)$_{122\,\mathrm{keV}}$. At high-energy region, the resultant P/C ratios have shown to be 43% (at 662 keV), 44% (at 1173 keV) and 45% (at 1333 keV) higher than the corresponding energies in the unfiltered energy spectrum.

6.7 Results Stage II

6.7.1 Extended 2D Risetime Filter

Results Stage I have shown how the optimum spectroscopic performance following the application of the PSA has been reached when filtering the data set of pulse shapes with the combined 2D risetime filter, g(t30, t90)$_{122\,\mathrm{keV},\ 1333\,\mathrm{keV}}$.

In an attempt to further optimise the performance of the P/C and ratio efficiency responses, the polygonal gate limits of the filter g(t30, t90)$_{122\,\mathrm{keV},\ 1333\,\mathrm{keV}}$ have been extended.

It must be remembered that, what has been merged in the sort code when combining risetime filters is the outputs of the single risetime filters forming the combination not the polygonal gates themselves. The post-filtered energy spectrum of any combined risetime filter is obtained from events that pass each single risetime filter in the combination and those events matched by the single gates are counted once. Therefore, generating the post-filtered risetime map of g(t30, t90)$_{122\,\mathrm{keV},\ 1333\,\mathrm{keV}}$ from which the final polygonal gate would be shaped was required, as the map represents the combined output of g(t30, t90)$_{122\,\mathrm{keV}}$ and g(t30, t90)$_{1333\,\mathrm{keV}}$. By shaping the new gate, a set of (x, y) coordinate pairs was preferentially selected, in that all original limits of the post-filtered risetime map falls within the new gate. Subsequently, the original polygonal gate could be extended while maintaining its shape. The resultant gate is referenced in this work as "*Extended 2D Risetime Filter*".

The new polygonal gate limits were then defined in the sortfile to perform event-by-event risetime filtering on the NPRL 604 data set and a t30t90-gated energy spectrum was reconstructed, using the MWD based energy determination method, from those events matched the definition of the new gate.

In order to assess the efficacy of the extended risetime filter, first of all, P/C ratios of photopeaks were calculated for the MWD original energy spectrum, using Equation 6.1 and then normalised, for comparison, to those determined for the post-filtered energy spectrum according to Equation 6.4. Second, the percentage ratio efficiency values were determined using Equation 6.7.

To allow the comparison between g(t30, t90)$_{122\,\mathrm{keV},\ 1333\,\mathrm{keV}}$ and the extended gate, the MWD method was also used to reconstruct the t30t90-gated energy spectrum produced by g(t30, t90)$_{122\,\mathrm{keV},\ 1333\,\mathrm{keV}}$. A similar spectroscopic analysis for the MWD energy spectrum was then performed. The results obtained for the percentages of P/C ratios and ratio efficiencies, with their respective relative uncertainty calculated by Equation 6.6 and Equation 6.9, for both gates are summarised in Table 6.2. The final MWD energy spectra obtained before (i.e. the original or unfiltered energy spectrum) and after the individual application of g(t30, t90)$_{122\,\mathrm{keV},\ 1333\,\mathrm{keV}}$ and the extended risetime gate are shown in Fig. 6.25.

It can be noted from the table that, the extended gate has shown an improvement in the photopeak efficiency performance, compared to g(t30, t90)$_{122\,\mathrm{keV},\ 1333\,\mathrm{keV}}$, however

Nuclide	Energy (keV)	Risetime Filter I		Risetime Filter II	
		P/C(1σ) %	$\varepsilon(1\sigma)$ %	P/C(1σ) %	$\varepsilon(1\sigma)$ %
^{241}Am	59.5	63(1)	80(1)	72(1)	92(1)
^{109}Cd	88.0	55(1)	91(1)	68(1)	96(1)
^{57}Co	122.1	55(1)	92(1)	69(1)	95(1)
^{137}Cs	661.7	59(1)	84(1)	75(1)	88(1)
^{60}Co	1173.2	59(1)	85(1)	74(1)	89(1)
^{60}Co	1332.5	59(1)	85(1)	75(1)	88(1)

Table 6.2: Summary of the final results of the spectroscopic performance following processing the NPRL 604 data set with g(t30, t90)$_{122\,\mathrm{keV},\ 1333\,\mathrm{keV}}$ (Risetime Filter I) and the extended gate (Risetine Filter II). P/C (%) is the percentage of the peak-to-Compton ratios for the original energy spectrum normalised to those for the post-filtered energy spectrum constructed from events passed g(t30, t90)$_{122\,\mathrm{keV},\ 1333\,\mathrm{keV}}$ and the extended gate, as a function of energy. ε (%) is the percentage of the ratio efficiency (counts in the highest channel in the full-energy photopeak in each post-filtered energy spectrum divided by those in the corresponding photopeak in the unfiltered (or original) energy spectrum) as a function of energy.

at the expense of the relative decrease in the P/C values. This behaviour agrees with the theoretical expectation that Compton background events are more likely to pass as the gate size increases, which can degrade the P/C response, whilst more events that correspond to full-energy depositions will be accepted by the gate.

6.8 Results Stage III

6.8.1 Environmental Data

The main risetime filters, g(t30, t90)$_{122\,\mathrm{keV},\ 1333\,\mathrm{keV}}$ and the extended gate, which are the optimum parametric PSA algorithm, have been reapplied in the MTSort program to perform event-by-event data risetime filtering on the data set of the environmental sample and laboratory room background. The t30t90-gated energy spectra were individually generated, using the MWD based energy calculation method, for those events matched by the definitions of these risetime filters as instructed in the sort file. Furthermore, the unfiltered energy spectra were separately reconstructed for the environmental sample and room background. A comparison of the energy spectra produced before and after the individual application of g(t30, t90)$_{122\,\mathrm{keV},\ 1333\,\mathrm{keV}}$ and the extended gate on the data set of the environmental sample is shown in Fig. 6.26.

Following processing the data sets in the MTSort program, the post-filtered and original energy spectra acquired were individually analysed using the GF3 software, allowing the calculation of the normalised peak-to-Compton ratios and the ratio photopeak efficiencies to be performed.

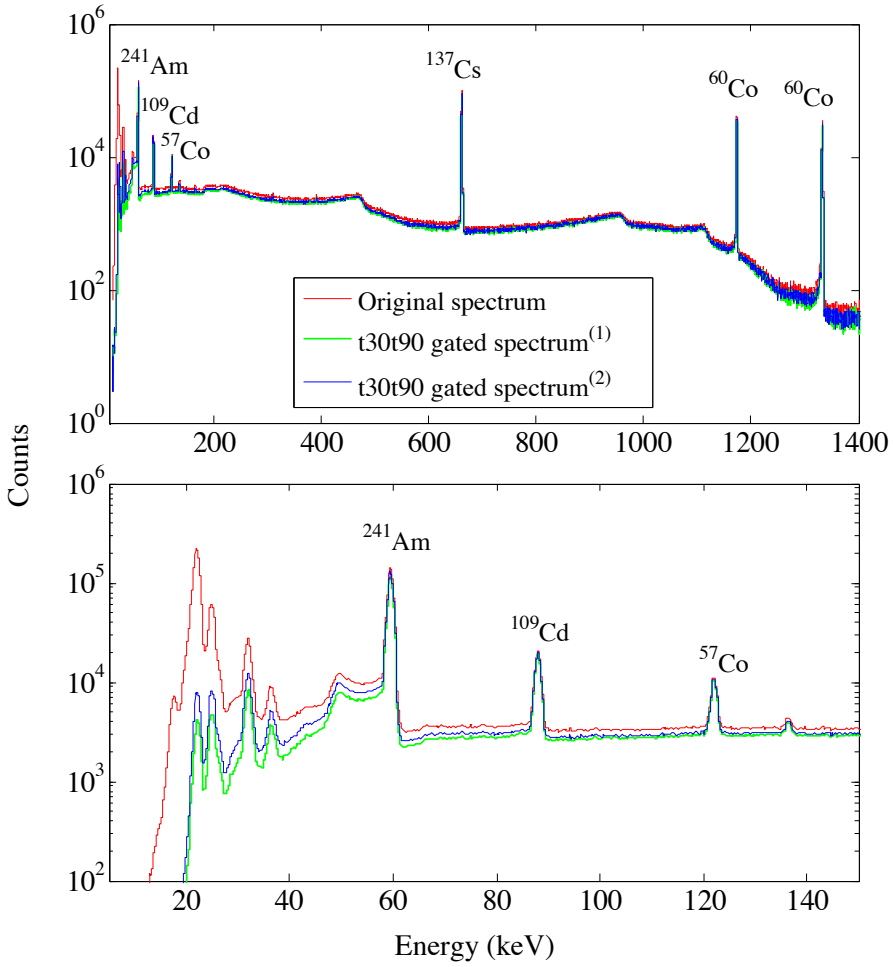

Figure 6.25: The MWD energy spectra generated before (Original spectrum) and after the application of g(t30, t90)$_{122\,\mathrm{keV},\ 1333\,\mathrm{keV}}$ (t30t90 gated spectrum$^{(1)}$) and the extended risetime gate (t30t90 gated spectrum$^{(2)}$) on the NPRL 604 data set. The upper panel shows a view of the whole energy range and the lower panel represents the low energy region, where it can be clearly noted that the fraction of counts remaining after risetime filtering is shown to be higher in t30t90 gated spectrum$^{(2)}$ with a reduction in the P/C ratio response as illustrated in the Table 6.2. This is also hold for the high energy region.

During the calculation process, the events in the max channel of the evaluated photopeak and those in the Compton region[9] were both background subtracted before calculating the ratio. It must be recalled that, as described in Section 6.4.4, there was an unintended difference between the acquisition live time of the sample measurement (4 days) and that of the background measurement (2.8 days), which was scaled out during the subtraction procedure. In such that, the counts in the max channel of the photopeak and those in the Compton region were converted into count rates for the sample and background spectra before the subtraction.

[9]Compton region that is linked to all evaluated photopeaks was assumed to be the same as the one used for the calibration data, which is in a 6.8 keV-wide region between 38.8 keV and 45.5 keV.

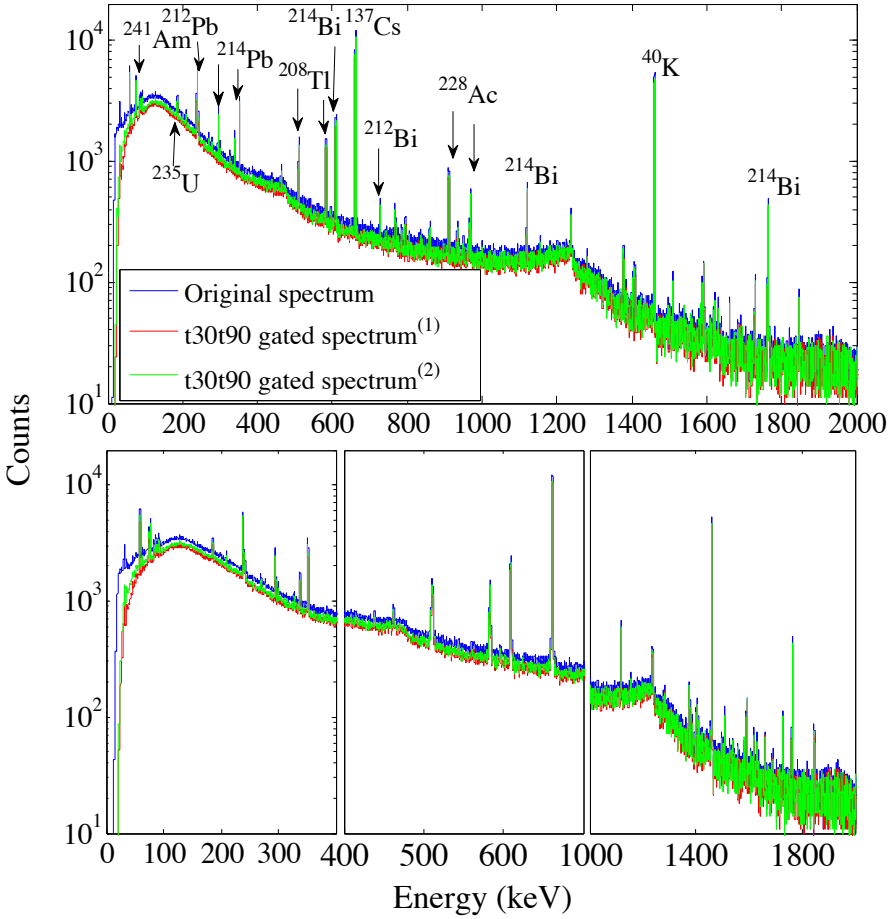

Figure 6.26: The MWD energy spectra generated before (Original spectrum) and after the application of $g(t30,\ t90)_{122\,keV,\ 1333\,keV}$ (t30t90 gated spectrum$^{(1)}$) and the extended risetime gate (t30t90 gated spectrum$^{(2)}$) on the data set of the environmental sample.

By performing background subtraction, the P/C ratios were then calculated for the unfiltered energy spectrum using Equation 6.1 and then normalised to those calculated for each post-filtered energy spectrum. The fraction of events remaining in the max channel of each evaluated photopeak following the application of risetime gates was also calculated using Equation 6.7. The terms in these equations are now corresponding to the background-subtracted count rate relevant to the quantity described by the equations.

In order to extract the relative uncertainty of both measured quantities, the uncertainty on the background subtraction was first combined in Equation 6.2 and Equation 6.8. The terms in these equations are now related to the background-subtracted count rate with its uncertainty, relevant to the quantity described by the equations. The uncertainty of each quantity is calculated separately in a similar fashion to Equation 5.11. The result of Equation 6.2 was executed by Equation 6.5 through Equation 6.6, while the result of Equation 6.8 was substituted in Equation 6.9 in order to estimate the relative uncertainty of the percentage normalised P/C ratios and the percentage ratio efficiencies

Nuclide	Energy (keV)	Risetime Filter I		Risetime Filter II	
		P/C(1σ) %	$\varepsilon(1\sigma)$ %	P/C(1σ) %	$\varepsilon(1\sigma)$ %
^{241}Am	59.25	67(4)	80(3)	78(3)	91(3)
^{226}Ra	185.75	58(9)	92(9)	80(9)	88(9)
^{212}Pb	238.63	58(4)	91(4)	75(4)	93(4)
^{137}Cs	661.50	63(3)	84(1)	80(3)	88(1)
^{40}K	1460.50	62(5)	86(4)	78(5)	91(4)

Table 6.3: Summary of the final results of the spectroscopic performance following processing the sample data set with g(t30, t90)$_{122\,\mathrm{keV},\ 1333\,\mathrm{keV}}$ (Risetime Filter I) and the extended gate (Risetine Filter II). P/C (%) is the percentage of the peak-to-Compton ratios for the original energy spectrum normalised to those for the post-filtered energy spectrum constructed from events passed g(t30, t90)$_{122\,\mathrm{keV},\ 1333\,\mathrm{keV}}$ and the extended gate, as a function of energy. ε (%) is the percentage of the ratio efficiency (counts in the highest channel in the full-energy photopeak in each post-filtered energy spectrum divided by those in the corresponding photopeak in the unfiltered (or original) energy spectrum) as a function of energy.

respectively. Both measured quantities with their relative uncertainty are tabulated in Table 6.3. The photopeaks of interest included in this discussion are those from the monoenergetic gamma-ray radionuclides such as 59.25 keV (from ^{241}Am), 661.50 keV (from ^{137}Cs) and 1460.50 keV (from ^{40}K) as well as other photopeaks such as 185.75 keV (from ^{235}U) and 238.63 keV (from ^{212}Pb), to show in particular the best measured quality of the low-energy photopeaks in the presence of high-energy photopeaks.

It can be noted that, the optimal risetime filters g(t30, t90)$_{122\,\mathrm{keV},\ 1333\,\mathrm{keV}}$ and the extended gate have successfully improved the P/C response. For comparison between the two data sets of the calibration source and the environmental sample, the general behaviour of the two risetime filters to the environmental data set has been compatible with that to the calibration data set, which reflects the stability in performance for these filters to the different data sets.

For instance, the P/C ratios for both data sets show to be superior after processing with the g(t30, t90)$_{122\,\mathrm{keV},\ 1333\,\mathrm{keV}}$ than those obtained using the extended gate. On the other hand, the photopeak intensities are higher after using the extended risetime filter than those using g(t30, t90)$_{122\,\mathrm{keV},\ 1333\,\mathrm{keV}}$. This can be clearly attributed to that, the filter, g(t30, t90)$_{122\,\mathrm{keV},\ 1333\,\mathrm{keV}}$, has removed more Compton background events at the expense of rejecting more full-energy events while the extended gate has maintained higher fraction of photopeak events at the price of passage of more Compton background events. This behaviour is expected to be the same for different data sets acquired from different applications. Having reduced the Compton background events, a reduction in the level of the minimum detectable activity measured by the system can be accomplished. This means that, when P/C ratios are high, the detector counting ability to measure low radioactivities from low-energy gamma emissions in the presence of Compton continuum from higher-energy gamma rays is improved, and subsequently increasing

Nuclide	Energy (keV)	Origin		Risetime Filter I		Risetime Filter II	
		ε_{abs}	1σ (%)	ε_{abs}	1σ (%)	ε_{abs}	1σ (%)
^{241}Am	59.5	4.55×10^{-2}	0.13	3.60×10^{-2}	0.14	4.15×10^{-2}	0.13
^{109}Cd	88.0	5.00×10^{-2}	0.44	4.60×10^{-2}	0.44	4.85×10^{-2}	0.47
^{57}Co	122.1	5.29×10^{-2}	0.79	5.06×10^{-2}	0.77	5.19×10^{-2}	0.88
^{137}Cs	661.7	1.29×10^{-2}	0.13	1.09×10^{-2}	0.14	1.14×10^{-2}	0.14
^{60}Co	1173.2	7.20×10^{-3}	0.18	6.06×10^{-3}	0.20	6.31×10^{-3}	0.20
^{60}Co	1332.5	6.42×10^{-3}	0.19	5.43×10^{-3}	0.21	5.65×10^{-3}	0.20
^{88}Y	1836.1	4.95×10^{-3}	5.8	3.92×10^{-3}	6.36	4.26×10^{-3}	6.1

Table 6.4: Energy versus experimental absolute full-energy photopeak efficiency (in arbitrary units) obtained before (Origin) and after processing the NPRL 604 data set with g(t30, t90)$_{122\,\mathrm{keV},\ 1333\,\mathrm{keV}}$ (Risetime Filter I) and the extended gate (Risetine Filter II), as a function of energy. The 1σ standard deviation is due to the uncertainty on the estimate of the net peak area defined by the GF3 fitting.

the detector sensitivity.

It should also be noted that, despite the low photopeak intensities for the environmental spectrum because of the low activity concentrations of the radionuclides, as determined in Chapter 5 (Table 5.3), the ratio of the efficiencies for ^{241}Am and ^{137}Cs, for example, is kept roughly the same for the two data sets using the two risetime filters. This means that, the fraction of events surviving following the processing of the data sets with these risetime filters is unaffected by the low statistics from the environmental data. In addition, the optimised P/C response determined for the environmental data set is higher than that for the calibration data set in spite of the higher activities of the calibration source. This emphasis that these optimum risetime filters, which are essentially the main parametric PSA algorithm in this work, have successfully provided the best tradeoff that is indeed well suited the low counting rate applications, which is the main motivation behind this work.

6.9 Other Results

6.9.1 Absolute Efficiency

The response of the full-energy photopeak absolute efficiency of the detector was also characterised offline using the detector pulse traces recorded for the NPRL 604 calibration source by the DAQ system shown in Fig. 6.6, p. 86. The absolute efficiency values were calculated for the MWD energy spectra generated before (original spectrum) and after processing the pulse traces with the gate g(t30, t90)$_{122\,\mathrm{keV},\ 1333\,\mathrm{keV}}$ and the extended gate (t30t90-gated spectra). The photopeaks in the generated energy spectra that were considered for analysis are: 59.5 keV (^{241}Am), 88 keV (^{109}Cd), 122 keV (^{57}Co), 661.7 keV (^{137}Cs), 1173.2 keV, 1332.5 keV (^{60}Co) and 1836.1 keV (^{88}Y). As mentioned in Section

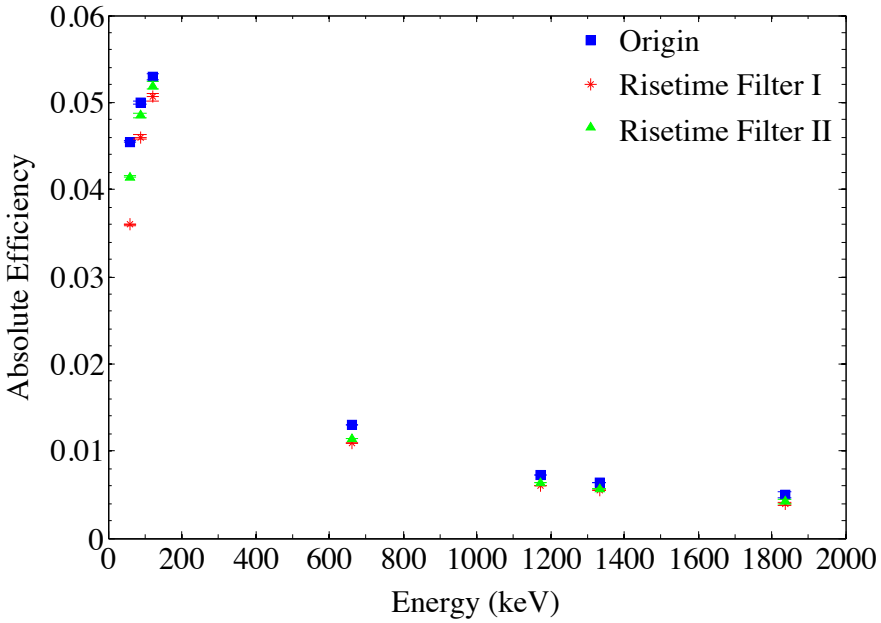

Figure 6.27: The measured absolute full-energy photopeak detection efficiency of the HPGe BE2825 (b12116) detector for the original energy spectrum and t30t90 gated spectra obtained after the implementation of g(t30, t90)$_{122\,\mathrm{keV},\ 1333\,\mathrm{keV}}$ and the extended gate on the NPRL 604 data set, as a function of energy.

6.5.3 that, the energy spectra were fitted using the GF3 peak-fitting program, allowing the photopeak net area to be extracted.

The procedures followed for calculating the absolute efficiency are included in Section 5.4.2 under the subtitle "Efficiency Calibration". The measured relationship between the absolute efficiency and gamma-ray energy obtained for the original and t30t90-gated energy spectra is presented in Table 6.4 and plotted in Fig. 6.27.

It can be seen that, the absolute efficiency response for the original energy spectrum is very consistent with that presented in Table 5.1 and shown in Fig. 5.5, which gives more confidence in the performance of the DAQ system used to acquire the signal traces from which the absolute efficiency response was determined. The absolute efficiencies at 165.9 keV (^{139}Ce), 391.7 keV (^{113}Sn) and 898 keV (^{88}Y) are not evaluated here due to the relatively large uncertainty because of the low statistics of their net photopeak areas.

The efficiency values extracted from the t30t90-gated energy spectra are all lower than those measured for the original spectrum, which is due to the removal of a fraction of events corresponding to full-energy photopeaks. The efficiencies obtained after the application of the extended gate is higher than those obtained after processing the data set with the gate g(t30, t90)$_{122\,\mathrm{keV},\ 1333\,\mathrm{keV}}$. This was the purpose of implementing the extended gate as explained in Section 6.7.1.

Nuclide	Origin		Risetime Filter I		Risetime Filter II	
	A_T (Bq kg^{-1})	1σ	A_T (Bq kg^{-1})	1σ	A_T (Bq kg^{-1})	1σ
^{241}Am	6.44	0.10	6.71	0.12	6.51	0.11
^{137}Cs	41.14	0.18	41.08	0.19	40.86	0.19
^{40}K	218.0	2.7	218.0	2.5	218.0	2.5
^{238}U	3.96	0.10	3.79	0.10	3.80	0.10
^{232}Th	3.48	0.12	2.15	0.10	2.05	0.10
^{226}Ra	0.27	0.10	0.31	0.10	0.32	0.10

Table 6.5: Summary statistics for the activity concentration of ^{241}Am, ^{137}Cs, ^{40}K, ^{232}Th, ^{238}U and ^{226}Ra detected in the selected soil sample (at depth of $25 - 30$ cm) estimated from the generated original and t30t90-gated energy spectra reconstructed before and after processing the sample data set with g(t30, t90)$_{122\,\mathrm{keV},\ 1333\,\mathrm{keV}}$ (Risetime Filter I) and the extended gate (Risetime Filter II) respectively. The 1σ standard deviation is due to the uncertainty on the estimate of the net peak area defined by the GF3 fitting.

6.9.2 Activity Analysis

After the absolute full-energy photopeak detection efficiency of the detector system has been determined for the original and the t30t90-gated spectra, the activity concentrations of radionuclides detected in the environmental sample could be evaluated and quantitatively compared for the three energy spectra.

The statistical analysis procedures followed to determine the activity concentrations are given in Section 5.4.2 under the subtitle "Sample Statistical Analysis". A summary statistics for the activity concentration of ^{241}Am, ^{137}Cs, ^{40}K, ^{238}U, ^{232}Th and ^{226}Ra obtained are given in Table 6.5. The activity concentration of ^{226}Ra has not been evaluated for the work presented in Chapter 5 because the uncertainties are relatively large due to low statistics of the photopeak in most of the soil samples. The way of calculating the activity concentration of ^{226}Ra from the 186.2 keV gamma-ray photopeak will be briefly outlined in the following section.

The determination of ^{226}Ra

The activity concentration of ^{226}Ra, from the ^{238}U decay chain, detected in the measured soil sample was separately evaluated from its direct single photopeak 186.2 keV, taking into consideration the contamination from the direct decay of ^{235}U to ^{231}Th at 185.7 keV. Therefore, the total activity, A_T, in 186.2 keV gamma ray is the sum of,

$$A_T[186.2keV] = A_{^{226}Ra} + A_{^{235}U} \tag{6.10}$$

To employ the ^{235}U correction, the following procedure was followed,

Assuming natural uranium abundances and radioactive equilibrium between the ^{238}U parent and the decay of ^{226}Ra. The ratio activity of ^{235}U to that of ^{226}Ra can be

estimated by employing the following equation that takes into account the branching ratios through which ^{235}U and ^{226}Ra are contributing to the peak intensity,

$$\frac{A_{^{235}U}}{A_{^{226}Ra}} = \frac{(B)_{^{235}U}(T_{1/2})_{^{238}U}(P_\gamma)_{^{235}U}}{(B)_{^{238}U}(T_{1/2})_{^{235}U}(P_\gamma)_{^{226}Ra}} \ , \tag{6.11}$$

where $(B)_{^{235}U}$, $(B)_{^{238}U}$ are the natural abundances of ^{235}U (0.72%) and ^{238}U (99.27%) respectively, $(T_{1/2})_{^{235}U}$, $(T_{1/2})_{^{238}U}$ are half-lives of ^{235}U (7×10^8 years) and ^{238}U (4.47×10^9 years) respectively, and $(P_\gamma)_{^{235}U}$, $(P_\gamma)_{^{226}Ra}$ are the branching ratios of ^{235}U (57%) and ^{226}Ra (3.6%) respectively.

So the ratio $\frac{A_{^{235}U}}{A_{^{226}Ra}}$ can be calculated as:

$$\frac{A_{^{235}U}}{A_{^{226}Ra}} = \frac{0.72 \times 4.47 \times 57}{99.27 \times 0.7 \times 3.6} = 0.73 \tag{6.12}$$

From Equation 6.10 and Equation 6.12, we obtain,

$$A_{^{226}Ra} = A_T/1.73 = 0.578 A_T \tag{6.13}$$

Consequently, the contribution of ^{226}Ra to the peak activity at the energy 186.2 keV is 57.8%.

The results recorded in Table 6.5 agree with theoretical expectations that the estimate of the activity concentrations of the evaluated radionuclides before and after the application of PSA is consistent (within 1σ).

These results, in comparison with those presented in Table 5.3, are found to be comparable within 1σ. A reference point can be drawn into conclusion that, these results confirm that the activity concentration values of radionuclides detected in the soil samples can be used as reference values for the sampling site, as both measurements were acquired using two different digital electronic systems.

Chapter 7

Conclusion and Future Work

In this work, the performance of BEGe detectors for gamma-ray spectroscopy has been improved through optimising their peak-to-Compton response. This has been achieved by the successful application of pulse shape analysis to the digital data collected using a full digital acquisition system. A brief Summary of the prominent findings in this thesis is highlighted as follows:

From Chapter 4, a complete characterisation of the spectroscopic performance of the BEGe detector under study has been determined. In this study experimental measurements of the energy resolution, absolute efficiency response as well as the P/C ratios have been performed. The theoretical characterisation was accomplished using Monte Carlo transport codes, MCNP and GAMOS. The response of the detector model has been simulated and tested against the experimental results. Discrepancy between the simulation and the experiment has been found and attributed mainly to the limitation in the accuracy of the unknown parameters withheld from the manufacturer. In addition, the characteristic charge collection properties of the detector, which are not accounted for them in the simulation. Considering these inadequacies, the level of agreement between the simulation and the experiment achieved is acceptable and the performance of detector model is considered validated.

The detector performance optimisation through improving its P/C ratio response was studied using an environmental sample and a calibration source in a Marinelli counting geometry. Therefore, a detailed description of the procedures of soil sample collection and preparation is given in Chapter 5 as a part of the work presented in this thesis. In this chapter, the gamma-ray spectroscopic measurements for environmental samples collected have also been carried out.

In Chapter 6, the highest improvement in the P/C response of the post-filtered energy spectra has been obtained when processing the data set with the risetime filter $g(t30, t90)_{122\,keV}$. For instance, the calculated ratios at 60 keV and 88 keV were shown to be 59% and 72% higher than those for the original energy spectrum while the ratios at higher energies such as 662 keV and 1333 keV, were shown to be 54% and 53% higher than the corresponding ratios for the original spectrum. The effectiveness of this risetime filter lies in supressing a significant number of Compton scattering events, in which the scattered photon has escaped from the detector before full energy deposition. In high rate applications where a higher statistics data set of recorded pulse shapes is obtainable, this gate is favoured over the other risetime filters.

The improved P/C response achieved by this filter is however at the expense of rejecting more full-energy events leading to a decrease in the number of counts in the photopeak channels of the post-filtered energy spectrum. The risetime gate g(t30, t90)$_{122\,\mathrm{keV},\ 1333\,\mathrm{keV}}$ and the extended gate represent two optimal case scenarios, where a tradeoff between maximising the P/C response of the post-filtered energy spectrum and maintaining high photopeak efficiency has been established in order to suit different applications. Results of P/C ratios obtained using these optimal risetime filters have shown that both filters resulted in remarkable gains in sensitivity by improving the P/C response through the reduction of Compton scattering events. Moreover, the photopeak efficiency values acquired by these filters have also been maintained high. When the maximisation of the P/C ratio response is desired over photopeak efficiency, the risetime gate g(t30, t90)$_{122\,\mathrm{keV},\ 1333\,\mathrm{keV}}$ is favoured while the extended gate is typically preferred for applications where maintaining high throughput is a priority such as environmental sample counting.

Future work could include that these optimum risetime filters, which are essentially the main parametric PSA algorithm in this work can be implemented directly into Caen DT5780 firmware and then be used to improve the spectral response of the detectors when used for detector applications such as in characterising radioactive waste.

Appendix A

The calibration certificate for the Marinelli calibration source NPRL 604

Composition of multinuclear source

Etalon Multi-Gamma in Resin 250ml Marinelli flask

(Type 9ML01EGRM[15] REFERENCE NO. 7724B/1)

Reference Date: 3^{rd} DECEMBER 2012 at 12h UTC

Radioisotope	γ-ray energy (keV)	Activity (kBq)	Gamma fraction (%)
^{241}Am	59.5	1.637	35.9
^{109}Cd	88.0	7.93	3.7
^{57}Co	122.1	0.394	85.6
^{139}Ce	165.9	0.397	80.0
^{51}Cr	320.1	16.22	9.9
^{113}Sn	391.7	2.35	65.0
^{85}Sr	514.0	1.584	96.0
^{137}Cs	661.7	2.39	85.1
^{88}Y	898.0	2.32	93.7
^{60}Co	1173.2	2.37	99.9
^{60}Co	1332.5	2.37	100
^{88}Y	1836.1	2.32	99.2
TOTAL		42.23	

Table A.1: The calibration certificate for the Marinelli calibration source NPRL 604.

Appendix B

A Guide to Fitzpeaks

This appendix provides a step by step guide to setting the software up, inputting energy spectra for the calibration source NPRL 604, the background and the sample as follows:

B.1 Loading the calibration spectrum

First of all, the initial setup of the detector requires to be defined. Go to **Set up/General set up** and check the default detector file number has been set to zero, to ensure that no previous detector settings will therefore be used. This number is used for a calibration spectrum. The user must make sure that, the option **Perform background subtraction** is not selected. Once the general set up has been completed, the calibration file of the Marinelli calibration source (NPRL 604) obtained from the measurement stage[1] can be loaded by selecting **File/Open spectral data file**.

B.2 Energy Calibration

Once the energy spectrum of the Marinelli source has been loaded, the energy calibration can be performed, this is done by clicking on **Calibrate/Energy**. The question will be asked if you want to **Clear the energy and peak-shape calibration?**. Yes is selected, to make sure no previous calibration is used. To complete the energy calibration, a file **.ENC** containing the energy calibration information (channel number versus the energy values of the calibration spectrum), is selected. From this a fit of 1st or 2nd order can be selected depending on which fits the data the best. When satisfied with the fit, then **calibrate and OK** is selected. The output of the energy calibration curve (energy as a function of the channel number), and the calibrated energy spectrum are shown in Fig B.1 respectively.

B.3 Peak Shape Calibration

The peak-shape fit option needs to be selected from the calibration list by clicking on **Calibrate/Peak Shape** and for a Marinelli beaker calibration the file to be selected is in the **.SHP** format. By selecting Fit all, the peak fitting will be performed for all

[1] All Experimental files data (calibration and sample spectra) acquired from Prospect program, which are in **.AVA** format, were converted into **.CNF** format that can be read by Fitzpeaks

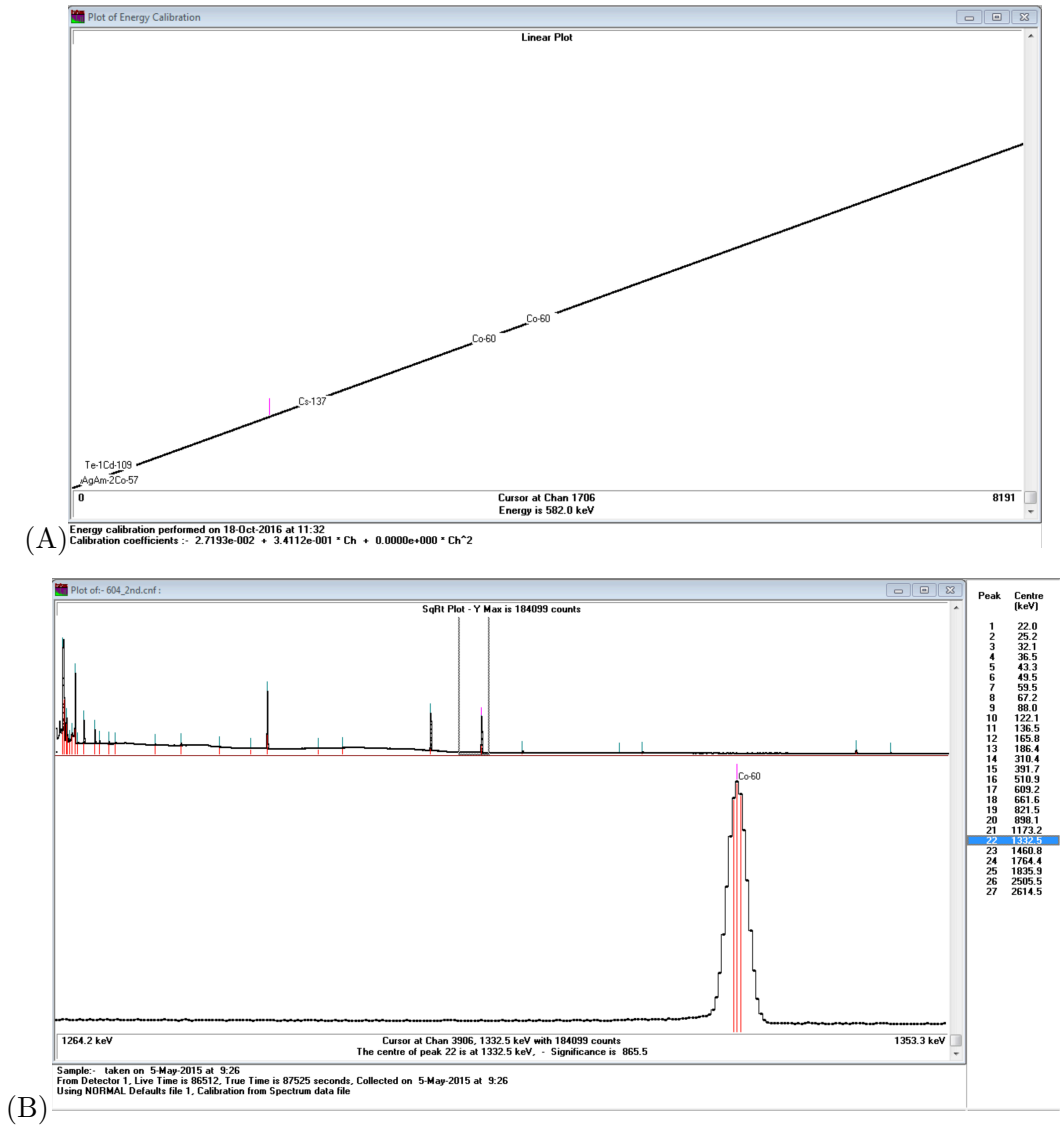

Figure B.1: Fitzpeaks output after energy calibration performance. (A) Energy calibration curve; the energy as a function of the channel number. (B) The generated energy calibrated spectrum of NPRL 604

peaks[2] in the spectrum as shown in Fig. B.2D. If the order of the fit is satisfied as shown in the figure, then **OK** is selected. The fittings of the peak width and the low and high energy tailing are reproduced in MatLab to show the peak shape calibration parameters, as presented in Fig. B.2A, B, and C respectively.

[2]The full energy photpeak of ^{241}Am (60keV) has been excluded from the **.SHP** input file because this peak has an anomalous low energy tailing width due to the adjacent Ge escape peak produced from the 60keV energy deposition. Therefore, data at this energy is not shown in the plots.

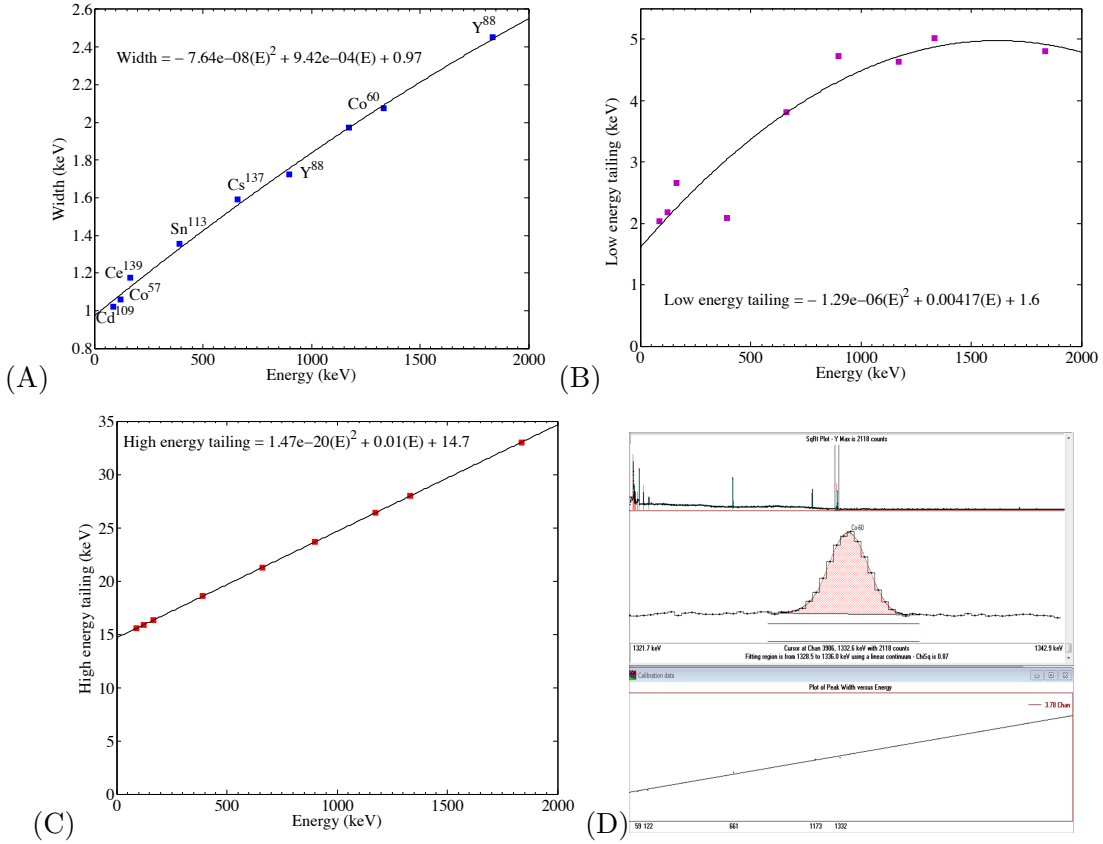

Figure B.2: Outputs of peak shape calibration. A MatLab plot of the (A) Width as a function of energy. (B) Low energy tailing as a function of energy. (C) High energy tailing as a function of energy. (D) Fitzpeaks output showing, the fitted peak shape of ^{60}Co (1332.6keV).

B.4 Efficiency Calibration

The third task is the efficiency calibration; this is done under the **Calibrate/Efficiency** heading and a question of **Do you want to perform a search and peak fitting?** will be asked- this is answered by yes. For the Marinelli calibration, the efficiency calibration source data file to be used is in the **.EFC** format and contains the calibration source information (the activity and the date). By selecting this file a table should appear now which shows these information. Each line in the table can be updated if the activity and the date need to be altered. Once this is complete, **calibrate/OK** is selected and the spectrum can now be efficiency calibrated. The effciency calibration output is shown in Fig. B.3. Then changes to the detector file can be saved. This detector file can now be used to identify the unknown peaks in the background and environmental spectra performed in the next two steps.

B.5 Adding a Background Spectrum

After performing the energy and efficiency calibrations, a background file needs to be added so that it can be subtracted from the unknown. This is performed under **Analyse/analyse and saves as bkg**. The background file can be overwritten as geom.bkg. The analysed background spectrum is shown in Fig. B.4.

B.6 Adding a Sample Spectrum

The spectra can be loaded in, as before, in the **Setup/General set up**, changing the number of the default detector file to the one saved from the calibration set up. The sample file can now be loaded from **File/Open spectra file** heading and a header data box will automatically be shown in which the values of the analysed sample (the sample size and units) can be entered. The correct detector file has to be checked from **File/Open detector file**, and to complete OK is selected. Under **Analyse/Full analysis**, the user can generate reports: Main report, Header, Peak fit and Activity. The generated spectra can also be plotted and printed under **Plot type/Print spectrum plot**. Peaks can also have their nuclides assigned by clicking on **Nuclide/show nuclides**. An example of the final analysed energy spectrum of the (25-30cm) sample from the wet core is presented in Fig. B.5.

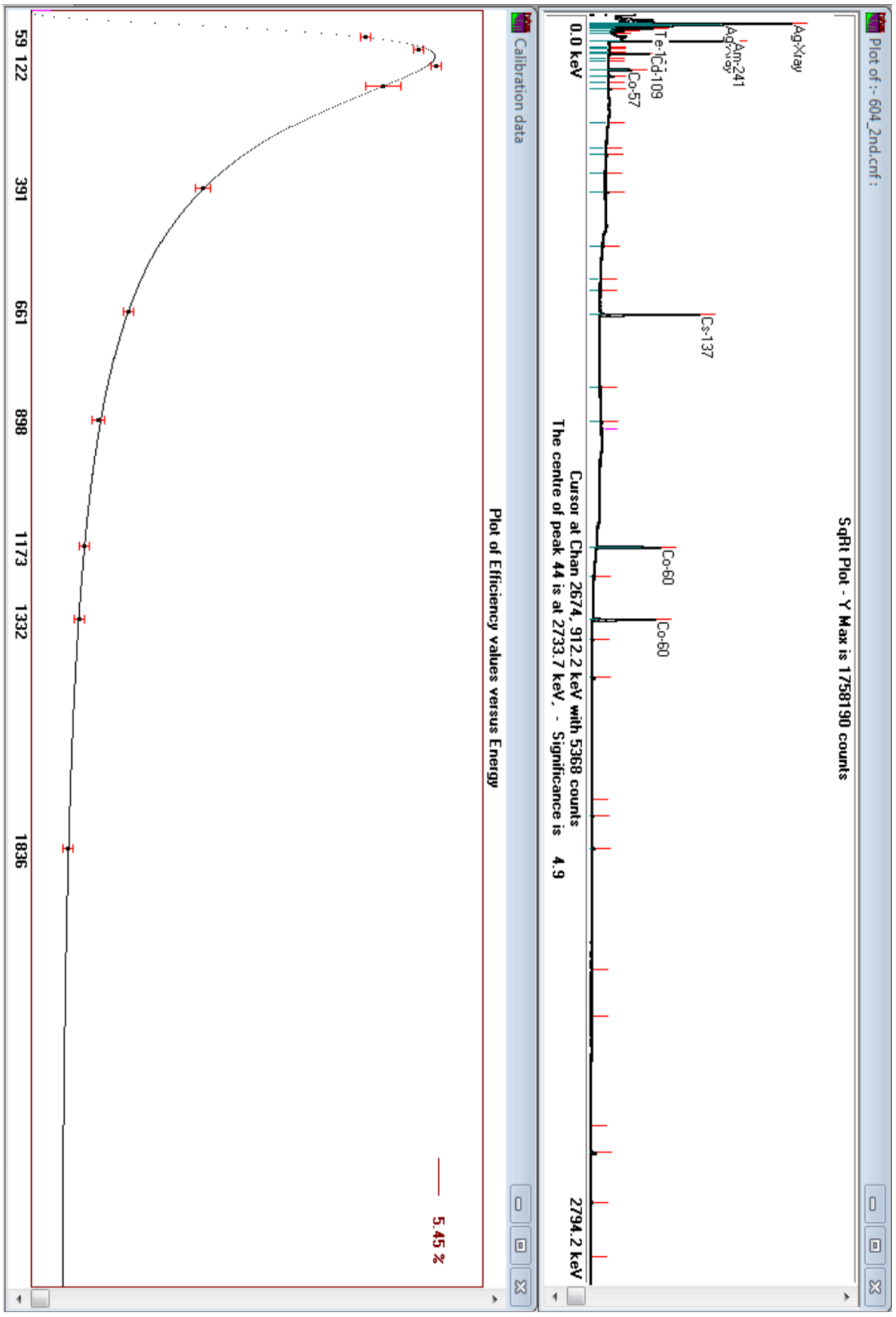

Figure B.3: Efficiency calibration output generated when the calibration source (NPRL604) information has been input.

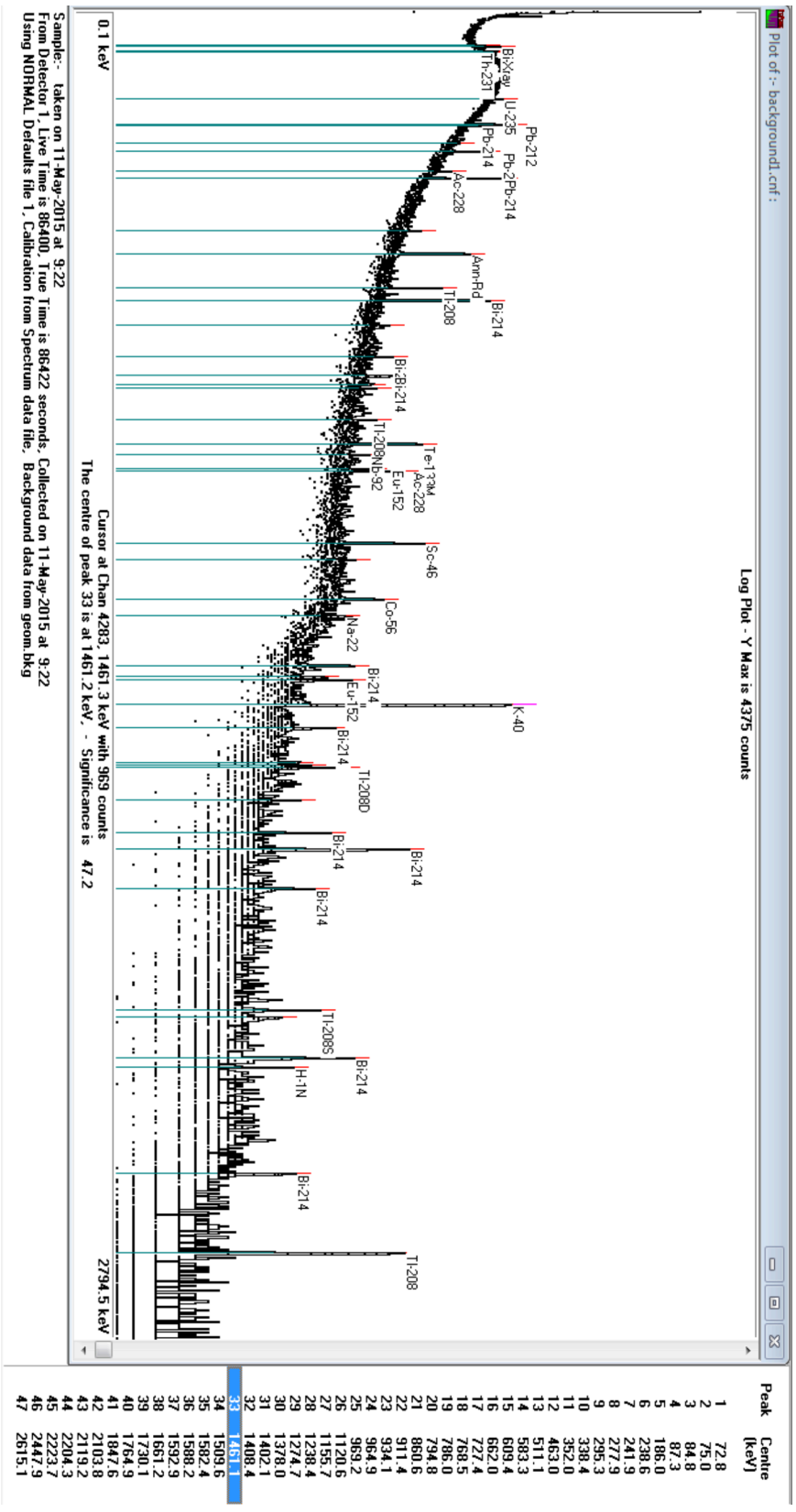

Figure B.4: Output of fitzpeaks analysis when entering the background spectrum data file obtained from the experiment. All peaks have their nuclides assigned. It is also shown at the bottom of the figure, the experimentally data collection information.

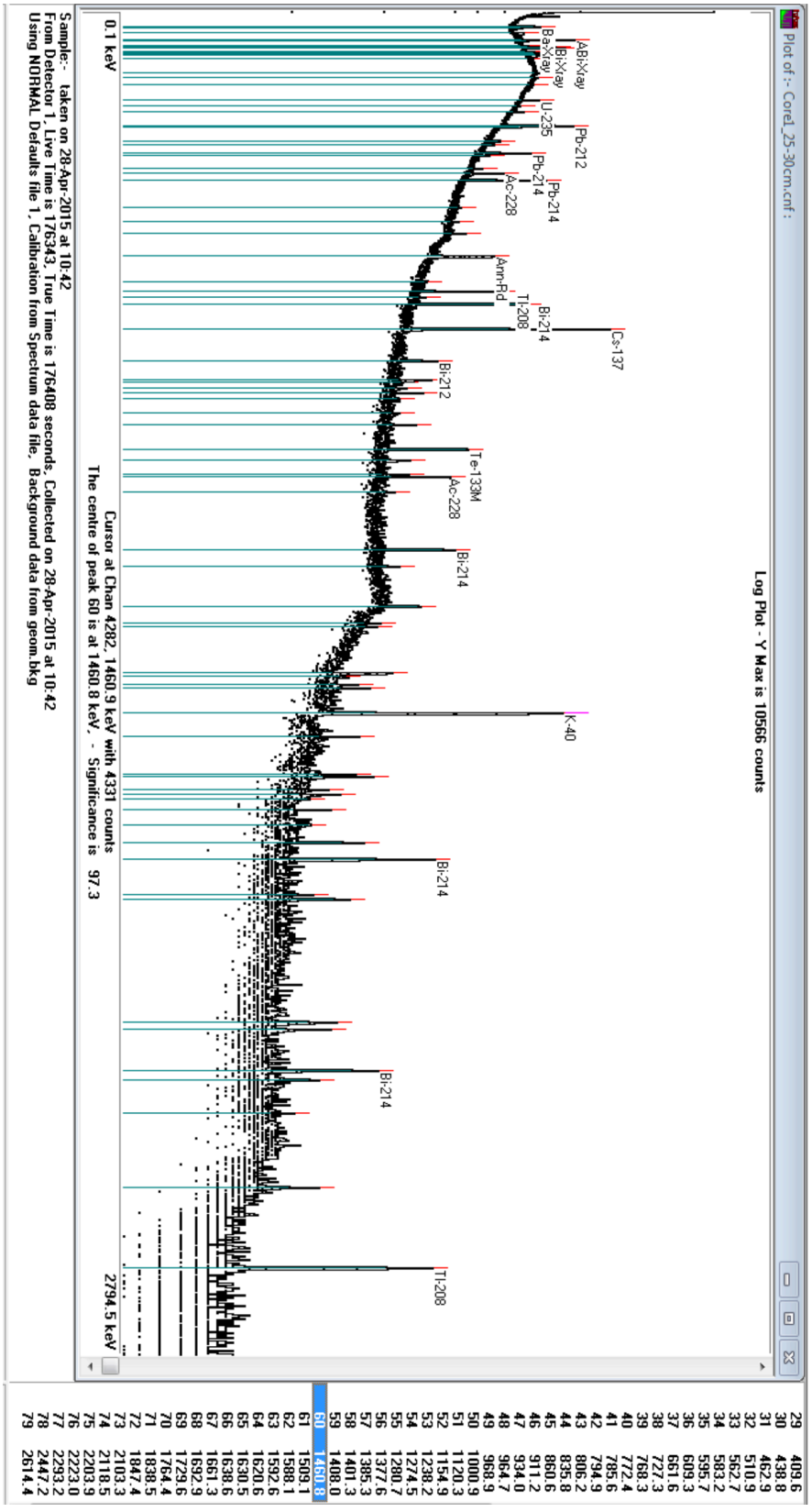

Figure B.5: Output of fitzpeaks analysis when entering a sample spectrum data file obtained from the experiment. All peaks have their nuclides assigned. It is also shown at the bottom of the figure, the experimentally data collection information.

Appendix C

MCNP Implementation

Introduction

The aim of this chapter is to describe how the MCNP input codes, implemented in this work, were created. The main input interface to MCNP supplied by the user is the input file that contains all input information required to demonstrate the experimental setup used for the current work. The input file has a fixed structure that must be obeyed in order to enable an experimental configuration to be constructed. A flow chart illustrating this structure is shown in Fig. C.1.

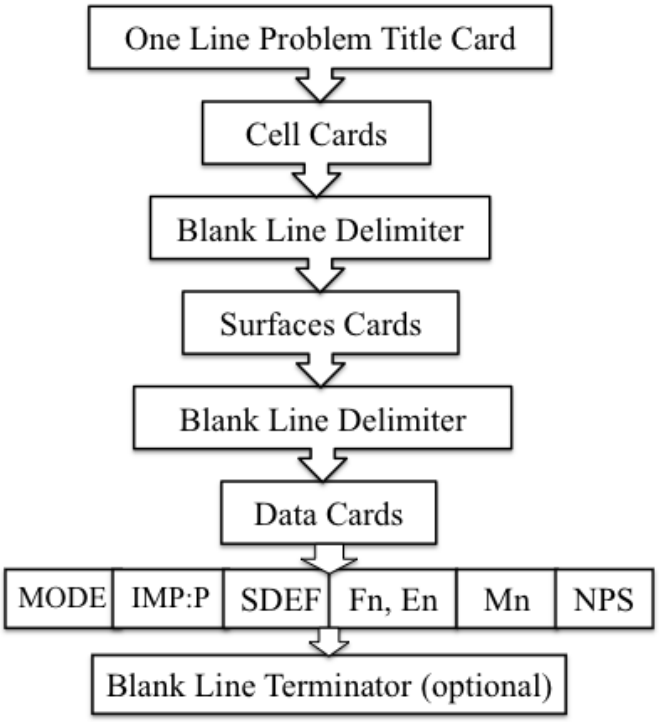

Figure C.1: A flow-Chart demonstrating the structure of the MCNP input file.

There are some important card categories; which all MCNP input cards shown in Fig. C.1 fall into, that need to be understood when writing an MCNP input file; they are:

1. Problem Title Card
2. MCNP Geometry Cards including:

   (a) Surfaces
   (b) Cells

3. Data Cards:

   (a) Problem Type Card
   (b) IMP Cell Importance Card
   (c) Source Specification
   (d) Tally Specification
   (e) Material Specification
   (f) Problem Cutoffs

Each of these categories is defined within the MCNP input file by using the relevant card(s) or "command(s)". The word card or command is used throughout this chapter to define one line of 80 characters long. The use of these cards must conform to the MCNP input file restrictions such as; each card must start on a new line and within the first five columns and the maximum line length in the input file is not exceeding 80 columns, which include one separation blank between all entries. Lines are included, which have more than 80 columns, by starting the continuation of the line five columns or more into the next line. A $ (dollar sign) is used to terminate data entry and to comment for a line. The comment lines have a C in one of the first five entries followed by one or more blank entries and they can be put anywhere in the input code after the title card line and before the terminator line. All card categories will be described in the following sections.

C.1 Problem Title Card

The title card is the first card in the input code describing the particular problem. It is a total of 80 columns long and is used as a title in several places in the MCNP output such as MCNP Plot output. The Title card description given for this work is:

```
Gdemo - demonstration BEGe gamma-ray detector
```

C.2 MCNP Geometry: Surfaces and Cells

The MCNP geometry is described by a 3-dimensional configuration of materials, specified in the input file, in geometrical cells bounded by first- and second-degree surfaces. The cells are described by intersections, unions and complements of the regions bounded by the surfaces. Surfaces are described by supplying coefficients to the analytic surface equations. MCNP is characteristic of its capability to check for geometry errors using the geometry plotter as will be discussed in Section C.4.
In MCNP, geometric cells are treated in Cartesian coordinates system. The allocation of the Cartesian axes x, y and z assumed in this work is shown in Fig C.2.

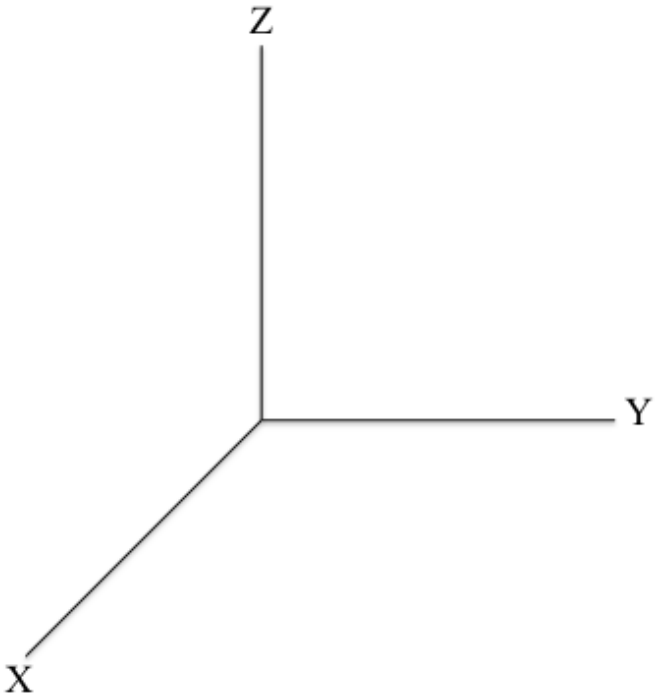

Figure C.2: Cartesian coordinate system adopted for this work.

C.2.1 Surfaces

Table C.1 presents a complete list of the surfaces used in the input file to construct the geometrical objects, which form the detection system used in this work.

Mnemonic	Type	Description	Equation	Card Entries
pz	Plane	Normal to Z-axis	z - $D = 0$	D
so	Sphere	Centred at origin	$x^2 + y^2 + z^2$ - $R^2 = 0$	R
sz	Sphere	Centred on Z-axis	$x^2 + y^2 + (z$ -$\bar{z})^2$ -$R^2 = 0$	$\bar{z}R$
cz	Cylinder	On Z-axis	$x^2 + y^2$ - $R^2 = 0$	R

Table C.1: MCNP Surface Cards used in the code.

To enable the surfaces to be proceeded, the following surface card form must be adhered to:

```
j    (n)    a    (list)
```

where `(j)` is the surface number, which uniquely identifies each cell. For the current work, it is entered in column 1 and is not exceeded 5 digits for all surface cards.
`(n)` is used for coordinate transformation. It is absent here; for no coordinate transformation used.
`(a)` is an alphabetic mnemonic representing the surface type, see Table C.1.
`(list)` the numerical coefficients of the equation of the surface in the proper order.
Examples of the use of the surface card are:

Example 1: 3 pz 2.6
Example 2: 1 cz 3.05

Example 1 defines a plane (labeled 3) normal to the z-axis at z = 2.6cm.
Example 2 defines a cylinder of radius 3.05cm on the z-axis at the origin point (0, 0, 0).

C.2.2 Cells

Cells are used to describe objects in MCNP. They are defined by intersections, unions and complements of the regions bounded by the surfaces. The form of the cell card is:

```
j   m   d   geom   (params)
```

where `(j)` is the cell number, which uniquely identifies each cell. Cell number is entered in column 1 and must not exceed 5 digits, in our input file; it is not exceeding 2 digits.
`(m)` is the material number, which corresponds to the number of a specific material Mm card (see Section C.3.5). If 0 is used the cell is a void.
`(d)`, is the material density. A positive number is translated as the atomic density in units of 10^{24} atoms/cm^3. A negative entry is interpreted as the mass density in units of g/cm^3. The mass density is used for this work.
`(geom)` this gives a complete specification of the geometry of the cell. It contains a list of surfaces (specified by their surface number j), which bounding the cell.
`(params)` this specifies the cell parameters by entries in a keyword.

```
Example 1: 1  1 -5.32   -111   21   -31  #(35 -36 -37 2)      imp:p 1
Example 2: 7   0   27                                        imp:p 0
Example 3: 21  0  -27   #(-1 2 -3)                           imp:p 1
```

Example 1 describes a cell (labeled 1) that models a detector, which is constructed of material number 1, which has a density of 5.32 g/cm^3. The cell consists of the intersection of the regions on the negative side of 111, positive side of 21 and negative side of 31 but excluding (# means not) the cell which is defined as everything above surface 35 intersected with everything below 36 intersected with everything to the left of surface 37 intersected with everything to the right of surface 2.
The `imp:p 1` is the *Cell Importance Card* which defines a value of a cell parameter. It is used to specify the relative importance for cell 1. The card has one entry for one cell (labeled 1), which shows that the cell has importance of 1, (see Section C.3.2 for more details).
Cell cards shown in the above examples are defined in a vertical (column) input format; in which the cell importance is entered within the same line of the cell card and has one entry specifying the relative importance for that cell.

The cell card can be also specified in a horizontal input format; in which the cell importance card is separately put on one input line in the data cards section rather than the cell cards section and the card will have a number of entries equals to the number of cells in the problem otherwise MCNP will terminate with an error, in this case, there will be one cell importance card for all cells in the input code.

For instance if the number of cells specified in a problem is 18 cells, the `imp:p` card will have 18 entries each defining the relative importance for a cell in the same order of the cells in the cell card block.
The column format; which is followed for defining cards in the input code, is particularly more useful than the horizontal one because, if a cell is deleted, one line of cell parameters is needed to be deleted rather than searching for the data item that related to the cell in each of many multiline cell cards. Further information on card formatting can be found in the *MCNP user manual*.
Example 2 is to define the world cell (labeled 7) for the problem. The cell is everything in the universe outside a sphere (labeled 27). The cell has an importance for photon of 0, this means, if photons move outside of the sphere then their importance is 0.
Example 3 defines the open space inside the world sphere excluding the cell -1 2 -3. Contrary to the second example, the photons moves inside the sphere are important to the problem and the particle transport should take place here. Without this line the photons would not get from the source to the detector.

C.3 Data Cards

As illustrated in Fig. C.1, all MCNP input cards except those used for defining geometry are data cards. they are entered after the second blank line dilimiter. Data cards used in the input code are summarized in Table C.2:

MCNP card name	Description
MODE	mode
IMP:P	cell parameter
SDEF	source specification
Fn, En	tally specification
Mn	material specification
NPS	problem cutoffs

Table C.2: MCNP Data Cards used in the input code.

A brief description of these cards is presented in the following sections:

C.3.1 Problem Type (mode) Card

MCNP can be run in several different transport modes. Mode card serves to specify the type of the particle to be transported. In the current work, the mode card is followed

by the photon choice as shown below:

```
mode p $ particle transport mode
```

The mode card is required in the input code as the MODE N is the MCNP default.

C.3.2 IMP Cell Importance Card

The Cell Importance Card is one of the cell parameter cards. It is required in the input code to termintae the particle transport if the importance of a cell is zero. This card needs a particle designator to distinguish between input data for neutrons, photons and for electrons. The particle designator comopsed of the symbol : (colon) and the letter N or P or E immediately following the mnemonic of the card as shown in the form below:

IMP:n x_1 x_2 ... x_i x_I

n = N for neutrons, P for photons, E for electrons.
x_i = importance for cell i
I = number of cells in the problem

Note that, in the current work, the IMP card is used with one entry for every cell as the vertical card format is used for writing cell cards (see examples 1, 2 and 3 in Section C.2.2).

C.3.3 Source Specification

There are several ways that can be utilised to define a source in MCNP. However, the most straightforward way to do so is by using the General Source Card (SDEF). The form of the card is:

```
SDEF   source variables = specifications ...
```

The source variables, assigned to the card, used in this work are:
`(pos)` which describes the x, y, z positions of the point source.
`(erg)` which defines the energy of the emitted particles in MeV.
Some advanced features of the SDEF card are utilised here to define the source in use accurately. The sources used in this work are basic discrete gamma-ray sources such as ^{241}Am with x-rays included. For example:

```
sdef pos=0 0 27.72 erg=d1
si1 l 13.927e-3 17.611e-3 20.997e-3 26.3445e-3 59.5364e-3
sp1 d 0.13 0.202 0.052 0.024 0.357
```

The first line defines a point isotropic source at (0,0,27.72) referenced to the original point (0,0,0) at the centre of the detector rear as considered in the simulation. The

energy of the source is defined by energy distribution `d1`.
`Si1` is a source information card for distribution `d1`. The `l` following the `si1` denotes the information supplied is for discrete source variable values. The following numbers define the two principle gamma-ray energies of ^{241}Am including the x-rays energies.
`Sp1` is a source probability card for distribution `d1`. The `d` following the `sp1` tells the card to interpret the following numbers as probabilities.

C.3.4 Tally Specification

Tally is defined as an accumulation of results from a problem. The tally cards can control the type of information the user wants to gain from the Monte Carlo calculations. MCNP can be instructed to make various tallies relating to particle current, particle flux, and energy deposition. MCNP tallies are normalized to be per starting particle. The type of tally used in the code is:
Pulse height tally: which provides energy distribution of pulses created in the detector by radiation. It also gives the total energy deposition in the detector cell.

C.3.4.1 Pulse Height Tally

To gain tally results, the fn card must be used. F8:P represents the pulse height tally providing a result in units of pulses. Appending a colon and the particle designator specifies the particle type (photon in this case). The tally type is followed by the cell number(s) in which the tally to be evaluated, for instance, f8:P 1 would evaluate the tally in cell 1. The tally is also evaluated over a number of energy bins, which must be specified following the tally type card in a separate line by using the e8 card. The energy bins must be equally spaced over the required energy range. This will lead to a large number of bins when evaluating a germanium detector. An example of the use of the f8 tally is as follows:

```
f18:P  1
e18    0    8190I    2.237
ft18   geb   5.7e-4    7.1e-4    2e-04
```

The `f18:P 1` enables the pulse height tally card to be proceeded. The use of `18` in the above example rather than `8` is not altering the type of the card used. Therefore, `f18:P 1` is the same as `f8:P 1`.

The `e18` card describes the energy bin size as 0.273keV per bin.

A special treatment can be added to the tally card by using the `ft` card. The use of this card ensures the response to photons is as accurate as possible in the detector system. The first entry of the ft card is the Gaussian energy broadening `(geb)` which ensures a better simulation for the radiation detector. The following three numbers are the parameters specifying the full width at half maximum of the observed energy

broadening in the radiation detector. A detailed description on how these three numbers were calculated for the detector used in this work can be found in Section 4.4.

C.3.5 Material Specification

As the material number is one of the parameters used to define a cell (see Section C.2.2), materials must be defined somewhere else in the code using the Material cards. The cards define the isotopic composition of materials in cells and which cross-section libraries are to be used. MCNP is provided with a large range of ENDF/B-VI and other cross section tables both with discrete and continuous data libraries. More details on the available libraries can be found in the *MCNP User Manual*. There are several choices of material cards and the most important card is:

```
Mm    ZAID_1    fraction    ZAID_2    fraction
```

`(m)` Corresponds to the material number on the cell cards. `ZAID` is a full ZZZAAA.nnX or ZZZAAA element or nuclei identifier for constituent i where ZZZ is the atomic number, AAA is the atomic mass, and X is the class of data. Fraction is the atomic fraction of constituent i in the material. This does not have to be normalized to 1.
Because photons are transported, the AAA can be set to 000 and nnX can be omitted. This means that ZZZAAA.nnX becomes ZZZ000. There is no distinction between isotope and element for photons and electrons, examples are shown below.

Example 1: m1 32000 1
Example 2: m5 6000 0.834 8016 0.093 1001 0.073

Example 1 represents germanium material, which our detector is made of.
Example 2 represents carbon epoxy. The compositions are 83.4%, 9.3% and 7.3% of carbon, oxygen and hydrogen respectively.

C.3.6 Problem Cutoffs

To terminate the execution of MCNP, one of the problem cutoff cards is required, the one that utilised in the input code is NPS card. It has a single entry that specifies the number of histories to transport from the source. The form of the card is:

```
NPS   N
```

N = number of particle histories

MCNP will terminate the Monte Carlo calculation after N histories have been transported. For the current work, nps is chosen to be 1.E+08. Alternatively, one more

advanced way to terminate MCNP is through the PTRAC card which is used to produce an output file containing the track histories of particle events. The user can obtain the tally output information and the PTRAC output at the same time with different output files. This will be explained in details in following Appendix D.

C.4 Geometry Plotter

The geometry plotter can be used to verify the geometry model, specified in the input file, before running the transport part of MCNP. Plotting geometry with MCNP is performed using the following command:

```
mcnp ip n=filename
```

where, ip stands for initiate and plot. The command is invoked in a prompt window as shown in Figure C.3.

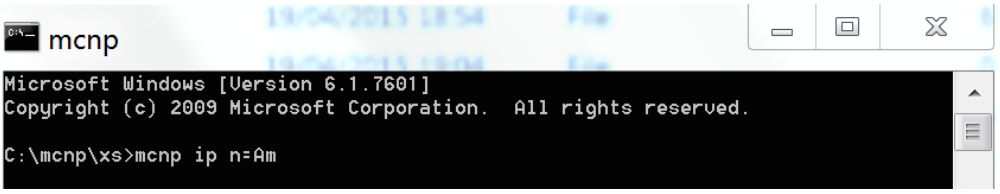

Figure C.3: Command window screen.

MCNP will process the input file called INPUT.txt, checking for errors and then the plot prompt `plot >` will start. The plot program displays part of a 3-dimensional scene as a 2-dimensional slice of the geometry model. The slice is defined on the same coordinate system as the surfaces in the MCNP input file. An example of MCNP plot of the geometry model of the Canberra BEGe type BE2825 (s/n b12116) detector, produced using the geometry plotter command "ip" is shown in Fig. C.5. A summary of the plot commands used to extract the plot is:
`Extent 20 20`, Sets the scale of the plot so that the horizontal distance from the origin to either side of the plot is 20 and the vertical distance is 20.
`Scales 2`, Puts scales and a grid on the plot.
`Label 0 1 cel`, Labels of surfaces are omitted because it is set to 0 and labels of size 1 are put in the cells.

C.5 Running MCNP

To run MCNP on the input file, the following command is entered at the command window:

```
mcnp ixrz n=INPUT
```

The cross sections will be processed and the particle transport will then begin. The above command will run MCNP on the input file called INPUT using the variables ixrz, which determine the form of the output. MCNP will produce an output file containing the results of the run with the filename "INPUTo", which is the input filename with o appended to the end. A file "INPUTr" will also be created; this will be a large file containing all the data processed in the run. This file can be used should we need to continue the run at a later stage.
The variables available with the mcnp command are defined in the following table.

Mnemonic	Type
i	Process problem input file
p	Plot geometry
x	Process cross sections
r	Particle transport
z	Plot tally results

Table C.3: Execution Options.

C.6 Description of MCNP Output File

Once the photon transport has completed using the run file "INPUT", an output file called INPUTo is generated. This file can be loaded into a textedit on MAC or a notpad on windows. The output file is devided into several discrete sections. The first part of the file is containing the input file with any error or warning messages that were created as it was being read. Afterthat, a list of the cells generated together with their volume and mass, in addition, a list of the cross section libraries used. Following this, a summary of the run describing how many particles have been transported in the run and the time taken. Some detailed statistics on the run follow this. Next are the tally results. These are quoted with:

- The energy bins that are specified in the run file
- The number of particles detected in this bin normalised to be per starting particle
- The error on this value

Afterthat, some detailed statistics specific to the tally that must be looked at which contains the 10 statistical checks which the run should pass, if not, the results obtained may not be reliable. If the error assigned to any of the tallies is too large. The error quoted is the estimated relative error defined to be one estimated standerd deviation of the mean divided by the estimated mean. The recommended guidelines on errors are outlined in table **??**.

The number of histories N is related to the estimated relative error R by

Relative Error	Quality of Tally
0.5 to 1.0	Not meaningful
0.2 to 0.5	Factor of a few
0.1 to 0.2	Questionable
<0.10	Generally reliable
<0.05	Genarally reliable for point detector

Table C.4: Guidelines on interpreting errors.

$$R = \frac{1}{\sqrt{N}}$$

The amount of computer time T consumed is proportional to N therefore;

$$R = \frac{C}{\sqrt{T}}$$

Where C is a positive constant. To reduce R we must either increase T or decrease C. C can be reduced by making geometry as simple as possible relative to the problem, as over complicating the geometry will mean MCNP will have to spend more time following unnecessary particles. To explain this behaviour, MCNP calculates a figure of merit (FOM) for one tally bin of each tally as a function of the number of histories and prints the results in the tally fluctuation chart at the end of the output. The FOM is defined as:

$$R = \frac{1}{(R^2T)}$$

The more efficient the Monte Carlo calculation is, the larger the FOM will be because computer time is required to reach a givien value of R.

C.6.1 Tally Plotter

Tally plotter is one of the methods that can be utilised to look at the output from MCNP. The tally plotter is used to plot the tally results either during the partcile transport or after transport is complete. We can look at a previously run problem so long as the filenamer ("INPUTr" in our example) file exists by using the following execute line at the command prompt window:

```
mcnp z runtpe=INPUTr
```

Where "z" invokes MCPLOT, the `mcplot>` prompt will then appear for MCPLOT commands. Pressing `<RETURN>` at the command prompt will result in a plot of the first tally specified in the input file. A list of useful commands which can be entered at the `mcplot` command prompt are presented in table **??**.

Command	Action
linlin	Linear x-axis linear y-axis
linlog	Linear y-axis linear y-axis
xlims min max nsteps	Define x-axis
ylims min max nsteps	Define y-axis
noerrbar	Suppress error bars
title “ ”	Put title on graph
xtitle “ ”	Define x-axis title
ytile “ ”	Define y-axis

Table C.5: Common mcplot commands.

Fig. C.4 shows an example of the tally plot output obtained from MCNP run. The command `linlin` is used to change the default from a lin-log plot to a lin-lin plot, and `xlims 0 0.07` is used to define a portion of the x-axis showing the energy range from 0 to 0.07MeV. MCNP can also be made to plot the results as transport is taking place.

To do this, `mplot` card was entered at the end of the input file as following:

```
C
mplot freq 50000                                $Define tally plot frequency
C
```

The mplot freq 50000 will plot the tally every 50000 histories.

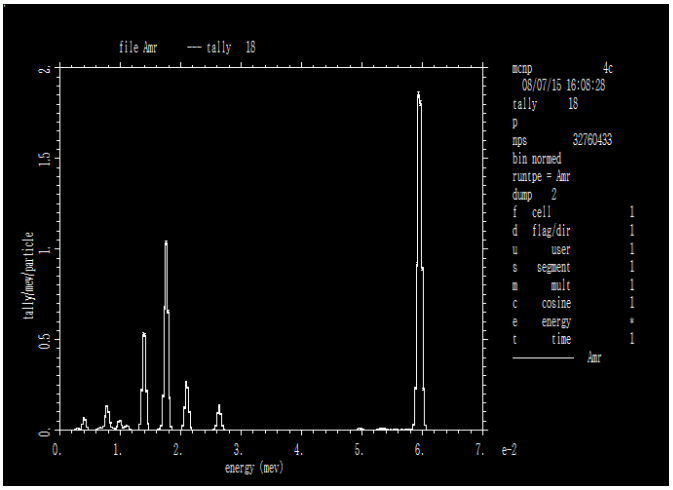

Figure C.4: Example of Tally Plot Output.

C.7 Model Optimization

Model optimisation was carried out using MCNP4C code. The unknown physical parameters of the detector setup are the internal dimensions of the material configuration within the cryostat. This includes the copper shell surrounding the detector crystal, the copper holder of the crystal, the aluminum endcap thickness as well as the dead layers in the detector crystal. No change was made in the crystal-to-window distance and the

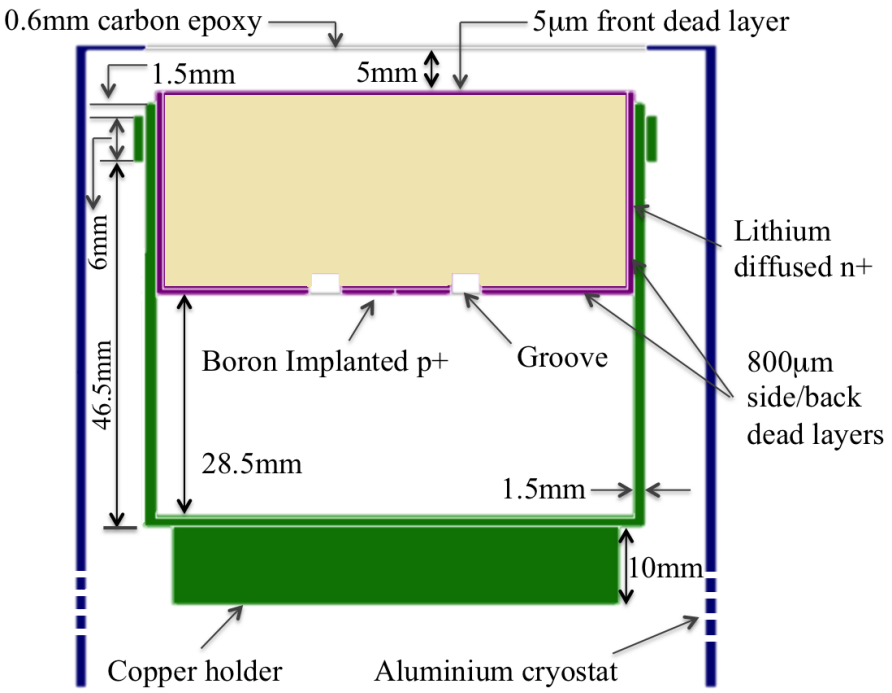

Figure C.5: A diagram showing the MCNP plot of the geometry model of the Canberra BEGe type BE2825 (s/n b12116) detector, produced using the geometry plotter command "ip" (see Section C.4). The plot shows a vertical section of the detector passing through the symmetry axis. The length of the aluminium cryostat, shown in Table 4.5, is not to scale in this figure.

crystal dimensions because of the reliable knowledge of these parameters taken from the manufacturer's data.

When optimising the model to match the experimental data, the only component that was tuned is the front dead layer of the detector crystal. The is because that, the dead layer in the front face of the detector crystal is suggested to be [B+13] the most/only critical element[1] that is between the detector and the source and hence resulting in a strong influence on the detector performance (i.e. P/T response) especially in the low energy region of a measured γ-ray energy spectrum.

The aim of this section is, therefore, to establish the most accurate thickness of the front dead layer. In addition to this, the relationship between the variation of the surface dead layer thickness and the P/T ratios could be determined. The front dead layer optimisation has been performed using low-energy gamma ray of ^{241}Am point source centrally positioned 25.1cm above the front face of the detector to examine the P/T ratios over a range of different values of front dead layer thicknesses and establish the value that has a good agreement with the experimentally determined value.

The side/back dead layer had to be estimated, as it is not expected to be critical component since the current detector performance characterisation only considers the standard detector top source geometry so, it was kept unchanged when optimising the

[1]It is made of Lithium atoms drifted into Ge crystal so the attenuation will be significant.

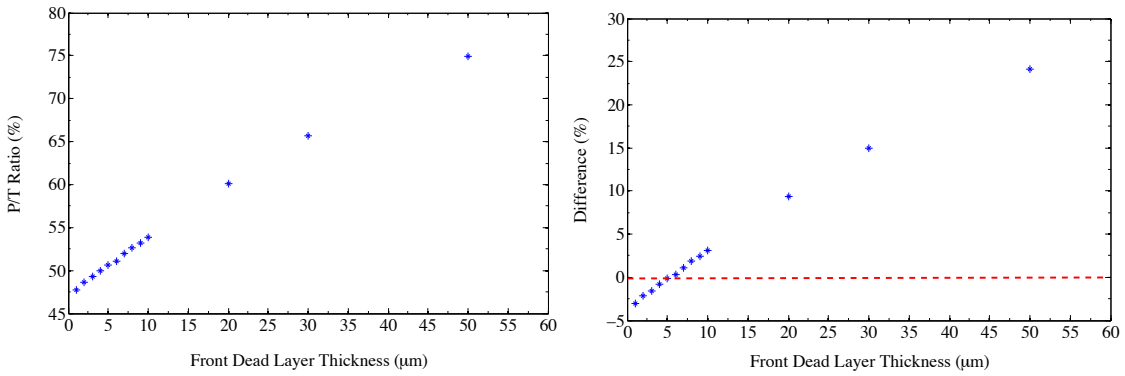

Figure C.6: (Left)The dependence of the P/T ratio on the front dead layer thickness using the low-energy gamma ray of ^{241}Am point source centrally positioned 25.1cm above the front face of the detector.
(Right) Difference between simulated P/T ratios and the experimental value (red dashed line at 0) as a function of front dead layer thickness. The relative uncertainty is less than 0.01% for all values presented on the plots.

front dead layer. However, after the front dead layer has been established (as will be shown below), it was attempted to tune the side/back dead layer using the energy of ^{137}Cs utilising the same detector top source geometry applied in the experiment. The thickness of the dead layer was varied from 200 to 800μm in steps of 200μm. It was found that the P/T values were not evidently sensitive to the thickness variation of the side/back dead layer hence, it was assumed to be 800μm. At the 800μm value of side/back dead layer, the model provided P/T values that match the experimental ones well when low and high energy point sources used (See Table 4.6).

For the copper material surrounding the detector, it was also estimated in the simulation, because (as mentioned previously) this characterisation accounts for only the standard detector top source geometry. However, in case of experimental measurements characterising the detector performance at unusual source geometry such as side-mounted sources, it will then be difficult to optimise the thickness of the side-mounted materials (i.e. copper shell, aluminium endcap and side dead layer) at the same time in the simulation. Therefore, it was not considered in the optimisation.

C.7.1 Results of the Front Dead Layer Optimization

Fig. C.6 (Left) demonstrates the relationship between the P/T ratios and the front dead layer thickness for the 800μm value of side/back dead layer using ^{241}Am point source. The P/T ratio increases as a function of front dead layers thickness. This can most likely be explained by the shielding effect caused by the front dead layer which plays a key role in the region of X-ray and low gamma-rays energy. The front dead layer comprises of impure germanium caused by the Lithium atoms drifted into the germanium crystal [F$^+$14] resulting in a significant attenuation of the X-rays. Therefore, the contribution of X-ray events to the total detector response decreases as the front dead layer thickness increases, in turn, the ratio of the P/T ratio rises.

The deviation of the simulated P/T ratios from the experimental value is also illustrated in Fig. C.6 (Right). It can be seen that, the optimum thickness of the front dead layer is 5μm. This value provided the best agreement between the MCNP and measured P/T ratio since the measured P/T ratio using ^{241}Am, is 50.78% $\pm$ 0.12% whereas the MCNP ratio at this thickness is 50.57% $\pm$ 0.35% with a relative difference of 0.21% which can be considered as a very good agreement.

Appendix D

PTRAC Particle Track Output Card

D.1 PTRAC Input Code

PTRAC card is classified under the peripheral cards category in the MCNP user manual, and is one of the data cards that is input after the optional blank card delimiter following the data cards block (See Fig. C.1). This card is entered in the input code according to the following format:

```
PTRAC       keyword=parameter(s)       keyword=parameter(s)
```

The card produces an output file called "INPUTp" which is the input filename with p appended to the end. The keywords used with this card in the input code, are presented below:

```
PTRAC    FILE=ASC    WRITE=all    TYPE=P    CELL=1     MAX=-1E+08
```

These keywords are arranged into three categories:

- Output control keywords
- Event filter keywords
- History filter keywords

The first category provides the control of the PTRAC file and I/O. The second category filters particle events on event-by-event basis. The third category is to write all filltered events for a history to PTRAC file, if that history conform to the history filter keywords. The function of each keyword is included in table D.1.
The PTRAC card shown above was used along with the MCNP input file "INPUT.txt" for tracing particle histories. The card is input at the end of the input file. The NPS card is excluded and the PTRAC card is used instead. This allows us to accumulate enough data form the PTRAC output, where this is not possible if the card entered somewhere else in the code.

D.2 Detailed description of the structure of the PTRAC output code

The PTRAC output file contains all the information defining the data structure of a parent particle and all resulting (daughter) particles, which in turn produce other

Keyword	Parameter Values	Function
OUTPUT CONTROL KEYWORDS		
FILE	ASC	Controls file type. ASC-generates an ASCII output file.
WRITE	ALL	Controls what particle parameters are written to the PTRAC file.
MAX	INTEGER $\neq 0$	Sets the maximum number of events to write to the PTRAC file.
FILTER EVENT KEYWORDS		
TYPE	P	Filters events based on particle type; P is used for photon events
HISTORY FILTER KEYWORDS		
CELL	INTEGER > 0	This keyword is used for history filtering, so all filtered events for a history enters a listed cell will be written to the PTRAC file.

Table D.1: The keywords and parameter values used with the PTRAC card

subsequent particles. The PTRAC code writes the entire history of each particle in a block of event lines, which are categorised into six groups. These six event types are:

1000 = source events (src). These are initial particles shooted by the source, which, commence with known energy and starting position specified by the user in the input code at time 0.

3000 = surface crossing (sur). These are written to mark the crossing surface defined by the user.

4000 = collisions (col). These events represent the scattered particles.

5000 = termination events (ter). These events are written when the particle is totally absorbed in the final interaction or no longer tracked if the particle energy is limited (filtered) in the input code.

20XX = banked events, which include secondary sources generated by PTRAC such as 2009 and 2016 which describe a photon from double fluorescence and bremsstrahlung from electron respectively.

9000 = this represents the final line in the history block.

Each event is described by a number of variables written in two adjacent event lines. In PTRAC terminology, these two event lines are called 1st and 2nd event lines. The first variable in the 1st event line represents one of these six designations. In our application, the number of variables describing the event is 16 except source events, which are defined by 15 variables. A brief explanation of the format of these six designations is given in Table D.2.

Event Type	Description	Line Number	Number of Variables	Event Line Variables ID$_s$								
Src	1000	1^{st}	6									
		2^{nd}	9	X	Y	Z	V	W	U	ERG	WGT	TME
Bnk	(2000+L*)	1^{st}	7									
		2^{nd}	9	X	Y	Z	V	W	U	ERG	WGT	TME
Sur	3000	1^{st}	7									
		2^{nd}	9	X	Y	Z	V	W	U	ERG	WGT	TME
Col	4000	1^{st}	7									
		2^{nd}	9	X	Y	Z	V	W	U	ERG	WGT	TME
Ter	5000	1^{st}	7									
		2^{nd}	9	X	Y	Z	V	W	U	ERG	WGT	TME

Table D.2: The categories of event types of photon interactions inside the detector crystal as written by PTRAC in a block of event lines.

D.2.1 Description of Variable ID$_s$

D.2.1.1 1^{st} Event Line

Event Type.

It presents the number of Nodes in Track From Source to here. When the particle enters a new cell, a node number is printed in the output file. This can be clear in all events.

NXS (2, IEX): - Gives the reference of the array that is associated with a particular data (cross section*) table. Cross-section tables are existed in the (2-dimensional) NXS array. IEX: - Index of the particular table in the MCNP problem. (*) Cross section (σ): It is defined as the probability per unit time that there will be a collision leading to a reaction. This probability depends on the flux (ϕ) of the incident particles and the number N of nuclei being irradiated.

N.B Each type of reaction (see NTYN Reaction Type) has its own probability (the constant of proportionality for a given reaction) given by a partial cross section. The total cross section for the collision is the sum of the partial cross sections.

NTYN Reaction Type: -

1. Incoherent Scatter
2. Coherent Scatter
3. Fluorescence
4. Double Fluorescence
5. Pair Production

NCL (ICL): - Problem Numbers of the Cells

MAT (ICL): - Material Numbers of the Cells

NCP: - Count of Collision per Track

NSR: - Source Type

NSF (JSU): - JSU Program number of the current surface

Angle with Surface Normal (degrees)

NTER: - Termination Type (Loss mechanism).

1. Compton Scatter
2. Capture
3. Fluorescence
4. Pair Production

Branch Number For This History

D.2.1.2 2^{nd} Event Line

MCNP Name	Discription
XXX	X- Coordinate of the particle position
YYY	Y- Coordinate of the particle position
ZZZ	Z- Coordinate of the particle position
UUU	Particle direction cosine with X-axis
VVV	Particle direction cosine with Y-axis
WWW	Particle direction cosine with Z-axis
ERG	Particle energy
WGT	Particle weight
TME	Time at the particle position.

Table D.3: 2^{nd} Event Line description.

D.2.1.3 NPS Line Description

Number of variables on the NPS line (I_1, I_2, ...)
I_1 = NPS.

I_2 = Event Type of the 1st event for this history.
I_3 = Cell Number if filtered otherwise omitted.
I_4 = Surface Number if surface filtered, otherwise omitted.
I_5 = Tally Number if tally filtered otherwise omitted.
I_6 = TFC bin tally if tally filtered, otherwise omitted.
All filtered events of a history are written by PTRAC in a block. A PTRAC block is defined as the entire history of a particle generated by MCNP. The following example is showing a block for NPS = 107305 using ^{241}Am source (59.536keV). The block contains all filtered events related to the specified history that enters cell number 1. Particles generated by MCNP can only interact with material contained in cell 1, which is HPGe as defined in the input code in our application.

```
107305    1000    1
    3000    1    40    21    0    0
0.00000E+00 0.00000E+00 0.27720E+02 -0.75980E-01 -0.67460E-01 -0.99482E+00 0.59536E-01 0.10000E+01 0.00000E+00
    3000    2    11    174    8    0    0
-0.18735E+01 -0.16634E+01 0.31900E+01 -0.75980E-01 -0.67460E-01 -0.99482E+00 0.59536E-01 0.10000E+01
0.82249E-01
    3000    3    20    174    6    5    0
-0.18804E+01 -0.16695E+01 0.31000E+01 -0.75980E-01 -0.67460E-01 -0.99482E+00 0.59536E-01 0.10000E+01
0.82551E-01
    3000    4    10    174    3    0    0
-0.18849E+01 -0.16736E+01 0.30400E+01 -0.75980E-01 -0.67460E-01 -0.99482E+00 0.59536E-01 0.10000E+01
0.82752E-01
    3000    5    3    174    12    1    0
-0.19185E+01 -0.17034E+01 0.26000E+01 -0.75980E-01 -0.67460E-01 -0.99482E+00 0.59536E-01 0.10000E+01
0.84227E-01
    4000    6    31    174    1    1    0
-0.19186E+01 -0.17034E+01 0.25995E+01 -0.75980E-01 -0.67460E-01 -0.99482E+00 0.59536E-01 0.10000E+01
0.84229E-01
    4000    6    6000    1    1    1    1
-0.19233E+01 -0.17076E+01 0.25379E+01 -0.27144E+00 0.91804E+00 -0.28901E+00 0.54730E-01 0.10000E+01
0.84435E-01
    4000    7    7000    4    1    1    2
-0.19281E+01 -0.16912E+01 0.25328E+01 -0.66907E+00 -0.65415E+00 -0.35274E+00 0.98870E-02 0.10000E+01
0.84495E-01
    5000    7    7000    3    1    1    3
-0.19281E+01 -0.16913E+01 0.25327E+01 -0.66907E+00 -0.65415E+00 -0.35274E+00 0.98870E-02 0.10000E+01
0.84495E-01
    2016    7    12    1    1    1    3
-0.19281E+01 -0.16913E+01 0.25327E+01 -0.66907E+00 -0.65415E+00 -0.35274E+00 0.98870E-02 0.10000E+01
```

```
0.84495E-01
    4000    8    0    0    1    1    0
-0.19281E+01 -0.16913E+01 0.25327E+01 0.22012E+00 -0.35831E+00 0.90728E+00 0.14947E-02 0.10000E+01 0.84495E-01
    5000    8    8000    3    1    1   1
-0.19281E+01 -0.16913E+01 0.25328E+01 0.22012E+00 -0.35831E+00 0.90728E+00 0.14947E-02 0.10000E+01 0.84495E-01
    2009    8    12    2    1    1    1
-0.19281E+01 -0.16913E+01 0.25328E+01 0.22012E+00 -0.35831E+00 0.90728E+00 0.14947E-02 0.10000E+01 0.84495E-01
    4000   7   32000   4    1    1    2
-0.19281E+01 -0.16912E+01 0.25328E+01 -0.11490E+00 0.39917E+00 0.90965E+00 0.12210E-02 0.10000E+01 0.84495E-01
    5000    7    7000    3    1    1   3
-0.19281E+01 -0.16912E+01 0.25328E+01 -0.11490E+00 0.39917E+00 0.90965E+00 0.12210E-02 0.10000E+01 0.84495E-01
    9000    7    12    3   1    1   3
-0.19281E+01 -0.16912E+01 0.25328E+01 -0.11490E+00 0.39917E+00 0.90965E+00 0.12210E-02 0.10000E+01 0.84495E-01
```

In PTRAC term, the first line is called NPS line, which has three entries since surface, tally and TFC are not filtered in input code. The first entry refers to the number of histories that has been transported by MCNP up to this point. The second element is used to identify the type of the first interaction (event type) for this history (N = 107305), which its variables are written in the following two lines, and this is the way followed by the PTRAC to identify each event in a block. The third element is the cell number filtered by the user.

The **1000** events are initial source events launched by PTRAC, they are written into the output at the beginning of each block. This has the advantage of knowing the initial energies especially if a multiple energetic source used in the code or x-rays are included in the gamma ray source.

The surface event **3000** is written in the output file where a particle crosses a surface defined in the input code. The surface event, therefore, has an advantage of identifying the entry energy to the crossing surface, as one of the variables describing this event is the energy of the particle penetrating that surface. Unlike the 1000 events, which are defined by 14 of 15 elements, the 3000 events are described by 15 of 16 entries written in the 1^{st} and 2^{nd} event lines. It should be recalled that, the first entry within the current event is always to identify the following event. Variables of each event reported by PTRAC have differing meaning depending on the type of interaction. Table D.3 summarises the variables definition of these events.

The **4000** events are real events describing collisions. The collision types are: incoherent (Compton) scatter, coherent (Rayleigh) scatter, fluorescence, double fluorescence and pair production. As mentioned in the above example, the collision is described as a 4000 event by the first entry of the 1st line in the previous event, which is a surface event. The first entry of the first collision event anticipates the next event type to be also a collision. The interaction type is shown as the fourth quantity in the 1st event line. One of the variables that most characterises this type of events is the reaction type

shown as the fourth quantity in the 1st event line of the 4000 event (1 for Incoherent Scattering in the above example).

The **5000** events are written to the PTRAC output to describe the termination events when the energy is completely deposited in the material, no longer traced by the PTRAC in the case of limiting the defined energy for the tracked particles or if it is out of the defined world specified in the PTRAC input code. The branch number is one of the variables used to define termination events, which is shown as the fourth entry in the first event line. It can be noted that, the first termination event with branch number 1 (shown in the block above) illustrating the complete deposition of 59.536keV in cell 1 and all following events (banked, collision and termination) are to express the secondary sources generated by PTRAC not from the Americium source and are not included in the energy calculation, this will be discussed in more details in the next paragraph. The termination events are also characterized by the termination type, which is shown as the third number in the first event line of the 5000 presented in the example.

The **20XX** are new particles (daughters) generated by the parent particles. They are separated from the parent particle, since PTRAC can only write events of the daughters following the parent particle in a two dimensional format. All banked events are written in a reverse chronological order and have the same format as the collision event lines as shown in Table D.2. All banked events are not involved in the energy calculations as these events are not instantiate the gamma source used in the input code but in fact they are secondary sources created by PTRAC. It can be concluded that, termination events with branch number of 1 separates the parent particle history from the daughters histories and this aids the process of reading the output code by analysis programs such as MATLAB.

Appendix E

Input Codes Created for MCNP and GAMOS Simulations

This appendix offers the final MCNP and GAMOS codes generated for the work presented in Chapter 4 in order to support future users for the purpose of characterising detector performance with similar geometry to the detector used in this work.

E.1 MCNP Input Code

```
INPUT.txt
Gdemo - demonstration Ge gamma-ray detector
C
C Material densities
C G = -5.32 Al = -2.7 Cu = -8.92 Pb = -11.34 natature carbon = -1.42 tin
= -7.31
C ####################Define Cells ####################
C
1 1 -5.32 -111 21 -31 #(35 -36 -37 2) imp:p 1                $ Detector
11 1 -5.32 -1 2 -31 #(-111 21 -31) #(35 -36 -37 2) imp:p 1  $ Lateral &
back dead layer
12 1 -5.32 -1 -3 31 imp:p 1                                $Front dead Layer
2 2 -2.7 -8 18 -11 #(-9 18 -10) #(-19 -11 10) imp:p 1    $ Aluminum (Al)
cap
3 0 -9 18 -10 #(-1 2 -3) #(-28 33 -4) #(-412 411 -41)
#(-415 34 -33) imp:p 1          $Vacuum between the Al cap and Cu holder
4 3 -8.92 -16 18 -17 #(-161 18 -17) imp:p 1            $Copper shielding
41 6 -7.31 -15 18 -17 #(-16 18 -17) imp:p 1               $tin shielding
5 4 -11.34 -14 18 -17 #(-15 18 -17) imp:p 1              $Lead shielding
6 5 -1.42 -19 -20 10 imp:p 1                          $Carbon Epoxy window
7 0 27 imp:p 0                                              $Define world
8 0 -19 20 -11 imp:p 1                    $Vacuum above the carbon window
9 3 -8.92 -28 33 -4 #(-29 32 -4) imp:p 1                   $Cu cylinder
91 0 -29 32 -4 #(-1 2 -3) imp:p 1  $Vacuum between detector and Cu shell
92 3 -8.92 -412 411 -41 #(-28 411 -41) imp:p 1  $Cu First notch cylinder
```

```
94 3 -8.92 -415 34 -33 imp:p 1                                  $Copper bottom
95 0 35 -36 -37 2 imp:p 1                                        $First groove
21 0 -27 #(-1 2 -3) #(-8 18 -11) #(-14 161 18 -17)
#(-28 33 -4) #(-412 411 -41)
#(-415 34 -33) imp:p 1                                           $Define world

C
C ####################Define Surfaces ####################
C
1 cz 3.05        $ Define detector (Active Diameter=61mm) ;including dead
layers
111 cz 2.97              $ Define lateral Dead Layer (0.08cm) [VARIABLE]
2 pz 0                                    $ Lower Limit of the detector
21 pz 0.08                       $ Bottom Dead layer (0.08cm) [VARIABLE]
3 pz 2.6                                  $ Upper Limit of the detector
31 pz 2.5995                   $ Front Dead layer depth (5um) [VARIABLE]
4 pz 2.45                                   $ Upper limit of Cu shell
41 pz 2.3               $ Upper limit of the first notch in the Cu shell
411 pz 1.7                             $ Lower surface of the first notch
412 cz 3.351       $ First notch cylinder (outside) (thickness is 1.5mm)
415 cz 2.851                                             $ Copper bottom
8 cz 4.1                              $ Outer Al cap (R = 4.1cm)D=82mm
9 cz 3.95                      $ Internal Al cap (Al thickness = 0.15cm)
10 pz 3.04                              $ Upper Al shell(Inner surface)
11 pz 3.19                        $ Al shell thickness supposed (1.5mm)
14 cz 17.5                                                 $ Outer Lead
15 cz 12.5                                               $ Internal Lead
16 cz 12.45                                $ Cd Liner (0.5mm thick)
161 cz 12.35                             $ Copper liner (1mm thick)
17 pz 20.25                             $ Upper Limit of the sheild
18 pz -13.75                             $Lower Limit of the sheild
19 sz 3.07 3.2                    $ Carbon windows defined as a sphere
20 pz 3.1                                  $ Carbon Epoxy thickness
27 so 100                                                  $ define world
28 cz 3.201                         $ Outer Cu cap (thickness is 1.5mm)
29 cz 3.051                                          $ Internal Cu cap
32 pz -2.85                   $Lower Limit of Cu shell (Outside surface)
33 pz -2.95                   $Lower Limit of Cu shell (Outside surface)
34 pz -3.95              $Lower limit of copper bottom (thickness = 1cm)
35 cz 0.7                             $Radius of P+ contact (ID = 14mm)
36 cz 1.1                      $OD = 22 mm to separate the P+ from n+
```

```
37 pz 0.3                                                    $Groove depth = 3mm

mode p                                                         $photon transport
C
C ####################Define Source ####################
C Source Definition Am-241(including X-RAYS)
C
sdef pos=0 0 27.72 erg=d1 $ The source-detector distance referenced to the original
point (0,0,0) at the centre of the detector rear as considered in the simulation.
si1 l 13.927e-3 17.611e-3 20.997e-3 26.3445e-3 59.5364e-3
sp1 d 0.13 0.202 0.052 0.024 0.357
C
C ####################Define Tally ####################
C
f18:P 1          $ A Pulse Height Tally will be evaluated in cell 1 only
e18 0 8190I 2.237                                      $ 0.273 keV bin size
ft18 geb 5.7e-4 7.1e-4 2e-04              $ BeGe-detector coefs (a, b, c)
C
C ####################Define Materials ####################
C
m1 32000 1                                                    $ Germanium
m2 13000 1                                                     $ Aluminum
m3 29000 1                                                       $ Copper
m4 82000 1                                                         $ Lead
m5 6000 0.834 8016 0.093 1001 0.073                        $ Carbon Epoxy
m6 50000 1                                                          $Tin
C
C ####################Define Materials ####################
C
mplot freq 50000
PTRAC FILE=ASC WRITE=all TYPE=P CELL=1 MAX=-100000000
```

E.2 GAMOS Input Code

```
GEOMETRY.geom

:MATE G4_Ge 32.  72.64 5.32

/////////////////////////// Material Properties ///////////////////////////
```

```
:MATE_TEMPERATURE G4_Ge 77*kelvin // -196.15
:MIXT G4_Carbon_Epoxy 1.42 3
   G4_C 0.834
   G4_O 0.093
   G4_H 0.073

////////////////////////////// Parameters ////////////////////////////////

:P InnerR_lead 12.5*cm
:P OuterR_lead 17.5*cm
:P Length_shielding 34*cm
:P InnerR_tin 12.45*cm
:P InnerR_Cu 12.35*cm
:P InnerR_Al 3.95*cm
:P OuterR_Al 4.1*cm
:P Length_Al 16.79*cm
:P InnerR_A4_top 3.2*cm
:P Length_Al_top 0.15*cm
:P InnerR_Cu_shell 3.051*cm
:P OuterR_Cu_shell 3.201*cm
:P Length_Cu_shell 5.3*cm
:P Length_Cu_base 0.15*cm
:P OuterR_Cu_bottom 2.851*cm
:P Length_Cu_bottom 1*cm
:P OuterR_Cu_first notch 3.351*cm
:P Length_Cu_first notch 0.6*cm
:P Length_Carbon_Epoxy 0.06*cm
:P Length_Ge 2.5195*cm
:P OuterR_Ge 2.97*cm
:P OuterR_Groove 1.1*cm
:P InnerR_Groove 0.7*cm
:P Length_Groove 0.3*cm

////////////////////////// Dead Layers Values ////////////////////////

:P Length_FrontDeadLayer 0.0005*cm
:P OuterR_FrontDeadLayer 3.05*cm
:P Length_BackDeadLayer 0.08*cm

////////////////////// World (Parent Volume) ////////////////////////
```

```
:VOLU world BOX 400 400 400 G4_AIR

/////////////////////////// Detector shielding ////////////////////////////

:VOLU lead TUBE $InnerR_lead $OuterR_lead $Length_shielding/2.  G4_Pb
:ROTM RMO 0 0 0
:PLACE lead 1 world RMO 0.  0.  0.
:COLOUR lead 1 -1 -1
:VIS lead ON
:VOLU tin TUBE $InnerR_tin $InnerR_lead $Length_shielding/2.  G4_Sn
:PLACE tin 1 world RMO 0.  0.  0.
:COLOUR tin -1 1 1
:VIS tin ON
:VOLU copper_liner TUBE $InnerR_Cu $InnerR_tin $Length_shielding/2.  G4_Cu
:PLACE copper_liner 1 world RMO 0.  0.  0.
:COLOUR copper_liner 1 -1 -1
:VIS copper_liner ON

//////////////////// Detector Aluminum case ///////////////////////

:VOLU Aluminum TUBE $InnerR_Al $OuterR_Al $Length_Al/2.  G4_Al
:PLACE Aluminum 1 copper_liner RMO 0.  0.  -8.605*cm
:VOLU Aluminum_top TUBE $InnerR_Al_top $OuterR_Al $Length_Al_top/2.  G4_Al
:PLACE Aluminum_top 1 Aluminum RMO 0.  0.  8.47*cm
:COLOUR Aluminum 1 1 1
:COLOUR Aluminum_top 1 -1 -1

//////////////////// Detector Carbon Epoxy ////////////////////////

:VOLU Carbon_Epoxy TUBE 0.  $InnerR_Al_top $Length_Carbon_Epoxy/2.  G4_Carbon_Epoxy
:PLACE Carbon_Epoxy 1 Aluminum_top RMO 0.  0.  -0.0375*cm
:COLOUR Carbon_Epoxy -1 1 1

/////////////////////// Detector Copper shell ////////////////////////

:VOLU copper_shell TUBE $InnerR_Cu_shell $OuterR_Cu_shell $Length_Cu_shell/2.
G4_Cu
:PLACE copper_shell 1 world RMO 0.  0.  -3.45*cm
:COLOUR copper_shell -1 1 -1
:VOLU copper_base TUBE 0.  $OuterR_Cu_shell $Length_Cu_base/2.  G4_Cu
:PLACE copper_base 1 world RMO 0.  0.  -6.175*cm
```

```
:COLOUR copper_base -1 1 -1
:VOLU copper_bottom TUBE 0.  $OuterR_Cu_bottom $Length_Cu_bottom/2.  G4_Cu
:PLACE copper_bottom 1 world RMO 0.  0.  -6.75*cm
:COLOUR copper_bottom -1 1 -1
:VOLU copper_first notch TUBE $OuterR_Cu_shell $OuterR_Cu_first notch $Length_Cu_first
notch/2.  G4_Cu
:PLACE copper_first notch 1 world RMO 0.  0.  -1.25*cm

////////////////////////////// Detector crystal ////////////////////////////

:VOLU crystal TUBE 0.  $OuterR_Ge $Length_Ge/2.  G4_Ge
:PLACE crystal 1 world RMO 0.  0.  -1.91*cm
:COLOUR crystal 1 -1 -1

////////////////////////////////// Groove //////////////////////////////////

:VOLU groove TUBE $InnerR_Groove $OuterR_Groove $Length_Groove/2.  G4_AIR
:PLACE groove 1 world RMO 0.  0.  -3.1*cm

////////////////////////////// Dead Layers /////////////////////////////////

:VOLU FrontDeadLayer TUBE 0.  $OuterR_FrontDeadLayer $Length_FrontDeadLayer/2.
G4_Ge
:PLACE FrontDeadLayer 1 world RMO 0.  0.  -0.65*cm
:COLOUR FrontDeadLayer 1 -1 -1
:VOLU SideDeadLayer TUBE $OuterR_Ge $OuterR_FrontDeadLayer $Length_Ge/2.  G4_Ge
:PLACE SideDeadLayer 1 world RMO 0.  0.  -1.91*cm
:COLOUR SideDeadLayer 1 -1 -1
:VOLU BackDeadLayer TUBE $OuterR_Groove $OuterR_FrontDeadLayer $Length_BackDeadLayer/2.
G4_Ge
:PLACE BackDeadLayer 1 world RMO 0.  0.  -3.21*cm
:COLOUR BackDeadLayer 1 -1 -1
:VOLU DeadLayerInGroove TUBE 0.  $InnerR_Groove $Length_BackDeadLayer/2.  G4_Ge
:PLACE DeadLayerInGroove 1 world RMO 0.  0.  -3.21*cm
:COLOUR DeadLayerInGroove 1 -1 -1

////////////////////////////////////////////////////////////////////////////

:CHECK_OVERLAPS * ON
```

A full explanation of the commands implemented in the Geometry code is given in the following table:

Parameter	Value (cm)	Description
InnerR_lead	12.5	Inner radius of lead shielding
OuterR_lead	17.5	Outer radius of lead shielding
Length_shielding	34	Length of the graded shielding
InnerR_tin	12.45	Inner radius of tin shielding
InnerR_Cu	12.35	Inner radius of copper shielding
InnerR_Al	3.95	Inner radius of aluminum (Al) cap
OuterR_Al	4.1	Outer radius of Al cap
Length_Al	16.79	Length of the Al cap
InnerR_Al_top	3.2	Inner radius of the top of the Al cap
Length_Al_top	0.15	Thickness of the top of the Al cap
InnerR_Cu_shell	3.051	Inner radius of the copper shell surrounding the detector
OuterR_Cu_shell	3.201	Outer radius of the copper shell
Length_Cu_base	0.15	Thickness of the copper shell
OuterR_Cu_bottom	2.851	Outer radius of the copper support
Length_Cu_bottom	1	Thickness of the copper support
OuterR_Cu_first notch	3.351	Outer radius of the first notch in the copper shell
Length_Cu_first notch	0.6	Thickness of the first notch
Length_Carbon_Epoxy	0.06	Thickness of the carbon epoxy window
Length_Ge	2.5195	Thickness of the germanium crystal
OuterR_Ge	2.97	Outer radius of germanium crystal
OuterR_Groove	1.1	Outer radius of the groove of the point contact
InnerR_Groove	0.7	Inner radius of the groove
Length_Groove	0.3	Groove depth inside the detector
Length_FrontDeadLayer	0.0005	Front dead layer depth
OuterR_FrontDeadLayer	3.05	Outer radius of the front dead layer
Length_BackDeadLayer	0.08	Rear dead layer thickness

Table E.1: GEOMETRY.geom description

input.in

```
# Set geometry, physics and generator
/gamos/setParam GmGeometryFromText:FileName BeGe.geom              # (1)

/gamos/geometry GmGeometryFromText                                 # (2)
/gamos/physicsList GmEMPhysics                                     # (3)
/gamos/generator GmGenerator                                       # (4)
/run/initialize                                                    # (5)
/gamos/generator/addIsotopeSource source Am241 384960*becquerel    # (6)
/gamos/generator/positionDist source GmGenerDistPositionPoint 0.  0.  24.47*cm
#(7)

#################### Visualization ####################

/control/execute /home/yazed/Packages/GAMOS/GAMOS.5.0.0/examples/visVRML2FILE.in
#(8)

################ Recording hits in the sensitive volume (crystal)
################

/gamos/userAction GmRecHitsHistosUA                                # (9)
/gamos/userAction GmCountProcessesUA                               # (10)
/gamos/setParam SD:EnergyResol:Ge 5.544e-04                        # (11)
/gamos/setParam SD:EnergyResolFluct:Ge 9.653e-04                   # (12)
/gamos/setParam SD:EnergyResolInstr:Ge 2e-04                       # (13)
/gamos/SD/assocSD2LogVol GmSDSimpleExactPos Ge crystal             # (14)
/gamos/SD/recHitBuilder GmRecHitBuilder1to1 Ge                     # (15)
/gamos/setParam rechits:FileName rechitsAm241Res.out               # (16)
/gamos/setParam SD:GmRecHitsWriteUA:BinFile 0                      # (17)
/gamos/userAction GmRecHitsWriteUA                                 # (18)

####################Run histories ####################

/run/beamOn 100000000                                              # (19)
```

A full explanation of the commands implemented in the input code is given in the following table:

Command No.	Function
1	Sets the name of the geometry file where the geometry is described.
2	To tell GAMOS to use the constructor of geometry from text file.
3	Sets GAMOS physics list as the electromagnetic Geant4 physics.
4	It tells GAMOS to use GAMOS generator.
5	To initialize Geant4 and run N events.
6	Sets an isotopes as a particle source.
7	Sets the position distribution at which all particles are generated.
8	For visualizing geometry.
9	A reconstructed hit builder to simulate energy-broadening effect.
10	Gives a list of the process names attached to each particle in the physics list. It is also required for executing the other commands.
11	Sets the energy broadening in the detector, which may be attributed to the incomplete charge collection.
12	Sets the statistical fluctuation in the charge production.
13	Sets the instrumental effects (electronic noise).
14	Specifies one of the Geant4 sensitive detector class to create deposits of energy inside the detector.
15	Reconstructed hit builder to enable to simulate the detector energy resolution.
16	To set the name of the output file.
17	To select text format for storing reconstructed hits.
18	To store the constructed hits for MATLAB analysis.
19	To run N events.

Table E.2: input.in description

Appendix F

Additional Outputs

Fig. F.1 shows the Compton continuum arising from the high-energy gamma emissions of ^{137}Cs that makes detecting low radioactivities from the low-energy gamma emissions of ^{241}Am difficult, hence minimising the detector sensitivity.

Fig. F.2 shows the MTSort outputs of the gated t90 versus t30 risetime maps produced by gating on energy region of interests on the full energy photopeaks for the calibration source NPRL 604. While Fig. F.3 shows the MTSort output of the ungated t90 versus t30 risetime map. The application of the polygonal gates that form the risetime filters is shown on these risetime maps.

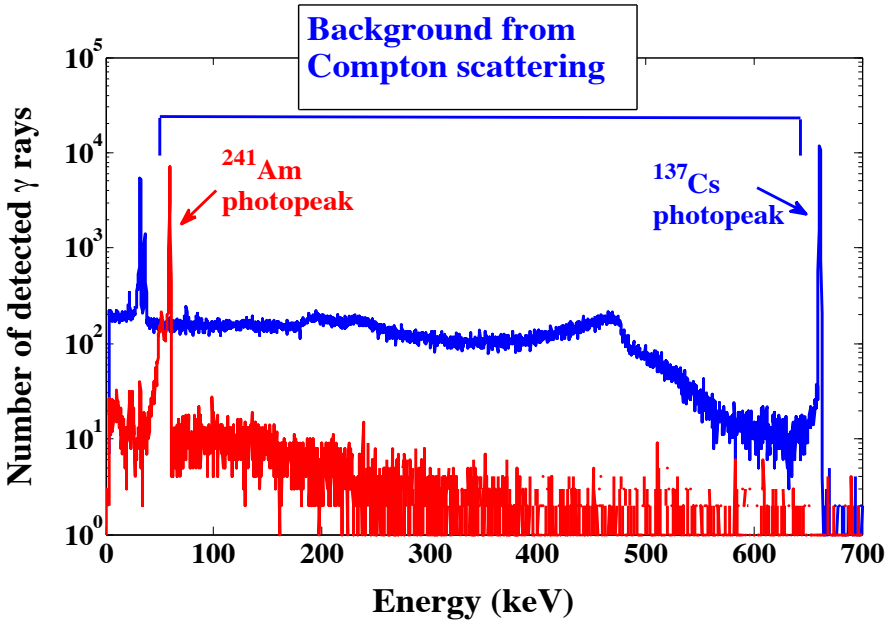

Figure F.1: An example of the distributions of energy detected using the high-resolution gamma-ray spectrometry system shown in Fig. 4.2(A) for incident low- and high-energy gamma emissions of ^{241}Am (0.071MBq) and ^{137}Cs (0.370MBq) respectively. The point sources were independently positioned at 15cm above the centre of the detector face, measured over a full acquisition system live time of 410.33 s.

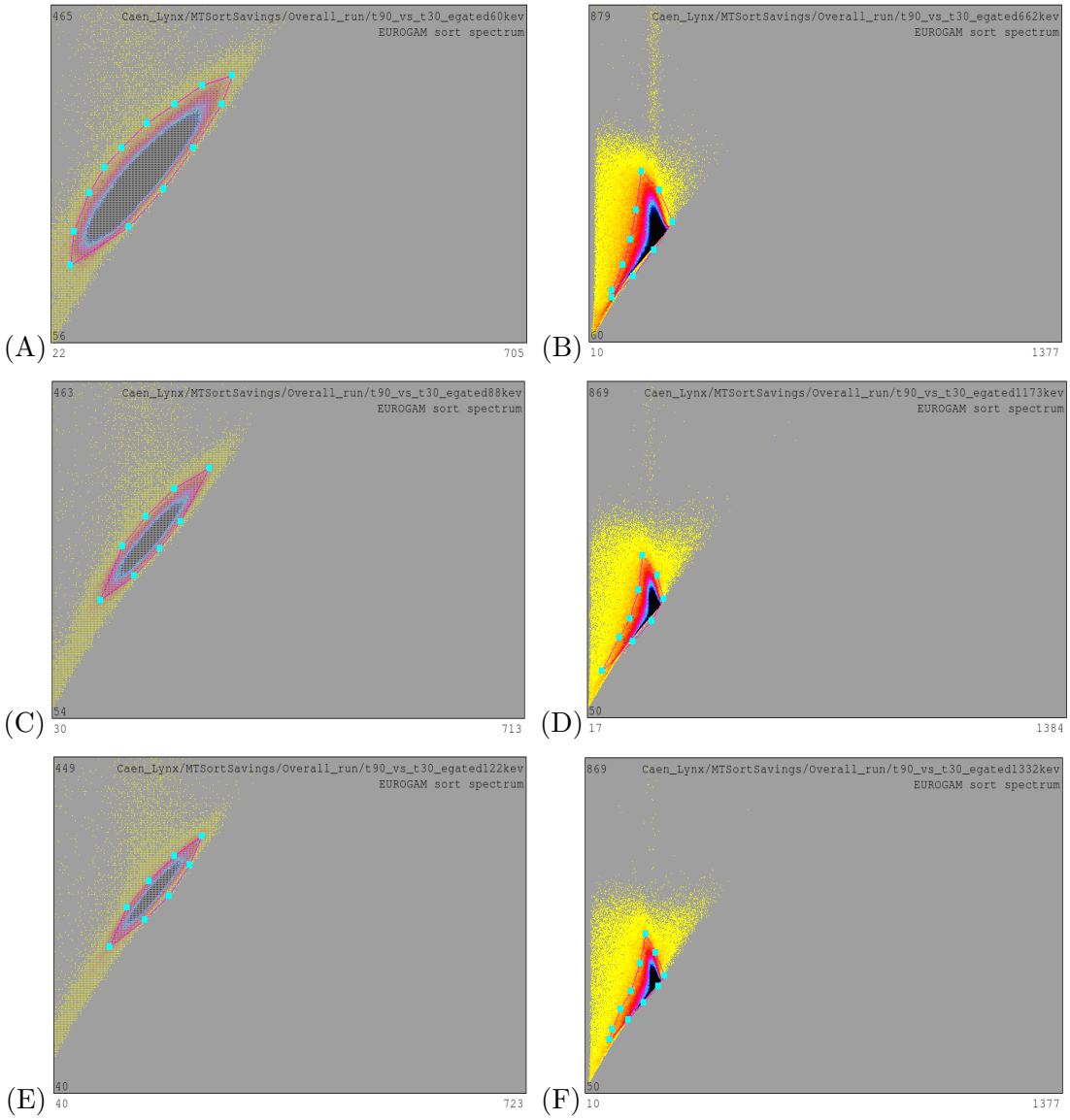

Figure F.2: Screenshots of the MTSort display of the polygonal gates (risetime regions of interest) applied on the gated t90 versus t30 risetime maps, shown in Fig. 6.17, of (Left panels; A, C and E) the full-energy photopeaks of 60keV, 88keV and 122keV respectively, and of (right panels; B, D and F) full-energy photopeaks of 662keV, 1173keV and 1333keV respectively.

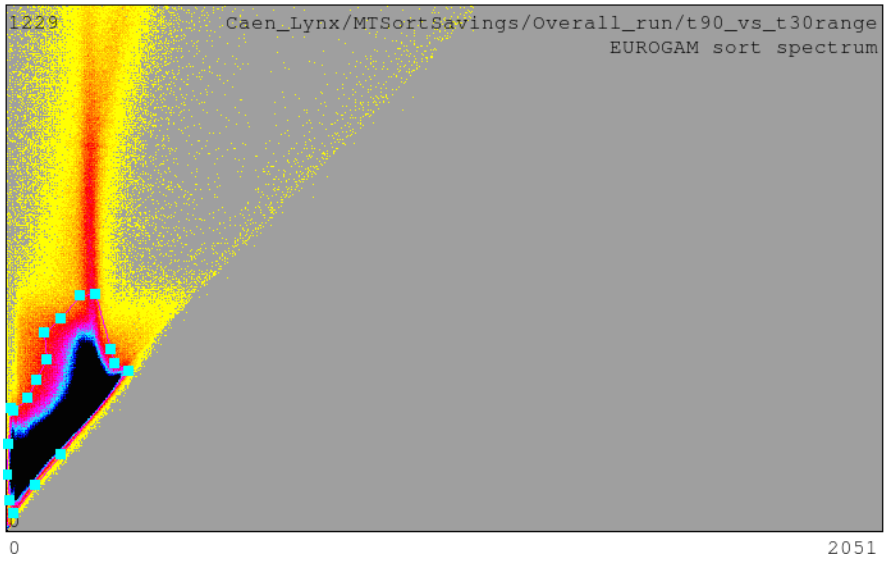

Figure F.3: Screenshot of the MTSort display of the polygonal gate (risetime region of interest) applied on the ungated t90 versus t30 risetime map, shown in Fig. 6.16.

Bibliography

[A+03] S. Agostinelli et al. GEANT4 - a simulation toolkit. *Nuclear Instruments and Methods in Physics Research A.*, 506:250–303, 2003.

[A+06] J. Allison et al. GEANT4 Developments and Applications. *IEEE Transactions on Nuclear Science.*, 53:270, 2006.

[B+68] G. Bertolini et al. Semiconductor Detectors. *Elsevier Science*, (1968).

[B+96] C W. Beausang et al. Large Arrays of Escape Suppressed Spectrometers for Nuclear Structure Experiments. *J. Phys. G: Nucl. Part. Phys.*, 22(5):527–558, May (1996).

[B+07] P.S. Barbeau et al. *Astropart. Phys.*, 09:009, 2007.

[B+10] D. Barrientos et al. Characterisation of a Broad Energy Germanium (BEGe) Detector. Simulation and Experimental Results. *IEEE Proceedings of the Nuclear Science Symposium*, 39:662–666, 2010.

[B+13] R. Britton et al. Determining the Efficiency of a Broad-Energy HPGe Detector using Monte Carlo Simulations. *Journal of Radioanalytical and Nuclear Chemistry.*, 295:2035–2041, 2013.

[B+16] N.A. Beresford et al. Thirty Years After the Chernobyl Accident: What Lessons Have We Learnt? *Journal of Environmental Radioactivity*, 157:77–89, 2016.

[Bil67] H.R. Bilger. Fano Factor in Germanium at 77 Degrees K. *Physical Review*, 136(2):238, (1967).

[Bos99] Andrew John Boston. Spectroscopy of neutron-deficient Tellurium isotopes using a large γ-ray spectrometer plus ancillary detectors. PhD thesis, University of Liverpool, 1999.

[C+11] R.J. Cooper et al. A Pulse Shape Analysis Technique for the MAJORANA Experiment. *Nuclear Instruments and Methods in Physics Research A.*, 629:303–310, 2011.

[C+16] J. A. Caborn et al. Spatial Trends on an Unglazed West Cumbrian Saltmarsh of Surface Contamination by Selected Radionuclides over a 25 Year Period. *Journal of Environmental Radioactivity*, 151:94–104, 2016.

[CA17] Chernobyl Accident 1986. http://www.world-nuclear.org/information-library/safety-and-security/safety-of-plants/chernobyl-accident.aspx, Online accessed: 20/1/2017.

[Cae16a] Caen. User Manual UM2606 DT5780 Dual Digital MCA Rev. 3 - 02 February 2016. http://www.caen.it/jsp/Template2/CaenProd.jsp?parent=64&idmod=756, Online accessed: 12/12/2016.

[Cae16b] Caen. User Manual UM3182 MC2 Analyzer User Manual Software for Digital Multi Channel Analyzer Rev. 2 - November 4th, 2016. http://www.caen.it/jsp/Template2/CaenProd.jsp?parent=64&idmod=756, Online accessed: 12/12/2016.

[Can14] Canberra. CANBERRA Broad Energy Germanium Detectors (BEGe) data sheet. available at:. http://www.canberra.com/products/485.asp, 2014.

[Cur68] L.A. Currie. Limits for Qualitative Detection and Quantitative Determination. Application to Radiochemistry. *Anal. Chem.*, 40:586–593, 1968.

[D+16] Branka Djurović et al. Chernobyl and Fukushima Nuclear Accidents: What have we learned and what have we done? *Vojnosanitetski Pregled: Military Medical & Pharmaceutical Journal of Serbia*, 73(5):484–490, 2016.

[Ell06] S. R. Elliott. *Journal of Physics Conference Series.*, 39:314, 2006.

[F+14] K. Fantnov et al. Monte Carlo Simulation of the BEGe Detector Response Function for in VIVO Measurements of ^{241}Am in the Skull. *Radiation Physics and Chemistry.*, 104:345–350, 2014.

[Fan47] U. Fano. Ionization Yield of Radiations. 2. The Fluctuations of The Number of Ions. *Physical Review*, 72(1):26–29, (1947).

[G+94] A. Georgiev et al. An Analog-to-Digital Conversion Based on a Moving Window Deconvolution. *IEEE Transactions on Nuclear Science.*, 41:1116–1124, 1994.

[G+95a] G.N. Gilmore et al. *Practical Gamma-Ray Spectroscopy.* New York: Wiley, (1995).

[G+95b] J. Gray et al. Discharges to the Environment from the Sellafield Site. *Journal of Radiological Protection*, 2:99–131, 1995.

[GAM14] GAMOS. User's Guide to GAMOS 5.0.0. http://fismed.ciemat.es/GAMOS/GAMOS_doc/GAMOS.5.0.0/GamosUsersGuide_V5.0.0.pdf, Online accessed: 10/7/2014.

[GF316] GF3. http://radware.phy.ornl.gov/gf3/gf3.html, Online accessed: 12/12/2016.

[Gou72] F. S. Goulding. *Nuclear Instruments and Methods*, 100:493, 1972.

[H+03] R.G. Helmer et al. The Use of Monte Carlo Calculations in the Determination of a Ge Detector Efficiency Curve. *Nuclear Instruments and Methods in Physics Research A.*, 511:360–381, 2003.

[HB+14] L.J. Harkness-Brennan et al. An Experimental Eharacterisation of a Broad Energy Germanium Detector. *Nuclear Instruments and Methods in Physics Research Section A.*, 760:28–39, (2014).

[He01] Zhong He. Review of the Shockley-Ramo Theorem and its Application in Semiconductor Gamma-Ray Detectors. *Nuclear Instrumentation and Methods in Physics Research A.*, 463:250–267, 2001.

[J+94a] V. T. Jordanov et al. Digital Synthesis of Pulse Shapes in Real Time for High Resolution Radiation Spectroscopy. *Nuclear Instruments and Methods*, A345:337–345, 1994.

[J+94b] V. T. Jordanov et al. Digital Techniques for Real-Time Pulse Shaping in Radiation Measurements. *Nuclear Instruments and Methods*, A353:261–264, 1994.

[K+14] O. Karadeniz et al. Radiological Mapping in the Granodiorite Area of Bergama (Pergamon)-Kozak, Turkey. *J. Radiational Nucl. Chem.*, 302:361–373, 2014.

[K+16] M. Karatasli et al. Natural and Fallout Radioactivity Levels and Radiation Hazard Evaluation in Soil Samples. *Environ. Earth Sci.*, 75:424, 2016.

[Kno10] G.F. Knoll. *Radiation Detection and Measurement*. Wiley, 4 edition, (2010).

[L+10] R. Lus et al. Parameter Optimisation of a Planar BEGe Detector using Monte Carlo Simulation. *Nuclear Instruments and Methods in Physics Research Section A.*, 623:1014–1019, 2010.

[Lyn16] Lynx. Lynx; Digital Signal Analyzer. http://www.canberra.com/fr/produits/radiochemistry_lab/pdf/Lynx-SS-C38658.pdf, Online accessed: 14/09/2016.

[M+97] D. S. McGregor et al. *Nuclear Instruments and Methods*, A395:101, 1997.

[M+11a] G. Meierhofer et al. *Journal of Physics Conference Series.*, 312:072011, 2011.

[M+11b] N. Menaa et al. Evaluation of Real Time Digital Pulse Shapers with Various HPGe and Silicon Radiation Detectors. *Nuclear Instruments and Methods in Physics Research Section A*, 652(1):512–515, (2011).

[M+15] S. Mohapatra et al. On the Radiological Assessment of Natural and Fallout Radioactivity in a Natural High Background Radiation Area at Odisha, India. *J Radioanal Nucl. Chem.*, 303:2081–2092, 2015.

[MCN] MCNP. User's Guide to MCNP4C Monte Carlo N-Particle Transport Code System.

[MID16] MIDAS. Midas Control & Data Acquisition for CAEN Digital ADCs. http://npg.dl.ac.uk/MIDAS/MIDASNewGenDataAcquisition/base.html, Online accessed: 12/12/2016.

[Muk76] T. Mukoyama. Range of Electrons and Positrons. *Nuclear Instruments and Methods*, 34:10–12, (1976).

[NIS16] NIST. http://physics.nist.gov/PhysRefData/Xcom/html/xcom1.html, Online accessed: 06/08/2016.

[Nuc13] Nuclear Data. Table of Radioactive Isotopes. http://nucleardata.nuclear.lu.se/toi/nuclide.asp?iZA=950241, Online accessed: 06/04/2013.

[O+04] A. Owens et al. *Nuclear Instruments and Methods*, A531:18, 2004.

[P+69] R.H. Pehl et al. Thin-Window Germanium Detectors - Fallacy and Fact. *Nuclear Instruments and Methods*, 75(1):175, (1969).

[P+11] A. Pedro et al. GAMOS: an easy and flexible way to use GEANT4. *Nuclear Science Symposium and Medical Imaging Conference.*, pages 2230–2237, 2011.

[P+14] A. Pedro et al. GAMOS: A Framework to Do GEANT4 Simulations in Different Physics Fields with an User-Friendly Interface. *Nuclear Instruments and Methods in Physics Research A.*, 735:304–313, 2014.

[Pri11a] Private Communication. Environmental Aspects Module. MSc Radiometrics Course, University of Liverpool, 2011.

[Pri11b] Private Communication. High Resolution Gamma Spectroscopy Module. MSc Radiometrics Course, University of Liverpool, 2011.

[Pri11c] Private Communication. Nuclear Instrumentation Module. MSc Radiometrics Course, University of Liverpool, 2011.

[Pro16] Prospect. Prospect; Gamma Spectroscopy Software. http://www.canberra.com/products/radiochemistry_lab/pdf/ProSpect-C40022.pdf, Online accessed: 14/09/2016.

[R+96] C. L. Rose et al. Radioactivity in Two Tide-Washed Marsh Areas in the Eastern Irish Sea: a Radiological Assessment. *The Science of the Total Environment*, 191:1–13, 1996.

[S+70] A.H. Sher et al. Variation of Effective Fano Factor in a Ge(LI) Detector. *IEEE Transactions on Nuclear Science*, NS17(1):39, (1970).

[S+05] S. Singh et al. ^{226}Ra, ^{232}Th and ^{40}K Analysis in Soil Samples from some Areas of Punjab and Himachal Pradesh, India using Gamma Ray Spectrometry. *Radiation Measurements*, 39:431–439, 2005.

[UNS88] UNSCEAR. Sources and Effects of Ionizing Radiation, 1988.

[V+05a] R. Venkataraman et al. Calculation of Peak-to-Total Ratios for High Purity Germanium Detectors using Monte-Carlo Modeling. *Journal of Radioanalytical and Nuclear Chemistry.*, 264:183–191, 2005.

[V+05b] R. Venkataraman et al. Improved Detector Response Characterization Method in ISOCS and LabSOCS. *Journal of Radioanalytical and Nuclear Chemistry.*, 264:213–219, 2005.

[Z+70] H.R. Zulliger et al. Fano Factor Fact and Fallacy. *IEEE, Transactions on Nuclear Science*, NS17(3):187, (1970).